5-2004

Three-Dimensional Mechanical Behavior of Kaolin Clay with Controlled Microfabric Using True Triaxial Testing

Amit Prashant
University of Tennessee - Knoxville

To the Graduate Council:

I am submitting herewith a dissertation written by Amit Prashant entitled "Three-Dimensional Mechanical Behavior of Kaolin Clay with Controlled Microfabric Using True Triaxial Testing." I have examined the final electronic copy of this dissertation for form and content and recommend that it be accepted in partial fulfillment of the requirements for the degree of Doctor of Philosophy, with a major in Civil Engineering.

Dayakar Penumadau, Major Professor

We have read this dissertation and recommend its acceptance:

Eric C. Drumm, Edwin G. Brudette, Christopher D. Pionke, Y. Jack Weitsman

Accepted for the Council:

Carolyn R. Hodges

Vice Provost and Dean of the Graduate School

(Original signatures are on file with official student records.)

To the Graduate Council:

I am submitting herewith a dissertation written by Amit Prashant entitled "Three-Dimensional Mechanical Behavior of Kaolin Clay with Controlled Microfabric Using True Triaxial Testing." I have examined the final paper copy of this dissertation for form and content and recommend that it be accepted in partial fulfillment of the requirements for the degree of Doctor of Philosophy, with a major in Civil Engineering.

Dayakar Penumadu

Dr. Dayakar Penumadu, Major Professor

We have read this dissertation
and recommend its acceptance:

Eric C Drumm

Dr. Eric C. Drumm

Edwin G. Burdette

Dr. Edwin G. Burdette

Dr. Christopher D. Pionke

Dr. Y. Jack Weitsman

Accepted for the Council:

Vice Provost and Dean of
Graduate Studies

THREE-DIMENSIONAL MECHANICAL BEHAVIOR OF KAOLIN CLAY WITH CONTROLLED MICROFABRIC USING TRUE TRIAXIAL TESTING

A Dissertation Presented for the

Doctor of Philosophy

Degree

The University of Tennessee, Knoxville

Amit Prashant

May 2004

Acknowledgements

I wish to express my sincere gratitude to all those who contributed in the successful completion of this research. I gratefully acknowledge the financial support provided by the National Science Foundation.

I am indebted to my research advisor, Dr. Dayakar Penumadu, for offering me the opportunity to be a part of his excellent research group, encouraging me throughout this study, giving me the flexibility in my research, and even providing help in my daily life.

I would also like to thank the other members of my committee, Dr. Edwin G. Burdette, Dr. Eric Drumm, Dr, Chris Pionke, and Dr. Jack Y. Weitsman, for giving me a chance to have their valuable inputs in my dissertation.

I extend my sincere thanks to my friends and colleagues, Doug Mandeville, Greg Goyette, Kelly Clawson, Dr. Rangda Zhao, Mr. Tedd Ritzko,Han Lin, Amal Dutta, Xin Chen, Alex Devis-Smith, Michael Parham, Mr. Ken Thomas for their help and friendship.

My parents, Dr. S. S. Kanaujia and Artika Kanaujia, and my sisters, Alpana Singh, Archana Singh, Aparna Singh, deserve special recognition for encouraging my education over the years. Their love and faith in me brought me to this point.

I would like to dedicate this thesis to my wife, Ajanta Sachan, for her love and moral support, and to my little angel Ishika Prashant for bringing new colors in my life.

Abstract

Clays in their natural state are mostly anisotropic because of their modes of deposition. Many boundary value problems in geotechnical engineering involve soil elements that are subjected to stress paths with varying relative magnitudes and orientation of principal stresses. In clay, these soil elements may also have different orientations of its microfabric. It is a well-known fact that the variation in relative magnitudes and orientation of principal stresses and the microfabric of clay have significant effect on the stress-strain, pore pressure and shear strength behavior of clay. In order to study this behavior of clay from a normally consolidated to heavily over-consolidated state, a series of strain controlled true triaxial undrained tests with constant intermediate principal stress ratio (b-value) are performed on cubical specimens of Kaolin clay with controlled microfabric. The true triaxial device used in the present research has flexible boundaries and uses three-axis electro-pneumatic Proportional–Integral–Derivative (PID) based real-time feedback control. A custom developed software that can automatically saturate, consolidate and apply shear stresses along predetermined stress or strain paths is also developed for this study. The cubical specimens are prepared in the laboratory with two distinct microfabric of Kaolin clay; flocculated and dispersed.

A comprehensive analysis of the observed three-dimensional behavior of clay is presented in this dissertation with its emphasis on the following factors; the effect of relative magnitudes and orientation of principal stresses, the influence of consolidation history and its role in the anisotropy of clay, and the effect of change in soil's microfabric

on its mechanical response. Strain localization issues are discussed in light of the experimental observations. A method for determining the onset of localization is proposed, which is eventually used in the identification of failure state of stress and strain. The effect of change in the test boundary conditions and specimen shape on the observed mechanical response of clay is evaluated by comparing the results obtained from true triaxial tests using cubical specimens, conventional triaxial tests using cylindrical specimens, and combined axial-torsional tests using hollow cylinder specimens. Two well-recognized constitutive models (modified cam clay model and single hardening model) are evaluated for the present true triaxial test data, and limitations in predicting various aspects of soil behavior within reasonable accuracy are identified. Based on the experimental observations and the past theories on the normalized behavior of clays, a dynamic failure surface as a function of stress state and the pre-consolidation history is proposed. Formulation of a new rate independent elasto-plasticity model is presented, which is based on the normalized clay behavior observed in this study. Validation of the proposed model from this study shows significant potential for predicting the three-dimensional mechanical response of clay.

Table of Contents

Chapter		Page
1.	**Introduction**	1
2.	**Description of True Triaxial Device and Specimen Preparation Procedure**	8
	Introduction	8
	True Triaxial Testing System – Hardware	10
	True Triaxial Testing System- Software	16
	Membrane Compliance in Strain Calculation	22
	Preparing Remolded Cubical Specimens of Kaolin Clay	23
	Assembly and Saturation	28
	Summary	32
3.	**Three-Dimensional Behavior of Normally Consolidated Kaolin Clay**	33
	Abstract	33
	Introduction	34
	Specimens for Testing	37
	Test Systems and Testing Procedures	38
	True Triaxial System	38
	Lubricated end Triaxial and Axial-Torsional Test Setup	39
	Isotropic Consolidation	42
	Results from True Triaxial Tests on Cubical Specimens	43

Stress-Strain and Pore Pressure Behavior 44
Failure Conditions 49
Observations from Three Different Laboratory Shear Testing Methods 55
Conclusions 61

4. **Effect of Intermediate Principal Stress on Overconsolidated Kaolin Clay** 64
Abstract 64
Introduction 65
Previous Investigations 66
True Triaxial Testing 69
PID Feedback Control during Overconsolidated Clay Testing 72
Stress–Strain and Pore Pressure Behavior 76
Yield Behavior 78
Failure Criteria 81
Strain Analysis and Localization Phenomenon 85
Bifurcation and Undrained Instability 85
Sum of Principal Strains 87
Localization with Shear Band Formation 92
Variation of Principal Strains and Strain Rates 93
Conclusions 97

5. **Development of Suitable Three-Dimensional Yield and Failure Surfaces from Experimental Data** 99
Abstract 99

Introduction 100
Consolidation Behavior of Clay 102
Shear Failure and Localization 105
Undrained Shear Behavior from Triaxial Compression Tests at Different 'OCR' Values 106
Influence of Intermediate Principal Stress 113
Shear Strength of Clay 115
Failure surface in triaxial plane 117
Failure surface in deviatoric plane 121
Conclusions 123

6. **Effect of Microfabric on the Three-Dimensional Behavior of Kaolin Clay** 126
Abstract 126
Introduction 127
Obtaining Pre-conceived Microfabric of Clay in Laboratory 130
Preparing Cubical Specimens 133
Consolidation Behavior for Flocculated and Dispersed Microfabric 135
Experimental Observation from True Triaxial Tests 142
Stress-Strain Relationship and Shear Failure 144
Evolution of Excess Pore Pressure and Stress Paths in q-p' Space 149
Strength and Pore Pressure Parameters 154
Failure Surface and Plastic Strain Increment Vectors in Deviatoric Plane 156
Conclusions 158

7. **Evaluation of Existing Constitutive Models for Cohesive Soil: Review, Formulation, and Predictions** 160

Introduction 160

Elasto-Plasticity Theory 161

Three-Dimensional Stress Space 164

Summery of Constitutive Theories Proposed to Describe Soil Behavior 164

Modified Cam-Clay Model 168

Modified Cam Clay Model Predictions for Kaolin Clay 171

Critical State Concept and Failure Criteria 177

Single Hardening Model 178

Determination of Single Hardening Model Parameters for Kaolin Clay 179

Computing Hardening Parameter from Plastic Work 187

Single Hardening Model Predictions for Kaolin Clay 189

Conclusions 194

8. **A New Unified Elasto-Plastic Three-Dimensional Constitutive Model for Cohesive Soil** 198

Introduction 198

Framework of the Proposed Model in Triaxial Compression Plane 200

Determination of Parameters for Kaolin Clay 210

Model Prediction for Kaolin Clay 215

Extension of the Proposed Model in Deviatoric Plane 219

Influence of Intermediate Principal Stress 220

Model Predictions for Constant b-value True Triaxial Tests ($\delta = 0°$) 222

Influence of Principal Stress Rotation 222

Model Predictions for extension tests ($\delta = 90°$) 226

Conclusions 227

9. **Conclusions and Recommendations** 229

Summary and Conclusions 229

Recommendations for Future Research 232

List of References 237

Appendices 252

Appendix 1: Stress Invariants 253

Appendix 2: Modified Cam-Clay Model: Formulation in Principal Stress Space 255

Appendix 3: Single Hardening Model Formulation 257

Appendix 4: Relationship between Third Invariant of Stress Tensor and Shear Stress Ratio 261

Appendix-5 Procedure for Projecting Principal Stress State onto an Octahedral/Deviatoric Plane 264

Vita 268

List of Tables

Table		Page
3.1	Properties of Kaolin Clay	37
3.2	Tests Performed on Normally Consolidated Specimens of Kaolin Clay	45
3.3	Strength Behavior Observed in Three Testing Methods	58
4.1	Summary on the Influence of Intermediate Principal Stress from Prior Research	70
4.2	Mean Effective Stress Values at Failure	81
6.1	Summary of Tests	143
7.1	Summary of Constitutive Models for Soil	166
7.2	Calculation of Yield Parameter h	186
7.3	Single Hardening Model Parameters for Kaolin Clay	190
8.1	Model parameters for Kaolin Clay	214

List of Figures

Figure		Page
1.1	Scanning Electron Microscopy Pictures of Pennsylvania Fire (natural) Clay with, (a) Flocculated, and (b) Dispersed Microfabric, (Penumadu, 1996)	2
1.2	Orientation of Principal Stress during True Triaxial Testing (Direction of Soil Deposition or Axis of Cross-anisotropy along z-axis)	5
2.1	Configuration of the True Triaxial Device	11
2.2	True Triaxial Device	11
2.3	Closeup Views of, (a) Space Frame, (b) Flexible Membranes, (c) Pressure Housing, and (d) Assembled Setup.....	12
2.4	Mold and Membrane used in Test Setup	15
2.5	Overview of the PID Control Loop	18
2.6	Logic Used in PID Control Setup	20
2.7	Membrane Compliance Tests, (a) σ_z and $\sigma_x = \sigma_y$ = constant, and (b) $\sigma_z = \sigma_y$ and σ_x = constant	24
2.8	Consolidometer used for Specimen Preparation, (a) Consolidometer, (b) Prepared Specimen (4 inch cube), and (c) Dimensions of Cubical Specimen	25
2.9	Water Content Analysis at the End of Slurry Consolidation (From Mandville and Penumadu, 2003)	27
2.10	Assembling the Specimen in True Triaxial Device	29
3.1	Principal Stresses Acting on Cubical Element during Shearing	40

3.2 Principal Stresses Acting on the Element from (a) Hollow, (b) Solid Cylinder Specimen during Shearing 42

3.3 Isotropic Consolidation Curves for Different Specimen Shapes 43

3.4 Maximum Shear Stress, $\tau = (\sigma_1 - \sigma_3)/2$, and Excess Pore Pressure Δu Evolution with Major Principal Strain for Different b-values – Cubical Specimen 46

3.5 Variation of Deviatoric Stress, Pore Pressure due to Shear, and Shear Stress Ratio with Shear Strain for Different b-values – Cubical Specimen 47

3.6 Stress Path in q-p Space for the Loadings Applied on Cubical Specimens 49

3.7 Three Dimensional Failure Surface for Kaolin Clay in Octahedral Plane (Symbols without Test Numbers are Located by Symmetry) 51

3.8 Angle of Internal Friction, ϕ', and Shear Stress Ratio at Failure, M, with b-values – Cubical Specimens 53

3.9 Variation Pore Pressure Parameters, A_f and a_f, with b-values 56

3.10 Stress-Strain and Pore Pressure Response for Tests on Cubical, HC , and SC Specimens (b=0 and 1) 57

3.11 Stress-Strain and Pore Pressure Response for Tests on Cubical and HC Specimens (b=0.25, 0.5 and 0.75) 60

4.1 Parameter A_f for Undrained Compression and Extension Test Data [From Parry (1960)] 67

4.2 Effect of PID Coefficients on Feedback Control, (a) Major Principal Strain Evolution, (b) Major Principal Strain Rate 74

4.3 Effect of PID Control on the Observed Stress-Strain Relationship 75

4.4 Stress-Strain Response for Different b-values 77

4.5	Excess Pore-Pressure during Shearing for Different b-values	79
4.6	Variation of Pore Pressure Parameter A_f with b-values	79
4.7	Determination of Yield Points from Strain Energy Approach	80
4.8	Three Dimensional Failure Surface in Octahedral Plane	83
4.9	Angle of Internal Friction Compared with Different Failure Criteria ...	85
4.10	Sum of Principal Strains during Undrained Shear Test for Different b-values	88
4.11	Deformation to Failure in Cubical Specimen, (a) Undeformed Specimen, (b) Deformed Specimen, (c) Strain Variation at Edges and Corners, (d) Strain Localization (Shear band), and (e) Deformation Zones in Cubical Specimen	90
4.12	Variation of Principal Strain with Time during Shear Test	94
4.13	Strain Rate Variation in Three Principal Directions during Shear Test (b = 0.5, 0.75 and 1.0)	95
5.1	Direction of K_o Consolidation for Vertical (V), and Horizontal (H) Specimens	104
5.2	Consolidation Curves for Vertical (V) and Horizontal (H) Specimens	104
5.3	Shear Stress-Strain Behavior from Undrained Compression Tests (b=0) at Various OCR Values	107
5.4	Effective Stress Path for Undrained Compression Tests (b=0) at Various OCR Values	108
5.5	Excess Pore Pressure (a) Total, and (b) Part due to Shear for Undrained Compression Tests (b=0) at Various OCR Values	111
5.6	Influence of Intermediate Principal Stress and Anisotropy on the Shear Stress-Strain Behavior of Clay	112
5.7	Variation of Normalized Undrained Strength with OCR	117

5.8	Isotropic Consolidation Curve for a Typical Clay	118
5.9	Failure Surface in Normalized q-p' Plane	120
5.10	Failure Surface in Deviatoric Plane	122
6.1	Mineral Structure of Kaolin Clay	132
6.2	Ionic Distribution on Kaolin Clay Platelet in Aqueous Medium	132
6.3	Arrangement of Particles or Particle Groups for Flocculated and Dispersed Microfabric	132
6.4	SEM Pictures of Clay for (a) Flocculated, and (b) Dispersed Microfabric	135
6.5	Consolidation Behavior from CRS Tests	137
6.6	Isotropic Consolidation Curves for Flocculated and Dispersed Microfabric, (a) Void Ratio, (b) Volumetric Strain	139
6.7	Individual Normal Strains along the Three Axes of Cubical Specimen during Isotropic Consolidation Curves for Flocculated and Dispersed Microfabric	141
6.8	Shear Stress-Strain Relationship for NC Clay	146
6.9	Shear Stress and Strain at Failure: (a) Shear Strain at Failure, (b) Undrained Shear Strength	147
6.10	Shear Stress-Strain Relationship for OC Clay	148
6.11	Excess Pore Pressure Evolution for NC Clay	151
6.12	Excess Pore Pressure Evolution for OC Clay	152
6.13	Effective Stress Paths for NC and OC Clay	153
6.14	Strength Parameters, (a) Effective Friction Angle, Shear Stress Ratio, (b) Pore Pressure Parameters, A_f and a_f	155
6.15	Failure Surface and Strain Increment Vectors in Deviatoric Plane	157
7.1	Triaxial and Deviatoric Plane in Three-Dimensional Stress Space	164

7.2 Stable State Boundary Surface in p'-q-v Space 169
7.3 Yield Surface and CSL in q-p' Plane 169
7.4 NCL, URL, and CSL in Compression Plane 170
7.5 MCC Predictions and Experimental Data from True Triaxial Undrained Tests on NC Kaolin Clay (b=0, 0.5, 1) 173
7.6 MCC Predictions and Experimental Data from True Triaxial Undrained Compression Tests (b=0) on OC Kaolin Clay 175
7.7 Stress Paths in q-p' Plane: MCC Predictions and Experimental Data from True Triaxial Undrained Compression Tests (b=0) on Kaolin Clay 176
7.8 Determination of Elastic Parameters for SH Model 181
7.9 Determination of Parameters for Failure Criterion for SH Model 181
7.10 Determination of Plastic Potential Function Parameters from Three Traditional Triaxial Tests 183
7.11 Determination of Hardening Parameters from Isotropic Consolidation Test, (a) Plastic Work Computation, (b) Hardening Parameters 185
7.12 Determination of Yield Function Parameter α from Three Traditional Triaxial Tests 187
7.13 Determination of Hardening Parameters From Isotropic Consolidation Test using Incremental Plastic Work Method 189
7.14 Single Hardening Model Predictions and Experimental Data from True Triaxial Undrained Tests on NC Kaolin Clay 191
7.15 Single Hardening Model Predictions and Experimental Data from True Triaxial Undrained Compression Tests (b=0) on OC Kaolin Clay (OCR=1.5 and 2.0) 195

7.16 Stress Paths in q-p' Plane: Single Hardening Model Predictions and Experimental Data from True Triaxial Undrained Compression Tests (b=0) on Kaolin Clay 196

8.1 Shape of Yield Surface in q-p' Stress Space, (a) Growth of Yield Surface with Change in Consolidation History p_o', and (b) Growth of Yield Surface with Change in State Variable L. 202

8.2 Typical Shapes of Yield Surface, Failure Surface, and Reference Surface in q-p' Stress Space 204

8.3 Components of Stress State Mapping Function ξ 206

8.4 Derivatives of Plastic Potential with respect to (a) Mean Effective Stress p', and (b) Deviatoric Stress q 207

8.5 Determination of Hardening Parameter n_L, and Initial L Value (L_o) ... 213

8.6 Determination of Plastic Potential Parameter n_g 214

8.7 Proposed Model Predictions and Experimental Data from True Triaxial Undrained Compression Tests (b=0) on OC Kaolin Clay 216

8.8 Stress Paths in q-p' Plane: Proposed Model Predictions and Experimental Data from True Triaxial Undrained Compression Tests (b=0) on Kaolin Clay 218

8.9 Constraining Failure surface to Positive Effective Stress Quadrant of Three-Dimensional Stress Space, (Triaxial Compression Plane) 221

8.10 Proposed Model Predictions and Experimental Data from True Triaxial Undrained Tests on NC Kaolin Clay 223

8.11 Proposed Model Predictions and Experimental Data from True Triaxial Undrained Tests on OC Kaolin Clay (OCR = 5) 224

8.12 Proposed Model Predictions and Experimental Data from True Triaxial Undrained Tests on OC Kaolin Clay (OCR = 10) 225

8.13 Proposed Model Predictions and Experimental Data from True Triaxial Undrained Tests on NC Kaolin clay (b=1, δ=90°) 227

A4.1 Lode Angle in Deviatoric Plane 261

A5.1 Three-dimensional Stress Space: Projection of Point P on σ_1-axis in Octahedral Plane 265

A5.2 Triaxial Plane: Offset of Point P along σ_1-axis from Origin in Octahedral Plane 265

A5.3 Co-ordinates of Stress Point P in Octahedral Plane with Basis along σ_1, σ_2, and σ_3 267

A5.4 Co-ordinates of Stress Point P in Octahedral Plane with Basis along x and y 267

List of Symbols and/or Abbreviations

a	Henkel's pore-pressure parameter for deviatoric loading
A	Skempton's pore-pressure parameter for deviatoric loading
a_f	At failure Henkel's pore-pressure parameter for deviatoric loading
A_f	At failure Skempton's pore-pressure parameter for deviatoric loading
b	Intermediate principal stress ratio
B	Skempton's pore-pressure parameter
β	Angle of principal stress rotation from axis of cylindrical specimen
C_{ae}	Coefficient of secondary compression
C_C	Compression index
C_f	Failure surface parameter in proposed model
C_S	Swelling index
C_y	Reference surface parameter in proposed model
CI	Hydrostatically consolidated
CK_o	Anisotropically consolidated
CRS	Constant rate of strain consolidation test
DSC	Directional shear cell
$d\lambda$	Loading factor
δ	Angle of principal stress rotation from axis of cross-anisotropy
E	Elastic Young's modulus

e	Void ratio
ε	Total strain
ε^e	Recoverable (elastic) strain
ε^p	Permanent (plastic) strain
ε_p	Volumetric strain
ε_q	Shear strain in invariant form
$\dot{\varepsilon}_1$	Major principal strain rate
$\Delta\varepsilon_1$	Major principal strains
$\Delta\varepsilon_2$	Intermediate principal strains
$\Delta\varepsilon_3$	Minor principal strains
$\Delta\varepsilon_m$	Mean of major, intermediate and minor principal strains
ϕ'	Angle of internal friction
γ	Plastic potential parameter in proposed model
Γ	Specific volume at unit pressure on critical state line
H	Material Hardening
I_1	First invariant of stress tensor
I_2	Second invariant of stress tensor
I_3	Third invariant of stress tensor
J_2'	Second invariant of deviatoric stress tensor
J_3'	Third invariant of deviatoric stress tensor

K_o	Coefficient of earth pressure at rest condition
K'	Elastic bulk modulus
k	Parameter for failure surface based on third invariant
k_1	Parameter for failure surface based on third invariant
κ	Slope of unload-reload line
L	State variable in proposed model
l_o	Anisotropic state variable in proposed model
LC	Lateral compression test
LSSV	Length of stress vector in three dimensional space
Λ_0	Failure surface model in proposed model, plasticity ratio
λ	Slope of normal compression line
M	Shear stress ratio at failure
n_L	Hardening parameter in proposed model
n_g	Plastic potential parameter in proposed model
ν	Poisson's ratio
η	Shear stress ratio
OCR	Overconsolidation ratio
p	Mean total stress in invariant form
PID	Proportional–Integral–Derivative based logarithm
PSE	Plain strain extension test

PSC	Plain strain compression test
p'	Mean effective stress in invariant form
p'_o	Pre-consolidation mean effective stress
q	Deviatoric stress in invariant form
q_y	Shear stress value at reference surface in proposed model
S_u	Undrained shear strength
σ_1	Major principal total stress
σ_2	Intermediate principal total stress
σ_3	Minor principal total stress
σ_{oct}	Octahedral normal stress
σ'_1	Major principal effective stress
σ'_2	Intermediate principal effective stress
σ'_3	Minor principal effective stress
σ'_c	Effective confining stress
σ'_p	Effective pre-consolidation stress
σ'_x	Normal effective stress along specimen's x-axis
σ'_y	Normal effective stress along specimen's y-axis
σ'_z	Normal effective stress along specimen's z-axis
σ'_{vo}	Pre-consolidation vertical effective stress
σ'_a	Normal effective stress along specimen's axial direction

σ'_θ	Normal effective stress along specimen's tangential direction
σ'_r	Normal effective stress along specimen's radial direction
T_{100}	Time for end of primary consolidation
TC	Triaxial compression test
TE	Triaxial extension test
TTT	True triaxial test
$\tau_{\theta z}$	Shear stress applied from torque
Δu	Excess pore-pressure
Δu_f	Excess pore-pressure at failure
Δu_p	Part of excess pore-pressure due to change in mean stress
Δu_q	Part of excess pore-pressure due to change in shear stress
v	Specific volume
v_λ	Specific volume at unit pressure on normal compression line
W	Internal strain energy
W_p	Plastic work
ω_σ	Lode angle
ζ_f	State variable

Chapter 1. Introduction

Soils consist of an assemblage of particles with different sizes and shapes, which form a skeleton, whose voids are filled with water and air or gas. However, a soil mass is commonly treated as a continuum for analysis and design, in which it is considered that the deformation process is dominated by displacements between particles and not by deformation of particles themselves. The interparticle deformations largely depend on the structure of soil, which represents the combined effect of the arrangements of particles, particle groups and pore spaces, and the interparticle forces. The structure and mechanical behavior of natural soil deposits are the result of their geologic history, and in particular of their depositional environment, pre-consolidation history, aging effects and thixotropic hardening, cementation, weathering, leaching and other chemical phenomena. These factors may have their independent or a combined influence on the mechanical properties of soil, which makes the study of soil behavior to be a rather complex task. Problems such as specimen repeatability, inhomogenity, and large volume change or pore pressure generation have further made soil a difficult material to "capture" or model under three dimensional stress conditions.

Soil particles which are finer than 2 μm are generally termed as clay particles as per the Unified Soil Classification System. Clay particles usually have a plate-like shape, which is formed with crystalline structures of minerals. The soil mass containing a majority of these particles is known as clay soil. Clays in their natural state are mostly anisotropic because of their modes of deposition. Most clays that were deposited in post-glacial age are over-consolidated and have varved, laminated or banded structures.

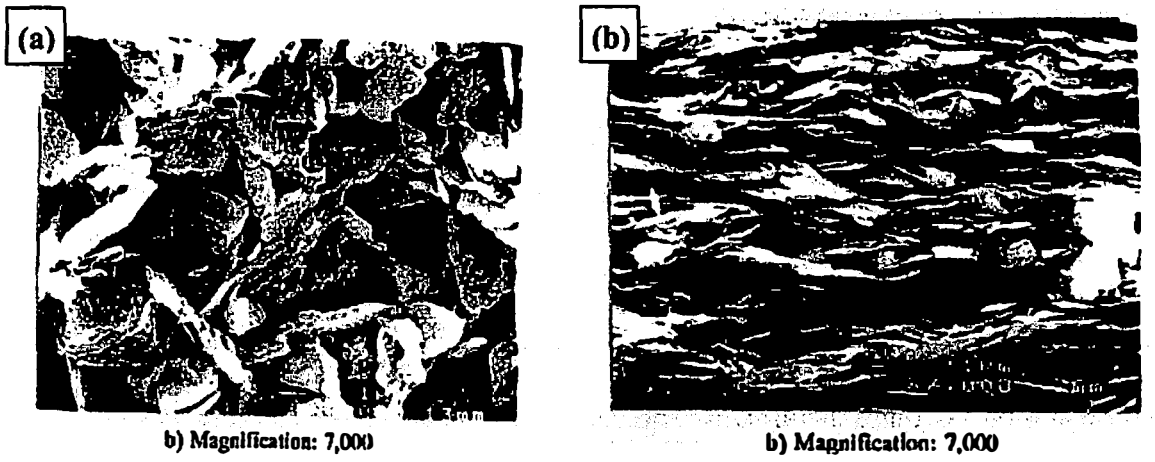

Figure 1.1 Scanning Electron Microscopy Pictures of Pennsylvania Fire (natural) Clay with, (a) Flocculated, and (b) Dispersed Microfabric, (Penumadu, 1996)

Electron microscopy has confirmed that these clays may have flocculated as well as dispersed microstructure with preferred particle orientation. A typical example of these particle orientations is shown in Fig. 1.1. Preferred orientation of clay particles can cause both strength and compressibility of clay to vary with direction, making them highly anisotropic. Even for clay with random orientation of particles, the interparticle force system may cause a considerable degree of anisotropy, which is usually induced because of its loading history. Therefore, the stress-strain behavior of natural clays is likely to be dependent on both the magnitude and the direction of principal stresses. Recent advances in digital computer technology and in numerical techniques such as the finite difference or the finite element methods, have rendered possible, at least in principle, the solution of properly posed boundary value problems in soil mechanics. Further progress in expanding analytical capabilities in geomechanics depends upon consistent mathematical formulations of generally valid and realistic soil constitutive models. The development of

realistic constitutive relationships for clay requires a comprehensive knowledge about its behavior based on accumulation of data relating to its response when subjected to a wide range of stress paths, giving a proper consideration to its anisotropy.

An increasing effort has been devoted since the 1950's to a comprehensive description of the fundamental behavior of clay. These tests often involved single axis loading conditions and formed the basis for several existing theories such as Critical State Soil Mechanics (Roscoe and Burland 1968) that attempt to explain the complex mechanical behavior of soil. However, the applicability of single axis tests (e.g. triaxial compression test) to model soil behavior is limited. The insitu stress conditions often involves three unequal principal stresses i.e. the intermediate principal stress (σ_2') varies from the major (σ_1') or minor (σ_3') principal stress (e.g., slope stability, excavations, and soil-foundation interactions). Recent advances in testing systems, data acquisition, and control methods provide an opportunity for evaluating the deformation and strength behavior of clay under truly three-dimensional states of stress and strain. Early devices that were capable of performing three-dimensional tests were limited in their capabilities. They were cumbersome, difficult to operate and typically required some sort of manual control to perform the tests. This made it difficult to be able to perform true stress and strain control tests, the results were not reproducible, and the accuracy of the test was significantly dependent on its operator. Recent advances in control hardware and software has allowed high-speed closed loop control to be used in soil testing. This allows accurate and repeatable tests to be performed on the soil specimens under true target state of stress/strain in real time.

Most experimental studies performed in the past are not conclusive on many facets of the generalized behavior of anisotropic clays. They are incomplete in many aspects of the soil behavior, such as the consideration of localized deformation within the specimens during shearing, consistency of the testing methods, and repeatability of the specimens tested for evaluating normally consolidated to highly overconsolidated clay behavior, influence of microstructure, and a clear understanding of the stress induced anisotropy and its influence on the soil's mechanical properties. A comprehensive experimental database for an identical clay soil under generalized stress conditions (especially true triaxial tests with minimal interference of loading boundaries), which can be used to understand the influence of various factors involved in the complex behavior of clays, is lacking from prior research, and is the motivation for the current study.

A need exists for good quality data using an experimental device built with an advanced feedback control system. The true triaxial device used in the present research performs tests on a 102mm cubical cohesive soil specimens. This device has flexible boundaries and uses three-axis electro-pneumatic Proportional – Integral – Derivative (PID) control with custom developed software that can automatically saturate, consolidate and apply shear stresses along predetermined stress or strain paths. With this fully automated testing system, the soil specimens can be subjected to a wide variety of stress paths to evaluate the three dimensional (3D) mechanical behavior of clays. The specimen can be subjected to three orientations of principal stress with respect to the direction of soil deposition as shown in Fig. 1.2. The relative magnitudes of principal stresses acting on the specimen can be varied, or a proportional loading can be applied to

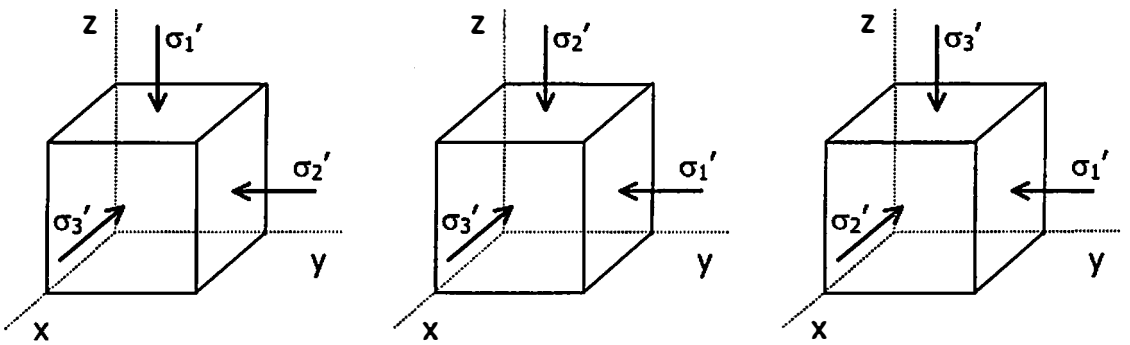

Figure 1.2 Orientation of Principal Stress during True Triaxial Testing
(Direction of Soil Deposition or Axis of Cross-anisotropy along z-axis)

the specimen, which is usually defined by the intermediate principal stress ratio b-value as shown in equation 1.1.

$$b = \frac{\sigma_2' - \sigma_3'}{\sigma_1' - \sigma_3'} \tag{1.1}$$

In the current study, a series of strain controlled constant b-value true triaxial undrained tests were performed on remolded cubical specimens of Kaolin clay with controlled microfabric (microfabric: arrangement of particles or particle groups). Specimens with two distinct microfabrics, flocculated and dispersed, were obtained by consolidating the Kaolin clay slurry under K_o condition (at 207kPa axial stress). The procedure for specimen preparation was developed such that reproducible and homogeneous specimens with controlled microfabric could be obtained. This is a necessary condition in evaluating the influence of a particular factor (such as loading history) on soil behavior with minimal interference of the other uncertainities. The specimens were first hydrostatically consolidated to their virgin consolidation stage (at

275 kPa isotropic stress), and then unloaded to attain various overconsolidation ratios before shearing.

This dissertation presents the results obtained from the above-mentioned series of true triaxial tests. A comprehensive analysis of the observed clay behavior is presented considering the following factors: effect of relative magnitudes and orientation of principal stresses, influence of consolidation history and its role in the anisotropy of clay, and the effect of change in soil's microfabric on its mechanical response. Chapter 2 describes the true triaxial device that was developed to test the cubical specimens of cohesive soils. It also includes details related to control methods employed for testing, the steps involved in the assembly of setup, and the procedure used for preparing the remolded specimens of Kaolin clay. Chapter 3 addresses the influence of stress anisotropy on the shear stress-strain-strength and pore pressure behavior of normally consolidated Kaolin clay, and evaluates the effect of change in the test boundary conditions and the specimen shapes on its observed mechanical response. Chapter 4 concentrates on the effect of intermediate principal stress on the undrained shear behavior of overconsolidated clay and the importance of identifying localized deformation within the specimen. A method for determination of onset of strain localization is proposed in this chapter based on the true triaxial test data. Chapter 5 evaluates the mechanical behavior of normally consolidated to heavily overconsolidated clay in three-dimensional stress space. Based on the experimental observations and from past knowledge on the normalized behavior of clays, a dynamic failure surface is proposed in this chapter, which is a function of stress state and the pre-consolidation history. Chapter 6 presents the influence of microfabric and fabric-induced anisotropy on the consolidation and shear

behavior of soil by comparing the experimental data obtained from the tests performed on Kaolin clay with flocculated and dispersed microfabric. Chapter 7 gives a brief summary of the constitutive models developed for geomaterials using classical elasto-plasticity theory, and evaluates the validity of two well-recognized constitutive theories (modified cam clay model and single hardening model) using present experimental data. Chapter 8 presents a new rate independent elasto-plasticity model that was developed in this study based on the analysis of normalized clay behavior presented in previous chapters. A procedure for determining the model parameters for Kaolin clay, and validation of the new model (by comparing the predictions with the experimental data obtained in the current study) is also included in chapter 8.

Chapter 2. Description of True Triaxial Device and Specimen Preparation Procedure

Introduction

The magnitude and orientation of the principal stresses acting on a soil element can change with the loading situation. Conventional triaxial testing on cylindrical specimens is often used to study the stress-strain behavior of soil in the laboratory. However, the soil element is only subjected to axi-symmetric state of stress in this type of testing. A true triaxial test with independent control of the three principal stresses can evaluate the effect of intermediate principal stress (σ_2) on the mechanical behavior of soil. It is important to study the effect of σ_2 on the yield and failure behavior of soil to accurately model certain boundary value problems associated with slope stability and foundation design.

A number of laboratory testing devices have been developed in the past four decades that facilitate testing of soil specimens in three dimensions. A true triaxial testing device applies three mutually perpendicular principal stresses on a cubical soil specimen using rigid end plates, flexible membranes, or a combination of rigid and flexible boundaries. Kjellman (1936) employed rigid platens to apply three normal stresses on a soil specimen. Ko and Scott (1967), Sture and Desai (1979), Sivakugan et al. (1988), Reddy et al. (1992) all used flexible boundaries. Lade (1978) used a combination of rigid and flexible boundaries. Lade and Musante (1978), and Kirkgard and Lade (1993) used a combination of flexible and rigid boundaries to perform tests on normally consolidated clay specimens. Callisto and Calabresi (1998) recently used flexible boundaries to

perform tests on natural Pisa clay. The advantages and disadvantages of different boundary conditions used in various true triaxial devices were summarized by Sture and Desai (1979), Jamiolkowski et al. (1985) and Arthur (1988). The main drawback of using rigid boundaries is the potential for a non-uniform stress state to exist at the corners of a deforming cubical specimen. For a flexible boundary system, the potential for non-uniformity of deformations at large strains is a concern. A discussion of the potential constraints at the corners in cubical triaxial devices is given by Arthur (1988).

The device described herein was recently developed by Mandeville and Penumadu (2004); which performs tests on a 102 mm cubical cohesive soil specimen. The system consists of a control panel, computer console, hardware to interface between the computer, space frame and six pressure housings. Currently, the device is capable of performing isotropic and K_o consolidation and shear testing via stress or strain control. Several modifications to specimen saturation, consolidation, and shear testing were made in the present study to evaluate the effect of intermediate principal stress on both normally and overconsolidated clay specimens. The issues related to hardware and software used in the system, and performance of tests, are described in this chapter. One of the main improvements with the current testing system is the development of three axis electro-pneumatic PID control and software that can automatically saturate, consolidate, and apply shear stresses along predetermined stress paths. Using this fully automated true triaxial system, the cubical soil element can be subjected to a wide variety of stress or strain paths to evaluate the three dimensional mechanical behavior of clays. The remolded cubical specimens of kaolin clay were obtained using a consolidometer

with 102x102mm square base. The procedure used for preparing the specimen, and assembling it in the true triaxial system for further testing, are described in this chapter.

True Triaxial Testing System - Hardware

The true triaxial device described in this chapter is similar to the one developed by Sture and Desai (1979) and Sivakugan et al. (1988). Figure 2.1 shows the overall configuration of the PID controlled true triaxial test setup developed in this study. Figure 2.2 and 2.3 show photographs of the true triaxial testing device used in this study. The main structural part of the device consists of a space frame (Fig. 2.3a) and six pressure housings. The space frame holds a cubical soil specimen. The six cylindrical pressure housings (Fig. 2.3c) are attached to the six faces of the space frame. A flexible rubber membrane (Fig. 2.3b) separates each face of the soil specimen and the pressure housing. Each pressure housing contains an LVDT (Linear Voltage Differential Transformer, Schaevitz, model GPD-121-500, 15 volts DC bi polar excitation) displacement transducer, for measuring the deformation at the center of each face of the specimen, and two access holes to pressurize the small volume between the housing and the membrane. There are three electro-pneumatic transducers (Fairchild T6000, 0-840 kPa), one for each axis of the space frame. An air supply line connects each axis of the frame to the corresponding electro-pneumatic transducer. Measurement of the total stress in each direction of the cubical sample is accomplished using pressure transducers (Ellison GS4002, 0-1034 kPa). Internal and external pore pressures are measured through the use of absolute pressure transducers (Data Instruments, AB-4, 0-1375 kPa). A photograph of the assembled setup is shown in Fig. 2.3(d). At four corners of the space frame, a diagonal access hole is provided that allows for saturation and drainage attachments. One

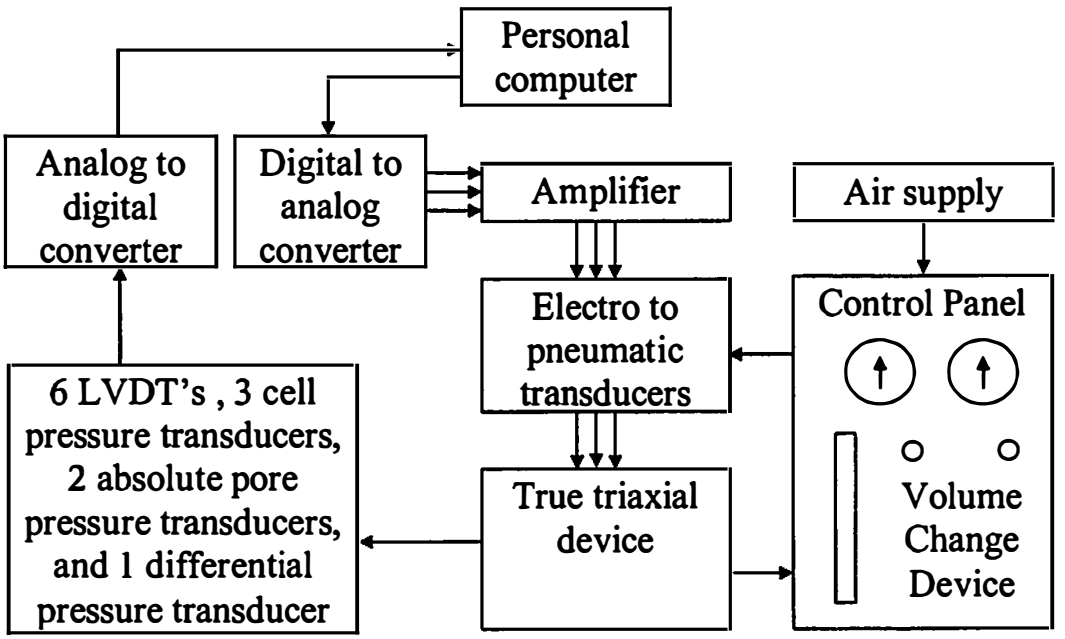

Figure 2.1 Configuration of the True Triaxial Device

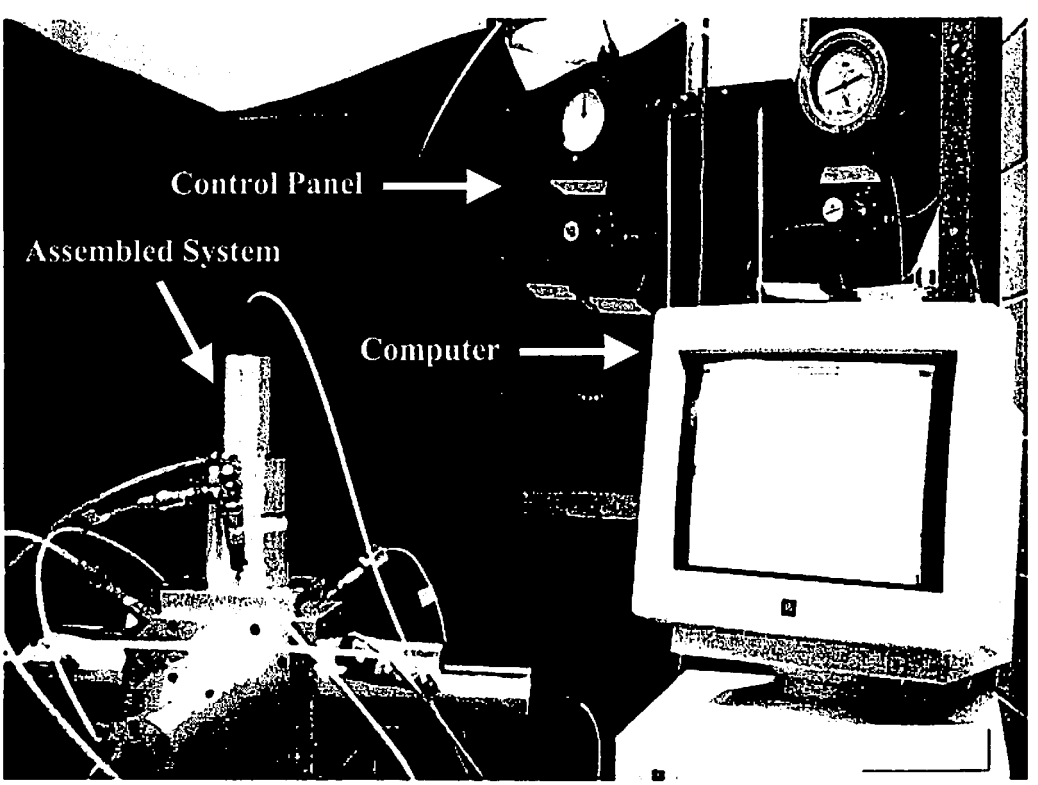

Figure 2.2 True Triaxial Device

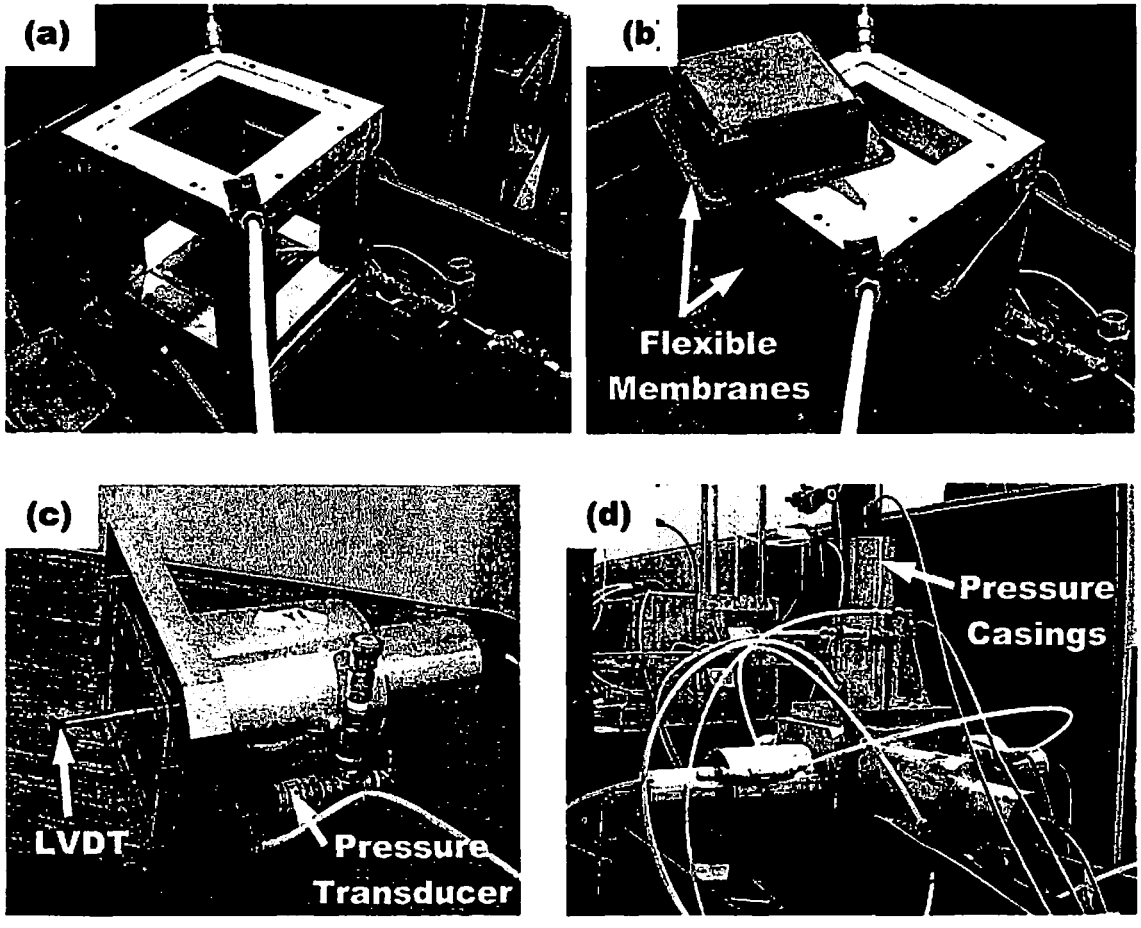

Figure 2.3 Closeup Views of, (a) Space Frame, (b) Flexible Membranes, (c) Pressure Housing, and (d) Assembled Setup

of these ports allows for the insertion of a piezometer needle into the specimen so that the internal pore pressure can be measured at all stages of testing. The needle has an outside diameter of 1.8 mm and a length of 150 mm. A porous plastic plug is inserted into the end of the water saturated needle before the needle is inserted into the clay sample diagonally through one of the access holes. This porous plastic plug prevents the needle from getting clogged with clay and allows for accurate measurement of the internal pore pressure. This piezometer allows for measuring the internal pore pressure at the center of the cubical clay specimen at all times during saturation, consolidation, and shearing. Two flexible drain lines lie against the specimen, one on the top face and one on the bottom face of the specimen. These flexible drain lines extend into the holes drilled in the space frame. These lines have a notch cut on the side that rests against the rubber membrane. The notch allows water to flow through the drain line and saturate the interface between the specimen and membrane. Before the specimen is inserted, the lines are wrapped in filter paper to prevent them from being clogged by the clay during saturation and consolidation stages of testing.

The control panel shown in Fig. 2.2 is used to manually regulate the supply air pressure as well as the back pressure in the system. Attached to the control panel are two low air flow pressure regulators and display gages (one for cell pressure and one for back pressure), and a volume change device. The volume change device consists of a differential pressure transducer and a burette. The differential pressure transducer (Validyne, model P305D, can measure a water height of 50 cm) measures the change in height of the water column as water is expelled from the specimen during consolidation to precisely monitor volumetric strains.

One of the important issues to be carefully considered with the flexible boundary setup is that of interference of membranes at the corners of the specimen. This is a particular concern at the maximum stress levels experienced during the application of shear stresses. The membranes need to meet to prevent the soil from squeezing between the membranes. At the same time, the membranes should not push into adjacent pressure cavities during application of unequal stresses around the sample. One way to overcome this problem is given by Sture and Desai (1979). In their study, membranes made of silicone rubber were made slightly thicker at the corners. Additionally, Teflon strips were placed at the contact points of the membranes. This prevents the membranes from bulging into the adjacent cavities. Teflon also provides a frictionless surface between the membranes so that no shear stress exists on the membranes. Sture and Desai also evaluated the uniformity of strains for a clay specimen tested with flexible boundaries. The specimen was tested in triaxial compression and direct, physical measurements were made on the sample after testing. The sample was measured along the edges and midplanes of the sample. They presented both the final dimension and the corresponding value of the axial strain at 24 different locations on the specimen. It was reported that the specimen remained prismatic with minimal boundary interference.

For the true triaxial testing system described in this chapter, the membranes are 3 mm thick at all points. Initially, silicone RTV was usedas the membrane material. RTV based elastomeric compounds have relatively high water vapor transmission (WVT) rates; this indicates that the RTV compound can let air diffuse across its surface. Air diffusion across the membrane during the consolidation and shear testing phases caused problems related to keeping the clay specimens fully saturated. Membranes with similar

elastic properties but with much more resistance to air diffusion were needed. Butyl rubber was selected as the membrane material and has a WVT rate approximately 210 times smaller than silicone based elastomers. The process to form these membranes requires heat (275 – 300° C) and compression molding. A custom mold was fabricated to be able to handle these process conditions. The bottom of this mold was designed as one solid piece to keep the material from leaking during the high compression forming process. A drawing of the mold and a membrane is shown in Fig. 2.4. These membranes were manufactured in collaboration with Polymeric Research Institute at the University of Akron, Ohio.

Lubrication, consisting of silicone spray, is used on the membranes to minimize the generation of shear stresses at the interface between the specimen and membrane. A test was initially performed by Mandeville and Penumadu (2004) to determine the

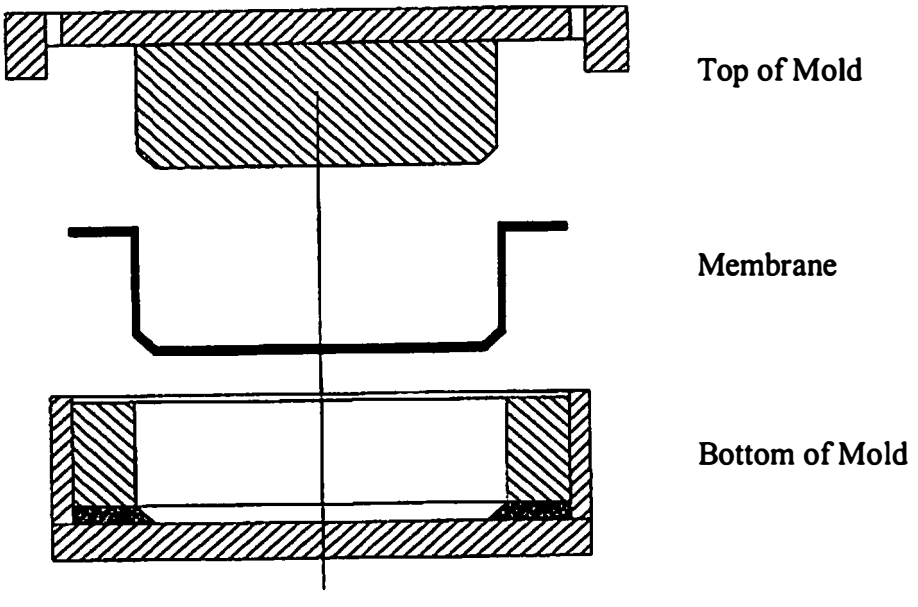

Figure 2.4 Mold and Membrane used in Test Setup

threshold pressure at which the membrane could bulge into adjacent cavities. A rigid block (102 mm cubical specimen) was inserted into the device, the pressure housings and membranes for only one axis were attached to the space frame, and pressure was supplied to the assembled axis. The supply pressure on the pressurized face would mimic the deviator stress encountered during the application of principal stresses in a real test. Only one axis was used so that a visual examination of interface of 2 membranes along an edge could be evaluated. There was very little bulging of the membranes; the thickness of the membranes used in this research was sufficient to prevent the membranes from entering adjacent cavities up to a stress level of 200 kPa. This value is approximately equal to the maximum deviator stress experienced during an undrained triaxial compression test at an effective isotropic consolidation stress of 275 kPa. A careful examination of specimens after shear testing also showed that edge interference was avoided for all of the undrained tests performed to date. A relatively uniform deformation pattern was also observed on all six faces of the cubical samples at the end of testing; this will be discussed further in a following section.

True Triaxial Testing System- Software

The software to perform automated control for this device was written using Viewdac® (Keithley Metrabyte Corporation) data acquisition and control software. It has a series of structured commands that can be arranged in a given order to complete a complex data acquisition or control task. The software has the ability to provide multiple window graphical displays. Data acquisition and control loops can be performed with loop update rates of up to 5 milliseconds. The various phases of triaxial testing such as saturation, consolidation, and application of normal stresses are fully automated.

Mandeville and Penumadu (2000) compared three techniques of control procedures in torsional tests in order to maintain a constant b-value throughout the shear test and showed the variation of strength parameters with different techniques of control. They concluded that the PID based closed loop control appeared to give the best overall control. Therefore, the control in this setup is maintained through the use of the PID algorithm. The algorithm is based on adjusting the output channel to match a target command using three terms: a proportional term P, an integral term I, and a differential term, D, using equation (2.1):

$$O(t) = Pe(t) + I\int e(t')dt' + D\frac{de(t)}{dt} \tag{2.1}$$

The e(t) term represents the error term and is the difference between the target value and the input value at any instant of time. The PID algorithm minimizes this difference by adjusting the output value. For example, if the command stress along a given axis is 5kPa and the actual stress is 2 kPa, the output signal to the electro-pneumatic transducer would cause an increase in the stress. The PID control loop will update all input variables every 20 milliseconds to reduce the e(t) term to a small value quickly. Figure 2.5 shows an overview of PID control loop employed, from the initial stage of acquiring signals to the application of the three principal stresses. The speed of the response and the amount of overshoot during feedback are controlled by using three terms: a proportional gain, P, an integral gain, I, and a differential gain, D.

PID control tuning involves the procedure of determining the appropriate values for these gain terms. Tuning is very important for acquiring the desired stress and strain control options. The P, I, and D coefficients are highly dependent on the material

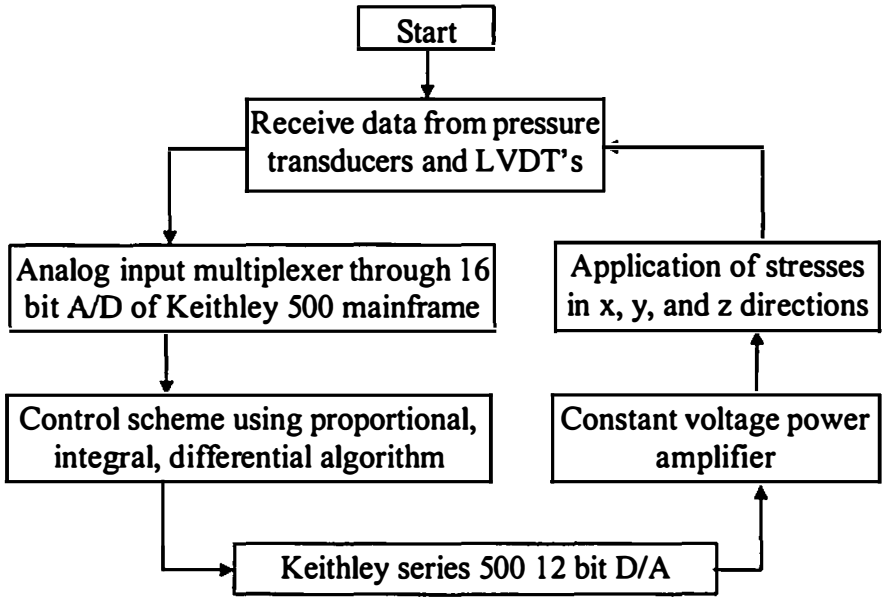

Figure 2.5 Overview of the PID Control Loop

stiffness. To a lesser degree, they are also dependent on the data acquisition and control elements (transducer response time, multi-plexer card, hardware interrupts, processor speed etc.). To find the initial values for the PID coefficients used in this control program, the Zigler - Nichols method of tuning was used (Perry, 1973). For determining the control parameters, this tuning procedure suggests increasing the P term until the variable of interest (stress or strain) starts to cycle continuously around a target value. The period of this oscillation is then used to determine appropriate coefficients for the integral and differential terms. Using this process, a set of PID values were obtained for both stress and strain control for kaolin clay. The control using these coefficients was further improved by adjusting the values to further reduce the response time for accurate control. Final values of P = .029, I = .052, D = 0 provided the best control in the majority of stress and strain path based shear testing for the Kaolin clay.

At several stages during a true triaxial test for cohesive soil, the type of PID control had to be varied from stress to strain control or a combination of both stress and strain control. This posed a unique problem in implementing PID control in various phases of soil testing. Figure 2.6 shows testing options, along with the information on the input and target signals that are currently being used. The PID algorithm can be used to maintain either a desired stress or strain, depending on how the input and target values are setup. For a stress controlled mode, such as applying a hydrostatic stress around the cubical sample during isotropic consolidation, an effective confining pressure of 275 kPa is maintained in excess of the existing back pressure. In a strain controlled mode, the input is the strain along a given axis and the target follows a ramp at a specified rate. The PID control will change the stress on the desired axis so that the target strain and actual strain match. A difficult problem that was encountered during control software development was changing between control modes (stress to strain) and at the same time, maintaining the target pressure during primary consolidation stage. For shear testing, under triaxial compression mode, the stress on one axis is increased to follow a target strain ramp. At this stage, for this axis, control needs to switch from stress control (maintaining constant strain rate) to strain control. A method was developed in Viewdac, whereby the type of control can be changed, and the desired initial stress state was maintained. This development was found to be crucial in being able to achieve precise stress or strain paths and fully automate the three stages of triaxial testing (saturation, consolidation, and application of shear).

The initial PID tuning for the current setup was performed on specimens in a drained condition at an isotropic normally consolidated (NC) state of stress. These values

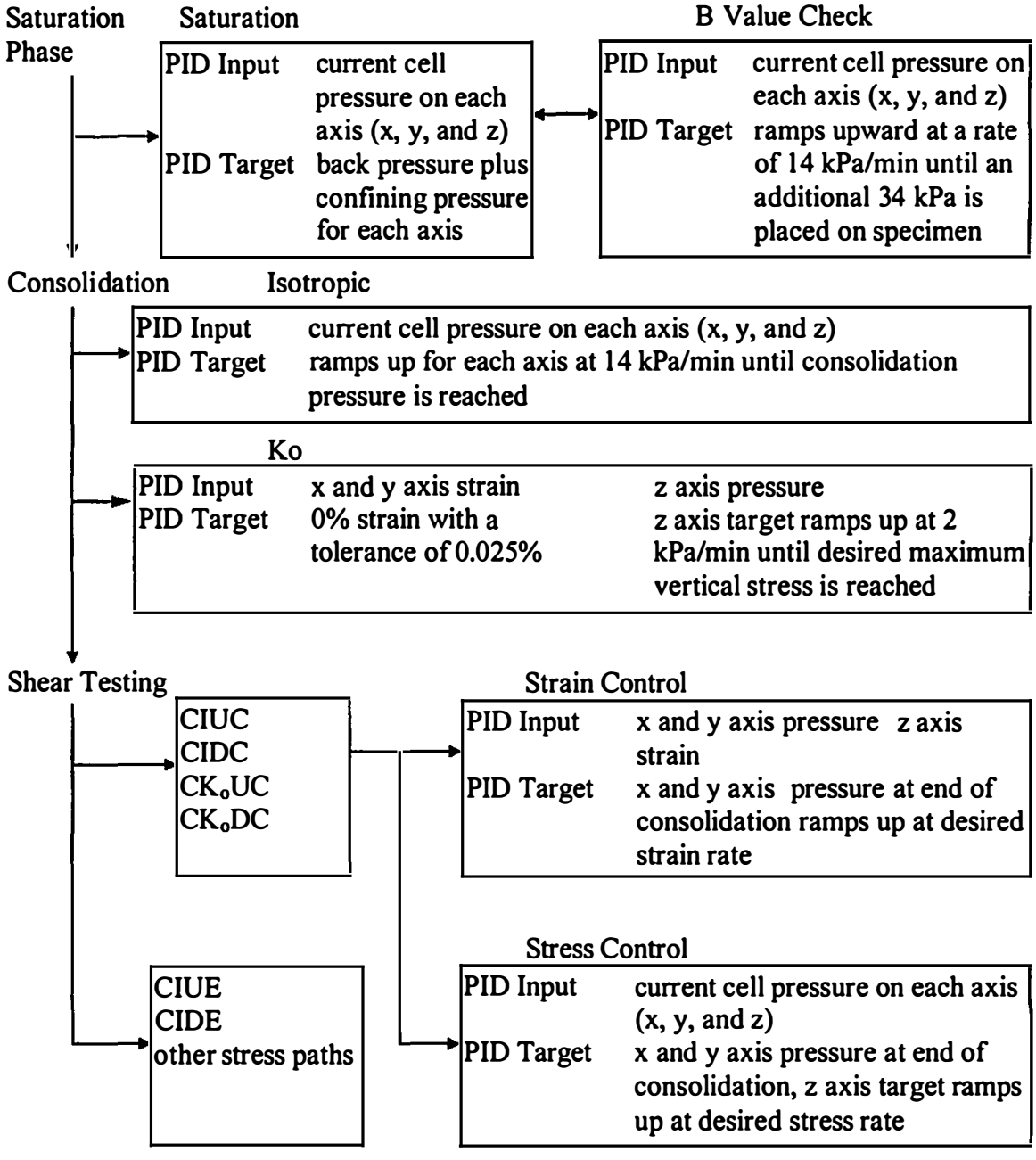

Figure 2.6 Logic Used in PID Control Setup

correspond to P=0.029, I=0.052 and D=0. During an undrained test, excess pore pressures are generated when the deviator stress is applied to the specimen. This results in lower mean effective stresses as the shear deformation increases and a corresponding decrease in the stiffness of the soil specimen with increasing deviator stress. The decrease in soil stiffness affects the accuracy of the PID control algorithm. As the soil stiffness decreases, a small increase in stress can cause a large increase in strain. Use of constant PID coefficient throughout shearing causes the PID control to overshoot the desired target, as the specimen deforms to higher shear strains. Mandville and Penumadu (2003) suggested that the values of P and I could be reduced by a factor of 10 at a threshold major principal strain of 3.5% to correct this problem. However, in the current study it was found that a better control could be achieved if the threshold axial strain was defined at 1%. During undrained shearing on NC specimens, close to 1% axial strain in the major principal stress axis, the PID coefficients were gradually decreased to their final values of P=.0029, I=.0052, and D=0. If the PID values were decreased too soon, the measured strain rate lagged behind the desired strain rate. Changing the PID values at 1% axial strain provided the best overall control, the desired and actual strain rates match well, resulting in a smoother stress strain curve. Test results for a true triaxial system employing pneumatic control with a combination of normally closed and normally open servovalves (Penumadu et al., 1998) could not achieve this precise control, and further demonstrates the potential of the present testing system. One of the main advantages in using PID control is that the target can be constant or a variable. The PID algorithm will always follow the target when accurately tuned parameters are used; which makes it relatively

easy to perform complex stress or strain paths (both monotonic and cyclic) under a true triaxial state of stress.

Membrane Compliance in Strain Calculation

The flexible membranes used in this setup are made of butyl rubber and have a uniform thickness of 3 mm. The deformability of flexible membranes can affect the observed strain values during shearing of a soil specimen. It is essential to measure this membrane deformation at a given value of normal stress and correct the soil strain information form LVDT measurements. In this study, the membrane compliance for strain measurement was determined by using a high strength cubical metal specimen and monitoring three normal strains as a function of stress amplitude within the working range of the device. The size of metal specimen was the same as the cubical clay specimens.

The metal specimen was assembled in the true triaxial setup, in which the stress was applied on the specimen through the flexible membranes. The deformation was recorded on all faces of the specimen, and the deformations on opposite faces were then averaged to calculate the strains along three principal axes of the specimen: x, y, and z. The recorded deformation was essentially from the membranes because the comparative stiffness of metal block was much higher. The strain calculation was based on the size of metal specimen (instead of membrane thickness), so that it could be directly related to the required strain corrections in soil test data.

Axial compression tests were performed on the metal specimens by increasing the stress along z-axis, σ_z, and maintaining constant stress along x-, and y-axis (σ_x, and

σ_y). Three such tests were performed to cover the range of stress amplitudes used in current research: σ_z = 40-130 kPa, 200-425 kPa, and 410-650 kPa. A lateral compression tests was performed, in which $\sigma_z = \sigma_y$ was increased from 410-650 kPa, and σ_x was kept constant. The calculated strain values from these tests are shown in Fig. 2.7 as a function of the applied stress along z-axis of the specimen. These values give a measure of the error induced in the observed and actual stain values for the soil specimens during shearing. Figure 2.7a shows that the strain correction required in the loading direction during a compression test should be approximately 0.03%/100kPa. The normal strain correction for lateral compression (See Fig. 2.7b) remains same as for axial compression; however, volumetric strain correction doubles (0.06%/100kPa) due to biaxial loading.

Strain corrections for the membranes used in current study were incorporated in strain computations during soil testing, although they were found to be very small (compared to soil specimen) within the stress range used in this study.

Preparing Remolded Cubical Specimens of Kaolin Clay

The cubical clay specimens used for all the tests performed in this study were prepared in a slurry consolidometer similar to the one described by Penumadu et al. (1998). The consolidometer and the prepared specimen are shown in Fig. 2.8. The soil specimens (See Fig. 2.8b, and Fig. 2.8c) were 102 mm cubes made of Kaolin clay. The slurry consolidometer (Fig. 2.8a) was made from Plexiglas. It consists of five major parts: a base plate, a 102 mm high bottom, a 356 mm extension, a loading plate, and a load piston. Drainage is provided at the top and bottom of this slurry consolidometer. Both parts of mold (the 102 mm and the 356 mm) are also reinforced with Plexiglas to

(a)

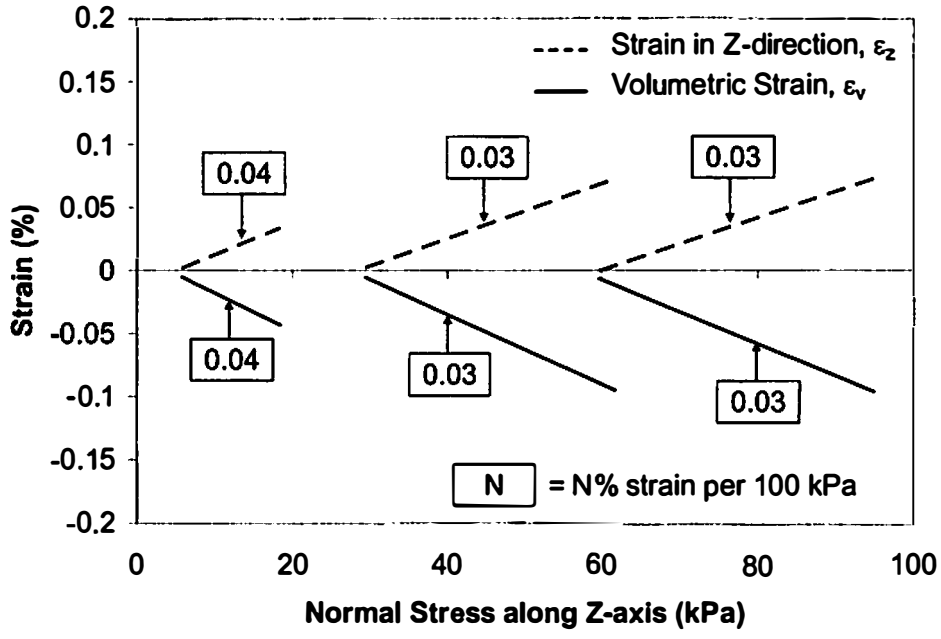

(b)

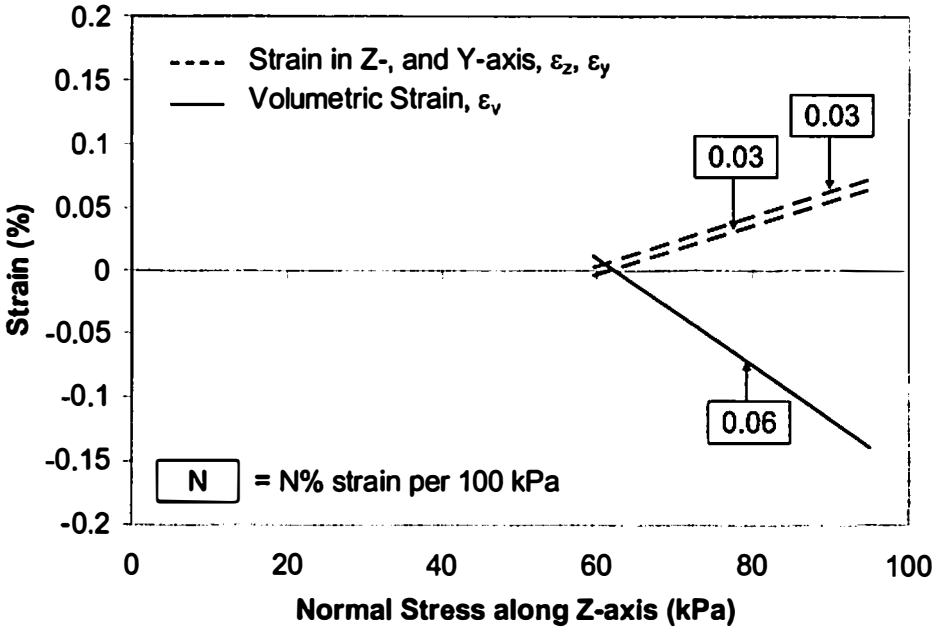

Figure 2.7 Membrane Compliance Tests, (a) σ_z and $\sigma_x = \sigma_y$ = constant, and (b) $\sigma_z = \sigma_y$ and σ_x = constant

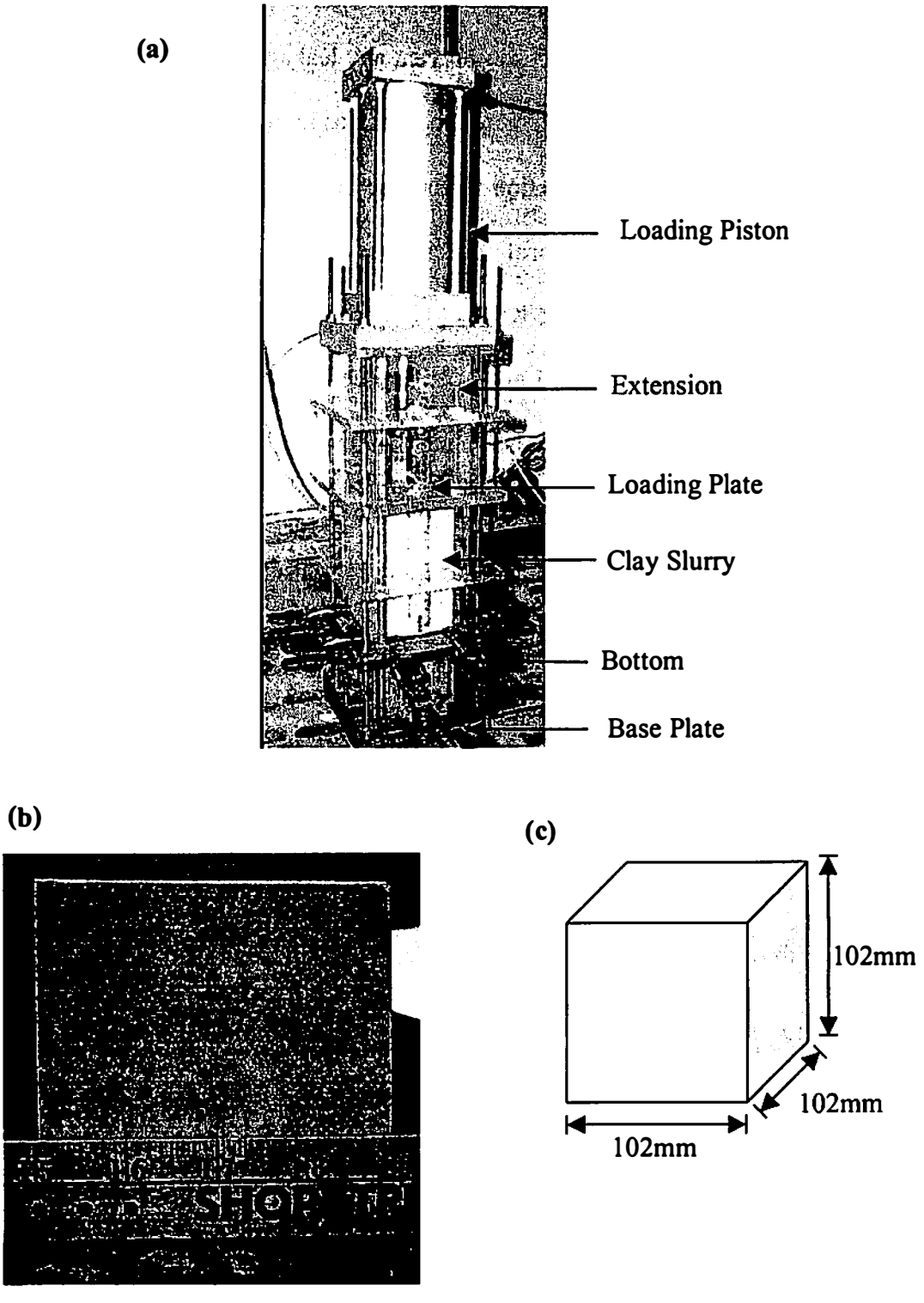

Figure 2.8 Consolidometer used for Specimen Preparation, (a) Consolidometer, (b) Prepared Specimen (4 inch cube), and (c) Dimensions of Cubical Specimen

limit lateral deformations and ensure K_o consolidation of initial slurry. A rubber gasket is used between adjacent Plexiglas pieces to prevent any leakage at the interface. Threaded rods are used to attach the loading piston to the Plexiglas mold.

The method of slurry preparation affects the quality of the specimen obtained at the end of consolidation. Uniform specimens are a condition necessary for therepeatability of tests. Sheeran and Krizek [1971] found that specimens prepared from a higher water content slurry would not be influenced by the method of placement of slurry into the consolidometer. They also found that a water content of 2 to 2.5 times the liquid limit of the soil would be appropriate for slurry preparation. A water content of 155%, corresponding to 2.5 times the liquid limit, was used to make the slurry in the present research. The high water content slurry was transferred into the consolidometer using a funnel. Friction between the consolidometer wall and the slurry plays a major role in consolidation of the slurry. In order to minimize the frictional effects between the consolidometer and the slurry, the bottom of the consolidometer was lined with Teflon in this research. The inner walls of both the bottom and its extension were also sprayed with silicon before the transfer of the slurry.

Initially, the slurry was consolidated under K_o conditions at a vertical effective stress (σ_v') of 25 kPa. The slurry was allowed to consolidate at this stress state for 1 hour. This serves two purposes: ensures that no leaks exist in the assembly of the consolidator, and allows a cake to build up which will help prevent leaks during consolidation at higher stresses. The vertical effective stress on the specimen of kaolin clay was then increased to 207kPa, and the specimens were consolidated under K_0 conditions until the completion of

primary consolidation. End of primary consolidation was determined using the square root of time method (ASTM D2435-96). Mandville and Penumadu (2003) performed a water content analysis on three different specimens at the end of slurry consolidation to evaluate the uniformity in water content across the sample. They divided the 102 mm cubical specimen into 64 smaller samples and the water content distribution was evaluated. The average water content was found to be 42%, with an observed range of 40.03% to 42.88%. Fig. 2.9 shows a typical variation of water content for cubical specimens. Variation of the water content at the end of second stage isotropic consolidation in the true triaxial device was less than 1%. Thus, very homogeneous and repeatable specimens were obtained prior to the application of shear stress.

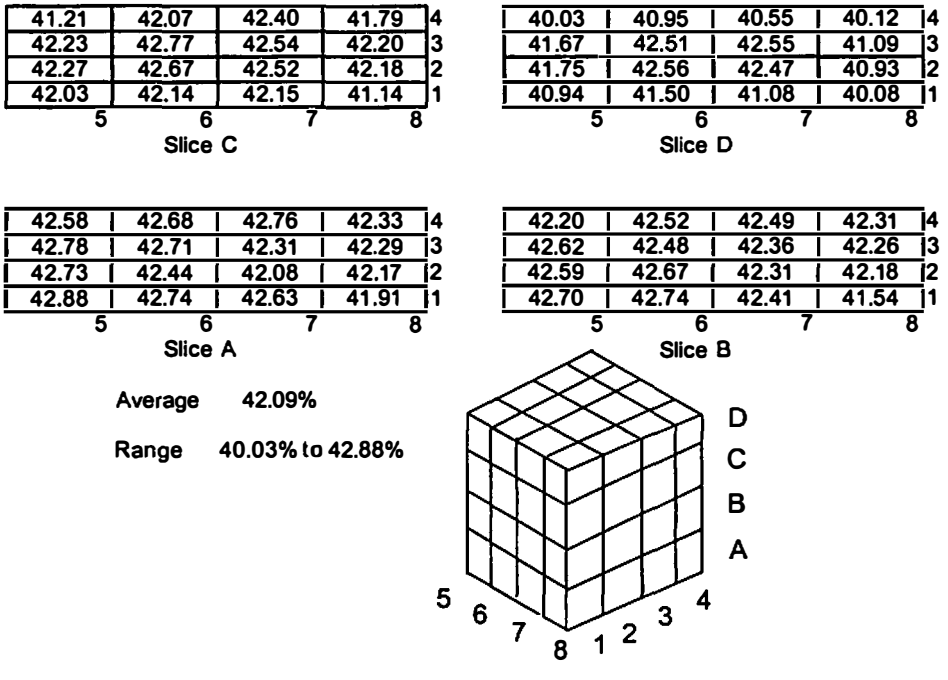

Figure 2.9 Water Content Analysis at the End of Slurry Consolidation (From Mandville and Penumadu, 2003)

Assembly and Saturation

After one dimensional slurry consolidation, the cubical clay specimen was assembled in the true triaxial device with minimum disturbance. Figure 2.10 shows the details of the procedure that was followed during the assembly.

(a) The dimension along each principal axis of the specimen was measured at three different locations, and then averaged to get a representative length.

(b) Filter paper was applied on the six faces of specimen for proper drainage during the consolidation stage. The size of filter paper was kept slightly larger than the size of specimen face in order to have them interconnected by overlapping. This arrangement allowed the water collected from each face during consolidation to move freely towards the outlet drain. The specimen faces were then wetted with de-aired and deionized water to keep the specimen faces saturated and to stop the filter paper movement during the handling of the specimen.

(c) Filter paper was applied on the inlet and outlet drain lines to protect them from getting clogged from clay particles. Three axes were identified on the space frame, x, y and z, and the specimen was placed on the space frame such that the σ_1-axis at the end of slurry consolidation coincided with z-axis.

(d) The location of the specimen was then adjusted to make it approximately at the center of the cuboidal space frame. The outlet drain line was allowed to rest on top face of the specimen.

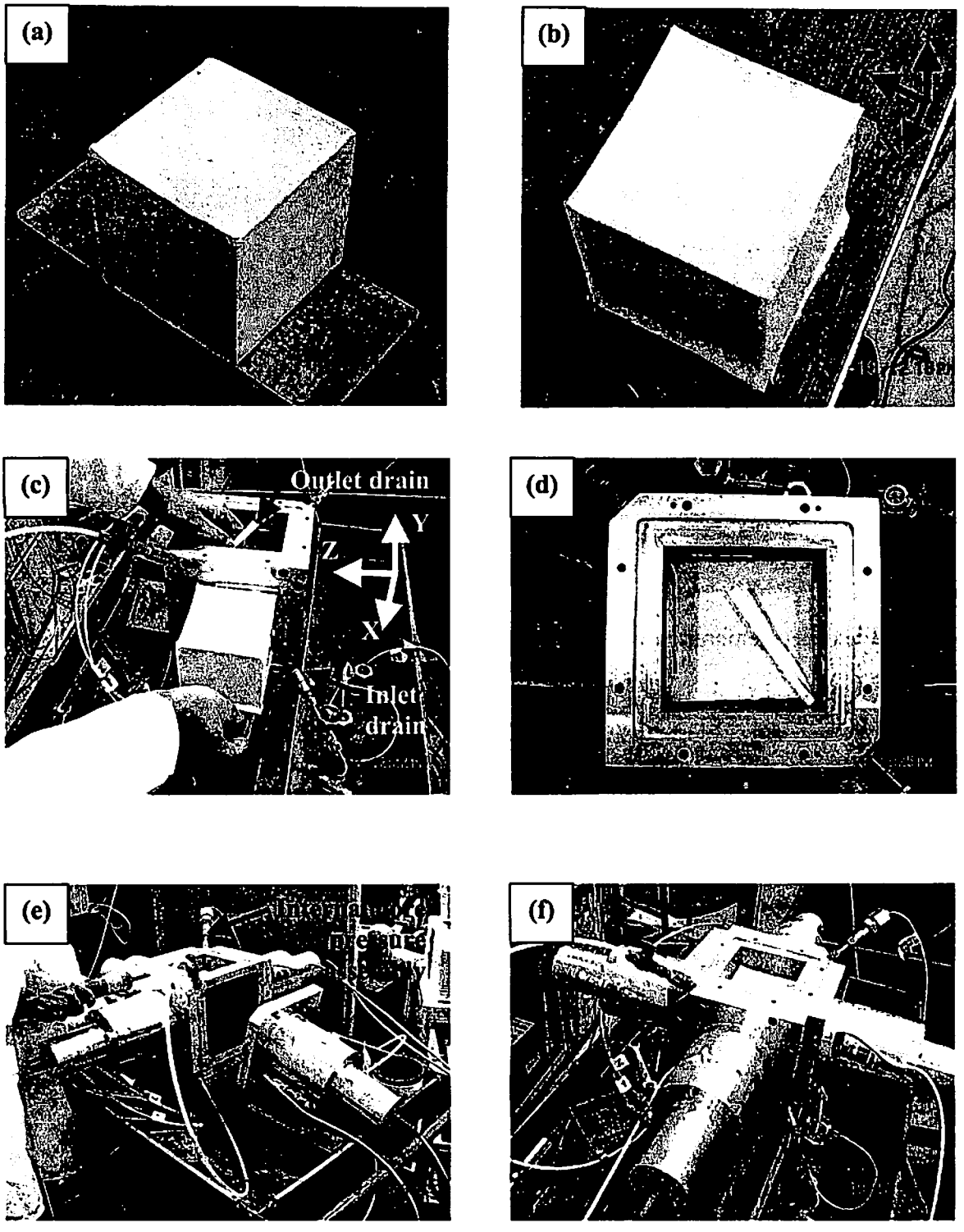

Figure 2.10 Assembling the Specimen in True Triaxial Device

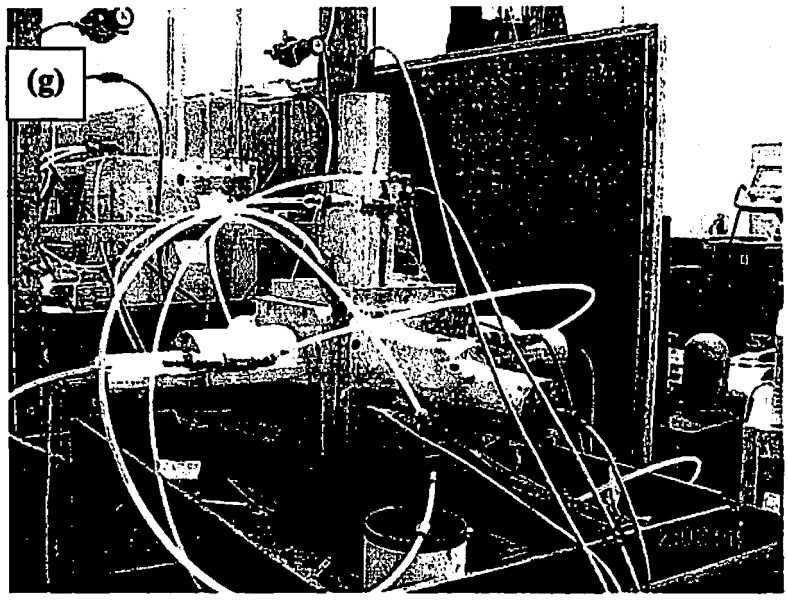

Figure 2.10 Continued

(e) Flexible membranes were placed on four sides of the specimen (excluding top) from outside the space frame. On the same four sides, pressure casings were attached. Internal Pore pressure assembly was placed.

(f) External pore pressure transducer was attached to inlet drain line. De-aired and deionized water was then allowed to flow from bottom of the specimen at low pressure until the water level was approximately 10mm above the specimen's top surface.

(g) The top membrane was placed and a pressure casing was attached on top. To remove more trapped air from inside of the system, de-aired and deionized water was continued to be flushed from bottom to outlet drain at the top. The pressure casings on opposite sides of the specimen were then interconnected to allow equal pressure on two opposite faces of the specimen. Air supply lines were connected

to each axis of the frame, and the corresponding pressure transducers were attached. All transducers and LVDTs were then connected to the Data Acquisition System; which connected the computer to the assembled system.

Using the controls from computer, a small pressure of 1 kPa was applied isotropically on the specimen, while the inlet drain was closed. This allowed the water and the remaining air bubbles from around the specimen to come out through the outlet drain at top. After reaching an equilibriated state (water stopped coming out from top), more water was flushed from the bottom. This whole process was then repeated at the isotropic seating pressure of 35kPa. At the end of this process, it was ensured that no more air bubbles were observed in the drain lines. The specimens were left in this state for few hours to reach equilibrium at an isotropic confining pressure of 35 kPa.

After assembly, the specimens were saturated using backpressure. In this process, the back pressure was increased incrementally. For each backpressure increment, the specimen was allowed to equilibriate, and then the Skempton's pore pressure parameter B was checked by increasing confining pressure on the specimen by an increment of 35 kPa under undrained condition. Skempton's parameter B obtained from the internal pore pressure measurements using a hypodermic needle agreed well with that obtained from the external pore pressure measurements. A minimum B-value of 0.98 was used as the criteria for ensuring full saturation. A constant back pressure of 138 kPa was used during saturation stage for all the tests performed in this study, at which the condition for desired B-value was achieved.

Summary

A flexible boundary electro-pneumatic true triaxial system with independent control of the three principal stresses was used in the current study to evaluate the three dimensional mechanical behavior of a cohesive soil. This device uses a Proportional – Integral – Differential (PID) based closed loop control algorithm to maintain the desired testing conditions. A wide range of stress or strain states can be achieved using this system. The use of PID algorithm allows for precise, repeatable control with minimal operator involvement. It was found that the PID parameters should be properly tuned for accurate control, and they need to be changed with the specimen's stiffness. This device has the ability to measure both the internal and external pore pressures for a 102 mm cubical specimen and uses custom developed Butyl rubber membranes. Measurement of the internal pore pressure was accomplished using a needle piezometer. Issues related to the interference of the flexible membranes, and the air diffusion across flexible membranes were avoided. A 3mm thick membrane made of butyl rubber was found to be adequate. Membrane compliance in strain computations was determined by performing compression tests on high strength metal block specimen. The strain corrections corresponding to membrane compliance were found to have little influence on the accuracy of total strain measured during a test on soil specimen.

The remolded cubical specimens of kaolin clay were obtained by K_o consolidation of 155% water content slurry, and the procedure was described in this chapter. The specimens obtained from this procedure were found to be uniform and homogeneous. The specimens used for testing were saturated using backpressure; and the Skemption's parameter B=0.98 was used as the minimum criteria to ensure full saturation.

Chapter 3. Three-Dimensional Behavior of Normally Consolidated Kaolin Clay

This chapter is a slightly revised version of a paper submitted to the Canadian Geotechnical Journal in 2003 by Amit Prashant and Dayakar Penumadu:

Prashant, A., and Penumadu, D. "A laboratory study of normally consolidated Kaolin clay." In review, Canadian Geotechnical Journal.

My primary contribution to this paper includes (1) selection of the topic and development of the problem into a work relevant to my study of constitutive behavior of cohesive soils, (2) identification of the study areas, (3) gathering and interpretation of literature, (4) performing laboratory experiments, (5) interpretation and analysis of test results, (6) associated writing.

Abstract

In recent years many researchers have attempted to address the need for a comprehensive understanding of the three dimensional mechanical behavior of frictional materials. Advances in testing methods have added the capability of studying various aspects of generalized stress-strain behavior in a controlled environment. Strain-controlled true triaxial undrained tests on normally consolidated kaolin clay are performed in this study using a fully automated flexible boundary experimental setup with real-time feedback control system. Influence of the intermediate principal stress and principal stress rotation on the stress-strain-strength and pore pressure behavior is investigated considering the occurrence of strain localization within the specimen. The strength behavior observed in this study for kaolin clay is used to evaluate existing failure

criteria for cohesive soil. Comparative laboratory tests such as the lubricated end triaxial tests on solid cylinder and combined axial-torsional tests on hollow cylinder kaolin specimens were also performed to evaluate the corresponding mechanical behavior in different loading systems. Despite using identical techniques for specimen preparation and similar consolidation stress states, the soil behavior obtained from the three types of tests showed observable variations, demonstrating the importance of specimen shape and loading/boundary conditions.

Keywords: Normally consolidated clay, Stress-strain behavior, Pore pressure, Anisotropy, Testing Methods.

Introduction

An increasing effort has been devoted since the 1950's to obtain improved description of the fundamental mechanical behavior of soil. Laboratory tests in earlier studies (Henkel 1959; Parry 1960) often involved single axis loading conditions (triaxial compression testing) and formed the basis for several existing theories that attempt to explain the mechanical behavior of soil (Cam-clay model). The stress conditions corresponding to the in-situ state often involves three unequal principal stresses, i.e., the intermediate principal stress (σ_2) can vary from major (σ_1) to minor principal stress (σ_3), or the direction of principal stresses acting on the soil elements may rotate (e.g., slope stability, excavations, and soil-foundation interactions). A number of testing devices have been developed in the last four decades that facilitate the testing of soil specimens in three dimensions. Early devices that were capable of performing these tests were limited in their capabilities. They were cumbersome, difficult to operate and

typically required manual control to perform experiments. Recent advances in electronic data acquisition control hardware and software have allowed high-speed closed loop control to be used in soil testing. This allows for accurate and repeatable tests to be performed on the soil specimens. Shibata and Karube (1965), Broms and Casbarian (1965), Yong and McKyes (1971), Vaid and Campanella (1974), Saada and Bianchini (1975), Lade and Musante (1978), and Kirkgard and Lade (1993) took advantage of these technologies and performed traditional triaxial tests, axial-torsional tests and true triaxial tests. This research indicated significant influence of the magnitude and orientation of principal stresses on the mechanical behavior of cohesive soils. However, comprehensive experimental data for identical clay soil under generalized stress conditions (especially true triaxial tests with minimal interference of loading boundaries) is lacking from prior research. Specifically, the past literature does not address the role of using different apparatus (true triaxial, axial-torsional, traditional triaxial) and specimen shapes (cubical, hollow cylinder, cylinder) for determining mechanical behavior of cohesive soil.

A need exists for good quality data using an experimental device built with an advanced feedback control system. The true triaxial device used in the present research performs tests on a 102 mm cubical cohesive soil specimen. This testing system uses three axis electro-pneumatic Proportional – Integral – Derivative (PID) control and applies three mutually perpendicular principal stresses on cubical soil specimens using flexible membranes. Using this fully automated testing system, soil specimens were subjected to a wide variety of stress paths to evaluate the three dimensional (3D) mechanical behavior of clays. This chapter presents an experimental study of the influence of the stress anisotropy on the stress-strain-strength and pore pressure behavior

of normally consolidated (NC) Kaolin clay under undrained conditions. A series of true triaxial (TT) tests were performed for various values of the intermediate principal stress ratio, b, defined as

$$b = \frac{\sigma_2 - \sigma_3}{\sigma_1 - \sigma_3} \tag{3.1}$$

where σ_1 and σ_3 are the major and minor principal stress values and σ_3 is the intermediate principal stress.

Lin and Penumadu (2003) performed combined axial-torsional tests on hollow cylinder (HC) specimens of the same clay for an identical consolidation state of stress and using a similar specimen preparation technique. They presented the details of the custom developed testing equipment and the testing procedures used for a series of shear tests with fixed principal stress rotation angle, β (= 0, 30, 45, 60 and 90°):

$$\frac{1}{2}\tan(2\beta) = \frac{\Delta\tau_{\theta z}}{\Delta\sigma'_z} \tag{3.2}$$

Data from axial-torsional tests with fixed inclination of principal stress may be used to investigate the combined influence of initial and stress induced anisotropy for frictional materials. During the application of shear stress on cylindrical specimens, the applied loading would follow a relationship between the b-value and the rotation of major principal stress, β-angle, as

$$b = \sin^2(\beta) \tag{3.3}$$

In this paper the direction of major principal stress relative to the direction of soil deposition is represented by δ-angle. For cylindrical specimens, the δ-angle was always same as the β-angle. The compression (b=0) and extension (b=1) test with identical initial

stress conditions were also performed on solid cylinder (SC) specimens of the same clay using a lubricated end triaxial system. A comparative study of the data obtained for the normally consolidated cubical, hollow cylinder, and solid cylinder specimens is presented in this chapter to develop an understanding of the associated soil behavior in three dimensions. The influence of specimen shape and boundary conditions (Jamiolkowski et al. 1985) is investigated by comparing the data obtained from the three testing methods.

Specimens for Testing

Tests were performed on slurry consolidated specimens of kaolin clay. The cubical clay specimens were prepared in a slurry consolidometer with square cross-section (102x102 mm) as described in Chapter 2. Solid cylinder and hollow cylinder specimens were prepared in similar consolidometers with circular cross-sections. Kaolin clay powder with the properties shown in Table 3.1 was mixed with de-aired and de-ionized water at a water content of 155% and poured into the appropriate consolidometer. It was then consolidated under K_0 condition at a vertical effective stress of 207 kPa until the completion of primary consolidation. The end of primary consolidation was

Table: 3.1 Properties of Kaolin Clay

Soil Property	Value
Liquid Limit	62%
Plasticity Index	32%
Specific gravity	2.63
Percentage finer than 10□m	92%
Percentage finer than 2□m	62%
Activity	0.44

determined using the square root of time method (ASTM D2435-96) from consolidation test data. The specimen was then extruded with minimum disturbance and the desired height of the specimen was obtained by carefully trimming the excess material. In this research, the cubical specimen had three sides of 102 mm long, and full cylinder specimen had a height of 100mm and base diameter of 100 mm (H/D=1). Rowe and Barden (1964) showed that the lubricated end triaxial tests performed best for the cylindrical specimens with slender ness ratio (H/D) of 1. The H/D =1 provided appreciably stable geometry, which led to uniform distribution of stress and deformation throughout the test. The typical height of the HC specimen was about 230 mm, outer radius, 50.8 mm and inner radius, 35.6 mm. The dimensions of HC specimen were chosen as per the procedure recommended by Saada (1988).

Test Systems and Testing Procedures

True Triaxial System

True triaxial tests were performed using a device recently developed by Mandeville and Penumadu (2003) that applies three mutually perpendicular principal stresses on cubical soil specimens using flexible membrane boundaries. Three axes were identified on the space frame, x, y and z, and the specimens were placed on the space frame such that the σ_1-axis at the end of slurry consolidation coincides with the z-axis. Details of the true triaxial device and the procedure of specimen assembly were discussed in Chapter 2. After assembly, the specimens were saturated using backpressure. A minimum B-value (Skempton's pore pressure parameter) of 0.98 was used as the criteria for ensuring full saturation. The Kaolin clay specimens were then hydrostatically

(isotropically) consolidated to 275 kPa resulting in NC cubical clay specimens. A strain rate of 0.05%/min along σ_1-axis was found suitable for present clay to ensure pore pressure equilibrium under undrained condition. In order to ensure a constant b value (equation 3.1), the required σ_2 was generated along the y-axis in a stress control mode. During shearing, the normal stress was recorded in all the three principal directions. Deformation was recorded on all the six faces of the specimen and the values along opposite faces were averaged to get the strain in three directions.

A series of consolidated undrained cubical triaxial tests (T1-5) on remolded NC Kaolin clay specimen was performed for b=0, 0.25, 0.5, 0.75 and 1.0, and the tests were repeated for each b-value in order to ensure the reproducibility of experimental data. All of these tests were compressive in nature in terms of total stress applied on the specimens during shearing. This means that even for the b=1 case, the shear stress was applied by increasing the same amount of normal stress in σ_1 and σ_2 directions and maintaining a constant total stress in the σ_3 direction. An extension test (T6) was also performed on the cubical specimen, which is another case of b=1. For this test, at the end of isotropic consolidation, principal stress along z-direction was decreased to simulate the extension stress path that is often used for cylindrical specimens. The directions of principal stresses acting on the specimen during shearing in the T1-5 and T6 tests are shown in Fig 3.1.

Lubricated end Triaxial and Axial-Torsional Test Setup

Lubricated end triaxial tests with radial drainage were performed on cylindrical kaolin clay specimens with diameter of 100 mm and a height of 100 mm (H/D = 1.0).

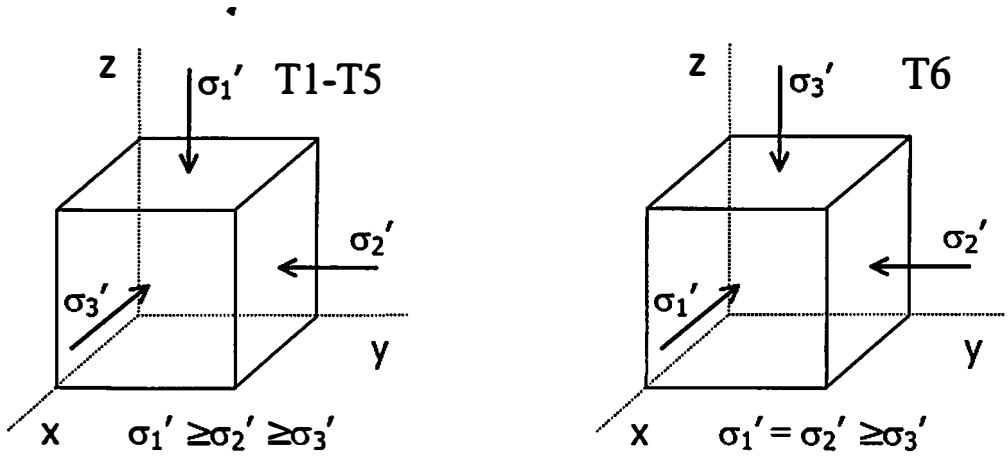

Figure 3.1 Principal Stresses Acting on Cubical Element during Shearing

The lubricated end caps have a diameter of 108 mm and allow the specimen to deform as a right cylinder during shearing, resulting in negligible frictional end boundaries during the application of deviator stress. Drainage is provided through the use of holes which are drilled into the side of the end caps. A complete drainage path from the sample to the drainage lines was provided using filter paper strips. Lubrication is provided through the use of 0.6 mm thick latex membranes and a thin layer of vacuum grease.

Triaxial tests on hollow cylinder specimens were performed using an MTS 858 loading equipment with a Series 359 Axial-Torsional Load Unit. Transducers for measuring and controlling axial load, torque, axial displacement, and rotation were interfaced with TEST STAR® electronic interface and TESTWARE-SX® software. To measure the cell and pore pressure, two external pressure transducers were used. The volumetric change is measured by monitoring the amount of water coming out of the specimen by using a differential pressure transducer and burette system. In addition, by

using an electro-pneumatic transducer, automated control of cell pressure was achieved. Applied stresses and deformations were controlled through the computer using the proportional, integral, and derivative (PID) feedback control algorithm, and any desired stress path with different rotation of principal stresses were achieved in a precise and completely automated manner.

The assembly of the SC and HC specimens in their respective apparatus follows the general procedures in ASTM Standard D4767-95 for consolidated undrained triaxial compression test for cohesive soils. After saturation, the HC or SC specimens were hydrostatically consolidated to 275kPa resulting in NC specimens. In order to reduce the necessary time for consolidation and pore pressure equalization, filter paper strips were used around the outer surface of the specimen to provide radial drainage.

Figure 3.2 shows the direction of principal stresses acting on the specimen during shearing for hollow and solid cylinder specimens. The angle between the major principal stress direction and the axis of the specimen was defined as β-angle, as shown in Fig 3.2a. Five different loading paths, corresponding to a fixed principal stress rotation angle, β = 0, 30, 45, 60 and 90 degrees, were applied on HC kaolin clay specimens to investigate the effect of principal stress rotation. β was kept constant throughout the shear phase by maintaining a constant ratio of incremental shear stress, $\Delta\tau_{\theta z}$ generated by the torque, and the vertical stress, $\Delta\sigma_z$ generated by the axial loading. A more detailed approach for interpreting the complete state of stress and strain during isotropic consolidation and the subsequent phase of applying shear stress during a combined axial-torsional test, including the correction for specimen geometry and correction for the

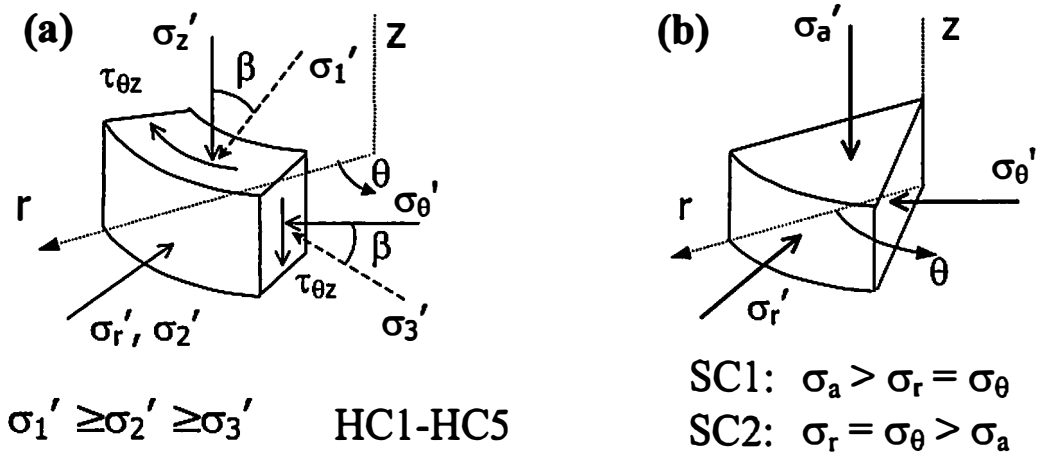

Figure 3.2 Principal Stresses Acting on the Element from (a) Hollow, (b) Solid Cylinder Specimen during Shearing

forces taken by the membrane, was given by Lin and Penumadu (2002). Using the lubricated end triaxial system, compression (b=β=0) and extension (b=1, β=90) tests were performed on SC specimens.

Isotropic Consolidation

Before undrained shearing, the specimens were hydrostatically consolidated under a higher effective confining pressure, $p' = 275$ kPa, compared to the 207 kPa of vertical stress applied during the first stage of slurry consolidation for specimen preparation. The higher confining pressure can overcome any disturbance to the specimen during assembling and increases the uniformity of the specimen. Typical consolidation curves (volumetric strain – square root of time) for the three specimen shapes are shown in Fig 3.3. The observed difference in the time corresponding to the completion of primary consolidation for the three specimen shapes was due to the varying external drainage

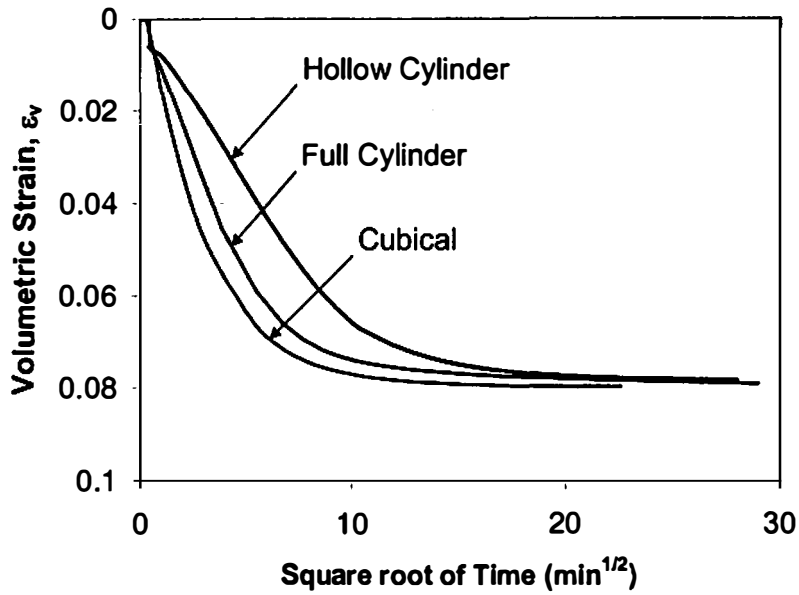

Figure 3.3 Isotropic Consolidation Curves for Different Specimen Shapes

Results from True Triaxial Tests on Cubical Specimens

In a true triaxial test on a cubical specimen, the principal axes of stress coincide with the axes of the specimen, i.e. x, y and z-axes. From the normal stress acting along these axes, mean effective stress, p′, and deviatoric stress, q, values are calculated from the general invariant expression, as shown in equation 3.4, and 3.5. The axes of measured strain values coincide with the principal stress axes. From these strain values, (ε_x, ε_y and ε_z) in principal directions, the shear strain, ε_q, is computed using equation 3.6.

Mean Effective Stress
$$p' = I_1/3 = (\sigma_1' + \sigma_2' + \sigma_3')/3 \tag{3.4}$$

Deviatoric Stress
$$q = \sqrt{3J_2} = \sqrt{\frac{(\sigma_1' - \sigma_2')^2 + (\sigma_2' - \sigma_3')^2 + (\sigma_3' - \sigma_1')^2}{2}} \tag{3.5}$$

Shear Strain

$$\varepsilon_q = \frac{1}{3}\sqrt{2\left\{(\varepsilon_1-\varepsilon_2)^2+(\varepsilon_2-\varepsilon_3)^2+(\varepsilon_3-\varepsilon_1)^2\right\}} \tag{3.6}$$

Stress-Strain and Pore Pressure Behavior

Table 3.2 provides a summary of the test types used in this research. During shearing, the z-axis of the specimen was made to coincide with the direction of K_o consolidation of slurry during specimen preparation. The tests T1-T5 had the major principal stress acting along the z-axis; therefore, these tests were defined to have δ=0°. The extension test T6 was defined to have δ=90° due to the minor principal stress acting along z-axis during shearing. In Fig 3.4, the maximum shear stress in σ_1-σ_3 plane, τ (equation 3.7), is plotted against major principal strain, ε_1, and shows significant influence of the variation of b-value or δ-angle. The failure points for different tests in this figure are identified using the legend shown in Table 3.2.

$$\tau = \frac{(\sigma_1-\sigma_3)}{2} \tag{3.7}$$

This demonstrates the need for considering the observed behavior in three-dimensional (3-D) space. The invariant form of deviatoric stress, q (from equation 3.5), represents a form of the maximum shear stress in 3D stress space and is plotted against the corresponding shear strain, ε_q in Fig 3.5. The failure points for different tests are identified using the legend shown in Table 3.2.The stress-strain relationship in this space is identical for the tests T1 (b=0), T4 (b=0.75), and T5 (b=1), therefore under these loading conditions, the specimens may be assumed to be yielding with the same shear stiffness until failure. The tests T2 (b=0.25) and T3 (b=0.5) show a slight increase in the shear stiffness. For all practical purposes, the tests T1-T5 may be assumed to be

Table: 3.2 Tests Performed on Normally Consolidated Specimens of Kaolin Clay

Tests	Stress Path	Graph Legend and Designation	
TTT test on Cubical Specimen	b = 0, δ=0°	●	T1
	b=0.25, δ=0°	△	T2
	b=0.5, δ=0°	○	T3
	b=0.75, δ=0°	✳	T4
	b=1, δ=0°, comp.	□	T5
	b=1, δ=90°, ext.	◇	T6
Axial- torsional Test on HC specimen	δ=0°, b=0	⬡	HC1
	δ=30°, b=0.25	◺	HC2
	δ=45°, b=0.5	⬢	HC3
	δ=60°, b=0.75	◣	HC4
	δ=90°, b=1.0	◆	HC5
Triaxial Test on SC specimen	δ=0°, b=0	⛁	SC1
	δ=90°, b=1.0	■	SC2

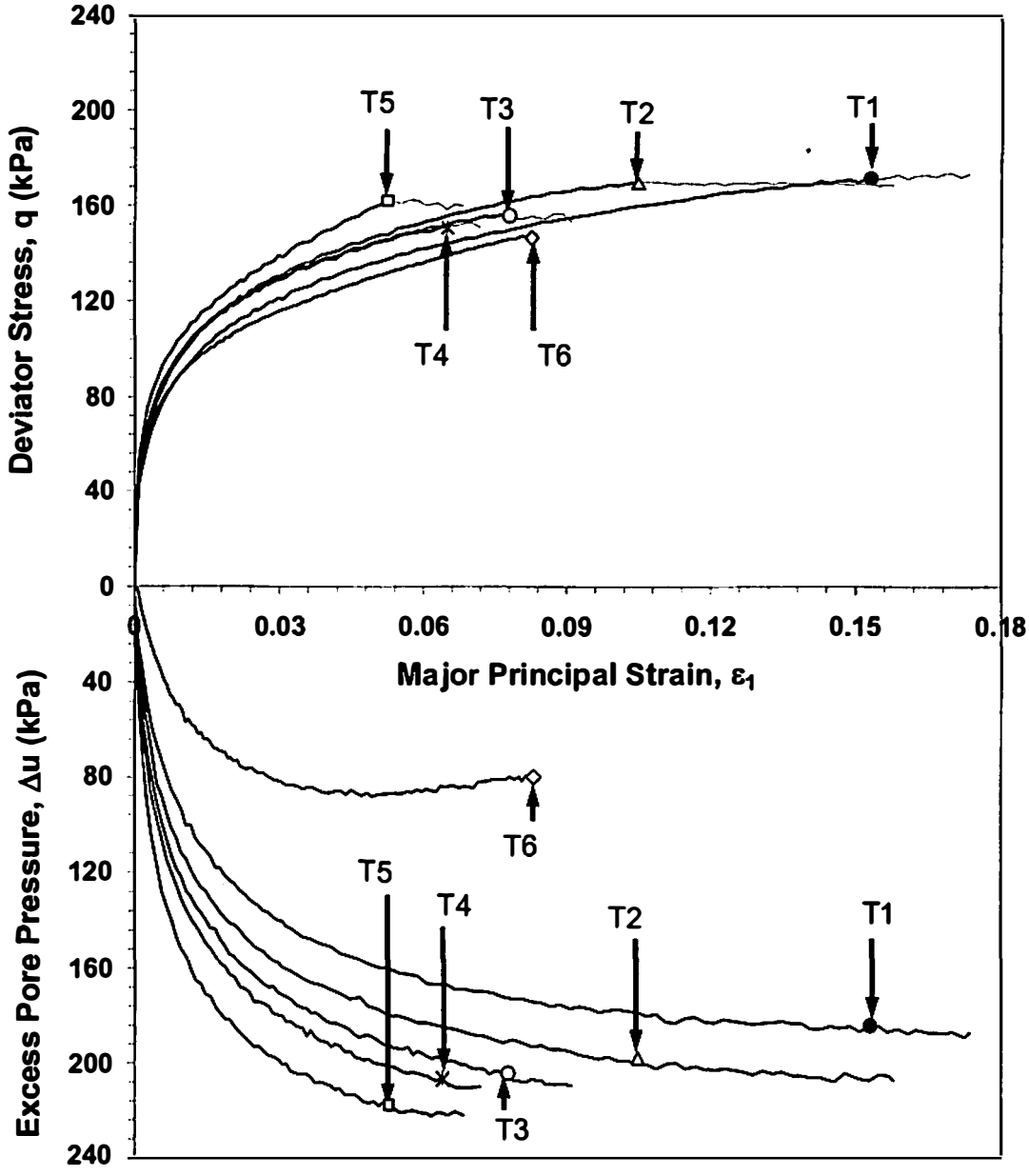

Figure 3.4 Maximum Shear Stress, $\tau = \left(\frac{\sigma_1 - \sigma_3}{2}\right)$, and Excess Pore Pressure Δu Evolution with Major Principal Strain for Different b-values – Cubical Specimen

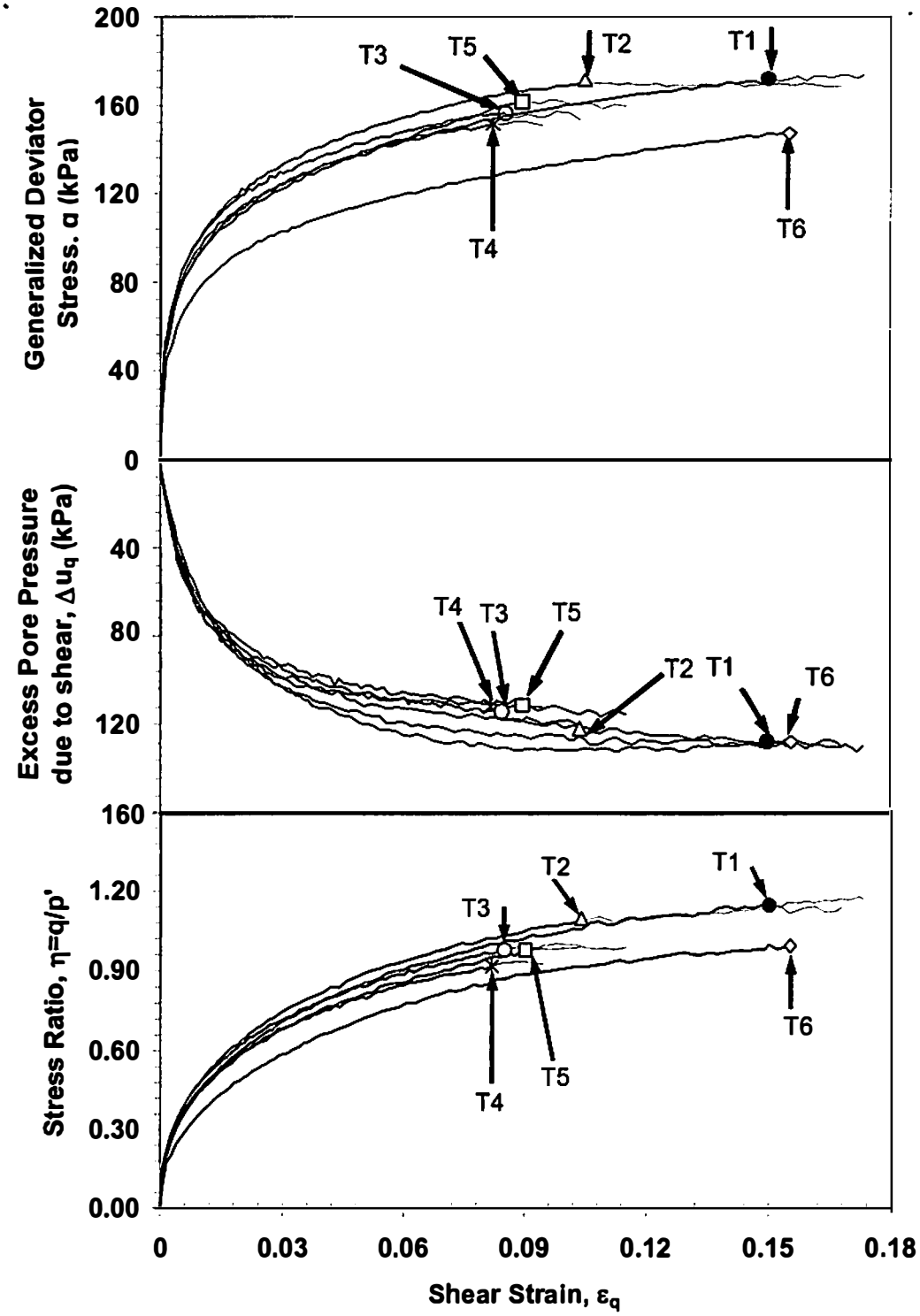

Figure 3.5 Variation of Deviatoric Stress, Pore Pressure due to Shear, and Shear Stress Ratio with Shear Strain for Different b-values – Cubical Specimen

providing identical shear stress-strain response until failure when compared with the response from the extension test, T6. Tests T1-T5 had the same orientation of principal stress (δ-angle) whereas the T6 had a rotation of 90°. It gives an indication that the stress anisotropy under undrained condition may not have significant influence on the shear behavior of soil when compared to the inherent anisotropy (induced during the specimen preperation). A shear stress ratio can be defined by η, as the ratio of the shear stress, q, and the mean effective stress, p'. Soil is a pressure dependent material; therefore, in order to study or characterize the shear behavior of soils, the shear stress ratio, η, can be plotted against ε_q, as in Fig 3.5. A decreasing trend for η evolution may be observed with increasing b-value from tests T1-T5, and the test T6 shows the lower limit of this trend.

Figure 3.4 shows the variation of excess pore pressure, Δu, generated during shearing for different stress paths indicating a significant influence of b-value for normally consolidated clay. Excess pore pressure increased with b-value for the tests with compressive loading (T1-T5) and showed much lower values for the extension test (T6). During an undrained test on saturated soil specimen, the excess pore pressure is generated in part due to a change in mean total stress applied to the specimen, while the other part is related to the shear deformation (Henkel 1960). When a saturated isotropic soil is subjected to hydrostatic loading under undrained condition, the change in excess pore pressure is equal to the change in mean total stress. Figure 3.6 shows the total and effective stress paths followed during different types of undrained shear loading in this study. The difference between the mean total stress and effective stress, at a given shear stress level, corresponds to the pore pressure generated within the specimen. The change

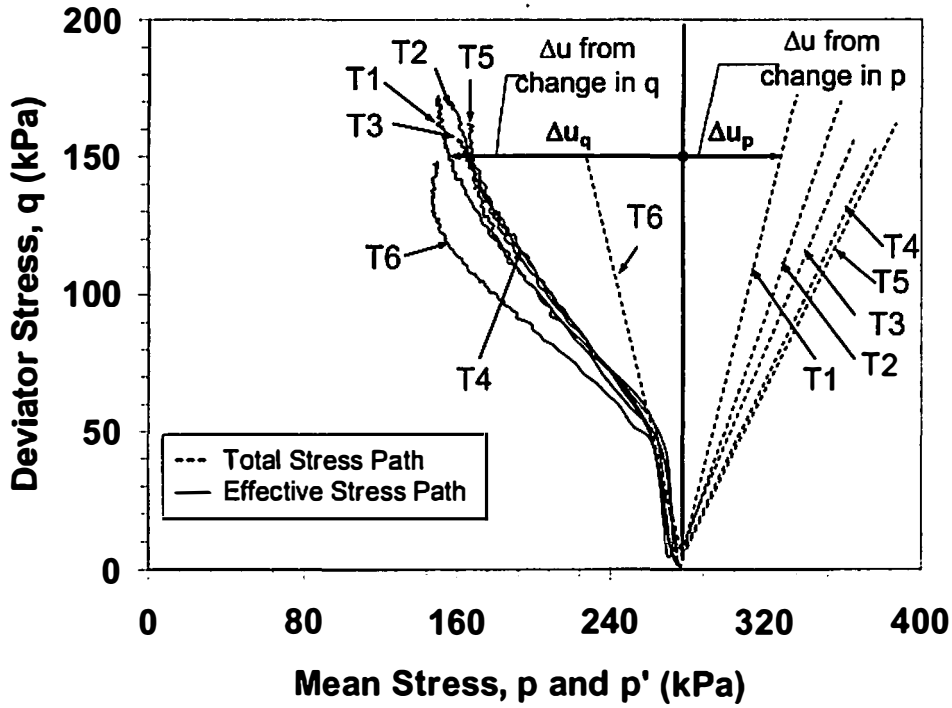

Figure 3.6 Stress Path in q-p Space for the Loadings Applied on Cubical Specimens

in pore pressure due to the change in mean total stress is represented by Δu_p, and due to the applied shear is represented by Δu_q ($=-\Delta p'$). Figure 3.5 shows the evolution of Δu_q with the shear strain. A decreasing trend of Δu_q evolution may be observed with the increasing b-values; however, the extension test (T6) shows Δu_q close to T1 test.

Failure Conditions

The failure point in this analysis is defined as the point of peak deviator stress just before the specimen shears to large strains with negligible change in shear stress. The specimens were observed to have strain localization at or beyond the peak deviator stress location. Prashant and Penumadu (2003), for overconsolidated clay specimens, found that a method for determining the onset of strain localization was to plot the variation of

individual principal strains (ε_1, ε_2, ε_3) against their sum ($\varepsilon_1+\varepsilon_2+\varepsilon_3$). The onset of strain localization occurs when these curves have an abrupt change in slope. It becomes necessary to define the approximate location of the failure point at this location, because beyond this point the true strain state cannot be determined due to strain localization. Figure 3.5 shows that the observed shear strain corresponding to failure (as defined above) decreased in general with the increasing b-value for the tests T1-T5. However, for the extension test, T6, (b=1), failure occurred at much higher ε_q (=15.5%) than that for the lateral compression test, T5 (ε_q=8.9%).

The failure state of stress from all the true triaxial tests are shown in Fig 3.7, for a constant octahedral normal stress, σ_{oct}=160 kPa. In this figure, the experimentally observed failure envelope, in octahedral plane, is compared with the four major failure criteria often used by practitioners and researchers:

Extended Tresca: $$(\sigma_1' - \sigma_3')/I_1 = constant \tag{3.8}$$

Extended von Mises: $$J_2/I_1^2 = constant \tag{3.9}$$

Mohr-coulomb: $$\frac{\sigma_1' - \sigma_3'}{\sigma_1' + \sigma_3'} = \sin(\phi') \tag{3.10}$$

I_3 based failure criteria: $$\sigma_1'\sigma_2'\sigma_3'/I_1^3 = constant \tag{3.11}$$

Here, σ_1', σ_2', and σ_3' denote the major, intermediate and minor principal stresses respectively. The parameters for each failure envelope were calculated from the triaxial compression (b=0) test. The I_3 based failure criteria matches well with the observed failure surface for the NC Kaolin clay. The principal strain increment axes are superimposed on the principal stress axes and the strain increment vectors are presented

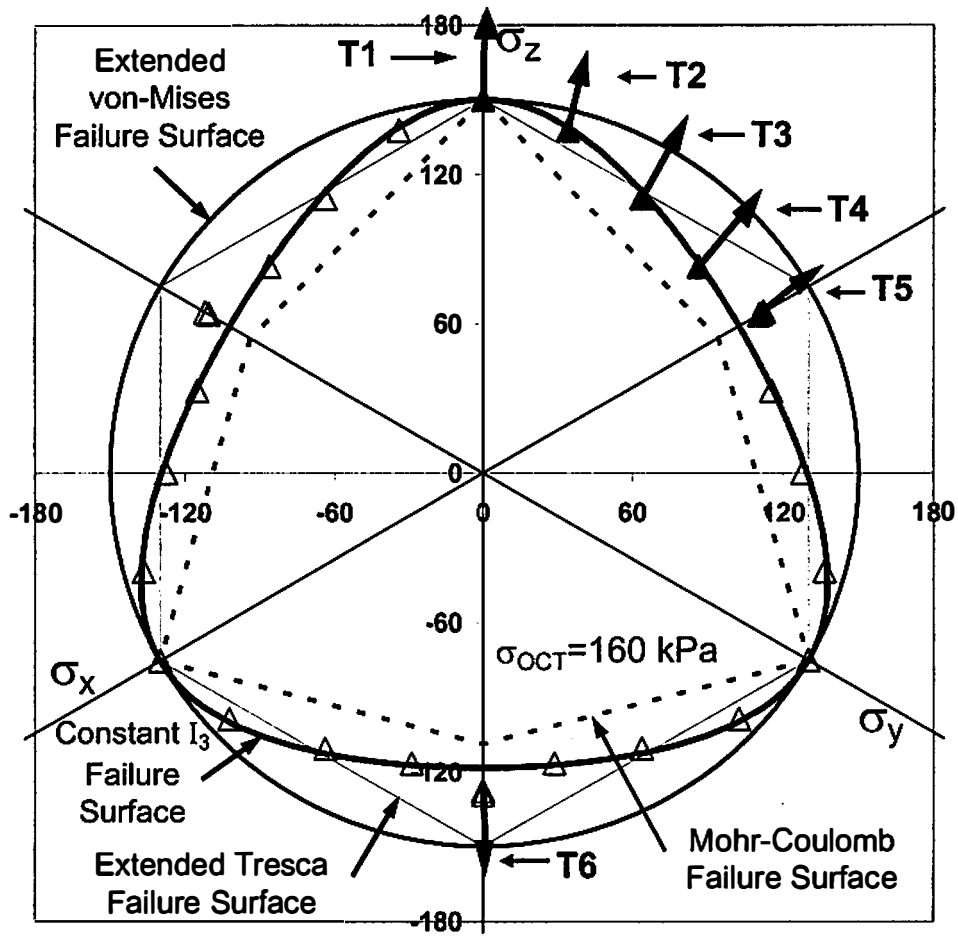

Figure 3.7 Three Dimensional Failure Surface for Kaolin Clay in Octahedral Plane (Symbols without Test Numbers are Located by Symmetry)

in octahedral plane (Fig 3.7) with their origin at their failure stress state. A plastic potential surface is defined as a surface to which the plastic strain increment vectors are normal and the strains at failure may be assumed to be purely plastic. The strain increment vectors from the current experimental data appear to be normal to a circular plastic potential surface in the octahedral plane, which is similar to the extended von Mises surface in this plane. Yong and McKyes (1971) also reported a similar plastic potential surface for Kaolin clay; however, in their study, the failure surface was reported to follow the Mohr-Coulomb criteria.

The σ_1' and σ_3' values at failure were used to calculate ϕ' and its variation with b-value is shown in Fig 3.8, along with the predicted relationships from four different failure criteria, identified in equations 3.8-3.11. The failure criterion based on the third invariant of stress tensor, I_3, seems to provide a good representation of the measured ϕ' values as a function of b-values. This failure criterion is similar to the one suggested by Lade (1990). In 3D stress space, a soil property that is of interest is the limiting shear stress ratio at failure, M. It is related to ϕ' as a function of b-value:

$$M = \frac{6\sin(\phi')\sqrt{1-b+b^2}}{3+(2b-1)\sin(\phi')} \tag{3.12}$$

M-values calculated from the experimental data are plotted against the corresponding b-values in Fig 3.8, along with the predicted variation for the different failure criteria. The variation of M-parameter is also best approximated by an I_3 based failure criterion. The predictions for ϕ' and M in Fig 3.8 are based on the calibration from the T1 (b=0) test. The M parameter was used in the critical state concept (Schofield and Wroth 1968) as a

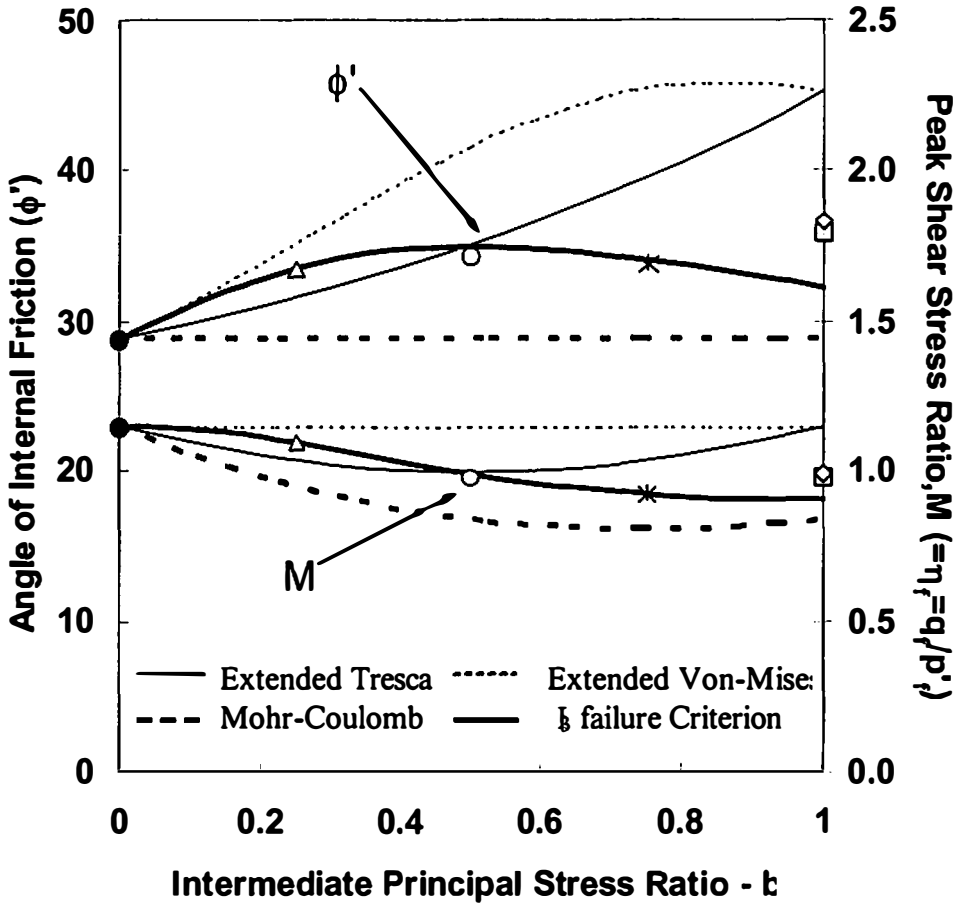

Figure 3.8 Angle of Internal Friction, ϕ', and Shear Stress Ratio at Failure, M, with b-values – Cubical Specimens

soil constant to define a unique critical state of the soil. Based on the observations from the later experimental studies performed by many researchers, Kirby and Wroth (1977) reported the M-parameter to be dependent on the b-value, and found that the M-value reaches its maximum for triaxial compression (b=0) and minimum for extension (b=1). For I_3 based failure surface, the variation of M-parameter as a function of b-value was derived in this study as

$$2M^3\cos(3\omega_\sigma) - 9M^2 = k = 2M_0^3 - 9M_0^2 \tag{3.13}$$

Here, ω_σ is the Lode angle, which is the angle of the stress vector from the σ_z axis in the octahedral plane. It is related to the b-value according to equation 3.14. M_0 is the M-value from b=0 case, for which ω_σ=0. An exact solution for equation 3.13 is provided in equation 3.15.

$$\tan(\omega_\sigma) = \frac{b\sqrt{3}}{2-b} \tag{3.14}$$

$$M = \frac{\sqrt{k/12}}{\cos\left(\frac{1}{3}\cos^{-1}\left(-\cos(3\omega_\sigma)\sqrt{k/27}\right)\right)} \tag{3.15}$$

For test T6, (in Fig 3.5), much lower shear stiffness throughout the test was observed when compared to the lateral compression test, T5; whereas, the failure stress state showed identical M values for these two tests. Therefore, the constitutive theories defining the yield parameters based on only the failure stress state (Cam-clay family of models, e.g. Schofield and Wroth 1968) might not be able to simulate this type of soil behavior. A similar problem arises for the other isotropic hardening models (e.g. Lade 1990) which assume their yield surface depending on the b-value but not the β-angle.

Along with the failure stress state, it would be necessary to consider the anisotropy of the soil structure to define the yield behavior of clays.

Henkel (1960) suggested a generalized form of the Skempton's (1954) parameter-A (equation 3.16), for saturated soils, and expressed the pore pressure evolution by parameter-a in equation 3.17.

$$\Delta u = \Delta\sigma_3 + A\left(\Delta\sigma_1 - \Delta\sigma_3\right) \tag{3.16}$$

$$\Delta u = \Delta p + a.\sqrt{2}\left(\Delta q\right) \tag{3.17}$$

Figure 3.9 shows the variation of A_f, and a_f as a function of b-value. A_f consistently increases with increasing b-values. The parameter a_f may be approximated to be a constant value for all the b-values, however, the extension test, T6 (b=1), shows a small increase in the value of a_f. This observation indicates that the a_f parameter may be independent of the applied stress anisotropy; however, inherent anisotropy may have some influence on this parameter.

Observations from Three Different Laboratory Shear Testing Methods

In this section, the influence of varying test conditions on the observed soil behavior will be discussed in light of the data obtained from the true triaxial (TT) tests on cubical specimens using flexible boundary conditions, axial-torsional (AT) tests on HC specimens using frictional end platens, and traditional triaxial tests on SC specimens using lubricated end platens. Researchers have commonly used these three testing methods to investigate various aspects of soil behavior. For isotropic material, it was believed that the results from a series of tests on cubical specimens with varying b-value should provide identical response when compared to the corresponding test data using

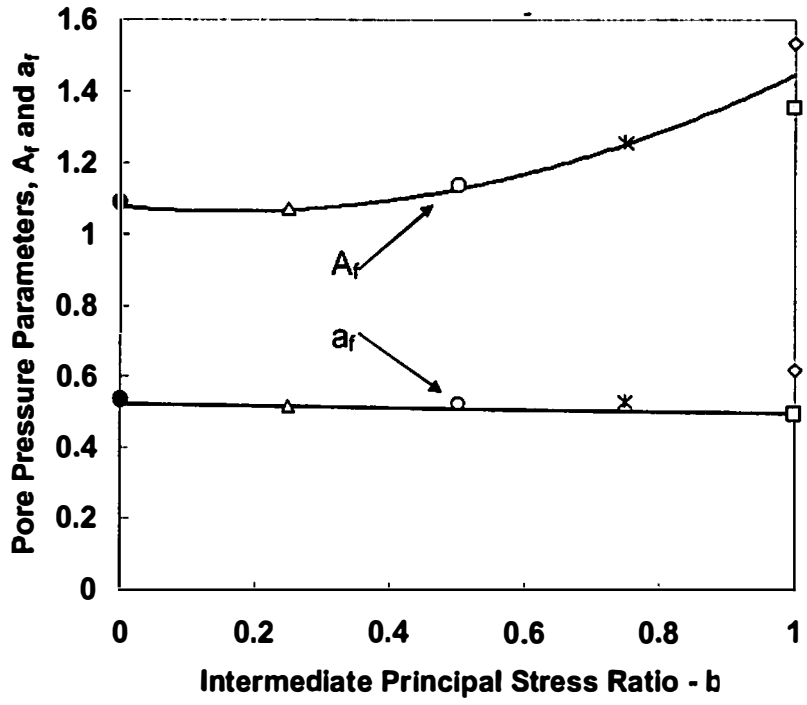

Figure 3.9 Variation Pore Pressure Parameters, A_f and a_f, with b-values

HC or SC specimens. However, for a cross-anisotropic material the response from the three types of tests would be identical for triaxial compression (b=0) and extension (b=1) tests only. Among all the tests performed in this study only the compression and extension tests would have the same orientation of principal stresses about the axis of cross-anisotropy (δ-angle) for the three testing methods and for such a material the δ-angle may have significant influence on the observed behavior. The specimens used in this study have a small degree of cross-anisotropy as the specimens were initially subjected to 1-D slurry consolidation (K_o condition), prior to a second stage isotropic consolidation at 275 kPa, during sample preparation.

In Fig 3.10, the deviatoric stress, q, and part of the excess pore pressure generated due to applied shear, Δu_q, are plotted against the shear strain, ε_q, for b=0 and b=1 tests on

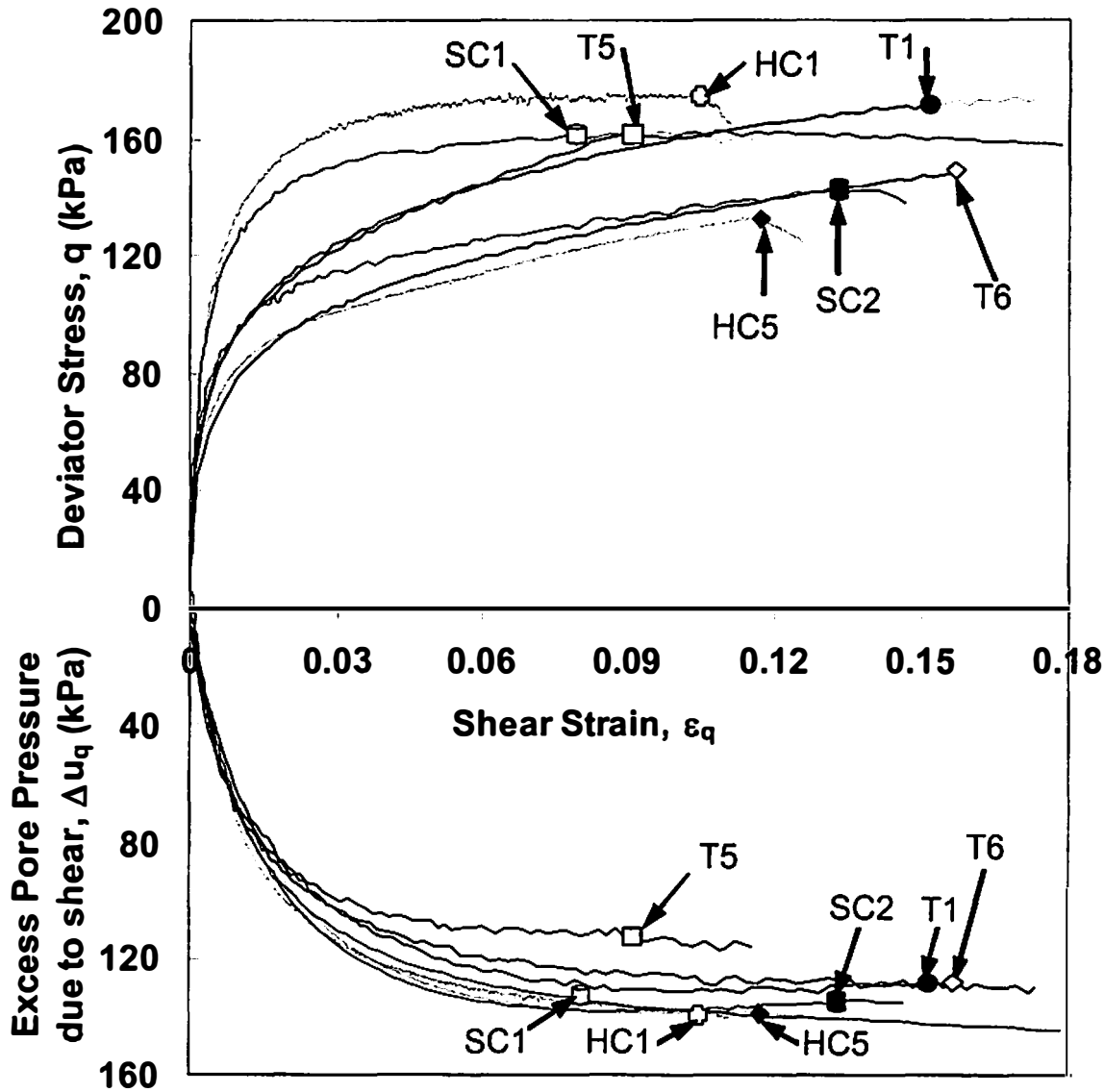

Figure 3.10 Stress-Strain and Pore Pressure Response for Tests on Cubical, HC and SC Specimens (b=0 and 1)

Table: 3.3 Strength Behavior Observed in Three Testing Methods

Specimen	δ	S_u/σ_c'	ϕ'	M
Cube	0°	0.31	28.8°	1.15
HC	0°	0.32	33.1°	1.34
SC	0°	0.30	29.3°	1.17
Cube	90°	0.27	36.4°	0.99
HC	90°	0.24	34.2°	0.95
SC	90°	0.26	39.5°	1.05

cubical, HC, and SC specimens. The failure points for different tests in this figure were identified using the legend shown in Table 3.2. Rotation of principal stress from axis of cross-anisotropy δ-angle was equal to the β-angle for all the tests performed on cylindrical specimens as listed in Table 3.2. Despite the same loading conditions (b=0 or δ=0°) in the three compression tests, T1, HC1 and SC1, the stress-strain relationship and the strength behavior were significantly different. However, the HC1 and T1 tests reached the same shear stress level at failure. For the extension tests (b=1, δ=90°), T6, HC5 and SC2, did not show significant difference in stress-strain behavior except for a small increase in the observed shear stiffness at small strains for SC2 test. The stress and strain values at failure were highest for cubical specimen and lowest for HC specimen.

Table 3.3 provides the strength parameters of soil, commonly used in practice, calculated using the data obtained from the three testing methods. All of the parameters were observed to be varying with the testing method, and the tests on HC specimens showed the upper limit in compression and lower limit in extension for the strength behavior. In the TT cubical test the principal stresses were directly obtained from the

pressure applied onto the flexible boundaries, whereas, in the tests on HC and SC specimens the stress tensor was obtained by dividing the external loading (axial or torsional) by an average cross-sectional area of the specimen assuming a uniform radial deformation from top to bottom. The variable methods of obtaining the stress information might be one reason behind the observed difference in the stress-strain behavior; however, this should not produce such a big difference. The other possible factor might be the variation in specimen shape and boundary/loading conditions, which may influence the observed stress-strain and strength behavior significantly. At present, it is difficult to say which test is more representative of the true behavior of soil. However, these tests may be used individually to study the soil behavior in relative terms but not in absolute terms. For example, the strength parameters (see Table 3.2) were significantly different for compression and extension tests in comparison to the variation observed for different test methods. Figure 3.10 shows that the pore pressure response was identical for the cylindrical specimens, HC and SC, and even for the cubical specimens it was not significantly different. Moreover, the compression and extension tests showed identical pore pressure response for each specimen shape.

For three intermediate b-values (0.25, 0.5 and 0.75), the shear stress-strain and pore pressure response is compared for the TT tests on cubical specimens and the axial-torsinal (AT) tests on HC specimens, in Fig. 3.11. The TT and AT tests had different angle of principal stress rotation (δ-angle) for identical b-values. For the three TT tests (T2, T3 and T4) the δ-angle was zero; whereas, for the AT tests it was 30°, 45° and 60° respectively for the tests HC2, HC3 and HC4. The shear stress-strain response for the TT tests showed that the specimen was yielding at lower shear stiffness with increasing

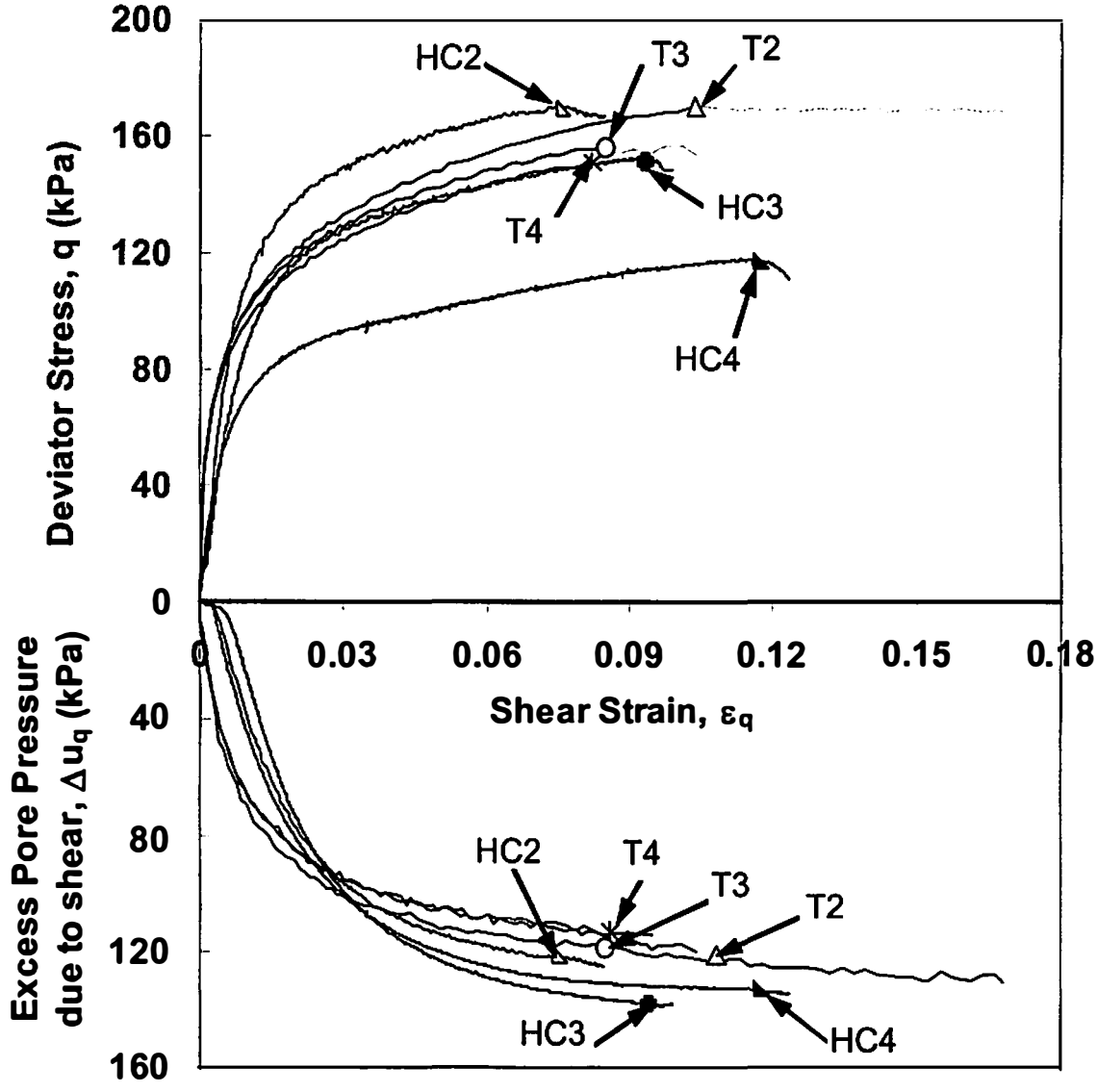

Figure 3.11 Stress-Strain and Pore Pressure Response for Tests on Cubical and HC Specimens (b=0.25, 0.5 and 0.75)

b-values. Similar observation can be made for HC specimens too but in this case, the reduction in shear stiffness with increasing δ-value is more significant. The variation in observed soil behavior from two testing methods may be in part due to the influence of specimen shapes and boundary conditions; however, the principal stress rotation in HC testing would also influence the behavior significantly. This observation was also supported by the significant variation found in the stress-strain and pore pressure response from the tests T5 and T6 on cubical specimens, as shown in Fig 3.10. Tests T5 and T6 had the same b-value (b=1), however, the angle of major principal direction with the z-axis of the specimen was changed from δ=0° for T5 to δ=90° for T6 test. This significant variation in the observed shear behavior, due to principal stress rotation, may be a result of the initial anisotropy of the specimen's structure (geometric arrangement of clay particles). The initial anisotropy in the structure of the specimen was induced during the specimen preparation when the slurry was consolidated to 207 kPa effective vertical stress along z-axis under K_o condition. In fact a similar cross-anisotropy in the structure of the soil may be found in most of the soil deposits. At higher initial confining stress, the influence of this anisotropy may not be that significant for varying b-values but the rotation of principal stresses may produce significant change in the response. At lower initial confining stress values, even the change in b-value may be able to cause significant variation in the observed shear response.

Conclusions

A series of true triaxial undrained tests on cubical normally consolidated kaolin clay specimens were performed to study the influence of the intermediate principal stress

value relative to the major and minor principal stresses. The experimental shear behavior could be summarized with the following observations.

1. The stress-strain relationship, with the shear stress and strain defined in their three-dimensional invariant form, was not significantly different for various b-values if the principal stresses had a fixed orientation relative to the axis of deposition. However, the rotation of principal stresses may have significant influence on the observed behavior.
2. The shear strength of the soil was strongly dependent on the relative magnitude of σ_2. The observed failure criterion may be defined by the third invariant of the stress tensor, regardless of the principal stress rotation. Internal friction angle, ϕ', and the limiting shear stress ratio, M, were also found to be described by this model. The plastic potential surface at failure was circular in shape on the octahedral plane.
3. Excess pore pressure due to shear, Δu_q, is used to compare the pore pressure response from various stress paths. Evolution of Δu_q with shear strain was observed to have a decreasing trend with increasing b-value when they were compared at a fixed rotation of principal stresses. Henkel's (1960) generalized pore pressure parameter, a_f, shows a constant value for the loadings with fixed principal stress rotation.

The stress-strain behavior observed from the three types of laboratory tests, axial-torsional tests on hollow cylinder, lubricated end triaxial tests on full cylinder and true triaxial tests on cubical specimens, was significantly different. The specimen shape and the influence of different boundary conditions played a role in this observation. However, the pore pressure response did not show a significant influence due to the changing

testing methods and specimen shapes. Comparison of the test data from HC and cubical specimens indicated that the rotation of principal stresses have much more significant influence on the observed shear behavior of an anisotropic soil than the influence of the changing relative magnitude of σ_2.

Chapter 4. Effect of Intermediate Principal Stress on Overconsolidated Kaolin Clay

This chapter is a slightly revised version of a paper by Amit Prashant and Dayakar Penumadu with the same title, published in the Journal of Geotechnical and Geoenvironmental Engineering, ASCE, in March 2004:

Prashant, A., and Penumadu, D. "Effect of Intermediate Principal Stress on Overconsolidated Kaolin Clay." In print , Journal of Geotechnical and Geoenvironmental Engineering, ASCE.

My primary contributions to this paper include: (1) selection of the topic and development of the problem to study the three-dimensional constitutive behavior of cohesive materials, (2) identification of the study topics, (3) gathering and interpretation of published literature, (4) performing all the laboratory experiments, (5) interpretation and analysis of test results, and (6) part of the writing related to manuscript preparation.

Abstract

The influence of intermediate principal stress on the mechanical behavior of overconsolidated kaolin clay is investigated using three-dimensional true triaxial testing on cubical specimens. A flexible boundary, true triaxial setup with a real-time feedback control system was used to test soil specimens under stress and strain-control modes. The importance of properly tuning PID control and adapting gain terms as a function of specimen stiffness for undrained testing is presented. Undrained tests on kaolin clay show that the following shear strength parameters vary with the magnitude of intermediate principal stress: stiffness at small strains, excess pore pressure generated during shear,

strength and strain to failure. Failure occurred at peak deviator stress followed by shear band formation and localized bulging. Prior theoretical formulations of bifurcation and undrained instability support these experimental observations. Analysis of data in the octahedral plane indicates that kaolin clay follows a non-associative flow rule, which is described by a constant third stress invariant failure criterion with von Mises plastic potential surface.

CE Database keywords: Bifurcation, Localization, Overconsolidated clays, Shear deformation, Strain, Three-dimensional analysis, Undrained shear tests, Yield surface.

Introduction

The influence of σ_2 variation on the shear strength and pore-pressure parameters of cohesive soils was initially studied by Rendulic (1936), Habib (1953), Henkel (1959), Parry (1960) and Wu et al. (1963). These studies included the traditional triaxial compression and extension tests on solid cylindrical specimens, and torsional tests on solid or hollow cylinder specimens. These studies were not conclusive regarding the effect of σ_2 on the soil's mechanical behavior. Later studies performed by Shibata and Karube (1965), Broms and Casbarian (1965), Yong and McKyes (1971), Vaid and Campanella (1974), Lade and Musante (1978), and Kirkgard and Lade (1993), all agree that the intermediate principal stress plays a significant role in stress-strain-strength behavior and pore pressure response of clay. The laboratory tests in the above studies were performed using traditional triaxial tests, torsional tests, and true triaxial tests with varying b-values (equation 3.1) on cubical specimens.

Most of these studies were performed on normally consolidated (NC) clays. Past studies related to evaluating the shear strength behavior of overconsolidated (OC) clay was limited to traditional triaxial compression and extension testing, and only provided the shear strength behavior for two extreme b-values, 0 and 1. This chapter presents an experimental study of the influence of σ_2 on the stress-strain-strength behavior and pore pressure response of OC Kaolin clay under undrained conditions. Strain localization issues are discussed in light of the experimental observations and in identifying the failure state of stress and strain. True triaxial tests on cubical specimens were performed using a device described in previous chapter. This device uses three-axis electro-pneumatic, PID based real-time feedback control system. The influence of feedback control parameters on the observed shear strength behavior of over-consolidated clay is also presented in this study.

Previous Investigations

Henkel (1959) performed strain controlled triaxial compression and extension tests on normally consolidated as well as overconsolidated specimens of remolded London clay and Weald clay. The undrained strengths $[(\sigma_1-\sigma_3)_f]$ obtained in extension tests were reported to be 14% lower than those obtained in compression test (as interpreted by Lade and Musante, 1978). However, if the undrained strength values are normalized by the corresponding mean effective stress values (σ'_{oct}) for these tests at failure, the shear strength in extension (b=1) is 25% lower than that for compression (b=0). This is based on the assumption that the failure surface varies linearly with the mean effective stress. Parry (1960) studied the behavior of the same clay along various

stress paths possible in a triaxial apparatus. The axial strain-controlled tests were carried out for a wide range of overconsolidation ratio (OCR) values. The undrained strength (normalized by σ'_{oct}) from extension tests were 24% lower than those in compression tests (b=0). At failure, the pore pressure parameter, A_f [= Δu / $(\sigma_1 - \sigma_3)_f$], for extension tests were lower than those for the compression tests by an average of 0.7, as shown in Fig. 4.1. Parry and Nadarajah (1973) studied the triaxial behavior of hydrostatically (CI) and anisotropically (CK_0) consolidated Kaolin clay specimens with OCR ranging from 1 to 2.6, using strain- controlled compression and extension tests. The CI specimens showed 28% lower normalized strength in extension than that in compression tests; however, this difference decreased to 8% for the CK_o specimens. The pore pressure variation from compression test to extension test was found to follow a similar pattern for all the specimens, as reported by Parry (1960).

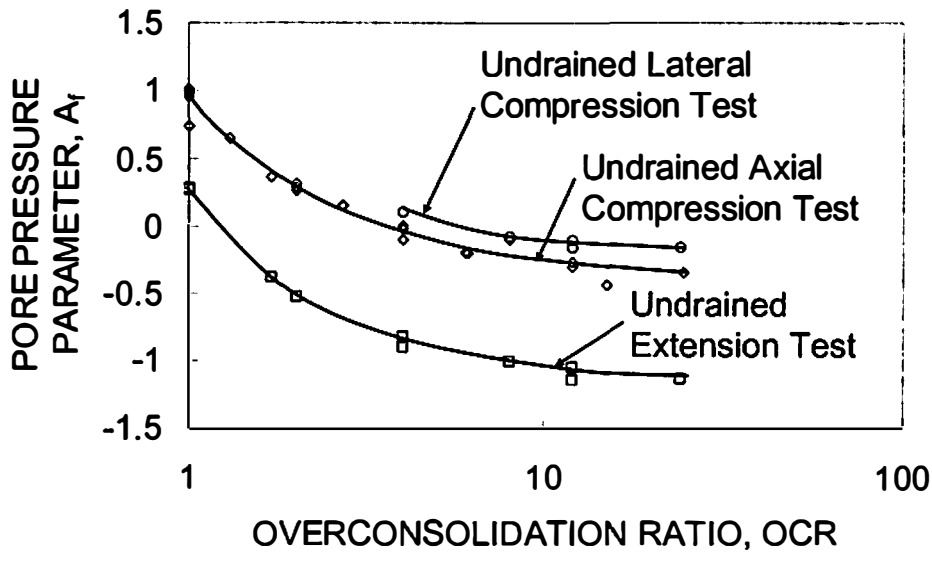

Figure 4.1 Parameter A_f for Undrained Compression and Extension Test Data [From Parry (1960)]

Wu et al. (1963) performed stress-controlled consolidated undrained torsional tests on hollow cylindrical specimens, and triaxial compression and extension tests on Sault Ste Marie clay using an axial strain rate ($\dot{\varepsilon}_1$) of 0.05%/min. The clay strength was found to agree with the Mohr-Coulomb failure envelope using Hvorslev's effective strength parameters, and the σ_2 was reported to have no influence on stress-strain behavior.

Shibata and Karube (1965) conducted three-dimensional (3D) strain-controlled undrained tests on NC rectangular specimens (60x35x20 mm) of remolded Osaka alluvial clay using a modified triaxial apparatus, with two pairs of rigid boundaries in the σ_1 and σ_2 directions and a pair of flexible boundaries in the σ_3 direction. Yong and McKyes (1967, 1971) also performed similar strain-controlled ($\dot{\varepsilon}_1$ = 0.075%/min) tests on remolded NC Kaolinite clay specimens (102x51x38 mm) using additional modifications, using a pair of rigid boundaries in the σ_1 direction and two pairs of flexible boundaries in the σ_2 and σ_3 directions. They showed significant influence of σ_2 on deformation, pore pressure and shear strength. In the later paper, they concluded that σ_2 affects pre-failure behavior and the failure envelope is best described by the Mohr-Coulomb criterion.

Vaid and Cmpanella (1974) performed strain-controlled consolidated undrained tests on undisturbed NC Haney clay using plane strain compression and extension. Lade and Musante (1978) and Kirkgard and Lade (1993) ran a series of strain-controlled true triaxial tests on cubical specimens of NC clay. Lade and Musante (1978) used remolded grundite clay, whereas Kirkgard and Lade (1993) used remolded San Francisco Bay mud. The apparatus used in both studies had lubricated end platens on the specimen top and

bottom with flexible membranes on the sides; the lubricated end platens were used to apply σ_1. These studies concluded that σ_2 has a significant influence on mechanical properties of clay and the failure envelope was located outside the Mohr-Coulomb failure surface in the octahedral plane.

Germaine (1982) and Seah (1990) investigated the influence of principal stress rotation on the undrained behavior of remolded Boston blue clay using a directional shear cell. Whittle et al. (1994) found that the data from this work was in agreement with the MIT-E3 anisotropic constitutive model (Whittle and Kavvadas 1994) for OC clays. These studies support the assertion that stress anisotropy has a significant role in the observed stress-strain and strength behavior of clay. Callisto and Calabresi (1998) conducted strain-controlled true triaxial tests on cubical specimens of natural Pisa clay reconsolidated to its natural OC stress state. The specimens were tested using different stress paths under flexible boundary conditions. The failure envelope in the octahedral plane was found to deviate from the Mohr-Coulomb and Lade's (1990) failure surface. Table 4.1 summarizes the key observations from all the above studies and illustrates the need for a more comprehensive study of the influence of σ_2 on clay behavior.

True Triaxial Testing

Using the true triaxial system described in Chapter 2, a series of consolidated undrained tests was performed on slurry consolidated Kaolin clay specimens in which σ_2 was varied to produce b-values of 0, 0.25, 0.5, 0.75 and 1.0. For a given value of b, two tests were performed to evaluate the repeatability of experimental data. The description of Kaolin clay used in the current study was provided in Table 3.1. The specimen

Table: 4.1 Summary on the Influence of Intermediate Principal Stress from Prior Research

Studies	Type of Testing	Influence of Intermediate Principal stress on soil behavior
Henkel (1959)	TC, TE	$(S_u)_{TE}$ was 25% lower than $(S_u)_{TC}$.
Parry (1960)	TC, TE, LC	$(S_u)_{TE}$ was 24% lower than $(S_u)_{TC}$. Excess pore pressure generated was lower for TE.
Parry and Nadarajah (1973)	TC, TE	For CI specimen $(S_u)_{TE}$ was 28% lower than $(S_u)_{TC}$. For CK_0 specimen $(S_u)_{TE}$ was 8% lower than $(S_u)_{TC}$.
Wu et al. (1963)	TTT, TC, TE	No influence of σ_2 on stress-strain behavior.
Shibata and Karube (1965)	TTT	Significant influence of σ_2 on the stress-strain-strength and pore pressure behavior. Mohr-Coulomb failure surface represented the lower limit of shear strength.
Yong and McKyes (1967)	TTT	
Yong and McKyes (1971)	TTT	σ_2 had influence only in the pre-failure behavior. Failure was represented by Mohr-Coulomb surface.
Vaid and Cmpanella (1974)	PSC, PSE	σ_2 had significant influence on the mechanical behavior of clay. Failure envelope was outside the Mohr-Coulomb failure surface in octahedral plane. Lade (1990) found this failure surface to depend on the third invariant of stress tensor.
Lade et al. (1978), Kirkgard and Lade (1993)	TTT	
Germaine (1982), Seah (1990)	DSC	Significant influence of σ_2 on the stress-strain and pore pressure behavior. Failure surface was not well represented by Mohr-Coulomb or Lade's (1990) criteria.
Callisto and Calabresi (1998)	TTT	

- TC = Triaxial Compression (b=0); TE = Triaxial Extension (b=1); LC = Lateral Compression (b=1)
- TTT = True Triaxial Tests (3D); PSC = Plane Strain Compression; PSE = Plane Strain Extension
- DSC = Directional Shear Cell; CI = Hydrostatically consolidated; CK_0 = Anisotropically consolidated.
- S_u = Normalized Undrained shear strength.

preparation procedure and its assembly in the true triaxial device were discussed in Chapter 2. Three axes are identified on the space frame, x, y and z, and the specimens were placed on the space frame such that the σ_1-axis at the end of slurry consolidation coincides with the z-axis. After assembly, the specimens were saturated using backpressure technique, and values of Skempton's pore pressure parameter B ($=\Delta u/\Delta\sigma_{confining}$) obtained from the internal pore pressure measurements agreed closely with that obtained from the external pore pressure measurements. A minimum B-value of 0.98 was used as the criterion for ensuring full saturation. The Kaolin specimens were hydrostatically consolidated to 275 kPa and the stress was then decreased to 55 kPa to obtain OCR=5. During the shear stage, deviator stress was induced on the specimen by applying a constant strain rate of 0.05 %/min in the z-direction; this strain rate ensured pore pressure equilibrium under undrained conditions. In order to ensure a constant b-value (equation 3.1), the required σ_2 was generated along the y-axis in a stress control mode.

All of the tests were compressive in nature in terms of total stress applied on the specimens during the shearing stage. This means that even for test corresponding to b=1 (lateral compression) case, the shear stress was applied by increasing the same amount of normal stress in σ_1 and σ_2 directions, and maintaining a constant total stress in the σ_3 direction. The major strain in the σ_1 direction, ε_1, was increased at a rate of 0.05% per minute and the total stress in the other two directions was maintained by feedback control using the PID algorithm. During shearing, normal stress was recorded in all the three principal directions and the pore pressure generated was recorded using external and

internal pore pressure transducers. For $\dot{\varepsilon}_1$ = 0.05 %/min, the internal pore pressure readings obtained from a needle piezometer, whose tip was located approximately at the center of the cubical specimen, was found to be equal to the external pore pressure data. Deformation was recorded on all six faces of the specimen, and the values at opposite faces were averaged to attain the strain in three principal directions. During these tests, the principal axes of stress coincided with the x, y and z axes of the specimen. Three-dimensional deviator stress value, q, is calculated from the general invariant expression, as shown in equation A1.8 of Appendix-1. For comparison of results, the deviator stress q and the excess pore pressure are normalized with pre-consolidation pressure (p'_o = 275 kPa).

PID Feedback Control during Overconsolidated Clay Testing

It was discussed in Chapter 2 that the tuning of P, I and D coefficients in PID algorithm plays an important role in the observed stress-strain, pore pressure, and shear strength behavior of clay. The values of PID coefficients needed for a good control depend on experimental setup, material type, and stiffness of the specimens. Initially in this study on overconsolidated clay, a series of tests were performed using PID values developed from a previous study for normally consolidated Kaolinite clay specimens. These values correspond to P=0.029, I=0.052 and D=0. These PID values were reduced to $1/10^{th}$ of their initial values after major principal strain reached a value of 1%, to maintain desired control in the three axes. Repeated tests in the present research showed that these PID values employed in first series of tests on overconsolidated clay appeared to overshoot the set point values, which resulted in relatively poor control of target value

of major principal strain rate (See Fig 4.2). With this observation, separate tuning was performed for PID values suitable for overconsolidated specimens. Tuning experiments resulted in lower PID values, i.e. P=0.0145, I=0.026 and D=0, at the early phase of shearing. These PID values were then reduced to $1/10^{th}$ of their initial values at ε_1=1% to account for a change in stiffness of the specimen during shear with increasing amplitude of major principal strain. This leads to the conclusion that the PID values depend not only on the experimental setup and soil type but also on the stress history of the soil. Thus, a second series of tests were performed with these specific PID values found suitable for Kaolinite specimens with OCR=5, whereas the first series was performed using the PID values suitable for normally consolidated Kaolinite clay. Therefore, the tests of first series in the figures 4.2, and 4.3are referred to as 'NC gain PID control tests' and the tests of second series are referred to as 'OC gain PID control tests'.

The pore pressure generated during shear for OC clay specimen differs from that for NC clay specimen (Henkel, 1959). Therefore, the effective stress path and thus the variation in stiffness of the specimens in these two cases are different. This variation of stiffness of specimen affects the accuracy of the PID control and thus requires separate tuning for the PID values. Improper tuning of PID coefficients causes the PID control to deviate from the desired target of maintaining a particular b-value resulting in fluctuations in the applied intermediate principal stress (σ_2) with increasing ε_1. These stress rate changes in σ_2 direction affect the observed stiffness and overall shear strength of the specimens. These fluctuations disappear in 'OC gain PID control tests' and typical results are compared with 'NC gain PID control tests' in Fig. 4.3. Therefore, proper

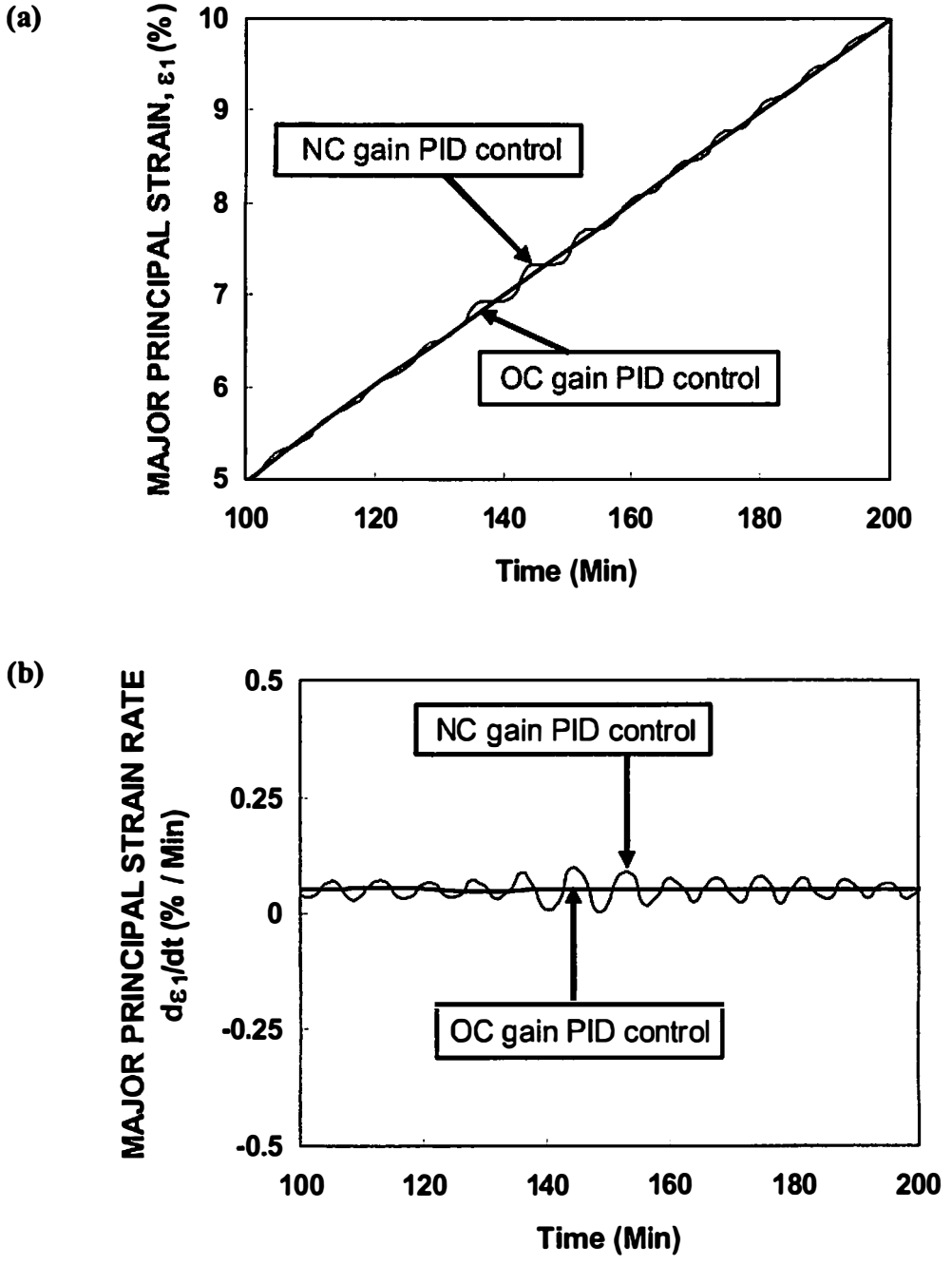

Figure 4.2 Effect of PID Coefficients on Feedback Control, (a) Major Principal Strain Evolution, (b) Major Principal Strain Rate

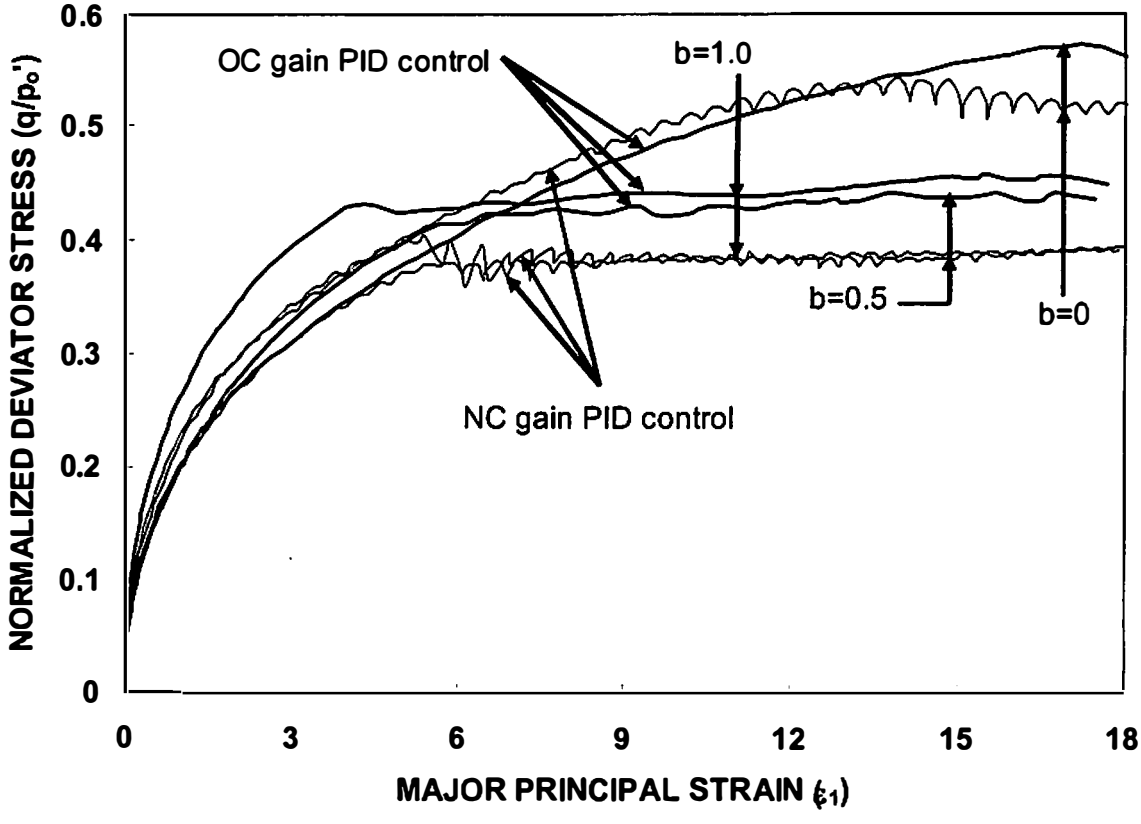

Figure 4.3 Effect of PID Control on the Observed Stress-Strain Relationship

tuning of PID coefficients is essential in order to perform good quality 3D tests. With this understanding, all of the analyses performed here are based on test data with appropriate feed back control parameters corresponding to 'OC gain PID control'.

Stress–Strain and Pore Pressure Behavior

Figure 4.4 shows the stress-strain response obtained from the true triaxial tests performed in this study for various b-values. The stress-strain variation for small strains is also shown in Fig. 4.4 to demonstrate the effect of b-value on the observed stiffness. The slope of the secant line drawn at 0.2% can be used as a measure of the specimen's stiffness at small strains. These slopes are constant for a b-value varying from 0 to 0.5, and show a large increase for higher b-values. This increase in the specimen's stiffness (and correspondingly its effect on shear modulus) with increasing b-value is due to the increase in mean effective stress for constant q or constant ε_1. The failure point in this analysis is defined as the point of peak deviator stress just before the specimen shears to large strains with negligible change in shear stress. This definition is necessary in this series of tests, since the specimens exhibited localized deformation at and beyond peak deviator stress. Failure points shown in Fig. 4.4 indicate that the values of ε_1 to failure decreases with increasing b-value. The deviator stress to failure is higher for specimens sheared with $b<0.5$, and its variation for stress paths involving $b \geq 0.5$ was small. The shear strength for b=1 was 26% lower than that for b=0. True triaxial tests are compared here with traditional triaxial tests with an assumption that, for isotropic material, these two types of tests are equivalent for the b=0 and b=1 cases.

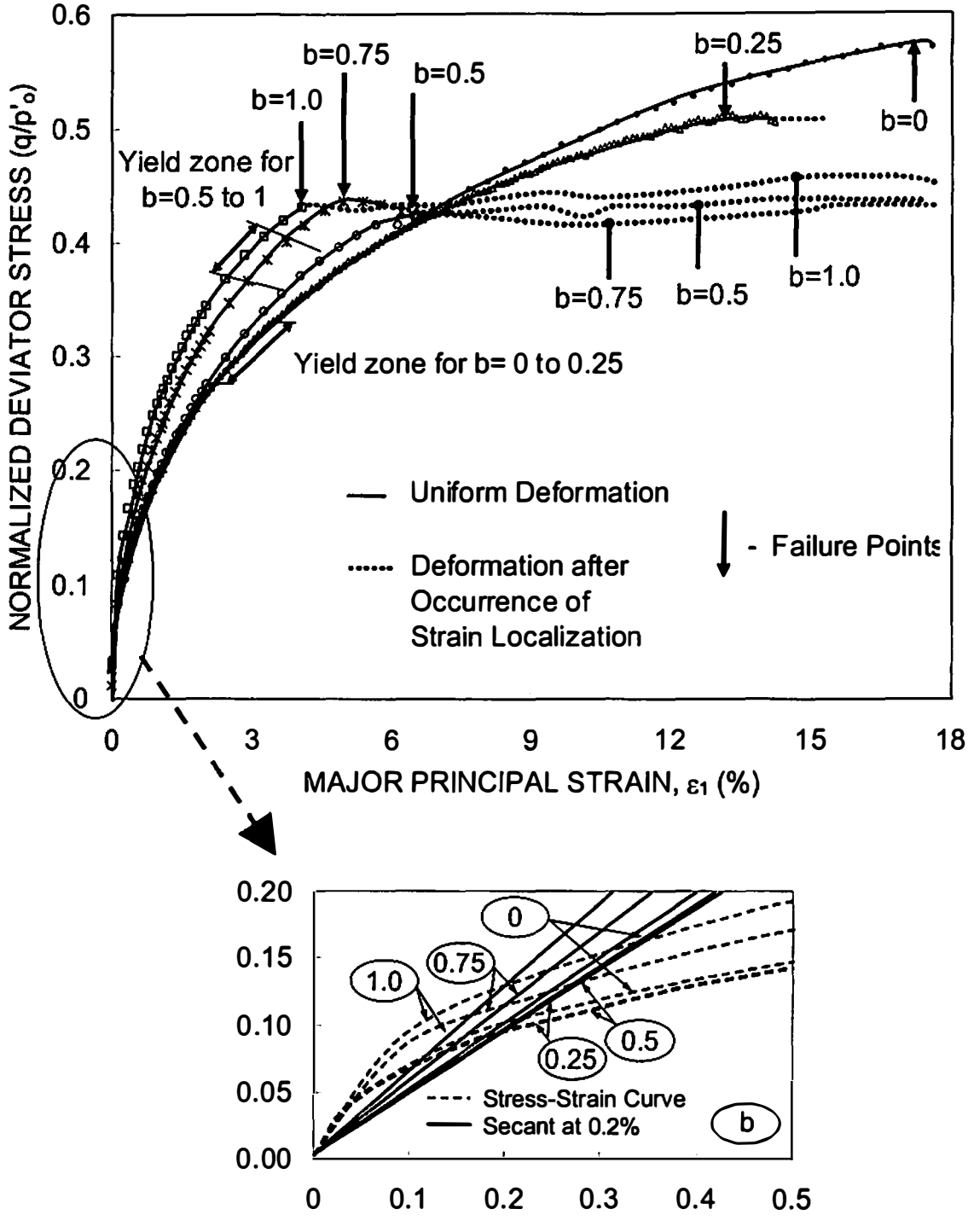

Figure 4.4 Stress-Strain Response for Different b-values

Test data for NC clay provided by Kirkgard and Lade (1993) shows negligible difference in developed excess pore pressure with b-value. However, in this study, the excess pore pressure developed during application of shear stress consistently increased with b-value from 0 to 0.75 and remained constant thereafter (Fig. 4.5). Figure 4.6 shows that the A-parameter (equation 3.12 in chapter 3) at failure increases with increasing b-value. Analysis of data from Parry (1960) in Fig. 4.1 shows that, for OCR=4, A_f decreases considerably when b-value changes from 0 (compression test, *UC1*) to 1 (extension test, *UE1*). Lateral compression tests (*UE2*) performed by Parry (1960) are also b=1 tests and followed the same total stress path as the b=1 test used in this study. Figure 4.1 shows that A_f changes only by a magnitude of 0.25 for OCR=5 from b=0 to b=1 (for lateral compression) and is consistent with the findings from this study as shown in Fig. 4.6.

Yield Behavior

Tavenas et al. (1979) and Graham et al. (1983) suggested the use of strain energy approach to provide a good estimate of state of stress at yield for soils. They found that the relationship between the length of the stress space vector (LSSV) and the strain energy absorbed by the specimen for deformation (W) should be bilinear for elastic-plastic material and the two lines should represent the pre-yield and post-yield behavior, and the intersection of these two lines corresponds to the yield point. This method was used in this study to determine the location of yield point, and the major principal strain values at these yield points are presented in Fig. 4.7. Non-linearity in the LSSV-W relationship suggests that, to some extent, plastic deformation has occurred even before

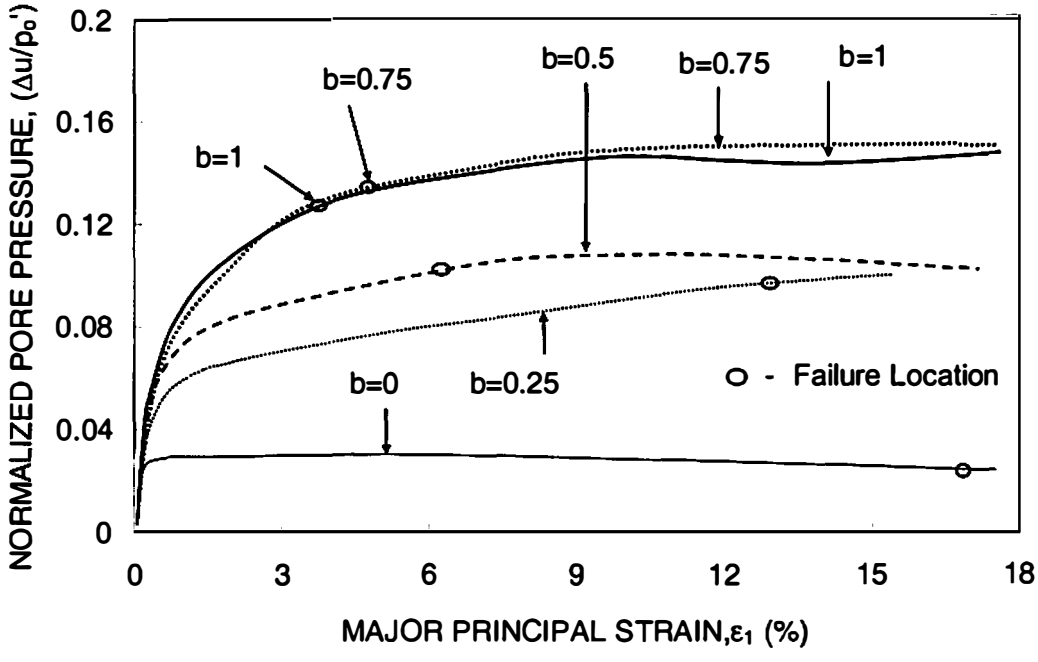

Figure 4.5 Excess Pore-Pressure during Shearing for Different b-values

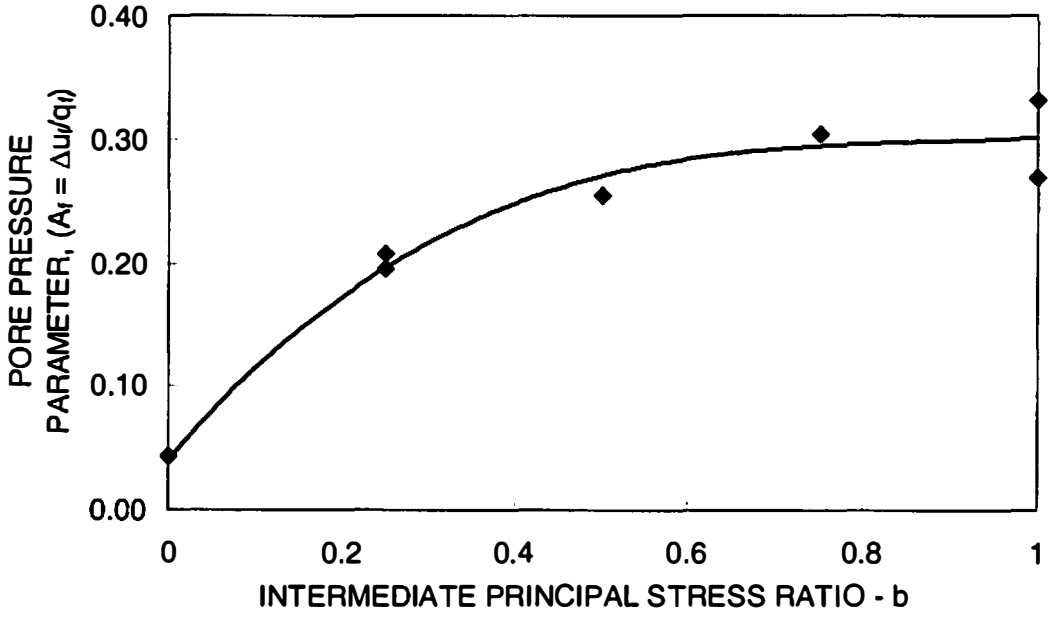

Figure 4.6 Variation of Pore Pressure Parameter A_f with b-values

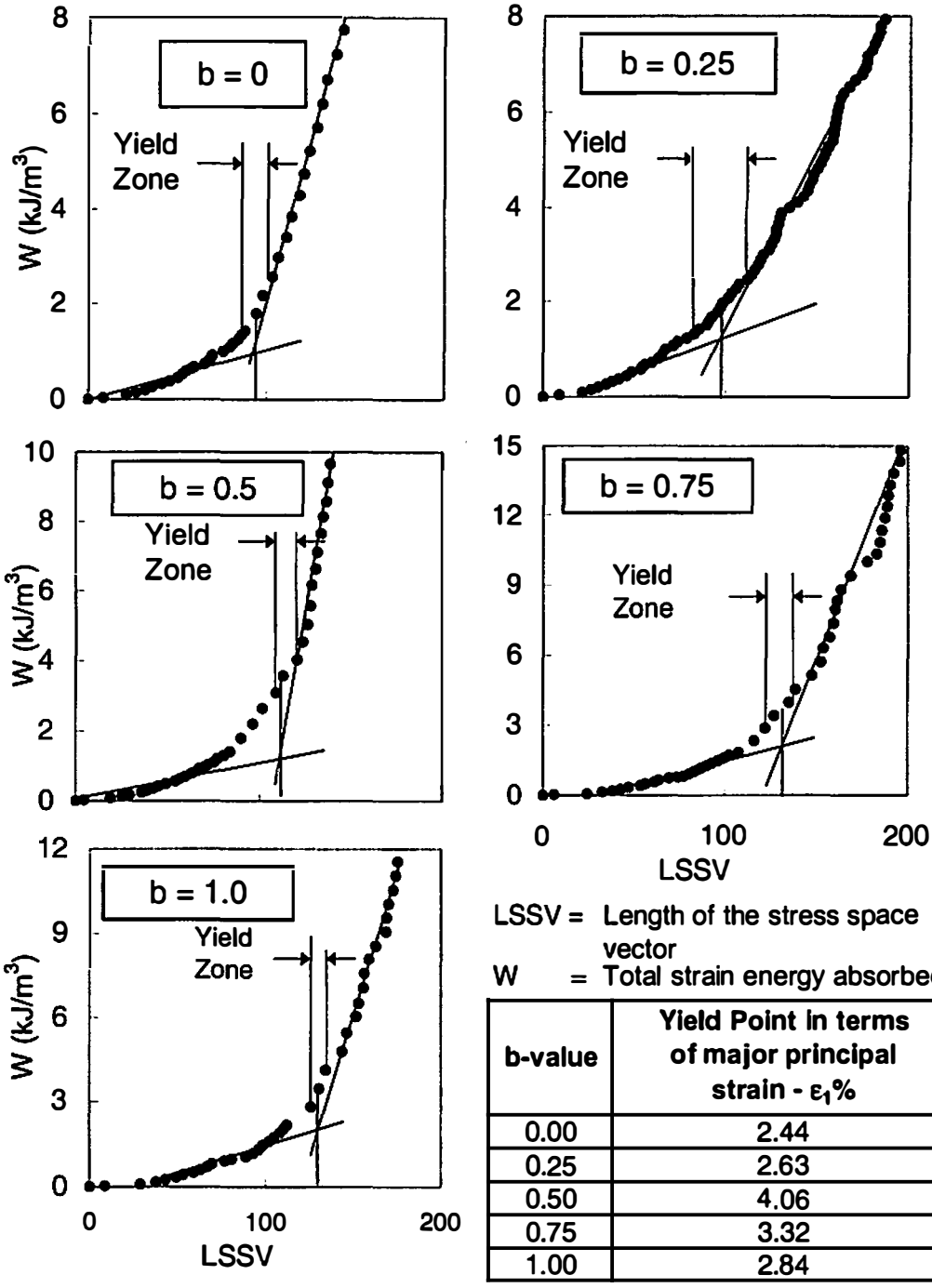

LSSV = Length of the stress space vector

W = Total strain energy absorbed

b-value	Yield Point in terms of major principal strain - ε_1%
0.00	2.44
0.25	2.63
0.50	4.06
0.75	3.32
1.00	2.84

Figure 4.7 Determination of Yield Points from Strain Energy Approach

these defined yield points. However, the behavior may be assumed to be predominantly elastic. Considering the judgment and approximations involved in determining the yield points, it seems reasonable to show the yield location as a zone in Fig. 4.4. For b-value 0.5 to 1.0, the yield zone is close to the failure points, whereas for b-value 0 to 0.25 it is well before the failure. It can thus be concluded that for specimens sheared with b-value 0.5 and greater, predominantly elastic pre-failure behavior was observed.

Failure Criteria

The analytical failure surface is often presented using an octahedral plane for a specified octahedral normal stress (σ_{oct}) value, where σ_{oct} is the mean value of three principal effective stresses acting on the specimen. For the analysis of the present test data, a σ_{oct} value of 95 kPa was used to illustrate the failure surface, and Table 4.2 shows the actual σ_{oct} values at failure for the different b-values used, and the percent deviation from the assumed 95 kPa value. These differences are small enough to allow stress path projection onto the same plane for all tests. This projection of stress points on a large

Table: 4.2 Mean Effective Stress Values at Failure

b-Value	Mean Effective stress (kPa)	% Difference from σ_{oct} = 95 kPa
0	98.0	3.10%
0.25	94.2	-0.84%
0.25	91.1	-4.24%
0.5	94.7	-0.36%
0.75	94.1	-0.93%
1	109.1	12.97%
1	97.5	2.58%

octahedral plane (σ_{oct} = 95 kPa for this study) was performed using a transformation equation,

$$\left(\sigma_1^*, \sigma_2^*, \sigma_3^*\right) = \left(\sigma_1, \sigma_2, \sigma_3\right) \frac{3.\sigma_{oct}}{\left(\sigma_1 + \sigma_2 + \sigma_3\right)} \tag{4.1}$$

where σ_1* is major, σ_2* is intermediate, and σ_3* is minor principal stress after transformation. These interpolated normal effective stress values at failure were then projected on to the two-dimensional octahedral stress space (Fig. 4.8) using equation 4.2.

$$x = \frac{\sqrt{2}}{2}\left(\sigma_2^* - \sigma_3^*\right) \qquad \text{and} \qquad y = \sqrt{\frac{3}{2}}\left(\sigma_1^* - \sigma_{oct}\right) \tag{4.2}$$

Failure points from all the tests including those repeated are shown on the octahedral plane in Fig. 4.8, and the plot is rotated assuming symmetry. Three major failure criteria are also presented for comparison: extended von Mises, Mohr-Coulomb criterion, and constant third invariant (I_3=k). The parameters for each failure envelope were calculated from the triaxial compression (b=0) test. The I_3=k criterion shows exactly the same shape in the octahedral plane as Lade's (1990) failure envelope and seems to match the observed failure surface for Kaolin clay with OCR = 5.

The directions of plastic strain increment vectors relative to the yield surface were studied in order to investigate the applicability of classical plasticity theory. The principal strain increment axes are superimposed on the principal stress axes, and the strain increment vectors are presented in the octahedral plane (Fig. 4.8) with their origin at their failure stress point, assuming that the strains at failure are purely plastic. If the principal strain increments are $\Delta\varepsilon_1$, $\Delta\varepsilon_2$, $\Delta\varepsilon_3$, and their mean value is $\Delta\varepsilon_m$, the direction of principal

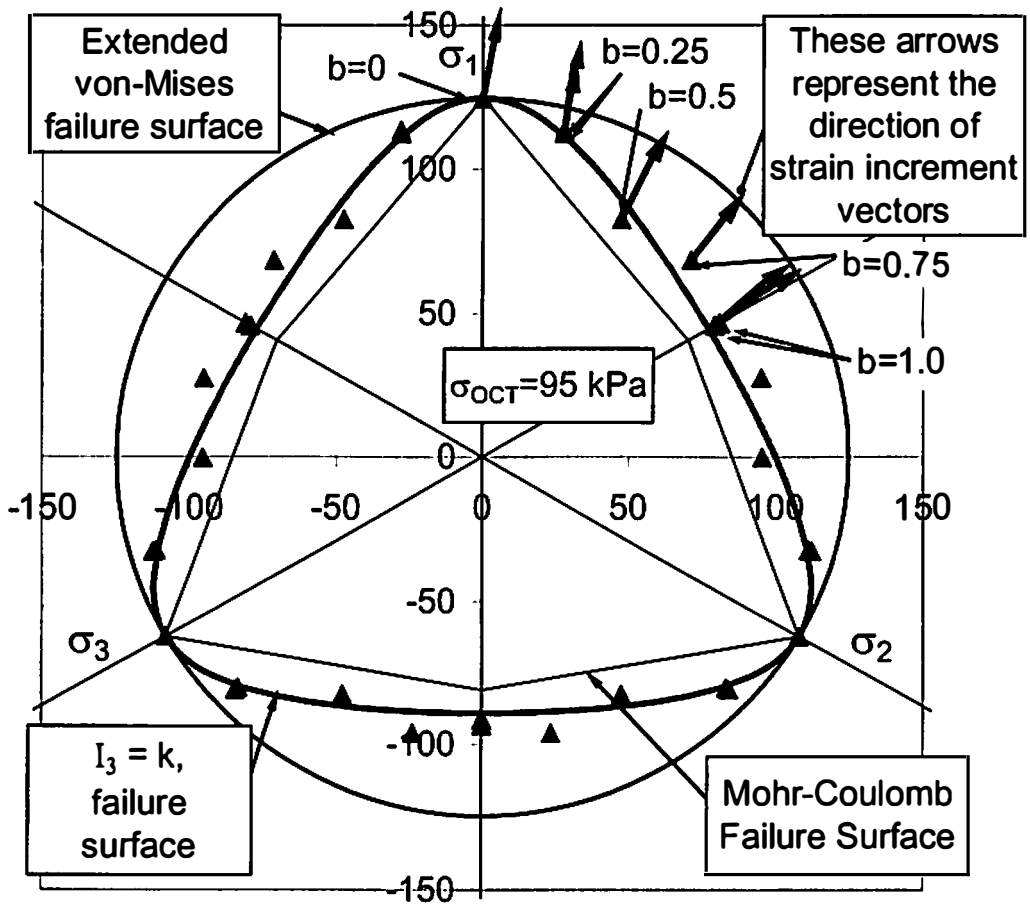

Figure 4.8 Three Dimensional Failure Surface in Octahedral Plane

strain increment vector in octahedral plane can be determined according to

$$\frac{dy}{dx} = \sqrt{3}\frac{(\Delta\varepsilon_1 - \Delta\varepsilon_m)}{(\Delta\varepsilon_2 - \Delta\varepsilon_3)} \qquad \text{where,} \qquad \Delta\varepsilon_m = \frac{1}{3}(\Delta\varepsilon_1 + \Delta\varepsilon_2 + \Delta\varepsilon_3) \qquad (4.3)$$

For the associative flow rule, the yield surface acts as a plastic potential surface (surface to which the strain increment vectors are normal), therefore the strain increment vectors are supposed to be normal to the yield/failure surface. However, Fig. 4.8 shows that the strain increment vectors from the current experimental data are more likely to be normal to a circular potential surface in octahedral plane as represented by extended von-Mises surface shown in the figure. Yong and McKyes (1971) reported similar plastic potential surface for Kaolinite clay, however the failure surface was reported to follow the Mohr-Coulomb criterion as opposed to I_3 = k surface as observed in this study. Callisto and Calabresi (1998), in the tests on natural Pisa clay, found that the strain increment vectors follow a circular potential surface more closely than the yield surface suggested in their paper. The experimental observations from the current study indicate that for OC Kaolin clay, a circular plastic potential surfaces with failure criterion corresponding to I_3=k surface was appropriate for varying intermediate principal stress values. Therefore, this clay exhibits a non-associative flow rule.

The Mohr-Coulomb criterion defines the angle of internal friction, ϕ', as a soil parameter with no dependence on σ_2. Other failure criteria previously noted are dependent on σ_2. The variation in ϕ' with b-value from the experimental data is shown in Fig. 4.9 and compared with the predicted relationships from different failure criteria. This figure also confirms that the I_3=k gives a reasonable prediction of measured data.

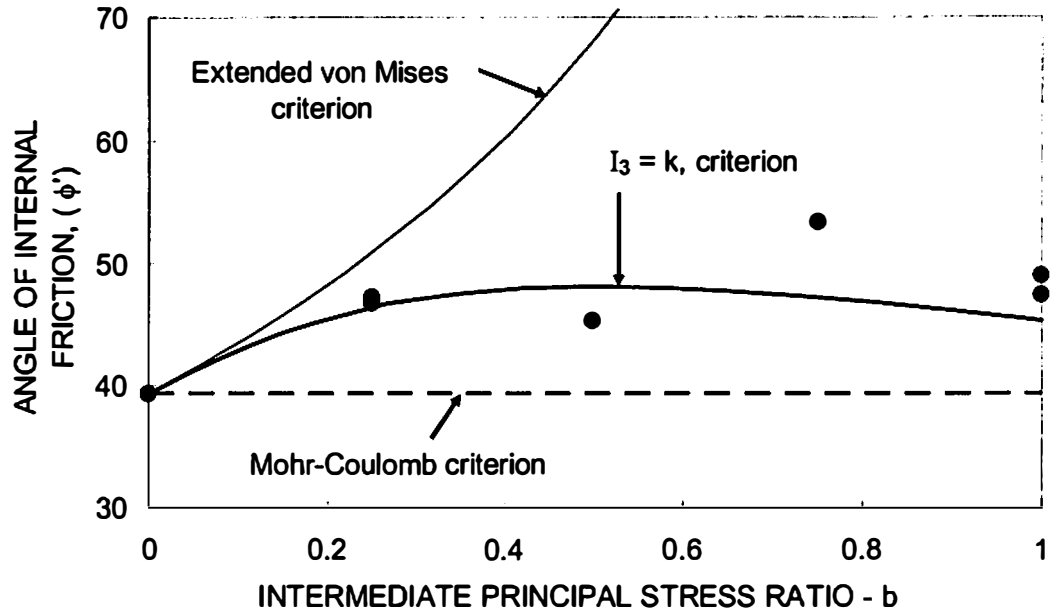

Figure 4.9 Angle of Internal Friction Compared with Different Failure Criteria

Strain Analysis and Localization Phenomenon

Bifurcation and Undrained Instability

Vardoulakis (1982) defined bifurcation as "*a critical state in deformation process when deformation does not follow its 'straight ahead' continuation but turns to an entirely different mode.*" Under 'perfect' boundary conditions, a 'perfectly' homogeneous material may undergo non-homogeneous deformation, as various 'bifurcation' modes of deformation can develop. Hill (1962) proposed that the weak stationary discontinuities of the velocity gradient during this bifurcation mode must be understood as localizations of the deformation into shear bands. Hvorslev (1960) observed these shear bands in a series of unconfined compression tests on clay specimens with particle orientation different from the geometric axis of specimen. In other series, the specimen with clay particle

orientation normal to the specimen axis showed considerable post failure bulging with non-uniformity in axial as well as radial direction. It was reported that the degree of this non-uniformity at large strains was much larger than theoretically expected non-uniformity due to the influence of frictional end restraint. Later Vardoulakis (1982) explained that "*these 'additional non-uniformities' are bifurcation and post-bifurcation phenomena which are linked by the constitutive properties of the soil, specimen geometry and boundary conditions, and by geometrical and/or material imperfections.*" Hambly (1972) performed strain controlled, plane strain tests with NC kaolin clay and reported that shear bands were observed when the stress path reached the Mohr-Coulomb limit surface, forming a rhombic pattern. First formulation for localization with shear band formation in OC clay was given by Palmer and Rice (1973).

Vardoulakis and Sulem (1995) formulated that even for plastically incompressible poro-elastoplastic material, undrained shear banding goes hand in hand with pore-water pressure shocks. Under locally undrained condition when the fluid flow is zero everywhere in the considered domain, these pressure shocks diffuse so quickly that in actual time scale of any soil testing it can be concluded that no pore-pressure shocks can develop across shear band boundaries and therefore undrained shear banding or bifurcation mode can not be sustained. Vardoulakis (1985) showed that under locally undrained condition Rice's (1975) linear stability analysis at the state of maximum deviator stress leads to a sharp transition from infinitely stable to infinitely unstable behavior. In globally undrained condition when internal flow of pore-water can be assumed to take place, shear banding is possible with global stability condition satisfied,

if the amount of water that has to flow across the shear band boundaries due to small shear band dilation or contraction can be accommodated by elastic deformation of the surrounding band soil mass. This phenomenon was further investigated and found to be possible only at large deformations. Han and Vardoulakis (1991) and Vardoulakis (1996) supported this experimentally by performing undrained biaxial tests.

Sum of Principal Strains

In most of the previous studies, principal strains were measured only in two directions and third principal strain was calculated from the volumetric strain information (sum of principal strains). In such an approach, the error in strain measurements for any non-uniformity in the deformed specimen is forced into the third principal strain only, whereas this non-uniformity might have equally affected all the three principal strains. Considering the fact that it is difficult to define the actual shape of deformed specimens in various test methods, this assumption was good at small strains when the deviation from actual deformation profile is considerably small. At larger strains when the level of deviation increases, it becomes necessary to measure all the three principal strains and analyze the data with these values only. In this process, at least the error is distributed equally among all the three principal strains.

In this study, the normal strains were measured at the center of six faces on a cubical specimen in all three principal directions. Summation of these normal strains in three principal directions is plotted against the major principal strain in Fig. 4.10. During an undrained shear test, the volumetric strain should be zero for incompressible pore fluid. The sum of principal strains would give the first approximation of this volumetric

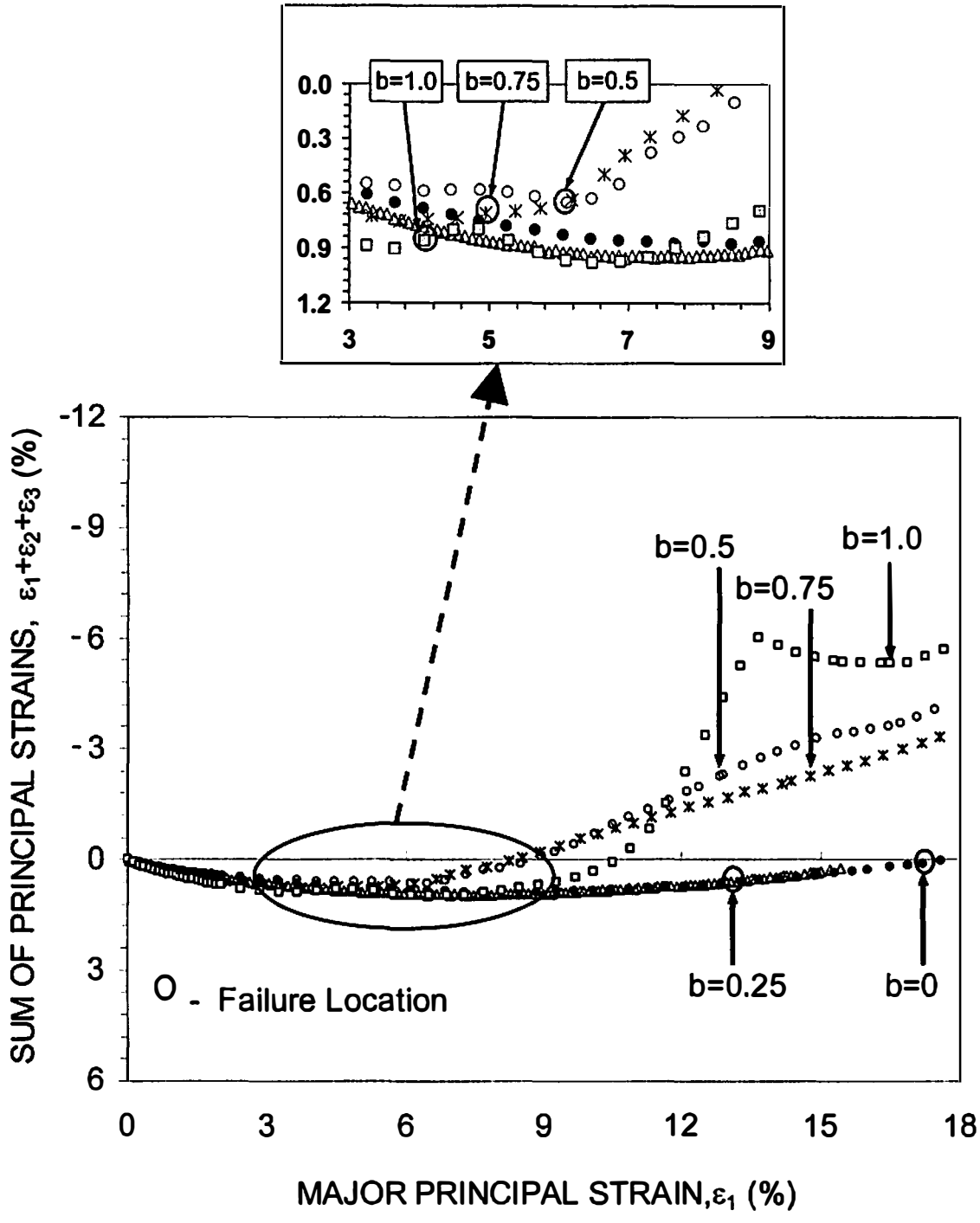

Figure 4.10 Sum of Principal Strains during Undrained Shear Test for Different b-values

strain. In this study, the sum of observed principal strains was found to provide nonzero values for all b-values. In fact these summation values were consistently larger than zero. The reason for this can be explained by the setup used for measuring strains on the cubical specimens. With a flexible membrane, true triaxial system, the deformation profile is not completely uniform on each face of the cube (Mandeville and Penumadu, 2003). In order to see the profile of deformed specimen at different stages in stress-strain curve, the b=1 test (most critical case) was repeated several times. A few tests were stopped just before the failure and others just after the failure. Fig. 4.11(a) shows the undeformed cubical specimen, which was later sheared to ε_1 = 4.2% (just past failure) and then unloaded to zero stress state with the same strain rate as in loading. Fig. 4.11(b), 4.11(c) and 4.11(d) show pictures of the same deformed specimen. Edges and corners in Fig 4.11(b) confirm that their overall configuration remains intact during shear; however, Fig. 4.11(c) shows that the center of each face deforms slightly more than the edges and corners. The system used in this study calculates the strain values on each face based on the deformations measured at the center of the specimen and those may be slightly different from the average strains on the entire face of the cube. Therefore, the sum of the normal strains measured in all principal directions was found to be nonzero. The edges and corners responsible for this small strain difference covered a very small area of each face. The measured strain in each of the three directions was uniform for a large central area as shown in Fig. 4.11(e). Therefore, the sum of the three principal strains should not be large during controlled undrained shear. The strain rate at the edges or corners would also be much smaller than the strain rate at the center representing most of the area of

(a)

(b)

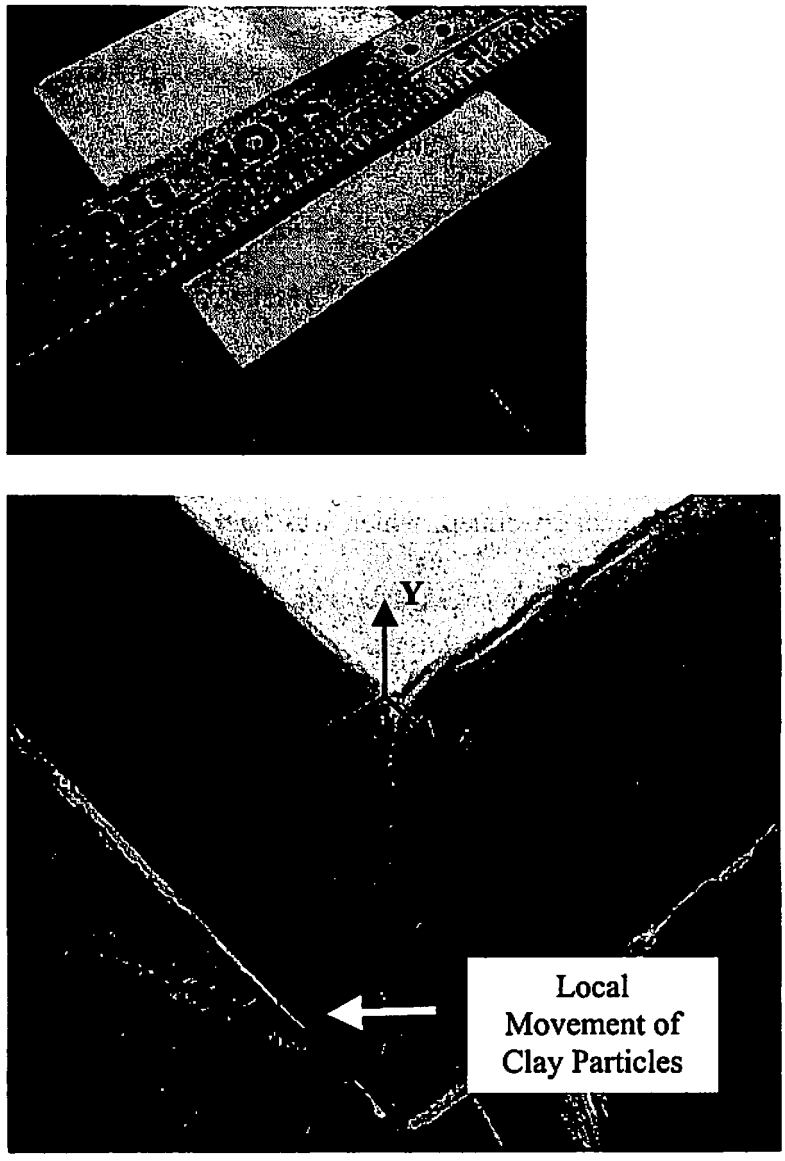

Figure 4.11 Deformation to Failure in Cubical Specimen, (a) Undeformed Specimen, (b) Deformed Specimen

(c)

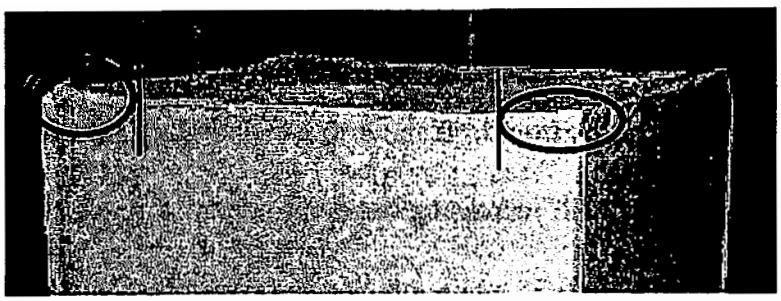

(d)

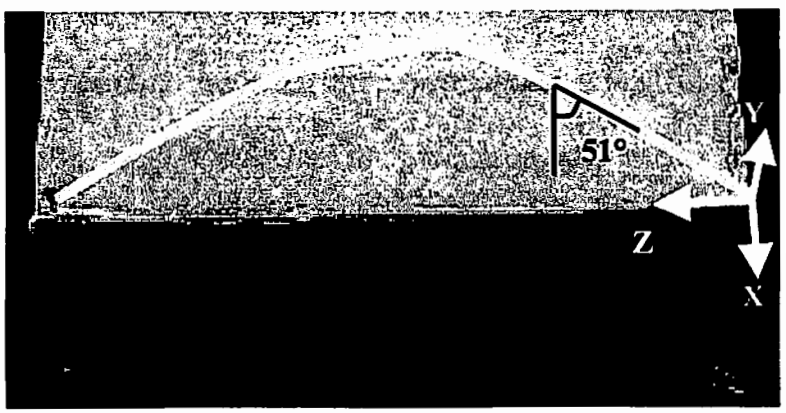

(e)

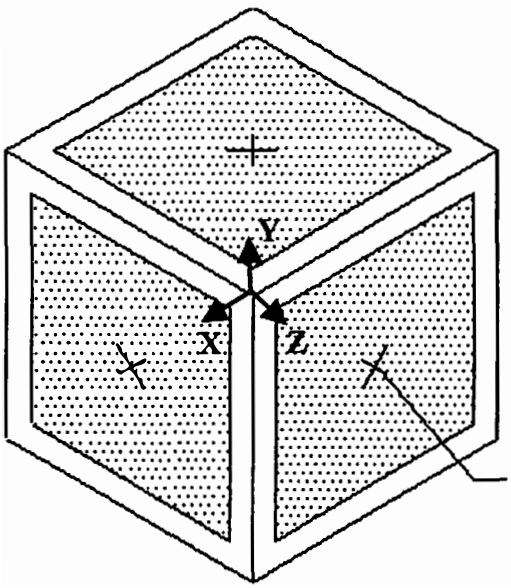

These marks represent the location for Measurement of deformation.

Figure 4.11 Continued. (c) Strain Variation at Edges and Corners, (d) Strain Localization (Shear band), and (e) Deformation Zones in Cubical Specimen

face and therefore any major change in sum of the strains should only be due to large irregularity on deformed shape produced by strain localization.

In Fig. 4.10, results from b=0 and b=0.25 conditions indicate smooth variation of the sum of the strains, with increasing major principal strain (ε_1), while the specimens sheared with b=0.5 and b=0.75 attain a high rate of volume change for ε_1= 6%. The b=1 case shows dramatic changes at ε_1= 4% and beyond. These observations indicate that the specimens sheared with a b-value less than 0.5 reach failure very smoothly at large principal strain values. The specimens sheared with b-value of 0.5 and above reach failure at smaller strains and then, for constant deviator stress, undergo uncontrolled deformation due to strain localization. This strain localization, which is due to shear band formation or undrained instability, leads to large irregularities on the faces of the specimen. Then an abrupt change in the rate of the sum of strains is observed. Post failure behavior of the specimens, sheared with b-values greater than 0.5, shows a small increase in deviator stress for a large increase in strain caused by localization. These observations were taken into consideration when identifying the failure point for various stress paths, with an understanding that the deformed specimen has significant non-uniformity beyond the onset of this bifurcation/undrained instability and therefore strain information in test data becomes unreliable.

Localization with Shear Band Formation

Specimens used in repeated b=1 tests, stopped just before the occurrence of failure, showed no evidence of any localization and the deformation was relatively uniform throughout the specimen. For b=1 tests stopped just after the failure, specimens

showed clear localization and was also confirmed by observing the variation of the sum of principal strains. The circled area in Fig. 4.11(b) shows defused localization on the z-face with a barely visible shear band formation, which moves the soil particles locally from the cube's z-face (σ_1-dir) to the x-face (σ_3-dir). The y-face (σ_2-dir) had more clear shear band formation as shown in Fig. 4.11(d). These shear bands were inclined at an angle of 51° (approx.) from the σ_3 direction. The specimens observed well after reaching failure in the original series of tests, showed similar but more complex shear-band formations for b=0.5 and higher, and they also had localized bulging in the σ_3 direction. For b<0.5, the specimen extruded after failure showed no visible non-uniformities.

Variation of Principal Strains and Strain Rates

In order to maintain a constant strain rate in the σ_1 direction (z-axis), total stress (σ_z) was applied on the corresponding face of cubical specimen through PID control. The total stress in the σ_3 direction (x-axis) was maintained constant and the total stress in the σ_2 direction (y-axis) was applied through PID control to maintain a target b-value. Figure 4.12 shows the variation of three principal strains with time. Figure 4.13 shows the time variation of the rates of these strains. The observed variation in ε_1 is identical for all the b-values ($\dot{\varepsilon}_1$=0.05%/min.), which confirms the excellent strain rate control provided by the PID algorithm employed in this test series. Pre-failure ε_2 and ε_3 values were observed to have linear relationships with time, while these strains (and their rates) at failure experienced abrupt changes. For the b=1 case, σ_1 and σ_2 had the same magnitude throughout the duration of the test, and assuming that the specimen was approximately isotropic, the corresponding strains also should have relatively close values. A similar

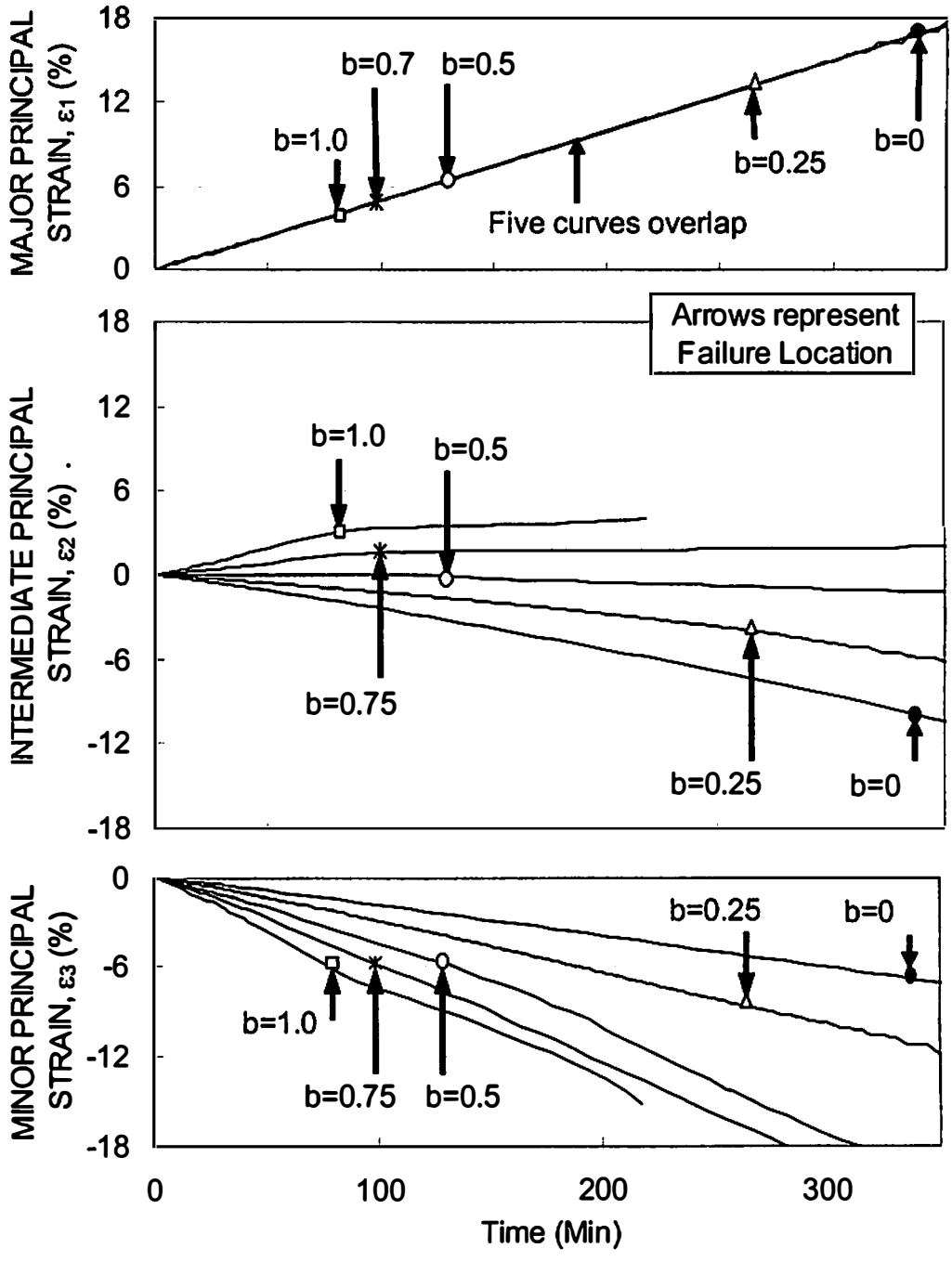

Figure 4.12 Variation of Principal Strain with Time during Shear Test

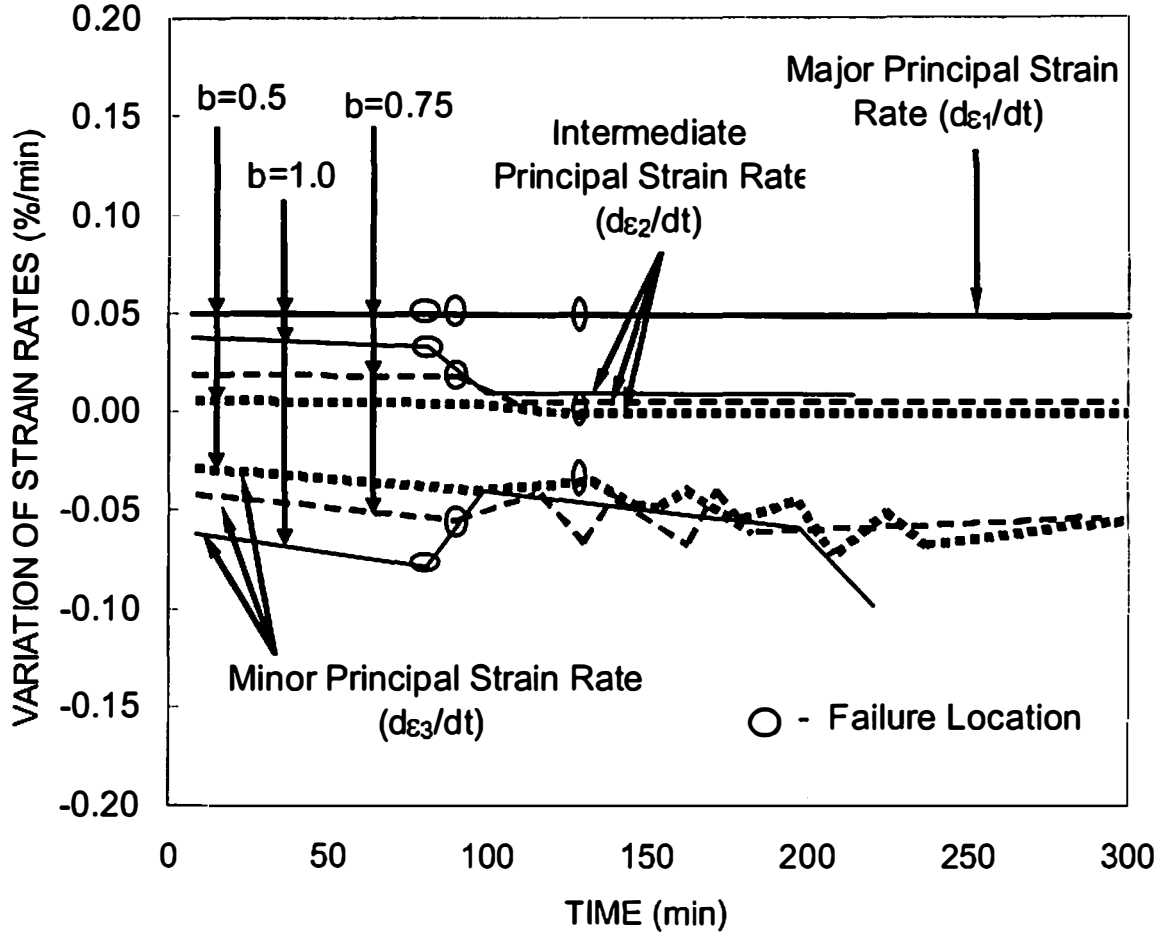

Figure 4.13 Strain Rate Variation in Three Principal Directions during Shear Test (b = 0.5, 0.75 and 1.0)

observation was expected between ε_2 and ε_3 for b=0 case. Experimental observations in Fig. 4.12 in fact show that the pre-failure strains closely followed this expected behavior and, because of the strain localization due to bifurcation or undrained instability in the soil, post-failure strains deviated from the expected behavior. Variation of ε_2 and ε_3 for the b=0.25 case show some fluctuation after failure. This indicates a possibility of localization after this point, but it was not prominent enough to be visible in this case. In the b=0.5 case, ε_2 was negligible until it reached the failure point, then after the failure, it showed an expansion with a rate of 0.005%/min. Therefore the b=0.5 case can beassumed to follow the plane strain condition. However, the Mohr-Coulomb criterion implicitly assumes the plane strain condition for all b-values. Tests with b-values of 0.5 and higher show significant changes in strain rate close to failure; therefore, only these tests are shown in Fig. 4.13. This figure indicates that for all these b-values, minor principal strain rates after the failure was approximately equal for varying stress paths, and the strain rates in the intermediate principal direction equal zero. This observation leads to a reasonable argument that, after failure, the deformation becomes inceasingly localized in shear band formation. The soil particles in other zones start to move from the σ_1 to σ_3 direction, and the σ_2 direction becomes more or less inactive. In a recent study, Wang and Lade (2001) observed a similar tendency along the σ_2 direction for drained tests on Santa Monica beach sand.

Conclusions

A three-dimensional flexible boundary true triaxial system with real time PID feedback control system is a good experimental tool to obtain reliable three-dimensional constitutive data. In this system, PID coefficients have to be chosen carefully with due consideration to the effect of specimen stiffness variation during shear. These control parameters should be tuned independently for a given soil type with different stress history. Present research shows that they do not need to be retuned for simulating different stress paths for a given OCR value.

The stress paths applied under 3-D conditions significantly affect the stress-strain-strength behavior and pore pressure response of OC clay. Key observations from this study are the following:

- Stiffness of the clay at small strains increases with the increasing value of σ_2.
- Shear strain to failure decreases with the increasing b-value.
- For kaolin clay with OCR=5, excess pore pressure generated during undrained shear is relatively small for all the b-values. The peak excess pore pressure increases with increasing b-value.
- Yield locations from stress-strain curves suggest that specimens sheared with $b \geq 0.5$, have predominantly elastic pre-failure behavior, whereas, for the specimens sheared with $b<0.5$, the elastic zone ends well before the failure.

Identification of strain localization onset is an important aspect in defining the failure point precisely, because, beyond this point, the test data without exact information about specimen deformation is not reliable. This study suggests that the following

information can be used as a possible tool for identification of strain localization in undrained true-triaxial testing:

- A sudden change in the variation of the sum of principal strains, ultimately reaching large values.
- An abrupt change or fluctuation in the evolution of intermediate and minor principal strains.

Under undrained conditions, shear banding was observed to occur on or after the peak shear stress location.

Experimental data for the failure stress states in the octahedral plane closely follows a constant third invariant failure criterion (I_3=k). Strain increment vectors drawn at corresponding failure points in the octahedral plane suggest that the plastic potential surface appears to be circular in shape and is supported by the findings of Yong and McKyes (1971) and Callisto and Calabresi (1998). Based on the experimental data presented, I_3=k, yield/failure criterion with extended von Mises plastic potential surface is suggested for modeling the 3-D shear behavior of the OC Kaolin clay used in this study.

Chapter 5. Development of Suitable Three-Dimensional Yield and Failure Surfaces from Experimental Data

This chapter is a slightly revised version of a paper submitted to the Journal Soils and Foundations in 2004 by Amit Prashant and Dayakar Penumadu:

Prashant, A., and Penumadu, D. "Three-Dimensional Mechanical Behavior of Kaolin Clay." In review , *Soils and Foundations.*

My primary contribution to this paper include: (1) selection of the topic and development of the problem to study the three-dimensional constitutive behavior of cohesive materials, (2) identification of the study topics, (3) gathering and interpretation of published literature, (4) performing all the laboratory experiments, (5) interpretation and analysis of test results, and (6) part of the writing related to manuscript preparation.

Abstract

A series of strain controlled undrained true triaxial tests on cubical specimens have been performed using a fully automated flexible boundary experimental setup, with real-time feedback control system to evaluate the three-dimensional mechanical behavior of kaolin clay. This chapter concentrates on the relative response of the soil elements under monotonic shear loading observed at various overconsolidation levels. A possible shape of the initial yield surface is explored based on the limit of purely elastic deformations. The discussion includes the influence of the relative magnitudes of the principal stresses on the clay behavior observed at different overconsolidation ratio values. Failure condition is shown to be governed by the onset of localizations developed within the specimens, and because of which the specimens show brittle response at

failure. Based on the experimental observations, a 3D dynamic failure criterion is developed, which involves a failure surface that grows in size as a function of pre-consolidation stress. A reference surface constraining the ultimate yielding of clay, commonly used in bounding surface plasticity, is found to be different from the observed failure surface, due to the brittle response of the clay.

Keywords: Localization, Overconsolidated clays, Shear deformation, Strain, Three-dimensional analysis, Undrained shear tests, Yielding.

Introduction

Cohesive frictional materials show complex mechanical behavior. The stress-strain behavior depends on the size, shape, mineral composition and packing of the particles, past stress history, type of pore fluid, magnitude and orientation of principal stresses during loading, rate of loading, and other factors. Single element laboratory tests were often used to characterize various aspects of the observed soil behavior, and the experimental data obtained was used to formulate constitutive equations (Roscoe and Burland 1968, Schofield and Wroth 1968, Prevost 1981, Defalias 1987, Lade 1990, Whittle and Kavvadas 1994 and many others). Laboratory tests in earlier studies for a comprehensive description of normally consolidated and overconsolidated clays (e.g., Henkel 1959; Parry 1960) often involved single axis loading conditions (e.g., triaxial compression testing). However, for better simulation of field conditions, the laboratory tests had to be designed to evaluate three-dimensional yield and failure behavior by subjecting a soil element to a true triaxial state of stress and strain. Early devices that were developed to perform these tests were cumbersome, difficult to operate and typically required manual control to perform experiments. Recent advances in control

hardware and software have allowed high-speed digital closed loop control to be used in soil testing. This allows accurate and repeatable tests to be performed on the soil specimens. Shibata and Karube (1965), Broms and Casbarian (1965), Yong and McKyes (1971), Vaid and Campanella (1974), Saada and Bianchini (1975), Lade and Musante (1978), and Germaine (1982) took advantage of these technologies in parts and performed traditional triaxial, plane strain, axial-torsional and true triaxial tests. However, most of these studies were limited to the description of normally consolidated clay behavior and the primary discussion was about the influence of the changing magnitudes and directions of the principal stresses. For a complete description of the clay behavior, it is essential to perform similar studies at various overconsolidation ratio (OCR) values using the same testing apparatus. Use of same testing apparatus should eliminate the influence of specimen shape and boundary conditions on the observed relative response of the clay.

The objective of the current research is to evaluate the relative response of the three-dimensional mechanical behavior of normally consolidated to heavily overconsolidated kaolin clay using the true triaxial device described in chapter 2. The influence of anisotropy on the consolidation behavior of clay was evaluated by performing two constant rate of strain (CRS) tests. In one test, the axial load for K_o consolidation was applied in the direction of initial slurry consolidation; whereas in the other test the axial load was perpendicular to it.

The true triaxial tests were performed on the cubical specimens at various intermediate principal stress ratio, b = 0, 0.25, 0.5, 0.75 and 1.0. Keeping the same initial isotropic pre-consolidation stress value (275 kPa), the tests were repeated for three OCR

values, OCR=1, 5 and 10. The observed stress-strain, pore pressure and strength behavior in a series of tests on normally consolidated (OCR=1), and moderately overconsolidated (OCR=5) kaolin clay were presented chapter 3 and 4, and the results were discussed to evaluate the influence of the relative magnitude of intermediate principal stress (σ_2) and the onset of localization. The influence of σ_2 for lightly overconsolidated clays may be assumed to be observed between these two OCR values (OCR=1 and 5), however for heavily overconsolidated clay the stress anisotropy might show significantly different behavior. Results obtained from a similar series of tests on heavily overconsolidated (OCR=10) kaolin clay are included in this chapter in order to compare them with the observations at OCR=1 and 5. To complete the description of overconsolidated clay, two triaxial compression (b=0) tests were also performed on the cubical specimens with lightly overconsolidated initial stress state i.e. with OCR=1.5 and 2. All of these tests were compressive in nature in terms of total stress applied on the specimens during shearing. This means that even for the b=1 case, the shear stress was applied by increasing the same amount of normal stress in σ_1 and σ_2 directions and maintaining a constant total stress in the σ_3 direction.

Consolidation Behavior of Clay

During the specimen preparation, the slurry was initially consolidated to 207 kPa effective vertical stress under K_o condition, and the direction of loading was marked as the z-axis of each specimen. As a result, the specimens were supposed to have a certain degree of cross-anisotropy (both stress induced and inherent) about the z- axis. In order to assess the influence of this anisotropy on the consolidation behavior of clay, a constant

rate of strain K_o consolidation tests [CRS test, ASTM:D4186-89 (1998)] were performed by consolidating the specimens in two directions. For the vertical consolidation, the direction of axial loading was along the z-axis; whereas for the horizontal consolidation, it was rotated by 90° from the z-axis. These specimens were taken from a single cubical specimen as shown in Fig. 5.1. The specimens were consolidated to 1000 kPa at the axial strain rate of 0.10 %/min and then unloaded to 100 kPa at the strain rate of 0.04 %/min. Figure 5.2 shows the consolidation curves (void ratio vs. vertical effective stress) obtained for the two specimens. The compression index, C_c, and the swelling index, C_s, have been commonly used to characterize the volumetric deformation properties of clay, and were assumed to be directionally independent. However, in this study these indices obtained for the vertical specimen (C_c=0.38, C_s=0.055) were higher than those obtained for the horizontal specimen (C_c=0.36, C_s=0.036) of the same clay. The recoverable deformation (elastic) property of clay, swelling index C_s, was observed to be significantly different for the vertical and the horizontal specimen. By repeating the tests it was ensured that the marked difference in C_c and C_s values was not a result of experimental scatter. The difference between the two indices, $(C_c - C_s)$, defines the permanent deformation (plastic) property of clay, which was observed to be a constant (0.33) for the two specimens. This observation leads to an argument that the relationship between the elastic component of volumetric deformation and the applied loading for an anisotropic clay material may not be directionally independent of the loading direction; however, for the plastic component, the relationship could be directionally independent.

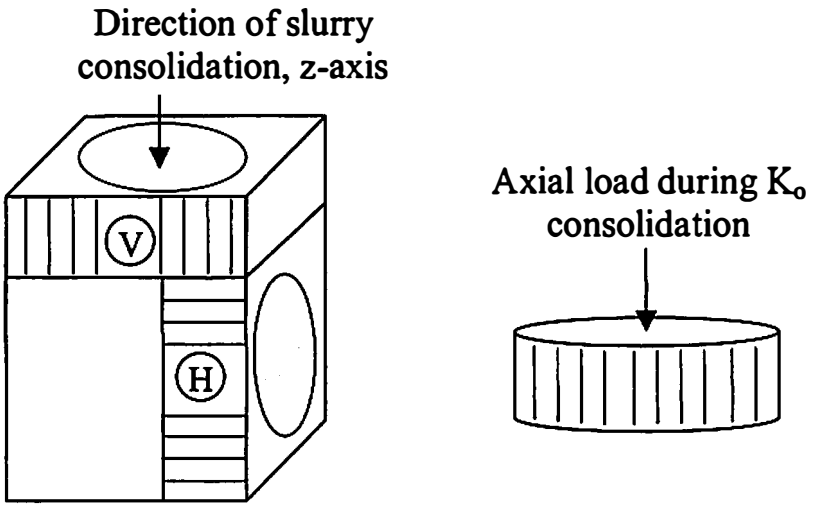

Figure 5.1 Direction of K_o Consolidation for Vertical (V), and Horizontal (H) Specimens

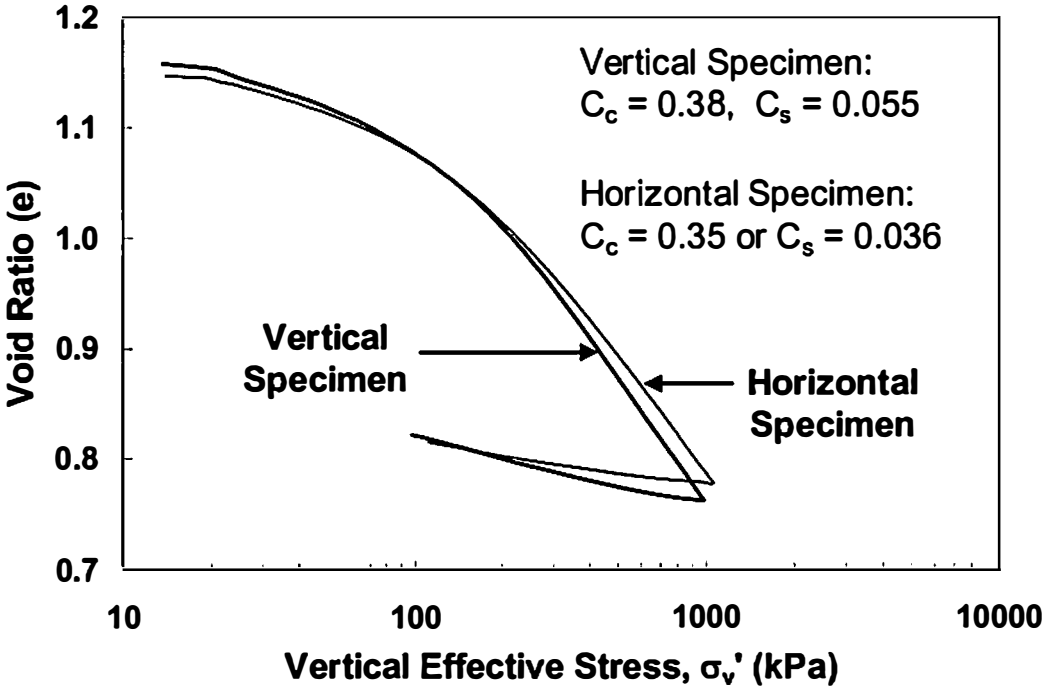

Figure 5.2 Consolidation Curves for Vertical (V) and Horizontal (H) Specimens

Shear Failure and Localization

During the shear behavior analysis of undrained true triaxial test data, the failure point was defined as the point of peak deviator stress just before the specimen sheared to large strains, with negligible change in shear stress. This definition of failure point was suitable in this series of true triaxial tests, because the specimens were observed to have localized deformation at and beyond peak deviator stress. A method of identifying the onset of localization using the strain information obtained from a true triaxial shear test was presented in Chapter 4. Shear bands and defused localizations observed in the specimens sheared from initial hydrostatic stress state corresponding to OCR=5 were presented in previous chapter. Similar patterns were observed for the specimens sheared with normally consolidated (OCR=1) to heavily overconsolidated (OCR=10) stress state. Hvorslev (1960) observed shear bands and/or post failure bulging in a series of unconfined compression tests on clay specimens. Vardoulakis (1982) explained that these non-uniformities are *"bifurcation and post-bifurcation phenomena which are linked by the constitutive properties of the soil, specimen geometry and boundary conditions, and by geometrical and/or material imperfections."* Bifurcation was defined as "*a critical state in deformation process when deformation does not follow its 'straight ahead' continuation but turns to an entirely different mode.*" Under "perfect" boundary conditions, a "perfectly" homogeneous material may undergo non-homogeneous deformation, as various bifurcation modes of deformation develop. Because of this phenomenon, we can say that the single element testing methods with different boundary conditions and specimen shapes may show different post-bifurcation shear behavior. Moreover, in the presence of the localized deformation, the strain state cannot be

determined accurately using global measurements of deformation, which is the case in most of the single element testing apparatuses used by researchers. In light of these observations and based on the data available to date in literature, one can say that the constitutive equations may only be developed to define the pre-localization behavior of clay, and the failure condition in such a model should be assumed at the onset of localization.. However, in most of the previous studies, this phenomenon was overlooked and was not considered during the development of various theories, which attempt to propose the use of normalized strength behavior for cohesive soil.

Undrained Shear Behavior from Triaxial Compression Tests at Different 'OCR' Values

Undrained triaxial compression (b=0) tests were performed by shearing the cubical specimens from the initial hydrostatic stress states corresponding to OCR=1, 1.5, 2, 5, and 10. The pre-consolidation stress before shearing was the same for all the specimens, as p'_o=275 kPa. The shear stress-strain behavior and the effective stress paths observed during these tests are shown in Fig. 5.3 and 5.4 respectively. The mean effective stress, p', deviator stress, q, and the shear strain, ε_q, were calculated from the general invariant expression shown in equation A.1, A.2, and A.3 of Appendix-A.

For each OCR value, the observed stress-strain relationship (Fig. 5.3) was nonlinear from start to failure. With due consideration to classical elasto-plasticity theories, the elastic zone (to define a yield surface) of shear deformation, for overconsolidated clays, was identified to correspond to small magnitude of shear strain values, where the stress-strain relationship was approximately linear. An approximate

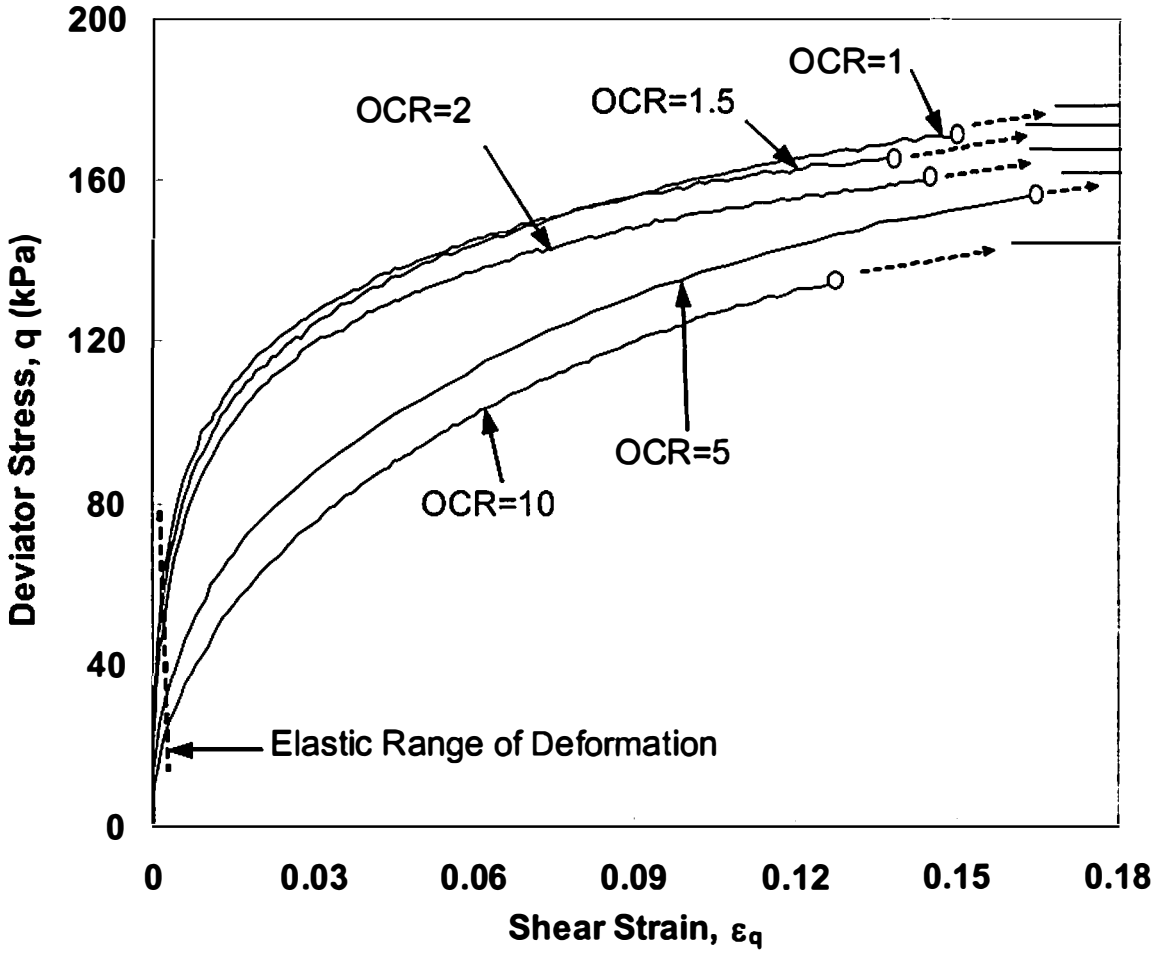

Figure 5.3 Shear Stress-Strain Behavior from Undrained Compression Tests (b=0) at Various OCR Values

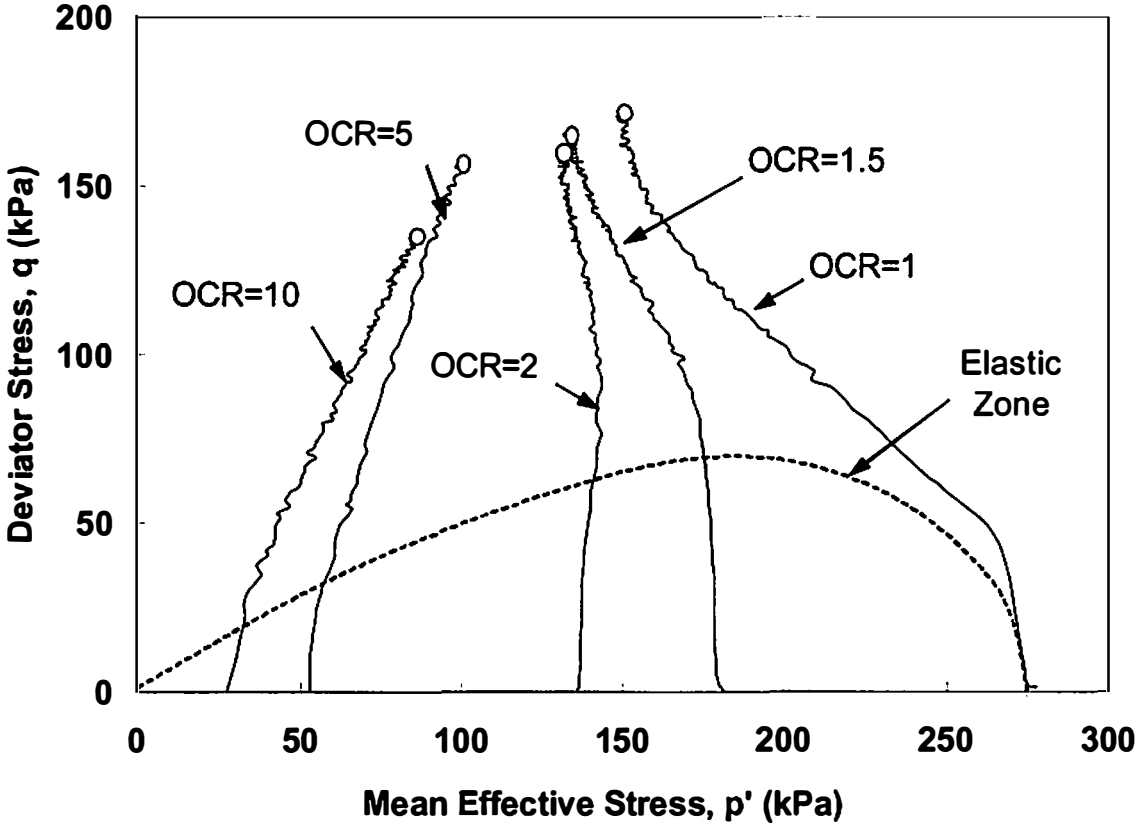

Figure 5.4 Effective Stress Path for Undrained Compression Tests (b=0) at Various OCR Values

limit of this elastic zone (defining yield points) is shown in Fig. 5.3. In elasto-plasticity theory, a yield surface was defined in the stress space as the limit of elastic deformation, and the stress state at this surface was assumed to be normally consolidated. A probable yield surface in q-p' stress space is shown in Fig. 5.4, by mapping the yield points determined from the stress-strain curves in Fig. 5.3. In 3D stress space, this surface defines the cross-section of a 3D yield surface of clay in triaxial compression plane; the p' axis would be along the hydrostatic stress line. The shape of this yield surface can be visualized as a teardrop; which is similar to the one suggested by Lade (1990) based on the contours of plastic work.

Considering the simplicity of formulation, most constitutive theories assume isotropic elasticity and define the elastic deformation to be uncoupled for volumetric and shear components. In such a case, the elastic volumetric deformation can be assumed to occur in the specimen, only if there was a change in the mean effective stress. During undrained shear, the total volumetric deformation (combined elastic and plastic componants) remains zero throughout the shearing; and therefore, in the elastic zone, the mean effective stress should remain constant to maintain zero elastic volumetric deformation. Within the limit of the initial yield surface shown in Fig. 5.4, the stress paths for the tests at various OCRs can reasonably be assumed to have constant mean effective stress. However, due to a combined influence of the specimen anisotropy and transitional plasticity, a small change in mean effective stress p' was observed before reaching the initial yield surface. In elasto-plastic region (beyond the initial yield surface), the change in mean effective stress p' during shearing shows the dilatancy

behavior of the clay. The change in mean effective stress, $-\Delta p'$, during an undrained test on saturated soil represents a part of the excess pore pressure Δu_q that developed due to the applied shear stress (discussed in Chapter 3). The rest of the pore pressure develops due to the change in mean total stress. Figure 5.5 shows the evolution of total excess pore pressure Δu, and its part generated due to shear Δu_q with increasing shear strain ε_q. This figure shows same pattern of variation for both Δu, and Δu_q, because the loading pattern (b=0, and σ_1 along the axis of cross-anisotropy) was same for all five tests. The decrease in p' ($+\Delta u_q$) during undrained shearing indicates the tendency of volumetric compression; whereas, the increase in p' ($-\Delta u_q$) gives the dilative potential of clay. The specimens sheared from OCR=1 to 2 showed consistent decrease in p' during yielding; however, the total change in p' through failure, as a result of the contractive nature, decreases with the increasing OCR. For higher OCR values (OCR=5 and 10), p' was increasing (dilative) throughout the shearing. From the data presented in Fig. 5.4, a threshold value of OCR=2.2 may be approximated at which the dilatancy potential can be assumed to be zero.

The specimen sheared at various OCR values showed failure at the shear strain of 13%-15%. During most of the tests, the specimen sheared at constant shear stress beyond failure; however, the shear stiffness just before the failure was not zero. The stress-strain relationship reached the failure smoothly and showed a sudden change in the slope at failure (See stress-strain relationships shown in Fig. 5.6). The reason behind this brittle behavior was probably the localization developed within the specimens at failure points. The specimen might have reached a higher shear stress level in the absence of

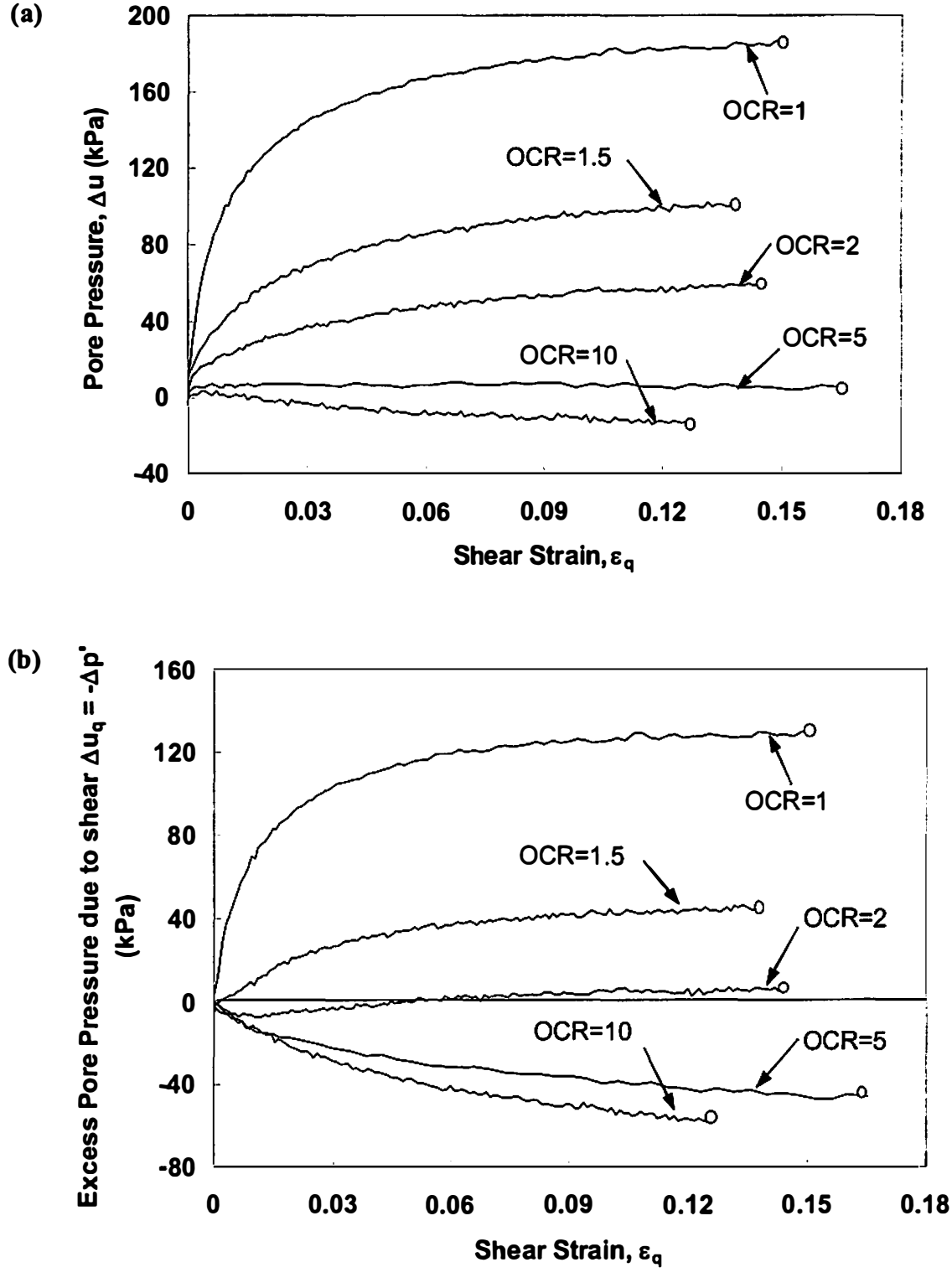

Figure 5.5 Excess Pore Pressure (a) Total, and (b) Part due to Shear for Undrained Compression Tests (b=0) at Various OCR Values

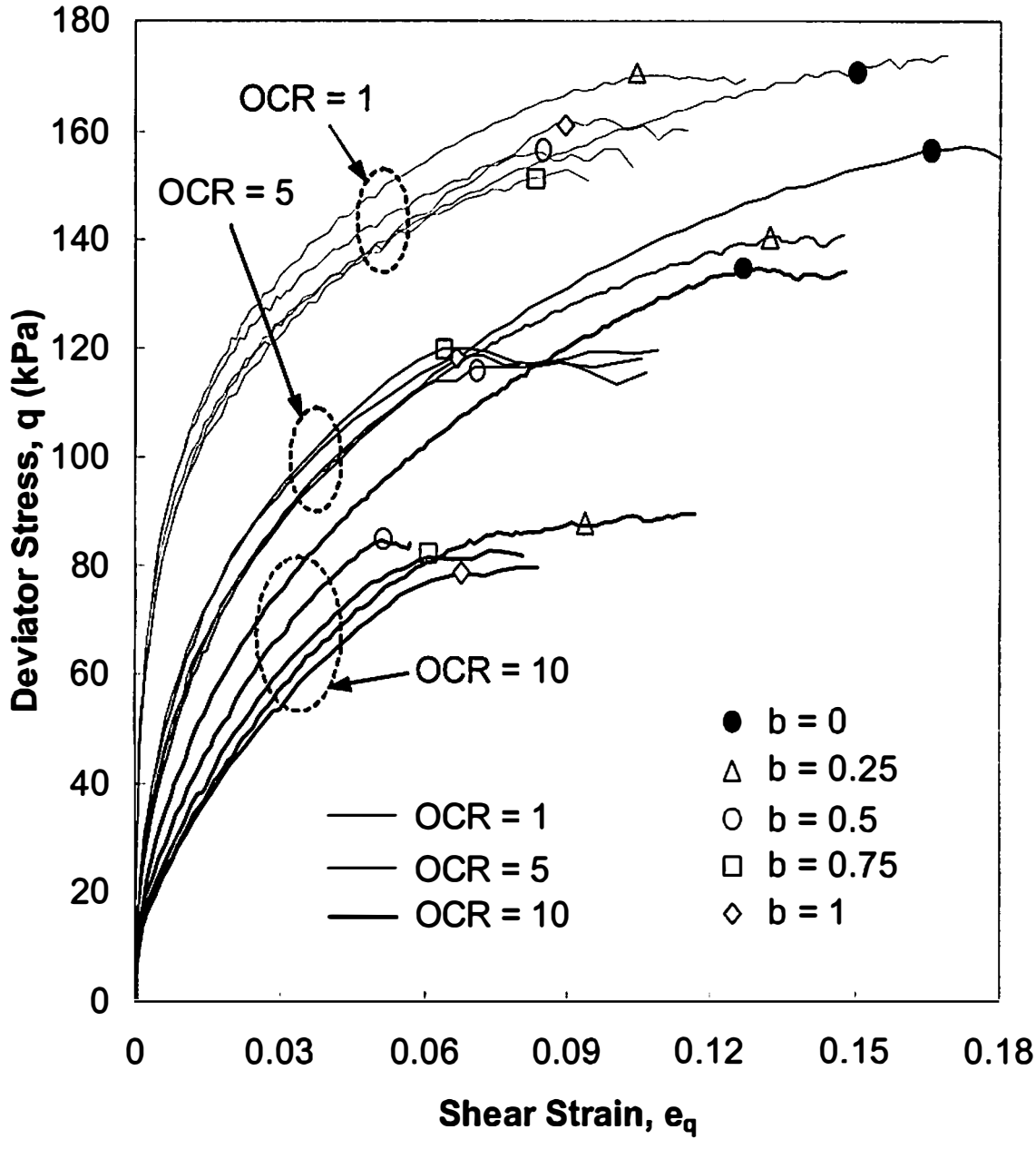

Figure 5.6 Influence of Intermediate Principal Stress and Anisotropy on the Shear Stress-Strain Behavior of Clay

localization. These hypothetical peak shear stress levels were determined for each test by extrapolating the stress-strain relationship to a point of zero shear stiffness and they are shown in Fig. 5.3, using straight lines in front of the curves. Based on these observations, one can say that a constitutive theory developed for such clay should define its limiting yield surface independent of the failure surface. Such types of reference surfaces constraining the ultimate yield surface have been commonly used in many bounding surface plasticity theories (Mroz 1963, Dafalias 1986), however, they did not differentiate between the reference surface and the failure surface. From the experimental observations in this study, the failure surface may be defined as a lower bound for the reference surface, and that would ensure the applicability of the definition of failure at peak deviatoric stress.

Influence of Intermediate Principal Stress

To study the influence of intermediate principal stress (σ_2') on the clay behavior, a series of constant b-value true triaxial undrained tests were performed for b=0, 0.25, 0.5, 0.75, and 1, at various OCR values. The data obtained from the series of tests performed on the normally consolidated (NC), and moderately overconsolidated (OCR=5) cubical specimens of kaolin clay was presented in Chapter 3 and 4, including a detailed discussion about the observed influence of σ_2' on the stress-strain, pore pressure and strength behavior. A similar series of flexible boundary true triaxial tests were performed on heavily overconsolidated cubical specimens with the initial hydrostatic stress state corresponding to OCR=10. For all the three series of tests (OCR=1, 5, and 10), the maximum pre-consolidation stress was the same as p_o'=275 kPa.

Figure 5.6 compares the undrained shear stress-strain behavior observed at OCR=10 to the observed behavior at NC and OCR=5 initial stress state. The variation in the shear stress-strain relationship for different b-values was more significant at OCR=10 than it was observed at OCR=1 or 5. The inherent anisotropy induced in the specimens during preparation can be used to explain this experimental observation. From the observed consolidation behavior of clay, it was determined that the elastic deformation had more significant influence from the inherent anisotropy than the plastic deformation. Based on this observation, one can also say that a part of the inherent anisotropy remains in the memory of soil during loading-unloading but the significance of its influence depends on the applied effective confining stress. Under this assumption, the increasing mean effective stress would reduce the influence of inherent anisotropy, and consequently reduce the variation in the stress-strain behavior for a change in the b-value. For a large reduction in the mean effective stress (such as in the case of heavily overconsolidated clay), a part of anisotropy of the specimen may recover and influence the stress-strain behavior.

The specimens sheared with higher b-values failed at lower shear strain values and the shear strain to failure decreased with the increasing overconsolidation. In the previous section, the triaxial compression tests were shown to have somewhat brittle failure behavior. With the increasing b-value, this brittleness in the failure behavior increased dramatically. For $b \geq 0.5$, the shear stiffness just before the failure was significantly higher than zero. As a result, there would be a remarkable difference between the shear stress values at the reference surface (bounding the ultimate yield surface for zero shear stiffness) defined in the previous section, and the failure surface.

Based on the experimental observations, the reference surface may be defined to have the same shape as the failure surface along the hydrostatic stress line; however, in the deviatoric plane these surfaces would have significantly different shapes.

Shear Strength of Clay

Over the last few decades, researchers have investigated various clays to establish a relationship that can define the shear failure in terms of the three-dimensional stress state and void ratio. Hvorslev (1937) showed that "*the peak shear stress at failure τ_f of clay is a function of the effective normal stress σ'_f on, and the void ratio e_f in, the plane of failure at the moment of failure and this function is independent of the stress history*". Roscoe et al. (1958) extended Hvorslev's theory and derived a relationship for failure surface in e-q-p' space using the critical state void ratio concept. This relationship showed that the critical state was reached by the clay at a constant shear stress ratio, M ($=q_f/p'_f$), which may be different from the peak shear stress ratio or the shear stress ratio at the peak shear stress level. Egan (1977) explained the relative positions of the "peak" and "critical" states of failure for soils. It is difficult to say if the specimens tested for the experimental data used in critical state concept had any localization before reaching the critical state void ratio. Mayne (1979) summarized the results from 60 different clays reported throughout the geotechnical literature and confirmed the finding of Ladd and Foott (1974) that the normalized strengths (S_u/σ'_{vo}) are a function of OCR. They defined the failure as the undrained strength at maximum deviator stress, and critical state strengths were not reported. This definition of failure is consistent with the

definition used in current research after considering the localization issues discussed earlier.

Mayne and Swanson (1981) compiled the data from 90 different clay and silt soils and showed that the undrained shear strength for overconsolidated clays, normalized with overburden pressure, S_u/σ'_{vo} could be expressed relative to the S_u/σ'_{vo} for the normally consolidated clay using a simple relationship:

$$(S_u/\sigma'_{vo})_{OC} = (S_u/\sigma'_{vo})_{NC} OCR^{\Lambda_o} \qquad (5.1)$$

where the parameter Λ_o is a soil constant, which is determined from hydrostatically consolidated or anisotropically consolidated shear tests or both, and the subscripts OC and NC denote "overconsolidated" and "normally consolidated" respectively. The normalized undrained strengths obtained from the compression tests (b=0) conducted at various OCR values in the current study were used to evaluate this relationship (equation 5.1). Figure 5.7 shows that the strength data follows this relationship, and provides a constant value of $\Lambda_o = 0.90$. Based on the Cam-Clay theory (Schofield and Wroth 1968), Λ_o was referred to the critical state pore pressure ratio and was defined by

$$\Lambda_o = 1 - C_s/C_c \qquad (5.2)$$

where C_C and C_S were defined as the slopes of normal compression line (NCL) and unloading-reloading line (URL) in (log p'-v) compression plane. The discrepancy in Λ_o values obtained experimentally from equation 5.1, and theoretically from equation 5.2 was explained to be due to the assumption of a constant κ value for a nonlinear unload-reload line in compression plane. To overcome this issue Mayne and Swanson

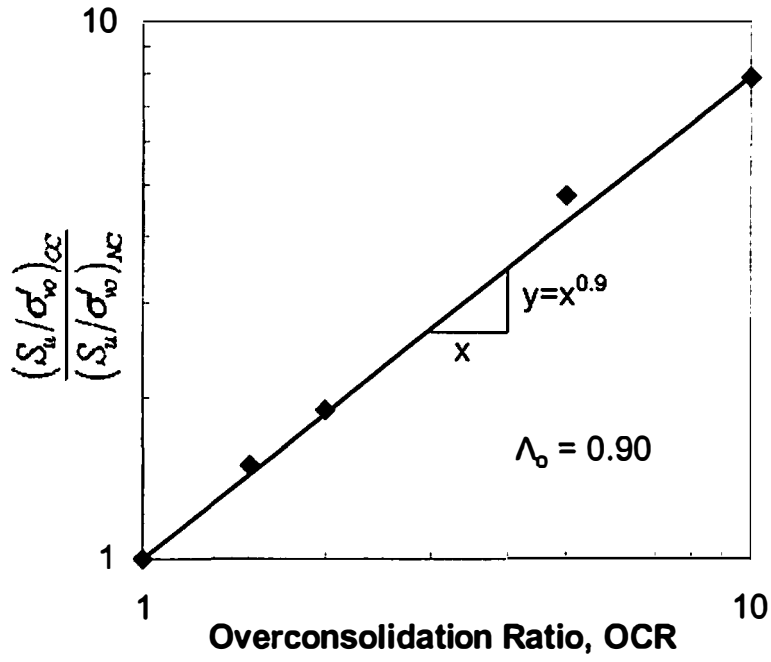

Figure 5.7 Variation of Normalized Undrained Strength with OCR

determined C_S from the value of Λ_o obtained from shear test data. The value of, $C_C - C_S$, represents the plastic component of the deformation; and therefore, the parameter $\Lambda_o = (C_C - C_S)/C_C$ may be referred to as plasticity ratio.

Failure surface in triaxial plane

Based on Mayne and Swanson's (1981) findings, the shear strength of clays may be assumed to be a function of its void ratio. In stress space, it may be represented using a corresponding value of mean effective stress, p'_e, on the NCL for a given void ratio. Figure 5.8 shows the consolidation behavior in compression plane for a typical clay. In this figure, a clay specimen at a mean effective stress p' has a void ratio e, whereas the mean effective stress and void ratio corresponding to the pre-consolidation stage are p'_o

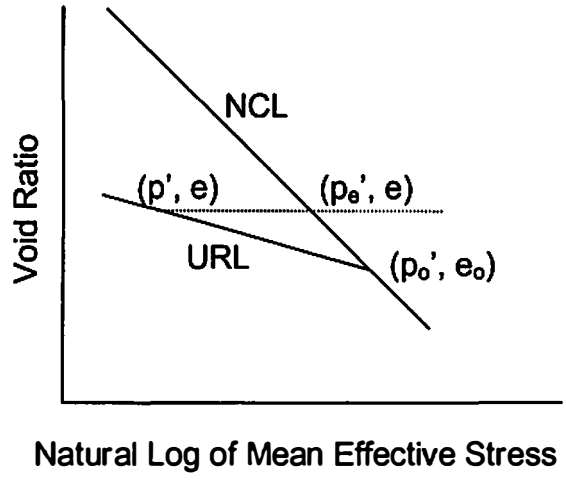

Figure 5.8 Isotropic Consolidation Curve for a Typical Clay

and e_o respectively. The representative mean effective stress at current void ratio is denoted by p'_e. From the equation of NCL and URL, void ratio e and e_o can be related using the following two equations:

$$e_o - e = C_C \log\left(p'_e / p'_o\right) \tag{5.3}$$

$$e_o - e = C_S \log\left(p' / p'_o\right) \tag{5.4}$$

Equations 5.3 and 5.4 may be solved to provide p_e' in terms of p' and p'_o:

$$p_e = p'^{1-\frac{C_S}{C_C}}_o \, p'^{\frac{C_S}{C_C}} = p'\left(p'_o / p'\right)^{\Lambda_o} \tag{5.5}$$

Void ratio has a constant relationship with p'_e, and therefore the shear strength q_f being related to void ratio should also have unique relationship with p'_e. This relationship may be assumed to be linear as shown in equation 5.6.

$$q_f = C_f p'_e \tag{5.6}$$

where, C_f could be a soil constant. Using equations 5.5 and 5.6, the failure surface in q-p' plane (stress space) can be defined as:

$$q_f = C_f p' \left(p'_o / p'\right)^{\Lambda_o} \tag{5.7}$$

During an undrained test, the p'_e remains constant throughout the test. For NC clay, the initial representative mean effective stress $p'_{e\ initial}$ is equal to the initial hydrostatic consolidation stress p'_o. In such a case the undrained shear strength:

$$q_{f\,NC} = C_f p'_{ef} = C_f p'_{e\ initial} = C_f p'_o \tag{5.8}$$

Similarly, for OC clay with initial mean effective stress p'_i and initial pre-consolidation pressure p'_o the undrained shear strength may be given by:

$$q_{f\,OC} = C_f p'_{ef} = C_f p'_{e\ initial} = C_f p'_i \left(p'_o / p'_i\right)^{\Lambda_o} \tag{5.9}$$

Here, the ratio p'_o / p' defines the OCR value of the specimen before shearing:

$$q_{f\,OC} = C_f p'_i \left(OCR\right)^{\Lambda_o} \tag{5.10}$$

Equations 5.8 and 5.10 can be rearranged to show the normalization of undrained strength in equation 5.1 suggested by Mayne and Swanson (1981):

$$\frac{q_{f\,OC}}{p'_i} \Big/ \frac{q_{f\,NC}}{p'_0} = \left(OCR\right)^{\Lambda_o} \tag{5.11}$$

Figure 5.9 shows the failure surface defined by equation 5.7 in q-p' plane for Λ_o= 0.5, 0.7, 0.9, and 1.0 with a constant value of C_f=0.5. The strength of OC clay relative to the NC clay increases with increasing Λ_o and reaches its maximum at the theoretical limit of Λ_o=1 when C_S=0. The p'/p'_o ratio at failure would depend upon the

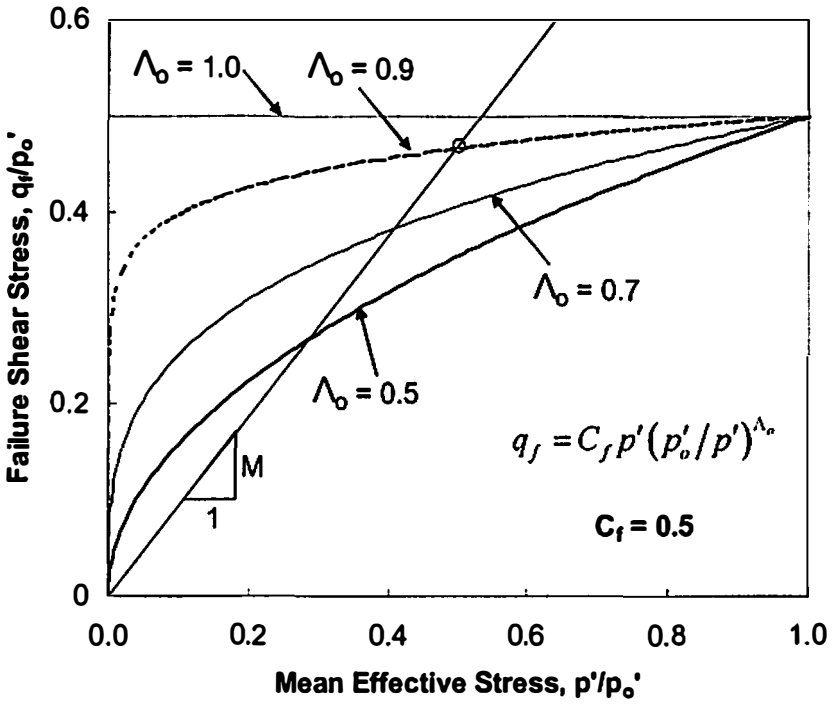

Figure 5.9 Failure Surface in Normalized q-p' Plane

dilative behavior of clay. The size of the defined failure surface increases with the pre-consolidation stress p_o'; therefore, it may be referred to as a dynamic failure surface. In the Modified Cam-Clay (MCC) model, soil was assumed to reach critical state at the mean stress ratio p'/p_o' = 2. The stress state attained at the critical state, during an undrained shear test on normally consolidated (NC) clay, did also correspond to the peak shear stress state and the state of peak shear stress ratio. The peak shear stress ratio at critical state was defined by a soil parameter M. To incorporate the current failure surface (equation 5.7) into the MCC constitutive framework, the parameter M can be related to parameter C_f based on the p'/p_o' ratio at failure, as shown in equation 5.12.

$$M = 2^{\Lambda_o} C_f \tag{5.12}$$

The dilative behavior at failure of clay may differ from a constant relationship of $(p'/p'_o)_f$=2 assumed in the MCC model. The current failure surface provides the freedom of p'/p'_o ratio being a soil property and that facilitates better prediction of pore pressure or volumetric strains at failure during shearing of clays.

Failure surface in deviatoric plane

In the previous section, the failure surface was defined in the triaxial compression plane, which described the influence of overconsolidation and the variation of pre-consolidation stress along the hydrostatic stress axis. In order to complete the description of failure surface in three-dimensional stress space, the strength of clay would now be considered in deviatoric plane (around the hydrostatic axis). For isotropic material, the shear strength may be assumed constant in a deviatoric plane and the failure surface would assume a circular shape in this plane similar to the extended von-Mises failure surface. However, soils are known to be cross-anisotropic about their axis of deposition due to the preferred orientation of deposited soil particles and the unidirectional (vertical) loading during and after the deposition. In the presence of this anisotropy, the strength of soil may be described as a function of the relative magnitudes of the principal stresses and their orientation about the direction of deposition.

Lade (1990) used the third invariant of the stress tensor (I_3) to describe the strength behavior of soil and showed the consistency of this assumption over a range of the types of soil. In chapter 3 and 4, the author presented the undrained strength data obtained from true triaxial tests on the specimens with initial stress state corresponding to OCR=1 and 5. They showed that the kaolin clay used in the current research follows the

$I_3 = k_1$ (a constant for a deviatoric plane) failure criterion in the deviatoric plane. The plots have been reproduced in Fig. 5.10. This figure also includes the data obtained from a similar series of undrained true triaxial tests on highly overconsolidated specimens (OCR=10). The value of k_1 varies with the mean effective stress at failure; therefore, the data corresponding to one OCR value has been plotted in one deviatoric plane at a constant mean effective stress. The k_1 value at each deviatoric plane has been calibrated from the triaxial compression test performed at corresponding OCR value. Figure 5.10 shows that the $I_3 = k_1$ surface presents a reasonable choice of defining failure criteria in deviatoric plane; the surface along hydrostatic axis should be defined in agreement with the equation of the failure surface in triaxial plane (equation 5.7). Considering the shapes

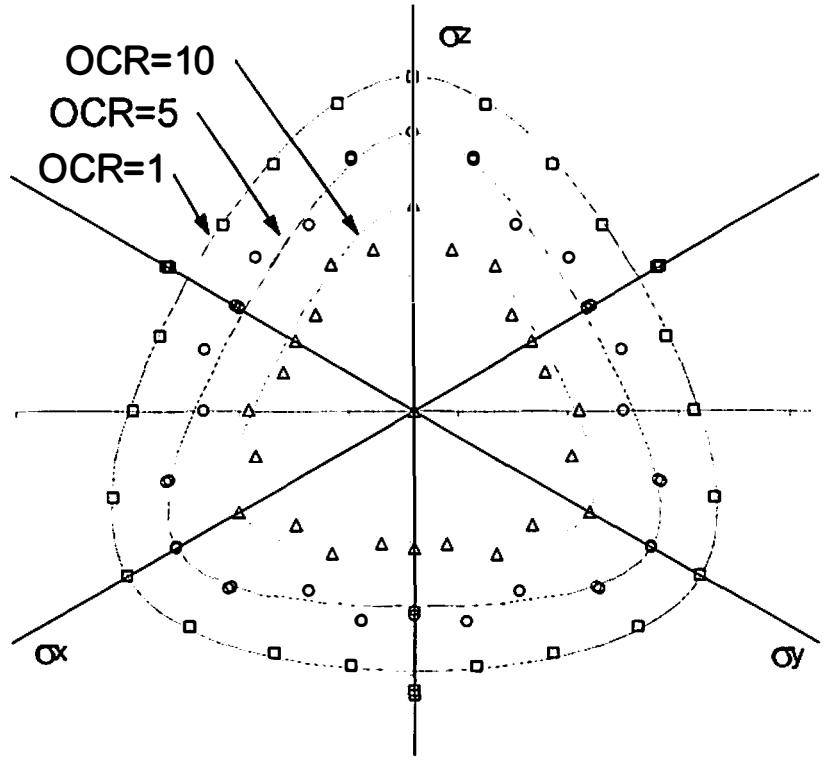

Figure 5.10 Failure Surface in Deviatoric Plane

in triaxial compression and deviatoric plane a failure surface in three-dimensional (3D) stress space can be defined as

$$I_3 = \left(1 - \frac{k}{27}\right) p'^3 \tag{5.13}$$

where,

$$k = \left(9 - 2\frac{q_f}{p'}\right)\left(\frac{q_f}{p'}\right)^2 \tag{5.14}$$

Here, q_f / p' was a function of mean effective stress in equation 5.7; therefore, it would be a constant for a deviatoric plane. Note that the parameter C_f should only be calibrated using triaxial compression tests in order to avoid the complexities of involving equation 5.14 along with equation 5.7 during its determination. The failure surface defined by equation 5.14 may be constrained to the positive quadrant of the 3D stress space where all principal stresses are compressive. This would correspond to the widely accepted assumption of no cohesion in frictional materials such as clay. In this case the k-value may be restricted to range from $0 \leq k \leq 27$.

Conclusions

In this chapter, the influence of overconsolidation and the relative magnitudes of principal stresses on the true triaxial behavior of kaolin clay was evaluated using the data obtained from a series of flexible boundary undrained tests on remolded cubical specimens. To study the influence of inherent anisotropy on the consolidation behavior of clay, the constant rate of strain K_o consolidation tests were performed by applying the axial stress along (vertical) and perpendicular (horizontal) to the axis of cross-anisotropy

in two different specimens. Based on the experimental observations, the following conclusions were made about the clay behavior.

a) Assuming the virgin consolidation as elasto-plastic and unloading as elastic deformation, it was observed from the consolidation behavior of the clay that the elastic component of the volumetric deformation, represented by C_s, may not be directionally independent for anisotropic clays; however, the plastic component, represented by $C_c - C_s$, may still be assumed constant along all directions.

b) During undrained shearing, the specimens were observed to have localized deformation close to the peak deviatoric stress location, which was therefore considered as the failure location.

c) Based on the shear stress-strain behavior and the undrained stress paths observed at various OCR values, a teardrop shape was found to be adequate to represent the initial yield surface assuming purely elastic behavior within this surface.

d) The influence of inherent anisotropy, reflected through the shear stress-strain behavior observed for different b-values, was found to be more significant at lower initial confining stress, showing that the inherent anisotropy may be in part a recoverable phenomenon.

e) To describe the brittle behavior of clay observed during this study, the authors proposed the use of a different bounding surface for yielding (reference surface) than the failure surface. It was observed that these surfaces might have similar shapes in triaxial plane (containing the hydrostatic line) but in deviatoric plane, they would have significantly different shapes.

f) Extending the concept of normalization of the undrained strength of clays proposed by Ladd and Foott (1974), the authors have formulated a dynamic failure surface for clays as a function of the pre-consolidation mean effective stress. It was observed from the tests performed at each OCR value that the failure surface in the deviatoric plane could be defined using constant third invariant of stress tensor, and it was incorporated in the formulation of the proposed failure surface to complete its description in 3D stress space.

Chapter 6. Effect of Microfabric on the Three-Dimensional Behavior of Kaolin Clay

This chapter is a slightly revised version of a paper with the same title submitted to the Journal of Geotechnical and Geoenvironmental Engineering of ASCE in 2004 by Amit Prashant and Dayakar Penumadu:

Prashant, A., and Penumadu, D. "Effect of Microfabric on Mechanical Behavior of Kaolin clay using Cubical True Triaxial Testing." In review , *Journal of Geotechnical and Geoenvironmental Engineering*, ASCE.

My primary contribution to this paper include: (1) selection of the topic and development of the problem to study the effect of microfabric on three-dimensional behavior of cohesive soils, (2) gathering and interpretation of published literature, (3) performing all the laboratory experiments, (4) interpretation and analysis of test results, and (5) part of the writing related to manuscript preparation.

Abstract

Various aspects of the mechanical behavior of Kaolin clay are discussed in light of experimental observations from a series of strain controlled true-triaxial undrained tests, performed on cubical Kaolin clay specimens with flocculated and dispersed microfabric, using a fully automated flexible boundary experimental setup with real-time feedback control system. The laboratory procedures used to prepare flocculated and dispersed microfabric specimens are presented. The influence of microfabric on the consolidation behavior of Kaolin clay is evaluated based on the data obtained from K_o consolidation during constant rate of strain tests and the isotropic consolidation during

true triaxial tests. Undrained tests on Kaolin clay show that the following vary with microfabric of specimen: the shear stiffness, excess pore pressure generated during shear, brittleness, and strength and strain to failure. For both microfabrics, the observed strength behavior using cubical triaxial testing shows a similar pattern of variation with applied stress anisotropy; hence, only a marginal influence of fabric-induced anisotropy.

Keywords: Consolidation, Failure surface, Microstructure, Shear deformation, Soil dispersion, Soil structure, Three-dimensional analysis, Undrained shear tests.

Introduction

The structure of soil is composed of fabric and interparticle force system that is governed by soil composition, history, present state, and environment. The influence of soil structure on the engineering behavior has been recognized from the early stages of soil mechanics, and many authors (e.g. Mitchell (1956), Lambe 1958a; Seed and Chan 1959; Mitchell 1964; Olson and Mesri 1970) have attempted to explain various aspects of the engineering properties of clays on the basis of its structure. The geometric arrangement of particles, particle groups, and pore spaces is usually defined as the "microfabric" of clays (Mitchell 1993); the existing interparticle force system is referred to as the "stability" of fabric; and, the term "structure" is used to define the combined effect of clay microfabric and its stability (Soga 1994). Various studies have been performed using structured and destructured specimens of natural clays, and the quantifying methods have been established to relate the fabric stability of clays to its engineering behavior (e.g. Houston and Mitchell, 1968; Burland, 1990). The concept of fabric has been used to explain the anisotropy, and its influence on the observed mechanical behavior of natural clays (e.g. Kirkgard and Lade, 1993). Also, the changes in

microfabric associated with shear planes and zones have been examined by the researchers (e.g. Morgenstern and Tchalenko, 1967; McKyes and Yong, 1971). However, the effect of deferent types of microfabric on the mechanical behavior (consolidation, anisotropy, shear stiffness, strength, etc.) of clay is relatively less understood, and that is the motivation of the current study.

There has been a proliferation of terms for the description of microfabric. Barden and Sides (1971) reviewed and clarified many of the terms used in previous literature. They described the general terms of microfabric such as "flocculated"–which described any soil that has an open-ended structure with edge-to-face contacts or random orientation of the platelets –and "dispersed" –which described a soil with a closed structure that consists of many face-to-face contact or preferred orientation of platelets. These two terms essentially define two extremes of the microfabric that can exist in nature. A method of quantifying intermediate microfabrics (maybe as a degree of dispersion) has not been established which can be used to directly relate the microfabric to its mechanical properties. Promising efforts have been made in this direction using the two extreme microfabrics as references (Penumadu, 1996). Since natural clays of the same mineral composition but different microfabric are difficult to find, it is preferred to prepare the specimens for research in the laboratory. The flocculated and dispersed specimens of Kaolin clay are prepared in this study using the recent techniques suggested by Soga (1994), and Hazen and Penumadu (1999). A brief review of the efforts made in the past to obtain flocculated and dispersed microfabric of Kaolin, and a possible mechanism of fabric formation in aqueous medium, are presented in this chapter. The influence of microfabric on the compressibility behavior of Kaolin clay is evaluated using

the data obtained from constant rate of strain K_o consolidation tests (ASTM: D4186-89, 1998) that were performed on both the flocculated and dispersed microfabric specimens

It has been recognized that the arrangement of particles or particle groups plays a significant role in the inherent anisotropy of the soil deposits. This results in the observed variation of shear behavior with the change in magnitude and orientation of principal stresses. Various studies (e.g. Broms and Casbarian, 1965; Lade and Musante, 1978) have been performed to investigate the effect of change in magnitude and orientation of principal stresses on the observed shear behavior of natural and remolded clays. However, different researchers have not collaborated to determine the effect of clay microfabric on the observed three-dimensional shear behavior. As an objective of the current research, the influence of microfabric on the three-dimensional mechanical behavior Kaolin clay was investigated using the previously described true triaxial device. During undrained shear, the strain rate of 0.05%/min for flocculated, and 0.008%/min for dispersed specimens along σ_1-axis was found suitable to ensure pore pressure equilibrium within the specimens. During shearing, the normal stress and strain were recorded in the three principal directions.

The results obtained from a series of constant b-value true-triaxial undrained tests (at overconsolidation ratio, OCR=1, and OCR=5) on the flocculated microfabric specimens of Kaolin clay were presented in chapters 3 and 4, and the experimental observations were discussed in terms of the influence of intermediate principal stress, and the inherent and stress induced anisotropy of the specimens. The b-value, $b=(\sigma_2-\sigma_3)/(\sigma_1-\sigma_3)$, was defined as the relative magnitude of intermediate principal

stress (σ_2) with the major (σ_1) and minor (σ_3) principal stress. In the present study, authors performed a series of true triaxial shear tests on the dispersed microfabric specimens of the same Kaolin clay. The specimens were first isotropically consolidated to reach the normally consolidated (OCR=1), or moderately overconsolidated (OCR=5) initial stress state, and then sheared by maintaining a constant b-value throughout shearing. Test results are presented with their associated b-values, in comparison with the experimental observations of flocculated microfabric. The effect of microfabric will be addressed from the view point of consolidation behavior, induced anisotropy, and effect of relative magnitudes and orientation of principal stresses on stress-strain, pore pressure and strength behavior.

Obtaining Pre-conceived Microfabric of Clay in Laboratory

Many different approaches have been investigated since the 1960's on how best to obtain differing fabrics in cohesive soils. Martin (1965) investigated the idea that desired forms of Kaolinite microfabric could be obtained through different types of consolidation. It was found that Kaolinite slurry, with a water content of 190%, would produce flocculated specimens when consolidated to 98.1kPa and dispersed when consolidated in a K_o state to 19.3MPa. McConnachie (1974) consolidated 250% water content slurry of purified monomineralic Kaolin to several consolidation pressures ranging from 0.1kPa to 100MPa. It was found that a threshold pressure range existed where the specimens went from a flocculated microfabric to increasing degree of dispersed microfabric. At 14.7kPa the Kaolinite fabric was considered to have been flocculated and beyond that pressure the microfabric showed an increasing degree of

dispersion up to 100kPa. After 100kPa, the orientation essentially remained constant and even at the highest pressure the fabric was far from being ideally dispersed. Based on a study of the influence of pore water chemistry and type of consolidation, Krizek, et al. (1975) reported that a medium-grained Kaolinite with 96% of its particles smaller than 2μm was best suited for inducing preferred microfabric. A 0.01M Sodium hydroxide (NaOH) solution was found to optimize the dispersion in a slurry while 0.0001 M $CaCl_2$ and 0.01M sodium chloride (NaCl) were found to optimize flocculation in a slurry. K_o consolidation was shown to produce dispersed microfabric with the degree of dispersion depending on the type of slurry from which it was consolidated, either flocculated or dispersed. Isotropic consolidation led to more flocculated microfabric. Experimenting with chemical additives in Kaolinite slurry, Soga (1994) discovered that a slurry pore fluid consisting of distilled water with 4% concentration of sodium hexametaphasphate (Calgon) led to a highly dispersed microfabric upon K_o consolidation. Hazen and Penumadu (1999) experimented with different concentrations of Calgon in de-aired, distilled, and deionized water used as the pore fluid in 150% water content slurry of Kaolin clay. After K_o consolidation of the slurry, they showed that the dispersed microfabric could be obtained by using 2% Calgon solution; whereas, the flocculated microfabric could be obtained without using any additives.

Figure 6.1-6.3 show various stages of Kaolin clay in the formation of its microfabric. Kaolin is a 1:1 sheet silicate, composed of a $(Si_2O_5)^{-2}$ tetrahedral layer and an $(Al_2[OH]_4)^{+2}$ octahedral layer (see Fig. 6.1). Clay particles carry a net negative charge which is balanced by exchangeable cations. In dry powder form, the cations cluster at the

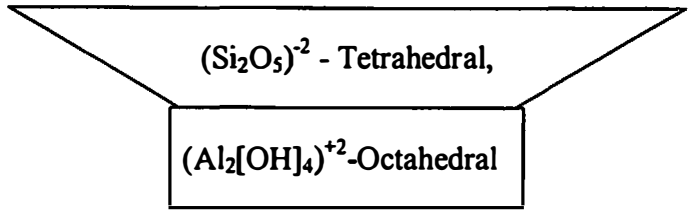

Figure 6.1 Mineral Structure of Kaolin Clay

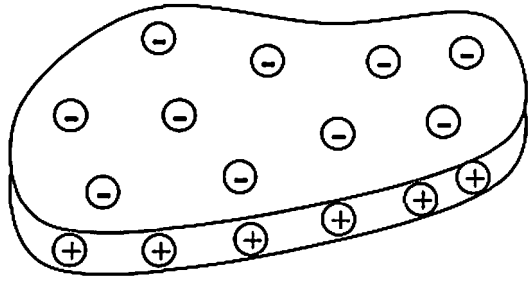

Figure 6.2 Ionic Distribution on Kaolin Clay Platelet in Aqueous Medium

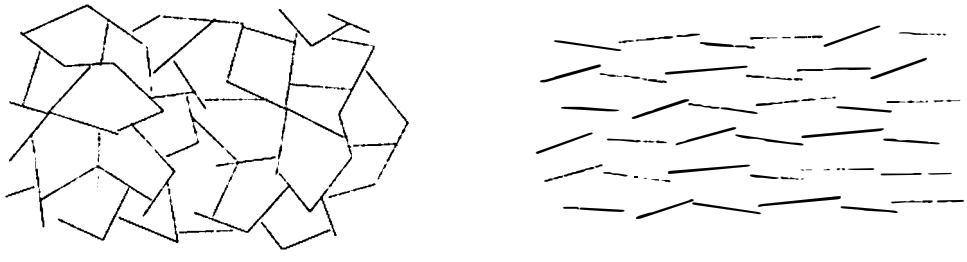

Flocculated Dispersed

Figure 6.3 Arrangement of Particles or Particle Groups for Flocculated and Dispersed Microfabric

clay surfaces and cause zero effective charge on the clay particles or particle groups (Lambe 1958a). As shown in Fig. 6.2, the nature of Kaolin in an aqueous medium (mixed in distilled and deionized water) changes; the faces of the particles (or platelets) get negatively charged, whereas the edges get positively charged (Carty 1999). Under this arrangement, edges (+ve) of a platelet get attracted to the faces (-ve) of another platelet; whereas, the faces of the two platelets try to repel each other as far as possible. As a result, these platelets form a *flocculated* microfabric of Kaolin clay. Additions of dispersants (Calgon) may change the ionic arrangement significantly. Carty (1999) showed that the dispersants, which are added to the pore fluid, get adsorbed by the positively charged particle edges only, when the edge thickness is significant enough. Consequently, when a desired amount of dispersant is dissolved in distilled and deionized water to make the slurry of Kaolin clay, the ionic distribution leaves the clay platelets with negatively charged faces only. Since the faces of all the particles are negatively charged, they try to repel each other and give the minimum free energy in parallelism. Under external loading condition (gravitational load or axial load during consolidation), they stack up on each other in the direction of loading due to the flaky shape of the particles, and form a *dispersed* microfabric of the clay. A typical arrangement of clay particles, normal to the loading direction, for flocculated and dispersed microfabric, is shown in Fig. 6.3.

Preparing Cubical Specimens

The batch of Kaolin clay powder used in the current study to make the cubical specimen was obtained from the same lot of clay used by Hazen and Penumadu (1999), with a liquid limit of 62%, a plasticity index of 0.32, and a specific gravity of 2.63. To

obtain flocculated microfabric, the 155% water content slurry was prepared by mixing Kaolin clay powder with de-aired, distilled, and deionized water; whereas, to obtain dispersed microfabric, 2% Calgon by weight of the water was mixed in the same slurry. The slurry was then consolidated under K_o condition using a consolidometer with 102x102mm square base. In order to minimize the frictional effects between the consolidometer and the slurry, the inner walls of the consolidometer were lined with teflon and were also sprayed with silicon before the transfer of the slurry. Initially, the slurry was consolidated under K_o conditions at a vertical stress of 30 kPa and allowed to consolidate for 1 hour; which helped prevent leaks during consolidation at higher stresses. This was especially a critical issue for the slurry made with dispersant (Calgon), due to the reduced particle-group size from deflocculation. The vertical stress was then increased to 207 kPa and consolidated until the completion of primary consolidation. The specimen was then extruded from the consolidometer; and the axis of uniaxial loading during K_o slurry consolidation was marked for future reference. Figure 6.4 shows the digital images of (a) flocculated and (b) dispersed microfabric of the cubical specimens, taken by Scanning Electron Microscope (SEM) at a magnification of 6000x along the direction of K_o consolidation.

Mandeville and Penumadu (2004) presented a water content analysis on the flocculated microfabric cubical specimens, obtained after K_o consolidation of slurry, to evaluate the uniformity in water content across the specimen. The average water content was found to be 42%, with an observed range of 40.03% to 42.88%. For the specimens with dispersed microfabric, a similar analysis was performed on several specimens, and

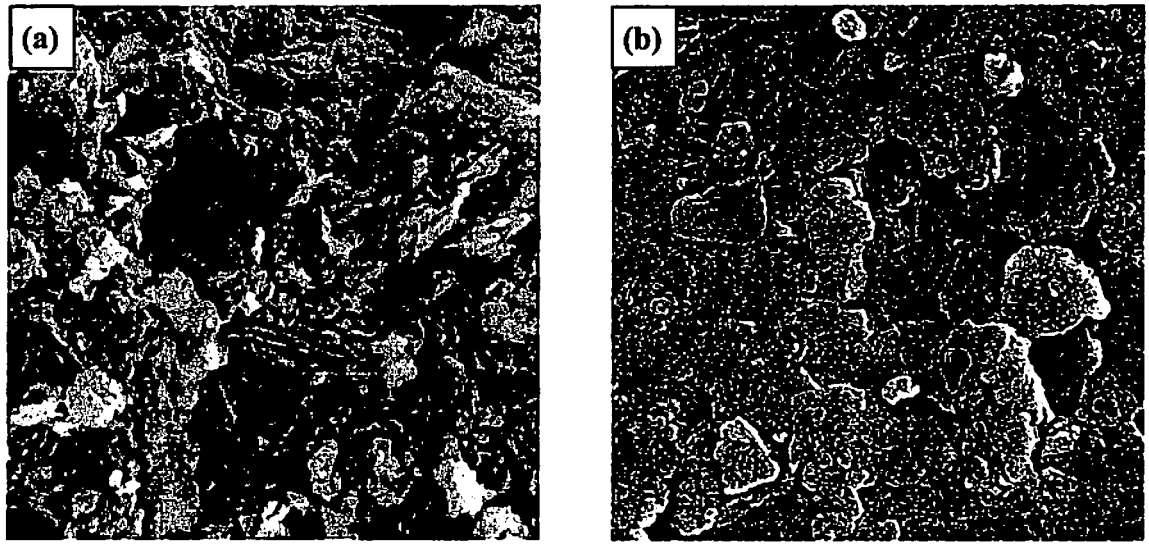

Figure 6.4 SEM Pictures of Clay for (a) Flocculated, and (b) Dispersed Microfabric

the average water content was found to be 29.5%, with an observed range of 29% to 30% indicating a very homogeneous and repeatable specimen state.

Consolidation Behavior for Flocculated and Dispersed Microfabric

Consolidation properties of clay have been commonly used in the practice to determine the settlement caused by loading from structures or fills. The consolidation behavior of clay depends on both compositional and environmental factors, which include the influence of minerals present in clay, shape and size of the particles, particle arrangement or microfabric of clay, and pore-water chemistry. Based on the observations from several studies (Seed et al. 1962, Quigley and Thompson 1966, and Houston 1967) on natural clays, and remolded de-structured clays, Mitchell (1993) enumerated various principals to explain the changing consolidation properties of soils with their microfabric. Different microfabric of clay can exist at the same void ratio or at the same effective stress. At constant void ratio, flocculated clay shows more rigidity against consolidation.

During K_o consolidation, the platy particles or particle groups of clay orient themselves with their long axes along the plane normal to applied axial stress. At constant effective stress, the change in microfabric of clay accompanies a change in void ratio, and the clay with dispersed microfabric, with lower void ratio, shows slower consolidation process.

To evaluate the consolidation behavior of the clay used in the current study, constant rate of strain K_o consolidation tests [CRS test, ASTM: D4186-89 (1998)] were performed on both flocculated and dispersed microfabric specimens obtained after the slurry consolidation. The average initial void ratio of the flocculated and dispersed specimens was determined to be 1.18 and 0.78 respectively. Using CRS test cell and load frame, the flocculated specimens were subjected to an axial stress of 1000 kPa at a strain rate 0.1%/min and then unloaded to 200 kPa at a strain rate of 0.05%/min. For dispersed specimens, the strain rate of 0.1%/min caused much higher pore pressure evolution (Δu_b) at the bottom of the specimen, and pore pressure ratio ($\Delta u_b/\sigma'_v$) exceeded a suggested maximum value of 0.3 by ASTM. The acceptable strain rate for loading of the dispersed specimen was found to be 0.015% per minute and for unloading to be 0.01% per minute. The void ratio vs. vertical effective stress relationship for the two types of microfabrics is shown in Fig. 6.5 using the data points recorded at 2 min interval. Assuming the relationship between the void ratio and log of the effective consolidation pressure to be linear, the volumetric deformation behavior is usually defined using two consolidation parameters, (1) compression index , C_C, and (2) recompression or swelling index, C_S. The dispersed specimen showed a much lower value of compression index (C_C=0.18) than the flocculated specimen (C_C=0.38). The swelling index observed for the dispersed

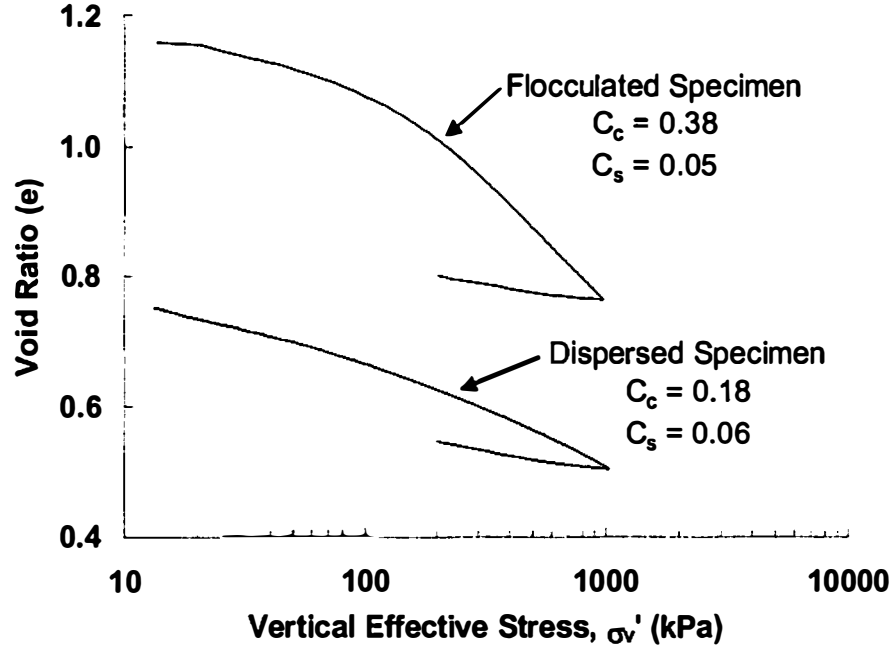

Figure 6.5 Consolidation Behavior from CRS Tests

(C_s=0.06) and the flocculated (C_s=0.05) specimens was not significantly different. Most constitutive theories use these parameters, in some form, to define the consolidation and shear behavior of clays. Classical elasto-plasticity theory idealizes the consolidation behavior by defining the unloading behavior to be elastic and the virgin consolidation to be elasto-plastic. Figure 6.5 shows that the plastic (permanent) volumetric deformation defined by (C_C-C_s) reduced significantly for dispersed microfabric. Based on the observed values of C_s, it appears that the elastic behavior does not change significantly with the changing microfabric. Additional data for various degrees of dispersion is needed to generalize this conclusion. The ratio C_s/C_C can be used to evaluate the rebound capacity of clay during settlement analysis, which was much higher for the dispersed microfabric (C_s/C_C =0.33) than the flocculated microfabric (C_s/C_C =0.13).

Using the true triaxial device, to achieve a normally consolidated state of stress, the cubical specimens were isotropically consolidated to the mean effective stress p'=275kPa. To represent the overconsolidated clay, the specimen were then isotropically unloaded from p'=275kPa to p'=55kPa. Typical consolidation curves (void ratio and strains – Time) obtained for the flocculated and dispersed specimens are shown in Fig. 6.6. The dispersed microfabric specimens had lower void ratio and much smaller size of the particles (or particles groups) in comparison to the flocculated specimens. Consequently, the consolidation process for dispersed specimens was much slower. From Fig. 6.6a, the end of primary consolidation observed for the flocculated specimens was at T_{100}=90min; whereas, for the dispersed specimens it was at T_{100}=800min. After primary consolidation, the specimens continued to creep at constant effective stress. Mitchel (1993) described the mechanism of this secondary consolidation to be the sliding at interparticle contact, expulsion of water from microfabric elements, and rearrangement of adsorbed water molecules and ionic charges into different positions. Therefore, the microfabric of clay should have significant influence on the observed secondary compression behavior, which can be evaluated by defining a coefficient of secondary compression $C_{\alpha e}$, as shown in Fig. 6.6a.

$$C_{\alpha e} = \frac{de}{d(\log t)} \tag{6.1}$$

where, t is time. Using equation 6.1, the calculated value of $C_{\alpha e}$ for flocculated specimen was $C_{\alpha e}$=0.010, and for the dispersed specimen $C_{\alpha e}$=0.006. Based on the data obtained for various natural clays, Mesri and Godlewski (1977) reported that the value of $C_{\alpha e}$ may

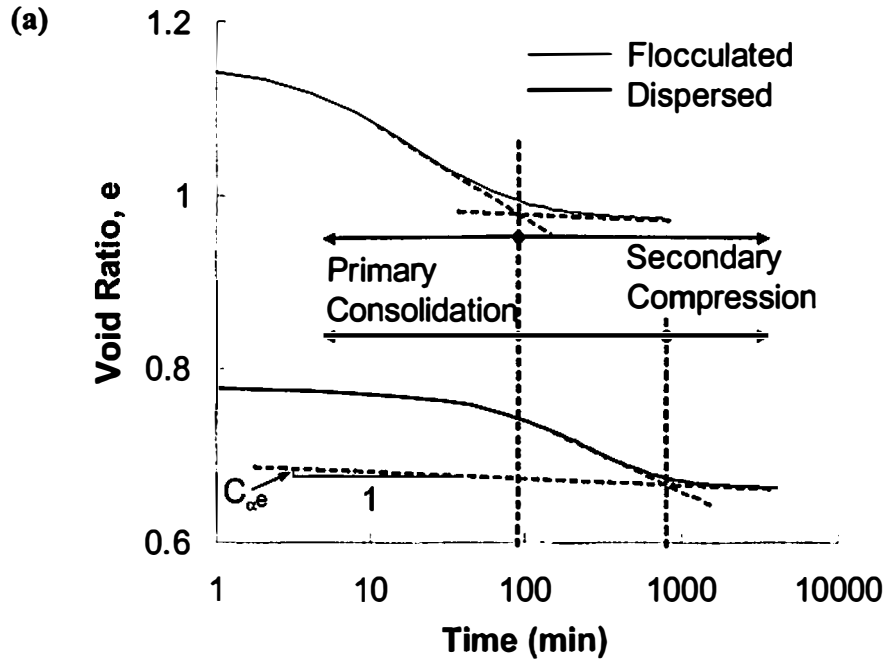

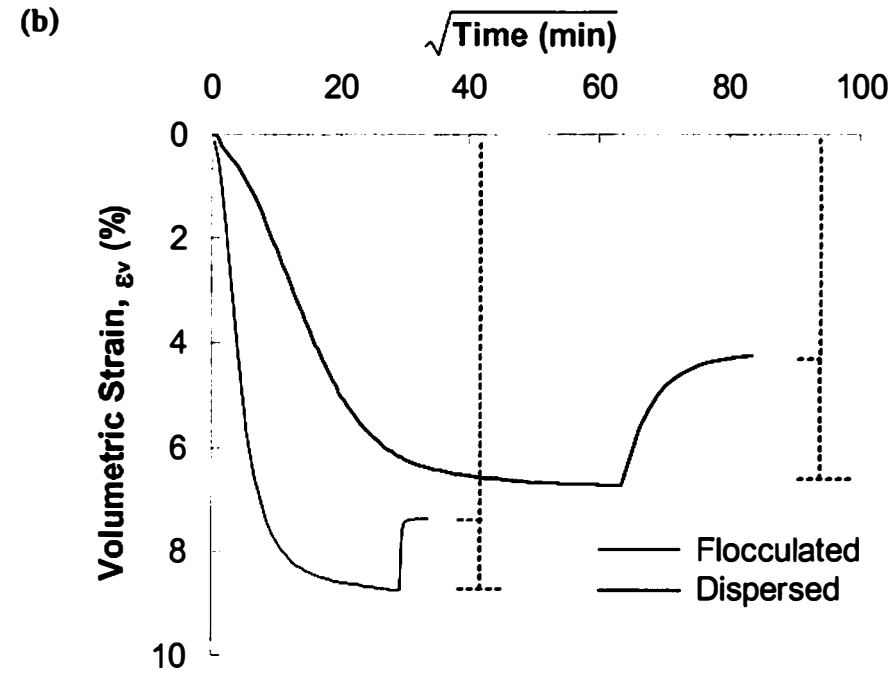

Figure 6.6 Isotropic Consolidation Curves for Flocculated and Dispersed Microfabric, (a) Void Ratio, (b) Volumetric Strain

be uniquely related to C_C. For most inorganic clays, the ratio C_{ae}/C_C was reported to range from 0.025 to 0.06. The flocculated specimens of Kaolin clay used in the current study showed C_{ae}/C_C =0.027 and the dispersed specimens showed C_{ae}/C_C =0.036.

As shown in Fig. 6.6b, the flocculated specimens showed higher compressibility by consolidating to ε_v=8.5% in comparison to the ε_v=6.5% for dispersed specimens. However, during unloading (p'=275kPa→ 55kPa) the equation reversed and the recovered volumetric strain for flocculated specimen, $\Delta\varepsilon_v$=1.4%, was much lower than the $\Delta\varepsilon_v$=2.5% for dispersed specimen. Despite the identical consolidation history for both the specimens before unloading, the dispersed specimen showed much higher recoverable strain due to their high rebound capacity (ratio of elastic to plastic deformation). The normal strains were measured along all the three axes of the specimen. In the true triaxial device, the normal strains were measured along all the six faces of the cubical specimens. The strains measured at the opposite faces were then averaged to get the normal strains along three principal axes, x, y, and z. Figure 6.7 shows the individual normal strains developed along the x, y, and z-axis during isotropic consolidation of flocculated and dispersed specimens. Thedirection of axial loading during specimen preparation was aligned with the z-axis of true triaxial device. Therefore, the cross-anisotropy induced in the specimen during their preparation, due to uniaxial loading, was about the z-axis. Therefore, along the two other axes, x and y, the specimen had same consolidation history. Since K_o<1, the pre-consolidation stress corresponding to x, and y axis was lower than what it was for the z-axis. A similar cross-anisotropy condition can be imagined for the orientation of particles in dispersed specimens, because during their preparation,

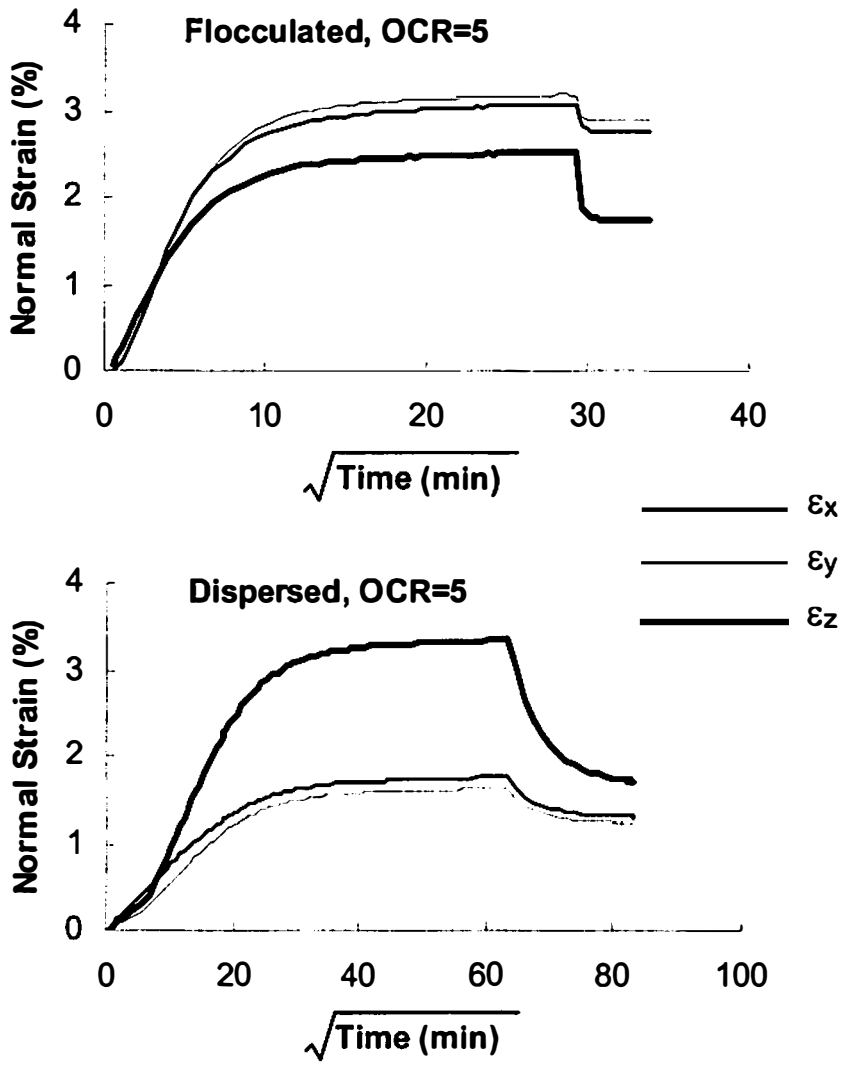

Figure 6.7 Individual Normal Strains along the Three Axes of Cubical Specimen during Isotropic Consolidation Curves for Flocculated and Dispersed Microfabric

the platy surfaces of the particles aligned themselves normal to the applied axial loading, which was again referred to as the z-axis of specimen. Flocculated specimens showed lower deformation in the z-direction (max ε_z-ε_x= −0.67%) because of the history of higher pre-consolidation stress along this direction. However, the dispersed specimens showed reversed relationship between the developed strains. The normal strain along the z-axis was much higher compared to the other two directions (max ε_z-ε_x= +1.6%). For both the flocculated and dispersed specimens, the normal strains developed along the x-axis were essentially same as along the y-axis, and that was because of the symmetry about the axis of cross-anisotropy (z-axis).

Experimental Observation from True Triaxial Tests

The cubical specimens used in the current research had a certain degree of cross-anisotropy due to their uniaxial loading history (Ko consolidation of slurry during specimen preparation). The dispersed microfabric specimens had a significant amount of fabric-induced anisotropy due to preferred orientation of clay platelets; as a result, they had a combined influence of fabric-induced and stress-induced anisotropy. To study the effect of relative magnitudes and orientation of principal stresses on the observed shear behavior, which should change with the anisotropy of the specimens, constant b-value true triaxial undrained tests were performed on the flocculated and dispersed microfabric specimens. In the current discussion, the axis of cross anisotropy is referred to as z-axis of the specimens and the other two principal axes are referred to as x-, and y-axis. A list of all the true triaxial tests from which the data has been used for the current discussion is given in Table 6.1. The angle δ in Table 6.1, defines the orientation of major principal

Table 6.1 Summary of Tests

NC* or OC**	Stress path	Graph Legend and Designation	
		Random	Dispersed
NC	b=0, δ=0°	● FN1	○ DN1
NC	b=0.5, δ=0°	▲ FN2	△ DN2
NC	b=1, δ=0°	◆ FN3	◇ DN3
NC	b=1, δ=90°	■ FN4	□ DN4
OC	b=0, δ=0°	★ FO1	☆ DO1
OC	b=1, δ=0°	⚑ FO2	⚐ DO2

*Normally Consolidated, **Overconsolidated (OCR=5)

(σ_1-) direction from the z-axis. For the tests FN3, and DN3, σ_1 was equal to σ_2 (b=1), the normal stresses applied during shearing were equal along z-, and y-axis; however, for the definition of δ (= 0°), the stress along z-axis was assumed to be σ_1, and along the y-axis to be σ_2. During the tests FN4, and DN4, the orientation of specimen was changed, and the $\sigma_1 = \sigma_2$ was applied along x- and y-axis of the specimen, therefore the δ angle was defined to be 90° (similar to the conventional triaxial extension test). These tests were performed on normally consolidated (NC) clay specimens. To evaluate the behavior of overconsolidated (OC) clay, for each microfabric, two constant b-value undrained tests corresponding to b=0 (FO1 & DO1), and b=1 (FO2 & DO2) were performed. In the case of NC clay, the specimens were isotropically consolidated under an effective confining pressure of 275kPa until it reached the end of primary consolidation, and for the OC clay, the specimens were then isotropically unloaded to reach effective confining stress state at

55kPa (OCR=5). The orientation of principal stresses in b=1 tests on OC clay was, δ=0°, same as it was in the FN3, and DN3 tests. The deviator stress, q, shear strain, ε_q, and mean effective stress, p', are defined in their invariant form of stress or strain tensor form.

Stress-Strain Relationship and Shear Failure

The stress-strain relationship in Fig. 6.8 shows that when the specimens were sheared from NC stress state the overall shear stiffness of dispersed specimens, in comparison with the flocculated specimens, was much higher. For the flocculated specimens, a close relationship between the stress strain behavior was observed for the tests performed with δ=0°, FN1, FN2, and FN3. However, the corresponding tests on dispersed specimens, DN1, DN2, and DN3, showed a significant variation in the stress-strain relationship. Because of higher stiffness along z-axis of the specimen, induced from their uniaxial loading history (induced during slurry consolidation), the test FN4 (σ_1 normal to z-axis) showed much lower shear stiffness throughout shearing in comparison to the other tests on NC flocculated specimens. Although, the flocculated and dispersed microfabric specimens experienced identical slurry consolidation followed by isotropic consolidation with identical stress level and same type of loading paths, the stiffness anisotropy from z-axis to x-axis was significantly different for the two microfabrics because of the difference in arrangement of particles. In the dispersed specimens, a part of the anisotropy induced by the loading history was compensated by the fabric induced anisotropy, which resulted in smaller difference between the stress-

strain relationship obtained from the test DN4 and from the other tests performed on dispersed specimens.

The failure point was defined as the point of peak deviator stress just before the specimen sheared to large strains with negligible change in shear stress. This definition of failure point was suitable for the current study, because the specimens were observed to have localized deformation at and beyond peak deviator stress. Prashant and Penumadu (2003a) presented a method of identifying the onset of localization using the strain information obtained from a true triaxial shear test. They documented the shear bands and defused localizations observed in the flocculated specimens sheared from initial hydrostatic stress state corresponding to OCR=5. Similar patterns were observed in the test data obtained for both flocculated and dispersed specimens. In Fig. 6.8, the failure points on the stress-strain curves are shown by using the legends listed in Table 6.1. Figure 6.9 shows the observed shear strain values at failure and the normalized undrained shear strength, S_u/σ_c'. Note that S_u was defined as the undrained shear strength in $\sigma_1-\sigma_3$ plane, $S_u=(\sigma_1-\sigma_3)/2$, and normalized with the initial confining stress, σ_c'. From Fig. 6.8b, and 6.9a, it can be observed that the dispersed specimens showed relatively more of brittle failure behavior, and failed at much lower shear strain values than the flocculated specimens. However, both the microfabrics shared a common trend that the shear strains at failure decreased as b-value increased, and the shear strains at failure for b=1 test with δ=90° and for b=0 test were close to each other. As shown in Fig. 6.9b, the dispersed specimens showed higher shear strength than the flocculated specimens. However, it is well known that the clay strength strongly depends on its void

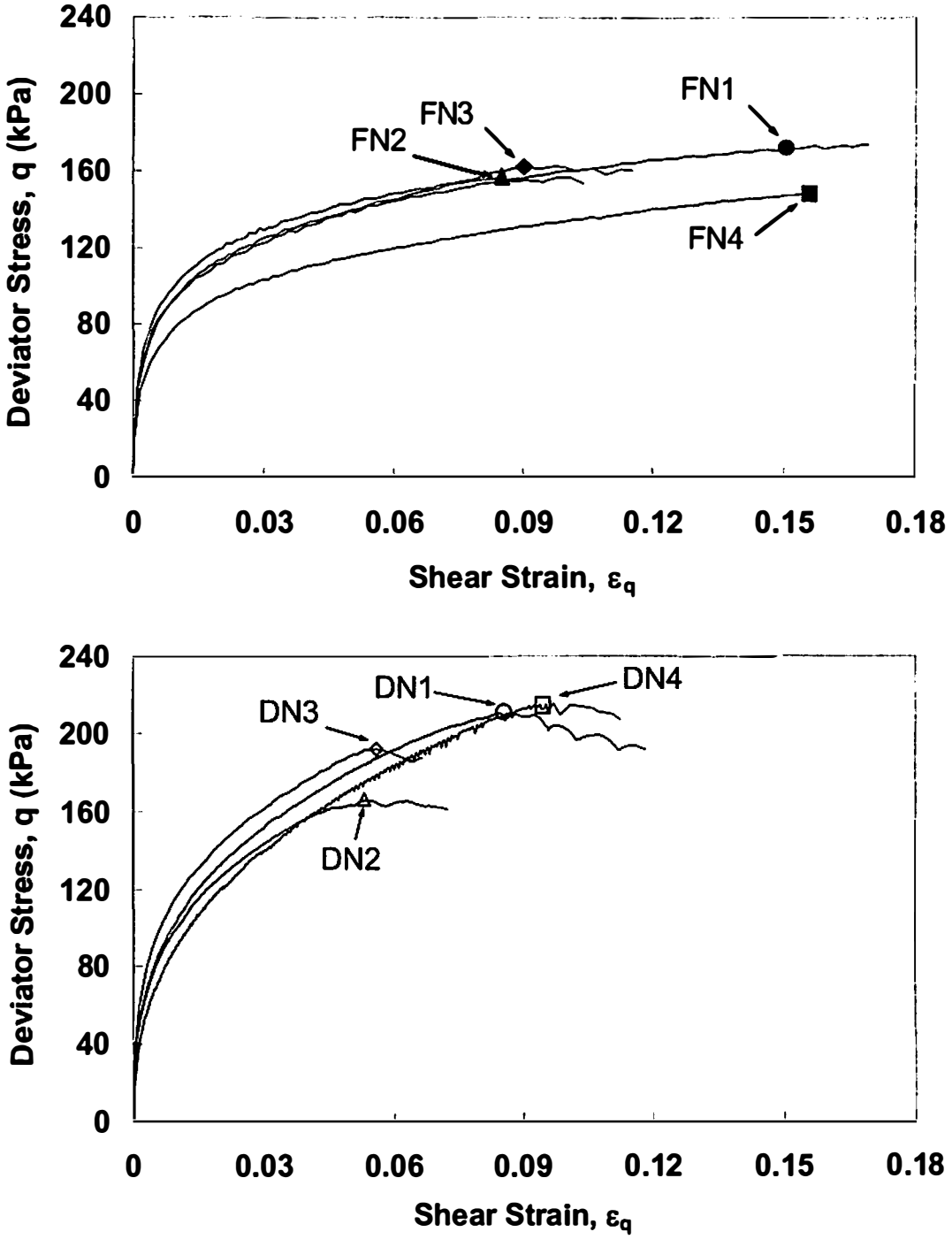

Figure 6.8 Shear Stress-Strain Relationship for NC Clay

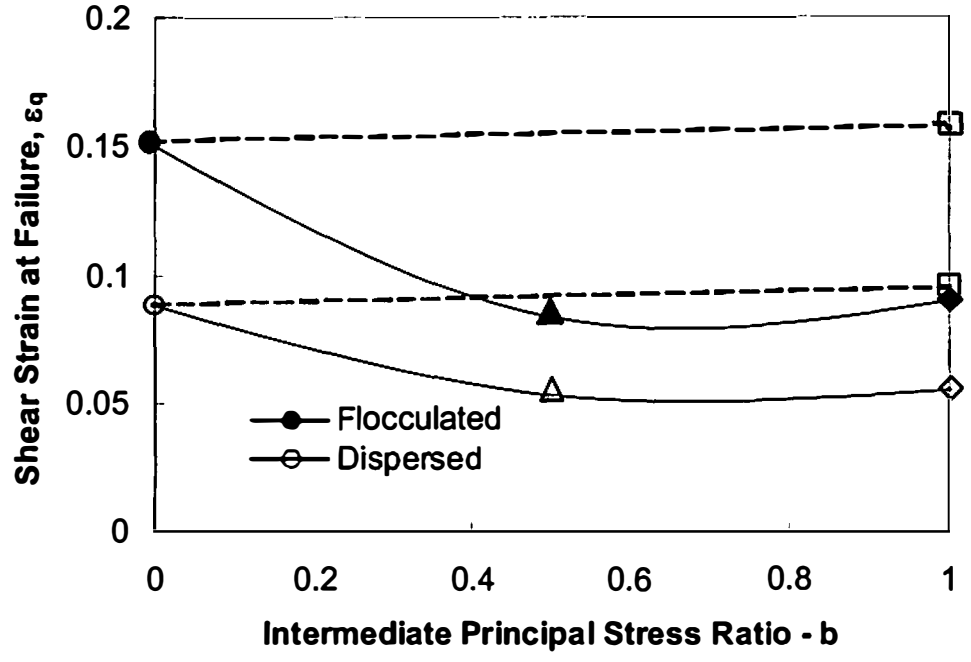

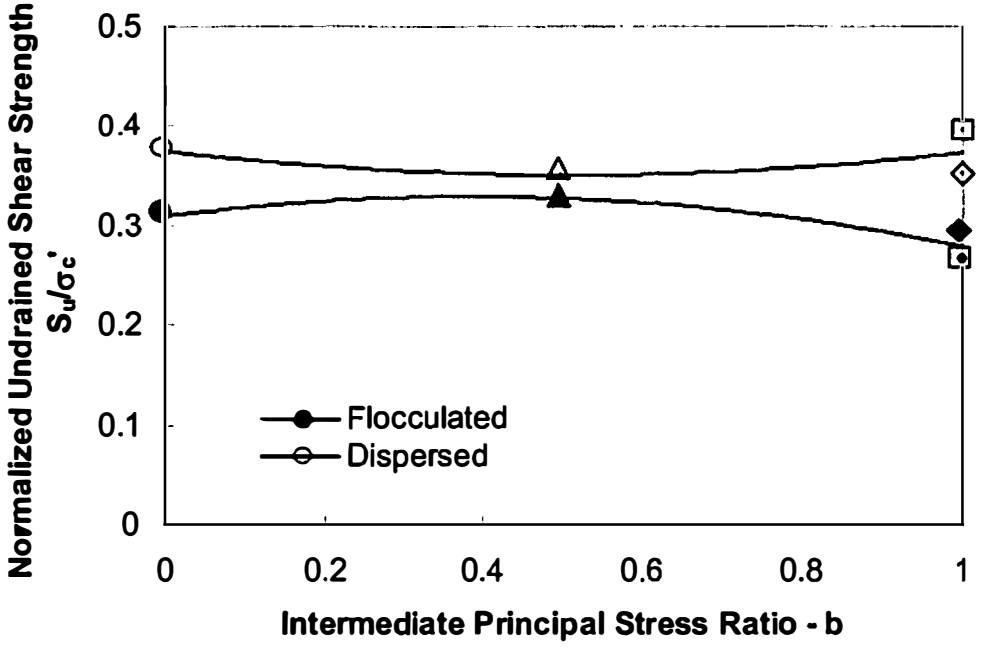

Figure 6.9 Shear Stress and Strain at Failure: (a) Shear Strain at Failure, (b) Undrained Shear Strength

ratio, and before shearing, the dispersed specimens had much lower void ratio (e=0.66) than the flocculated specimens (e=0.97). In a review of previous studies, Mitchell (1993) noted that at the same void ratio flocculated clay would show more rigid response and higher strength than dispersed clay. In the current study, a large difference in void ratio, and relatively less difference in the observed shear strengths of flocculated and dispersed microfabric specimens suggest that the argument made by Mitchell may be relevant for the present data. Figure 6.9b shows that the trend of strength variation with b-value for dispersed specimens was just opposite to the trend observed for the flocculated specimens.

The dispersed specimens, when sheared from the OC initial stress state, showed much lower shear stress-strain relationship than the flocculated specimens, as shown in Fig. 6.10. The observed shear strength and the shear strain at failure were also lower for

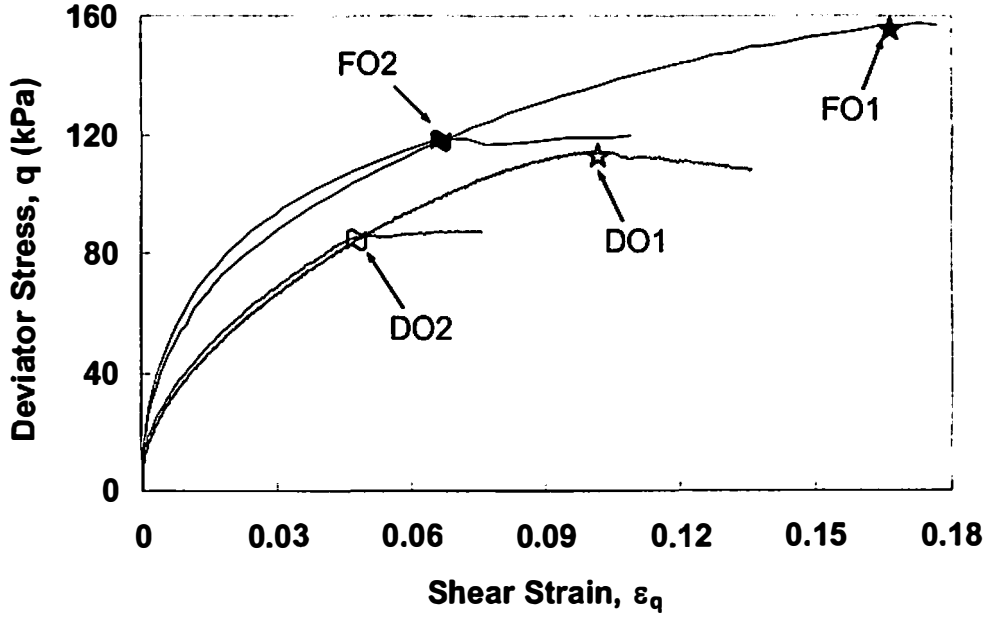

Figure 6.10 Shear Stress-Strain Relationship for OC Clay

the dispersed specimens. However, for both flocculated and dispersed specimens, b=1 tests (FO2 and DO2), in comparison with the b=0 tests (FO1 and FO2), showed much lower shear strength and shear strain at failure. Excluding the test FO1, all other tests showed significantly brittle failure. After reviewing the data available in literature for several clays, Mayne and Swanson (1979) showed that the undrained shear strength of OC clay can be normalized with the NC undrained shear strength of the same clay, as a function of OCR value, using a soil constant Λ_o. They found a correlation between the Λ_o value and the consolidation properties of clays, ($\Lambda_o = 1 - C_S/C_C$). In the current study, the Λ_o values for flocculated and dispersed microfabric obtained from their consolidation properties were Λ_o=0.87, and 0.67 respectively. A much lower value of Λ_o for dispersed specimen explains the significant drop in undrained strength of OC clay.

Evolution of Excess Pore Pressure and Stress Paths in q-p' Space

The excess pore pressure developed during undrained deformation represents the volume change tendency of soil. It is well known that for incompressible saturated soils, the change in mean total stress, Δp, develops equal amount of pore pressure under undrained condition, and on application of various stress paths, additional pore pressure develops due to particle rearrangement during shearing. For various stress paths, the pore pressure developed solely due to shear (or particle rearrangement), Δu_q, can be separated from the total excess pore pressure, Δu, which is essentially equal to the negative change in mean effective stress, $\Delta p'$, during undrained shear.

$$\Delta u_q = -\Delta p' = (\Delta u - \Delta p) \tag{6.2}$$

To assess the influence of specimen anisotropy on pore pressure evolution, a comparison of the Δu_q evolution observed from various stress paths is presented in Fig. 6.11 and 6.12, and corresponding effective stress paths are shown in Fig. 6.13. As shown in Fig. 6.11, the dispersed specimens, in comparison with the flocculated specimens, showed much lower Δu_q evolution, i.e. the dispersed specimen's response was less compressive/more dilative towards shearing. Unlike flocculated specimens, the dispersed specimens showed much different Δu_q evolution for various stress paths, which shows that the fabric anisotropy of dispersed clay had a significant influence on the developed pore pressure. It was observed that the pore pressure evolution was lower for higher b-value tests, and it was lowest for the DN4 test, in which σ_1 was applied perpendicular to the axis of fabric anisotropy (z-axis). As the relative magnitude of principal stresses acting perpendicular to the z-axis was increased (DN1→ DN4), more particles were forced to break the layered formation in dispersed microfabric and align themselves with their faces against the maximum normal stress, which required more room for the particles to rotate. As a result, the dilative behavior of soil increased, and the pore pressure generated during undrained shear decreased. As shown in Fig. 6.12, both flocculated and dispersed specimens developed negative pore pressure (dilative tendency) when sheared from an OC stress state corresponding to OCR=5, and the effect of b-value change was the same for both microfabrics.

As shown in Fig. 6.13, the effective stress paths for the dispersed specimens were notably different for various anisotropic loadings, largely due to fabric anisotropy and its

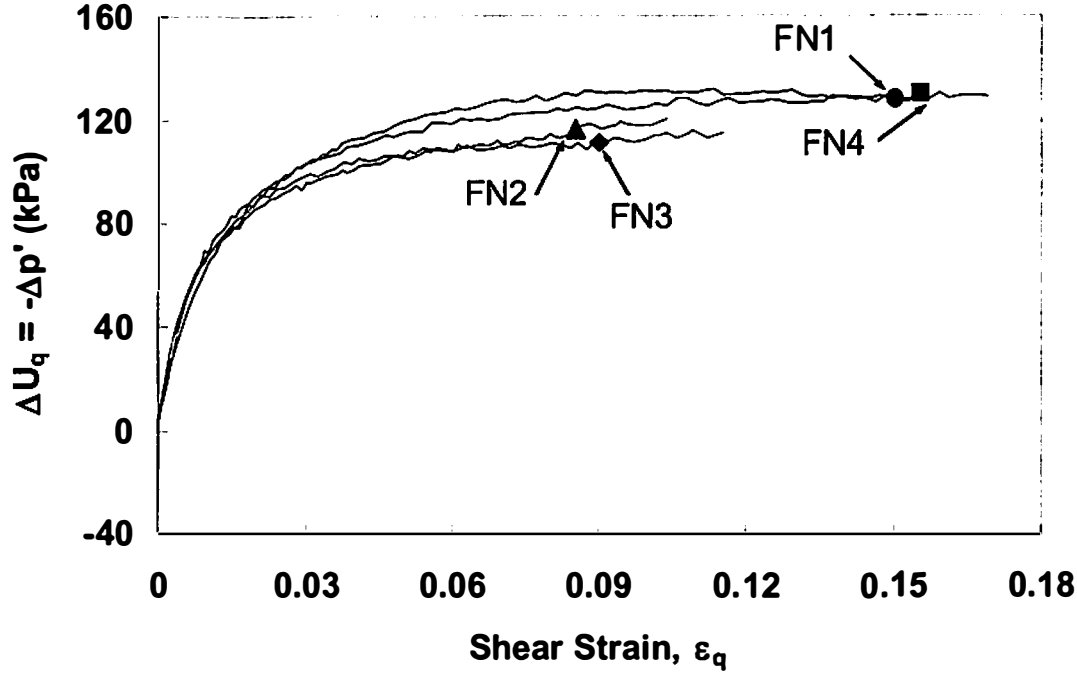

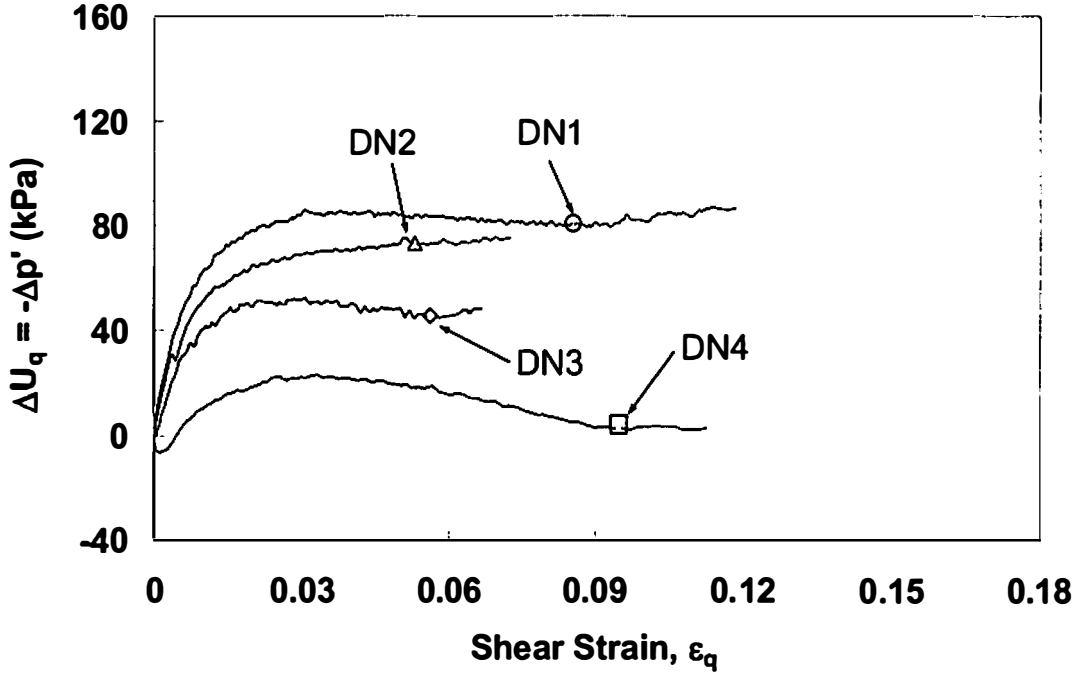

Figure 6.11 Excess Pore Pressure Evolution for NC Clay

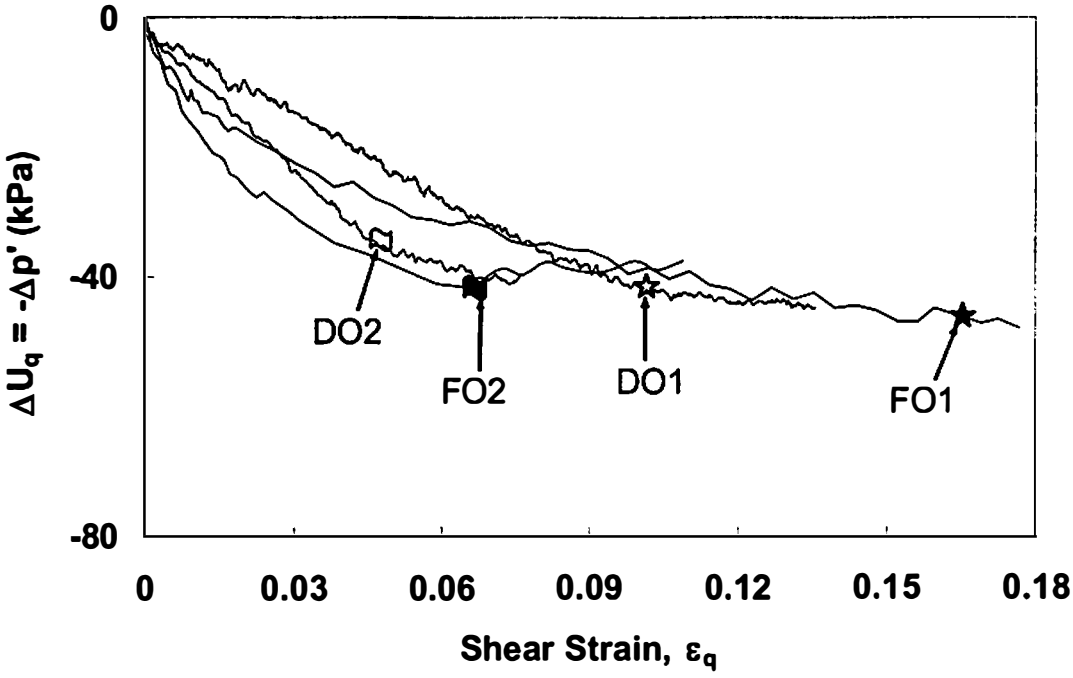

Figure 6.12 Excess Pore Pressure Evolution for OC Clay

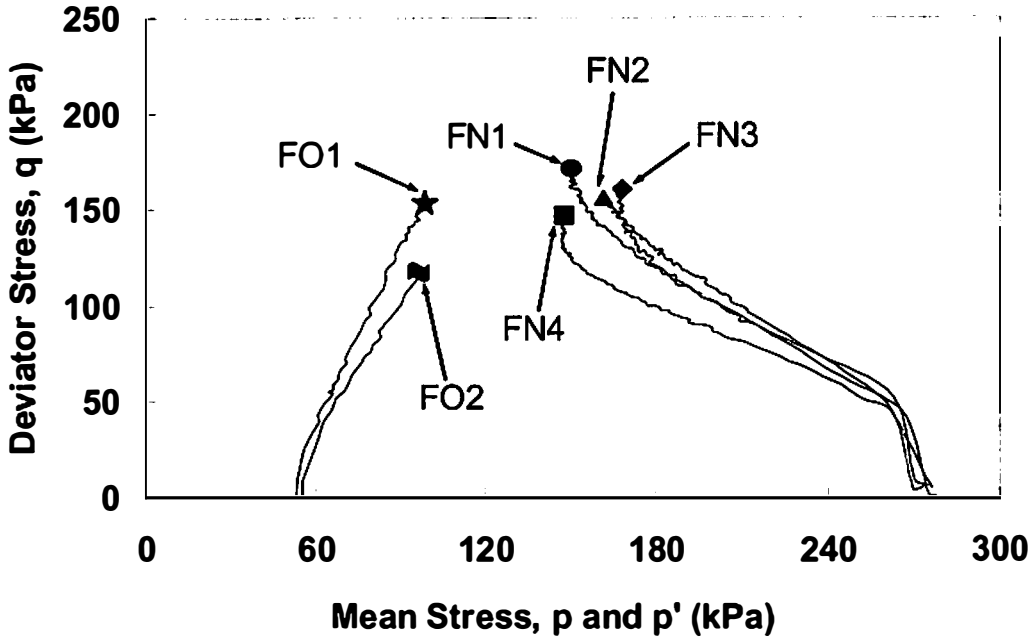

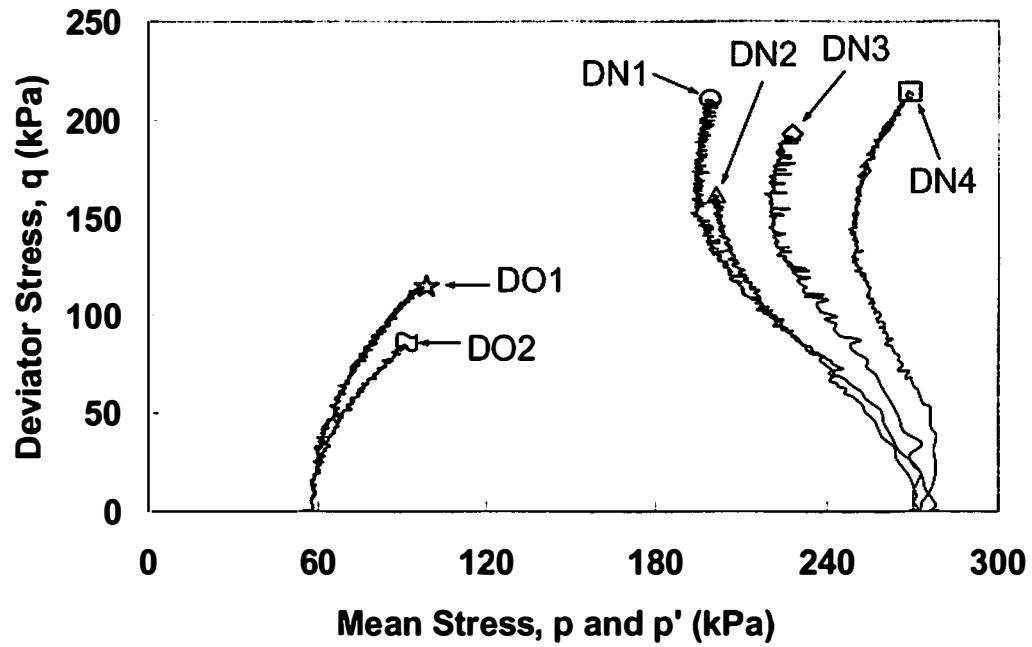

Figure 6.13 Effective Stress Paths for NC and OC Clay

influence on the developed pore pressure. As the σ_1 was rotated from δ=0° (along z-axis) to δ=90°, the flocculated specimen showed more of compressive behavior (decrease in p'), whereas, the dispersed specimen became more dilative (increase in p'). At OCR=5, no significant difference in the pattern of effective stress paths was observed for the two microfabrics.

Strength and Pore Pressure Parameters

Figure 6.14 shows the strength and Pore pressure parameters obtained from the true triaxial tests performed on NC Kaolin clay with flocculated and dispersed microfabric. In Fig. 6.14a, the effective friction angle, ϕ', defines the shear strength considering the stresses in $\sigma_1 - \sigma_3$ plane, and the peak shear stress ratio, M, defines the clay strength in 3D stress space, which is essentially the ratio of shear stress, q, and mean effective stress, p', at failure. The values of ϕ' and M, observed for the dispersed specimens (ϕ'=26.6° to 29.2°, M=0.80 to 1.05), were generally lower than those for the flocculated specimens (ϕ'=28.8° to 36.4 M=0.97o 1.15). Both the microfabrics shared a common trend of decreasing M with the increase in b-value. For both the microfabrics, the M values observed from the two b=1 tests with different δ angles were identical. Figure 6.14b shows the variation of A_f, and a_f as a function of b-value, observed for the two microfabrics. The a_f parameter is defined as a generalized form of the skempton's pore pressure parameter, A_f, in 3D stress space, as shown in equation 6.3 and 6.4.

$$A_f = (\Delta u - \Delta\sigma_3)_f / (\Delta\sigma_1 - \Delta\sigma_3)_f \tag{6.3}$$

$$a_f = (\Delta u - \Delta p)_f / (\sqrt{2}.\Delta q_f) \tag{6.4}$$

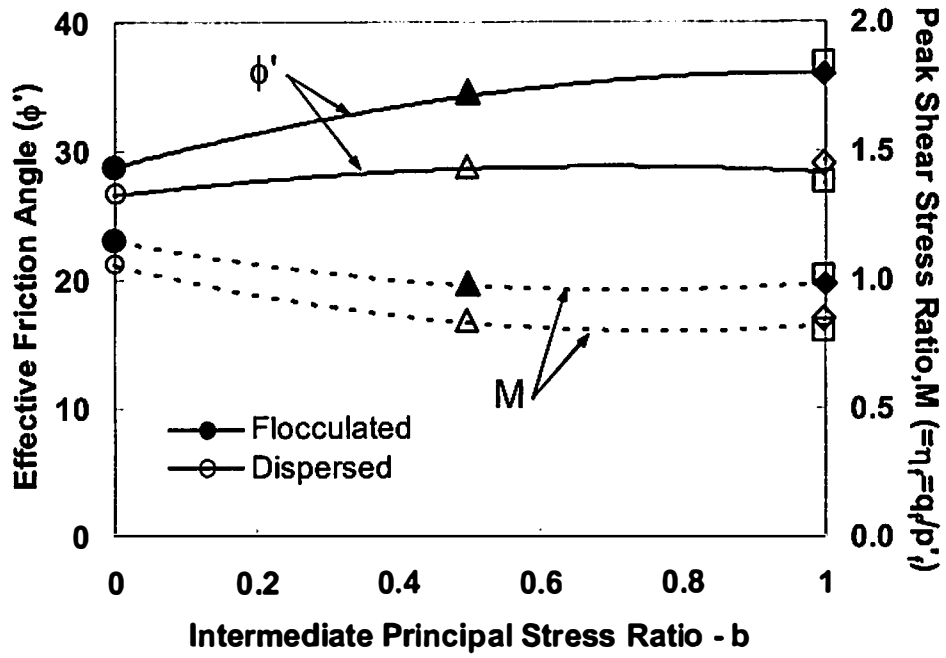

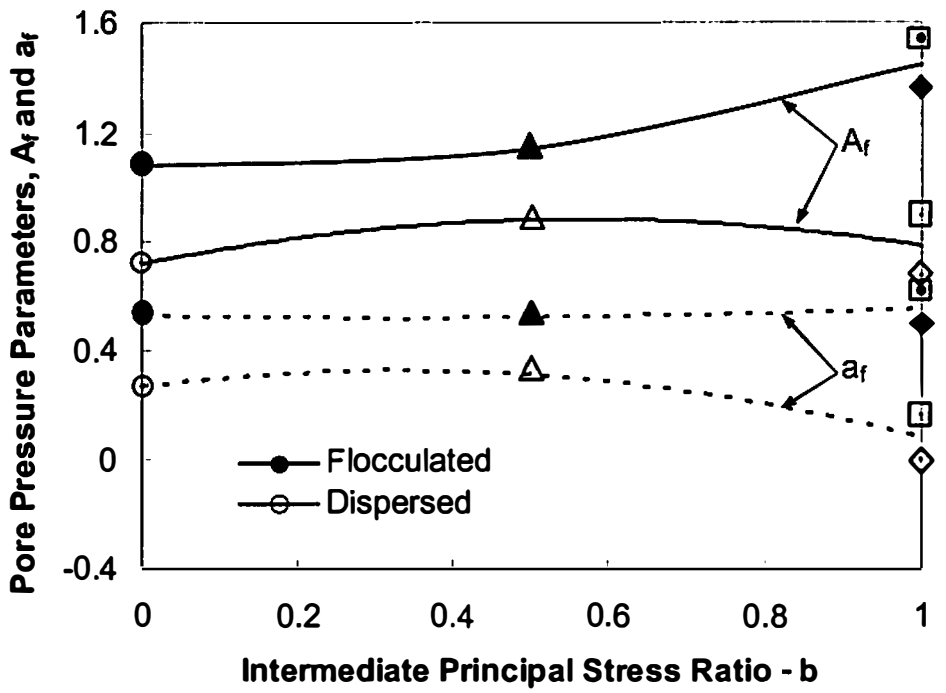

Figure 6.14 Strength Parameters, (a) Effective Friction Angle, Shear Stress Ratio, (b) Pore Pressure Parameters, A_f and a_f

Unlike flocculated specimens, for which A_f increased consistently with the increase in b-value, the dispersed specimens showed higher A_f for b=0.5. The a_f parameter was essentially constant for the flocculated specimens; however, for the dispersed specimens it decreased significantly at higher b-values. This observation indicates that the a_f parameter may be independent of the stress induced anisotropy; however, fabric induced anisotropy may have significant influence on this parameter.

Failure Surface and Plastic Strain Increment Vectors in Deviatoric Plane

To evaluate the influence of anisotropy on strength behavior of soil, the analytical failure surface is often presented on a deviatoric plane. The failure stress states observed for both flocculated and dispersed microfabric specimens are shown in Fig. 6.15 on a deviatoric plane. In this figure, the experimental data is compared with the predicted failure surface for Mohr Coulomb criteria, and for the third invariant of stress, I_3, to be constant (I_3=k). It can be observed that the experimental data for flocculated specimens follows a failure criterion defined by I_3=k; however, the data points for dispersed specimens fall in between the I_3=k and Mohr Coulomb surface. For each microfabric, the failure points corresponding to the two b=1 tests, which had a difference of 90° in the orientation of principal stresses, show no significant variation in their position on octahedral plane. Based on this observation it can be assumed that the failure surface was independent of the orientation of principal stresses, and it was simply a function of the relative magnitudes of principal stresses. Since, the observation was same for both flocculated and dispersed microfabrics; it can also be assumed that the failure condition was independent of the fabric-induced anisotropy. As shown in Fig. 6.15, for both the microfabrics, the strain increment vectors observed at failure were in the direction of

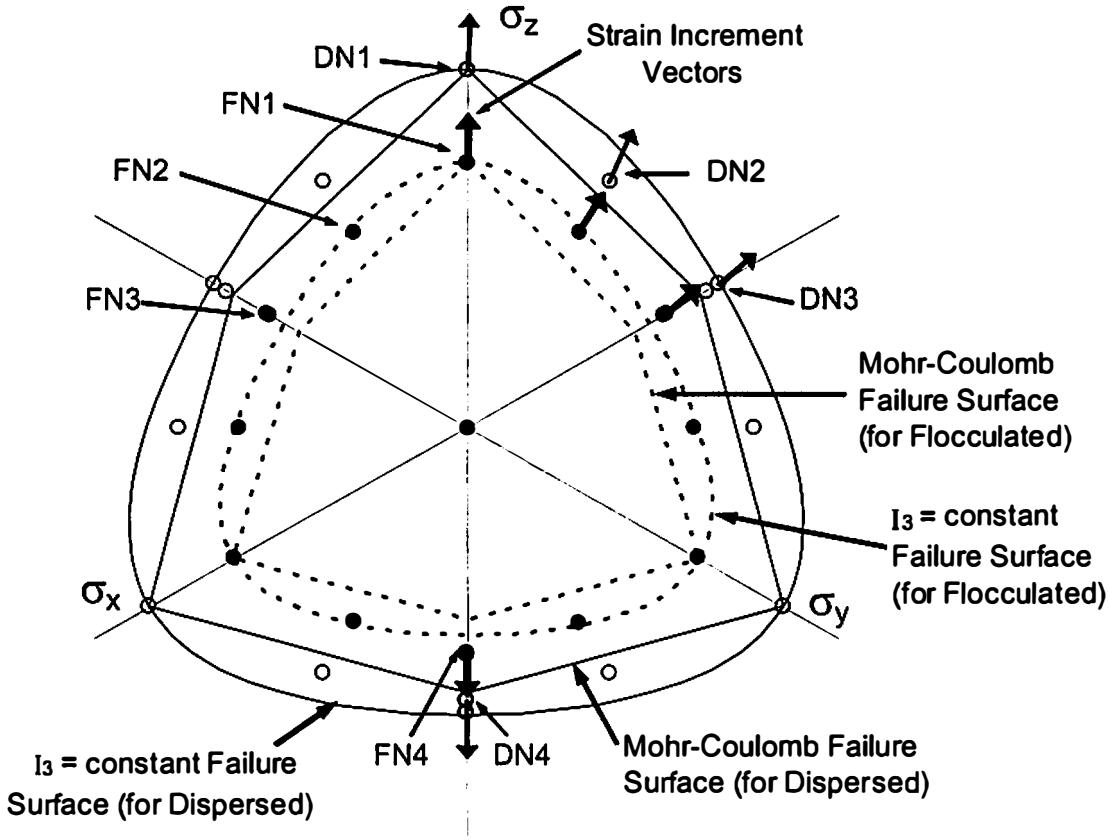

Figure 6.15 Failure Surface and Strain Increment Vectors in Deviatoric Plane

stress increments. Hence, the strain evolution at failure was observed to be independent of the anisotropy of specimens with both flocculated and dispersed microfabrics.

Conclusions

To investigate the influence of inherent microfabric (geometric arrangement of clay particles) on the fundamental behavior of Kaolin clay, such as induced anisotropy, consolidation behavior, stress-strain relationship, pore pressure evolution during undrained shearing, and strength behavior; a series of flexible boundary true triaxial undrained tests were performed on remolded cubical specimens with two different microfabrics (flocculated and dispersed) of Kaolin clay. The flocculated and dispersed specimens with two extreme particle arrangements (random and preferred orientation) were obtained by K_o consolidation of slurry made in deionized and de-aired water, in which 2% dispersant was used to obtain dispersed microfabric. Key observations from this study are summarized as follows:

a) The permanent deformation during consolidation was much lower for the dispersed specimens in comparison with the flocculated specimens; however, the recoverable deformation observed after unloading was relatively higher for the dispersed specimens. The fabric-induced anisotropy shows a significant influence on the mode of anisotropic deformations of the specimens during hydrostatic consolidation.

b) The dispersed specimens, when sheared from an NC stress state, showed much stiffer response in the stress-strain relationship, achieved higher strength, failed at lower strain values, and showed much lower pore pressure evolution in comparison with the flocculated specimens. However, the influence of microfabric was significantly

different when the specimens were sheared from an OC stress state corresponding to OCR=5.

c) Both flocculated and dispersed specimens generally showed localized deformation and brittle response at failure; particularly it was more significant for the dispersed specimens.

d) The fabric-induced anisotropy (preferred orientation of particles) in the dispersed specimens shows significant influence on excess pore pressure during shearing when the specimens were subjected to different stress paths.

e) The strength parameters (ϕ' and M) were significantly different for the two microfabrics; however, they showed similar patterns of variation with different anisotropic loadings for both flocculated and dispersed microfabrics. A similar behavior was observed when the failure stress states were projected onto deviatoric stress plane.

Chapter 7. Evaluation of Existing Constitutive Models for Cohesive Soil: Review, Formulation, and Predictions

Introduction

Successful calculation of stresses and deformation in soil deposits under changing loading conditions largely depend on constitutive models used for characterization of soil behavior under general three dimensional stress conditions. Since the 1950's, an increasing effort has been devoted to a description of the fundamental behavior of soil. Laboratory tests in earlier studies often involved single axis loading conditions and formed the basis for several existing theories that attempt to explain the mechanical behavior of soil. The stress conditions corresponding to the in-situ state often involves three unequal principal stresses i.e. the intermediate principal stress (σ_2) varies from the major (σ_1) or minor principal stress (σ_3) (e.g., slope stability, excavations, and soil-foundation interactions). Advances in testing methods have added the capability of studying various aspects of generalized stress-strain behavior in a controlled environment. These techniques were used to study the soil behavior under complex stress states; however, the constitutive models got increasingly complex when the attempts were made to address general soil behavior based on these studies. In the chain of these developments, theoretical ideas were implemented in the shape of constitutive models with emphasis on various aspects of soil behavior and with a goal of reaching the experimental observations to some extent. Constitutive theories presented by Drucker et al. (1957), Roscoe et al. (1963), Roscoe and Burland (1968), DiMaggio and Sandler (1971), Prevost (1978), Nakai and Matsuoka (1983), Desai and Faruque (1984),

Frantziskonis et al. (1986), Lade (1990) give an idea of the modeling capabilities achieved to date.

This chapter presents a brief review of the classical elasto-plasticity theory and the constitutive models developed to explain soil behavior. In particular, the emphasis has been given to the two leading constitutive theories:

1. Modified Cam-Clay (MCC) model (Roscoe and Burland, 1968), which was developed based on a big resource of experimental data obtained from single axis loading tests in laboratory. This model has been commonly used in practice to analyze various field problems.
2. Single hardening model (Lade, 1990), which was developed based on the observations from a variety of three-dimensional loading tests. This model has received attention from many researchers because it is commonly believed to have better potential to represent the soil behavior under general stress conditions.

Elasto-Plasticity Theory

The total strain of an elasto-plastic material may be considered as the sum of permanent (plastic) and recoverable (elastic) strains.

$$d\varepsilon = d\varepsilon^e + d\varepsilon^p \tag{7.1}$$

Here dε is incremental strain. Incremental stress-strains relationship for the elastic part of deformation can be defined using a fourth order elastic stiffness tensor K_e, which may need up to 81 parameters to define fully anisotropic behavior. It is usually reasonable and more convenient to assume the material to be elastically isotropic, which reduces required parameters significantly.

$$d\varepsilon_{ij}^{e} = C_{ijkl} d\sigma_{ij} \tag{7.2}$$

A yield surface is defined as a surface in stress space such that it bounds stress states which can be reached without initiating plastic strains. Mathematically, this surface can be represented by a yield function:

$$f\left(\sigma_{ij}, \zeta_f\right) = 0 \tag{7.3}$$

where σ_{ij} is the stress state and ζ_f is a state variable that defines the size of yield surface in stress space. ζ_f depends on the loading history and its growth can be related to the plastic strains developed in the material, as shown in equation 7.4.

$$d\zeta_f = \frac{\partial \zeta_f}{\partial \varepsilon_{ij}^{p}} d\varepsilon_{ij}^{p} \tag{7.4}$$

If the small variance in stress is such that $df > 0$, then this process is called loading and plastic strains are developed; if the variance induces $df < 0$, then this process is called unloading and it is assumed that there is no plastic strain during unloading. As a limiting case, if the stress increment is along the yield surface i.e. $df = 0$, then it is defined as neutral loading and no plastic strain is produced.

A flow rule is defined to estimate the incremental plastic strains $d\varepsilon_{ij}^{p}$ developed under a loading condition, as shown in equation 7.5.

$$d\varepsilon_{ij}^{p} = d\lambda \frac{\partial g\left(\sigma_{ij}, \zeta_g\right)}{\partial \sigma_{ij}} \tag{7.5}$$

A stress function $g\left(\sigma_{ij}, \zeta_g\right)$ is the plastic potential function and $d\lambda$ is a non-negative constant, which is related to the hardening rule H, as shown in equation 7.6. Equation 7.5 implies that the direction of incremental plastic strain increment vector is normal to a

surface defined by plastic potential function. This surface is referred to as plastic potential surface. The flow rule is considered to be associative if $g(\sigma_{ij},\zeta_g)$ coincides with $f(\sigma_{ij},\zeta_f)$, otherwise it is called non-associative.

$$d\lambda = \frac{1}{H}\left\langle \frac{\partial f}{\partial \sigma_{ij}} d\sigma_{ij} \right\rangle \tag{7.6}$$

where $\langle\ \rangle$ are Macaulay brackets, which ensure that the function inside will have its value only if it is positive, otherwise it will remain zero. The material hardening H is determined from the consistency condition that defines the stress state to remain on current yield surface throughout loading, as shown in equation 7.7.

Consistency condition: $$\dot{f} = \frac{\partial f}{\partial \sigma_{ij}} d\sigma_{ij} + \frac{\partial f}{\partial \zeta_f} d\zeta_f = 0 \tag{7.7}$$

From equation 7.4, 7.5, and 7.6, H can be determined as shown in equation 7.8.

$$H = -\frac{\partial f}{\partial \zeta_f}\left(\frac{\partial \zeta_f}{\partial \varepsilon_p^p} \frac{\partial g}{\partial \sigma_{ij}} \right) \tag{7.8}$$

Using equations 7.5, 7.6 and 7.8, the incremental plastic strains can be directly related to the stress increments, as shown in equation 7.9.

$$d\varepsilon_{ij}^p = \frac{-1}{\dfrac{\partial f}{\partial \zeta_f}\left(\dfrac{\partial \zeta_f}{\partial \varepsilon_{kl}^p} \dfrac{\partial g}{\partial \sigma_{kl}} \right)} \left\langle \frac{\partial f}{\partial \sigma_{mn}} d\sigma_{mn} \right\rangle \frac{\partial g}{\partial \sigma_{ij}} \tag{7.9}$$

From equation 7.1, 7.2, and 7.9, the incremental total strains can be obtained as a function of stress increments as shown in equation 7.10.

$$d\varepsilon_{ij} = C_{ijkl}d\sigma_{ij} + \frac{-1}{\dfrac{\partial f}{\partial \zeta_f}\left(\dfrac{\partial \zeta_f}{\partial \varepsilon_{kl}^p}\dfrac{\partial g}{\partial \sigma_{kl}}\right)}\left\langle \frac{\partial f}{\partial \sigma_{mn}} d\sigma_{mn} \right\rangle \frac{\partial g}{\partial \sigma_{ij}} \tag{7.10}$$

Three-Dimensional Stress Space

Yield and plastic potential surfaces are usually described in three-dimensional stress space. In order to represent a three dimensional stress space in two dimensional plots, the constitutive surfaces are often shown in the triaxial plane and deviatoric plane, as shown in Fig. 7.1. The triaxial plane is used to describe the pressure dependency of frictional materials, and the deviatoric plane is used to describe its anisotropic behavior.

Summary of Constitutive Theories Proposed to Describe Soil Behavior

In most classical plasticity theories, the stress-strain behavior was assumed to be elastic-perfectly plastic i.e. the material after reaching the yield surface deforms

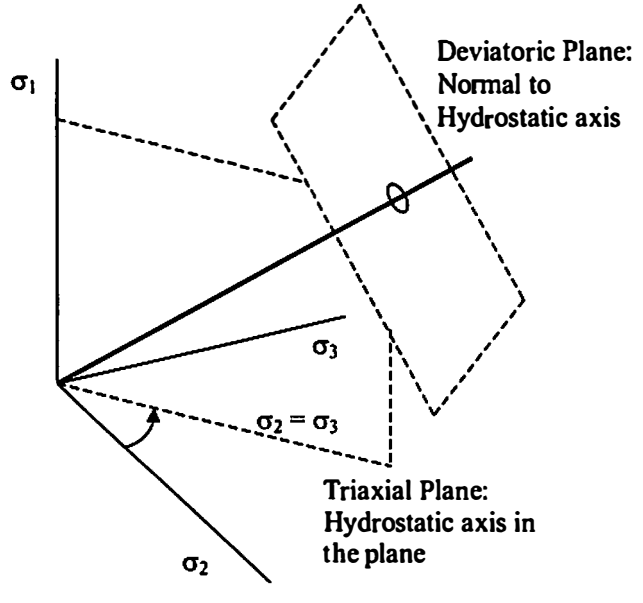

Figure 7.1 Triaxial and Deviatoric Plane in Three-Dimensional Stress Space

continuously under constant load. They did not differentiate between the yield surface and the failure surface. In this category, three most commonly used failure criteria proposed for frictional materials are: Extended Tresca, Extended von Mises, and Mohr-Coulomb criteria. Mathematical functions used to describe these criteria are given in equation 7.11 to 7.13.

Extended Tresca:
$$F = \sqrt{J_2'}\cos\left(\omega_\sigma - \frac{\pi}{6}\right) + \alpha I_1 + \beta = 0 \tag{7.11}$$

Extended von Mises:
$$F = \sqrt{J_2'} + \alpha I_1 + \beta = 0 \tag{7.12}$$

Mohr-Coulomb criteria:
$$F = \frac{I_1}{3} + \sqrt{J_2'}\left\{\frac{1}{\sqrt{3}}\cos\left(\omega_\sigma - \frac{\pi}{6}\right)\sin\phi' - \sin\left(\omega_\sigma + \frac{\pi}{6}\right)\right\} + C\cos\phi' = 0 \tag{7.13}$$

The shape of these failure criteria in deviatoric plane can bee seen in Fig. 3.7 of Chapter 3; in the triaxial plane, their sizes grow linearly with hydrostatic stress.

Later constitutive theories assumed different surfaces for yield and failure. However, most of these theories assumed that the two surfaces have same shape in deviatoric plane, and as the yield surface grows in size under shear loading it finally reaches the defined failure surface. Typical shapes of the yield surface and failure surface are shown in Table 7.1 for some important constitutive models. The surfaces are presented as their projection in triaxial and deviatoric plane. Some of these surfaces grow in size as the material yields under loading condition, and finally reaches a limiting condition usually defined as failure. The direction of growing yield and plastic potential surface is represented using arrows on the figures shown in Table 7.1.

Table 7.1 Summary of Constitutive Models for Soil

Reference	Yield Surface		Flow Rule	Plastic Potential Surface		Hardening Rule
	Triaxial Plane	Deviatoric Plane		Triaxial Plane	Deviatoric Plane	
Drucker et al. (1957)	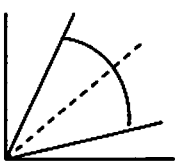	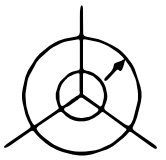	Associative			Plastic Work (Implied)
Stress Dilatancy Theory; Rowe(1962, 1971)	Not Defined		Not Defined	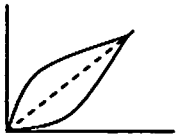	Not Defined	Normal Consolidation
Cam Clay Model; Roscoe et al. (1963), Schofield and Wroth (1968)	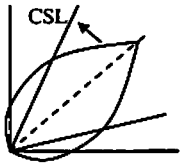	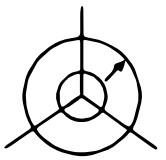	Associative			Volumetric Plastic Strain
Modified Cam Clay Model; Roscoe and Burland (1968)	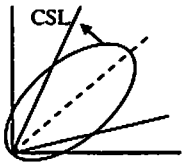	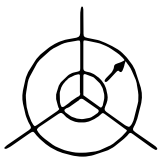	Associative			Volumetric Plastic Strain

Table 7.1 Continued

Reference	Yield Surface		Flow Rule	Plastic Potential Surface		Hardening Rule
	Triaxial Plane	Deviatoric Plane		Triaxial Plane	Deviatoric Plane	
Prevost and Hoeg (1975)	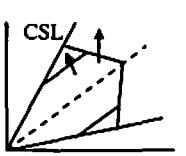	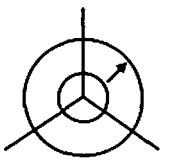	Associative			Plastic Work (Implied)
Lade (1977)	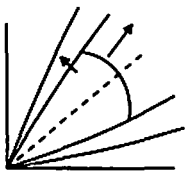	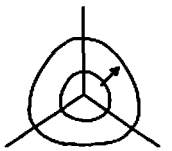	Associative Non-Associative	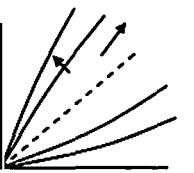	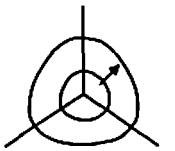	Plastic Work Plastic Work
Matsuoka and Nakai (1977), Nakai and Matsuoka (1983) (SMP Model)	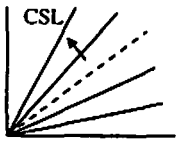	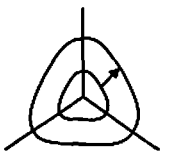		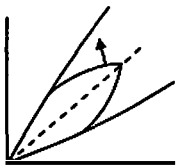	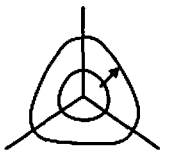	Strain Components on SMP plane
Lade (1990)	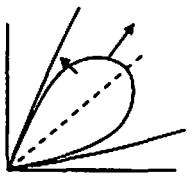	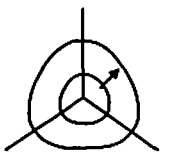		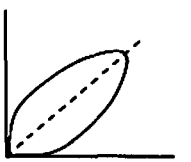	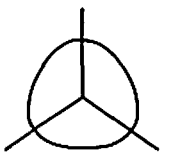	Plastic Work Hardening / Softening

Modified Cam-Clay Model

A unified framework for the mechanical behavior of clays, namely critical state soil mechanics (Schofield and Wroth, 1968), was originally formulated by the Cambridge Group, Roscoe et al. (1958). Considering some issues related to the direction of strain increment vectors at isotropic pre-consolidation stress state, the theory was modified later resulting in the modified Cam-clay model (Roscoe and Burland, 1968). In critical state soil mechanics, it is proposed that an element of soil undergoing uniform shear deformation eventually reaches a critical state. Therefore, it continues to undergo further deformation without any change in its state i.e. at constant p', q, and specific volume v. The p' and q are defined in equation A1.7 and A1.8 of Appendix-1, and $v = 1 + e$, where e is void ratio. The critical state line (CSL) is a smooth curve in the p'-q-v space as shown in Fig. 7.2. The shape of yield surface and CSL for MCC model is shown in Fig. 7.3, the compression plane with normal consolidation line (NCL), unload reload line (URL), and projection of CSL is shown in Fig. 7.4.

In MCC, it was assumed that the state of soil state remains on the stable state boundary surface when the plastic deformation occurs in loading condition, and the energy dissipated per unit volume of the soil, at any stage on the stable state boundary surface is given by

$$\delta W = p' \sqrt{\left(\delta \varepsilon_v^p\right)^2 + M^2 \left(\delta \varepsilon_q^p\right)^2} \tag{7.14}$$

where δW is dissipated energy, $\delta \varepsilon_v^p$ is plastic volumetric strain, and $\delta \varepsilon_q^p$ is plastic shear strain. The parameter M is a soil constant, which is associated with the critical state of

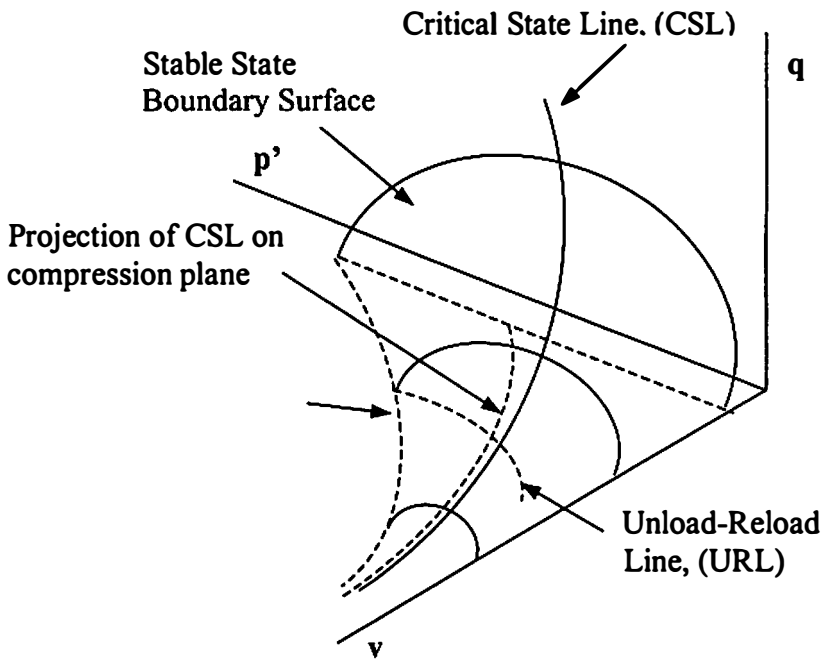

Figure 7.2 Stable State Boundary Surface in p'-q-v Space

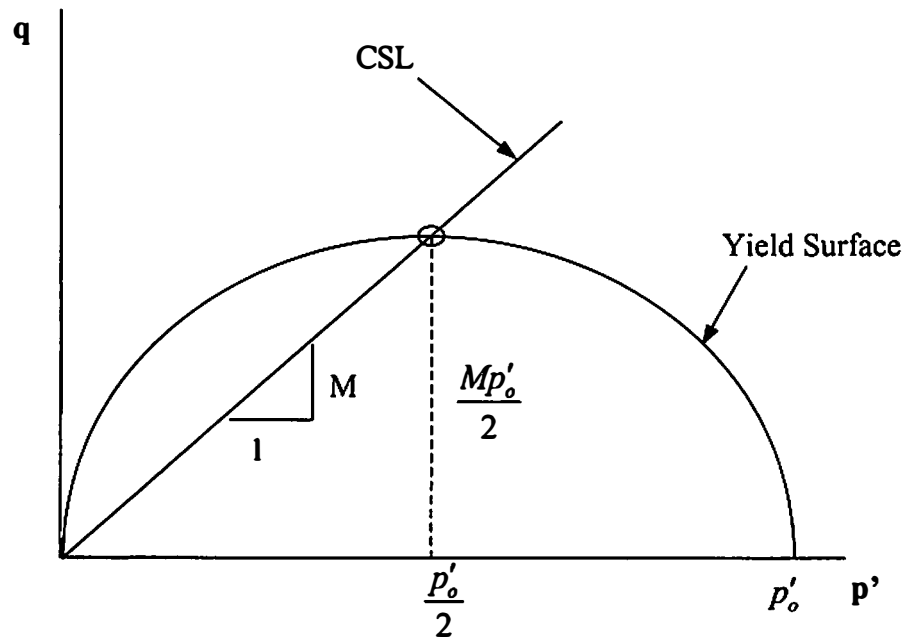

Figure 7.3 Yield Surface and CSL in q-p' Plane

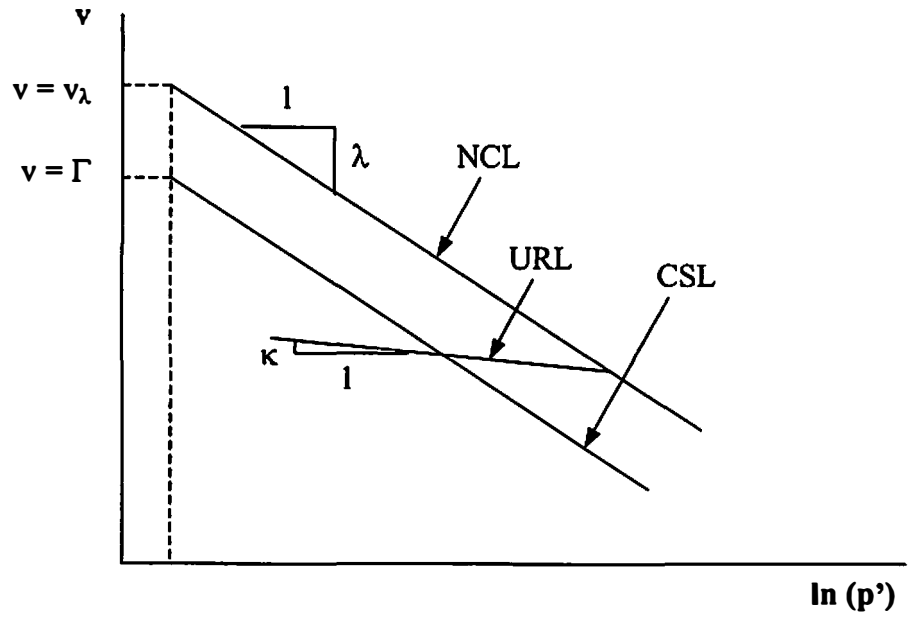

Figure 7.4 NCL, URL, and CSL in Compression Plane

soil. Based on equation 7.14 and the assumption of associative flow rule, it was derived that the ratio of plastic strains can be defined as

$$\frac{\delta\varepsilon_q^p}{\delta\varepsilon_v^p} = \frac{2\eta}{M^2 - \eta^2} = -\frac{dp'}{dq} \tag{7.15}$$

where η is the ratio of q and p', ($\eta = q/p'$). From equation 7.15, the yield surface can be derived as shown in equation 7.16.

$$q^2 - M^2\left[p'\left(p_o' - p'\right)\right] = 0 \tag{7.16}$$

Using the yield surface defined in equation 7.16 and consolidation parameters shown in Fig. 7.4, the stable state boundary surface can be represented as

$$\ln\left[\frac{M^2+\eta^2}{M^2}\right]=\frac{v_\lambda - v - \lambda \ln(p')}{\lambda-\kappa} \tag{7.17}$$

The CSL lies on the stable state boundary surface, thus substituting the equation of CSL in compression plane, $v=\Gamma-\ln(p')$, and $\eta=M$ in equation 7.17, the general equation of CSL is

$$\Gamma = v_\lambda - (\lambda-\kappa)\ln 2 \tag{7.18}$$

Modified Cam Clay Model Predictions for Kaolin Clay

The MCC model parameters λ=0.16, κ=0.02, and v_λ=2.8 were obtained from the consolidation data shown in Fig. 5.2 of chapter 5. The stress path for true triaxial compression test on NC clay was shown in Fig. 5.4, which gives the CSL parameter M=1.15. Lade (1979) found an empirical relationship between the plasticity index and Poisson's ratio by comparing these values for various clays. From this relationship the Poisson's ratio for kaolin clay (PI=0.32) was assumed to be $\nu=0.28$.

Using the formulation given in Appendix-2, a computer program was developed to get the MCC model predictions for the true triaxial undrained tests performed in this study. In this program, elastic and plastic strain increments are computed for a given effective stress increment. An effective stress increment vector of small magnitude was rotated along a constant b-value plane to satisfy the undrained condition within specified limits; i.e. the total volumetric strain (sum of total elastic and plastic strain values) at any stress state was within ±0.0001%. Excess pore pressure generated was computed as the difference between the total minor principal stress (constant during this test) and the effective minor principal stress. Predictions are made for NC and OC clay using model

parameters appropriate for current Kaolin clay and compared with experimental data. Results were numerically verified for triaxial compression tests by simulating the problem in FLAC (1999) by the finite difference approach and in SAGE CRISP4.3a by the finite element method.

The MCC model assumes isotropy and predicts the same shear stress-strain relationship for all b-values; however, excess pore pressure predictions can vary for different b-values due to change in total stress path, while the effective stress path remains constant. Figure 7.5 shows a comparison between the MCC model predictions (for b=0, 0.5, and 1.0) and corresponding experimental data obtained from a series of constant b-value true triaxial undrained tests performed on NC kaolin clay (p'_o=275kPa). A detailed analysis of the experimental data has been presented in chapter 2. In Fig. 7.5, it can be observed that in comparison with the experimental observations:

- MCC model predicts much stiffer response of the clay at small strain values (ε_q<1%); consequently, it predicts much higher shear stress values at that strain level and shows a poor approximation of the stress-strain relationship.
- MCC model predicts close values of shear strength for b=0 test; however, it shows much higher values of shear strength for b=0.5 and b=1.0 tests.
- MCC model exhibits much lower strain values at failure. In general, MCC model shows higher excess pore pressure response (when compared to the experimental data) during shearing. However, for b=0 case, it gives a good prediction of excess pore pressure at failure.

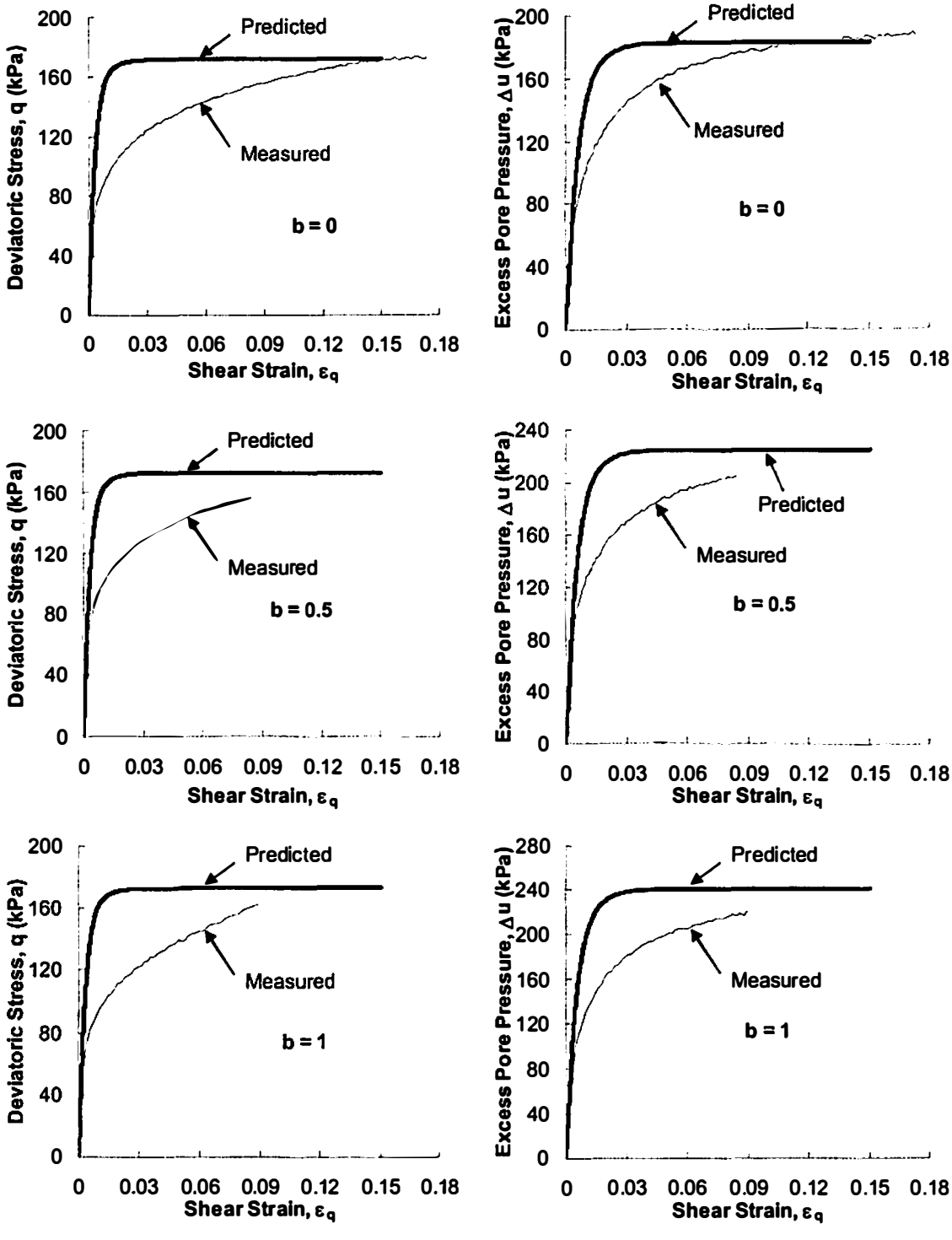

Figure 7.5 MCC Predictions and Experimental Data from True Triaxial Undrained Tests on NC Kaolin Clay (b=0, 0.5, 1)

In Fig. 7.6 and 7.7, the MCC model predictions are compared with the corresponding experimental data obtained from a series of true triaxial undrained compression tests (b=0) performed on OC kaolin clay at OCR=1.5, 2, 5, and 10. A detailed analysis of experimental data has been presented in chapter 5. The shear stress-strain relationship and excess pore pressure behavior are shown in Fig. 7.6, and the stress paths are presented in Fig. 7.7. It can be observed that in comparison with the experimental observations:

- MCC model gives a good prediction of initial shear stiffness (elastic behavior) of clay at each OCR value; however, it predicts much higher shear stresses at small strain values.
- The range of linear elasticity in stress space (the size of initial yield surface) assumed in MCC model appears to be much larger than the range, which can be acceptable for the highly non-linear stress-strain relationship obtained from experimental data. Experimental effective stress paths (in Fig. 7.7) show that the assumption of linear elasticity, which requires p' to be constant according to cam clay elasticity, is reasonable only for a small region in stress space. In chapter 5, a possible shape of this elastic range was described to have a tear drop shape with its axis along the hydrostatic line (See Fig. 5.4).
- MCC model gives a reasonable prediction of shear strength variation with OCR values. However, it predicts much lower strain values corresponding to failure condition.

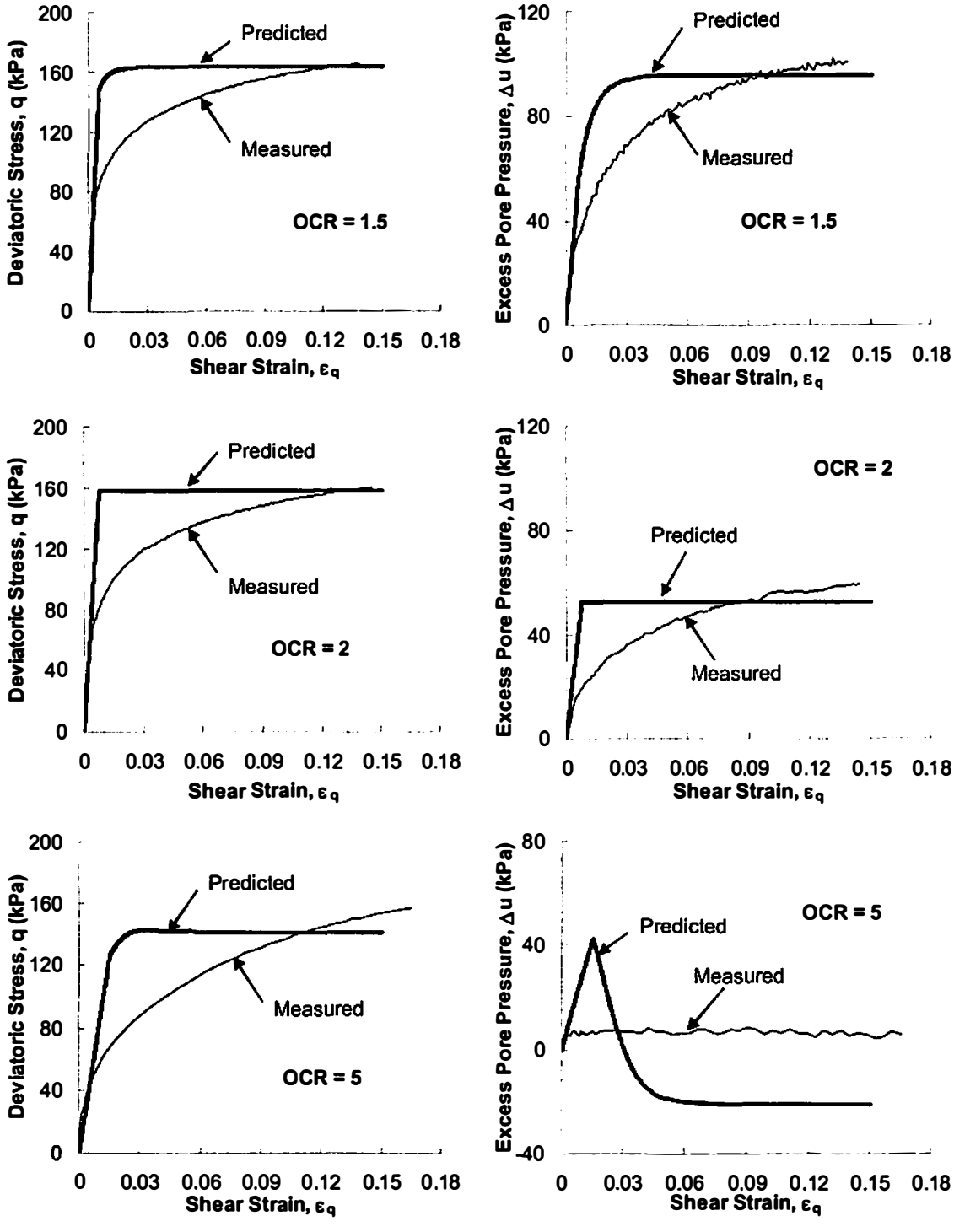

Figure 7.6 MCC Predictions and Experimental Data from True Triaxial Undrained Compression Tests (b=0) on OC Kaolin Clay

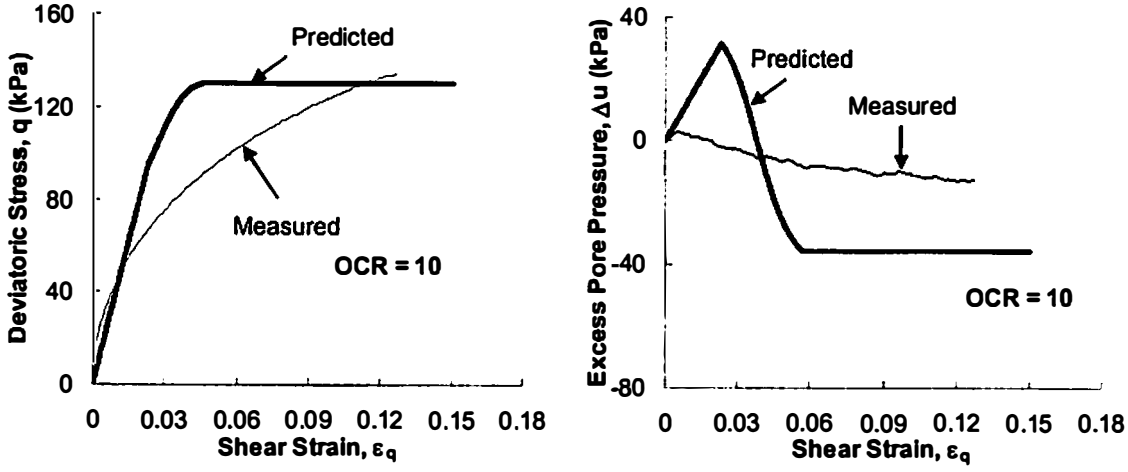

Figure 7.6 Continued

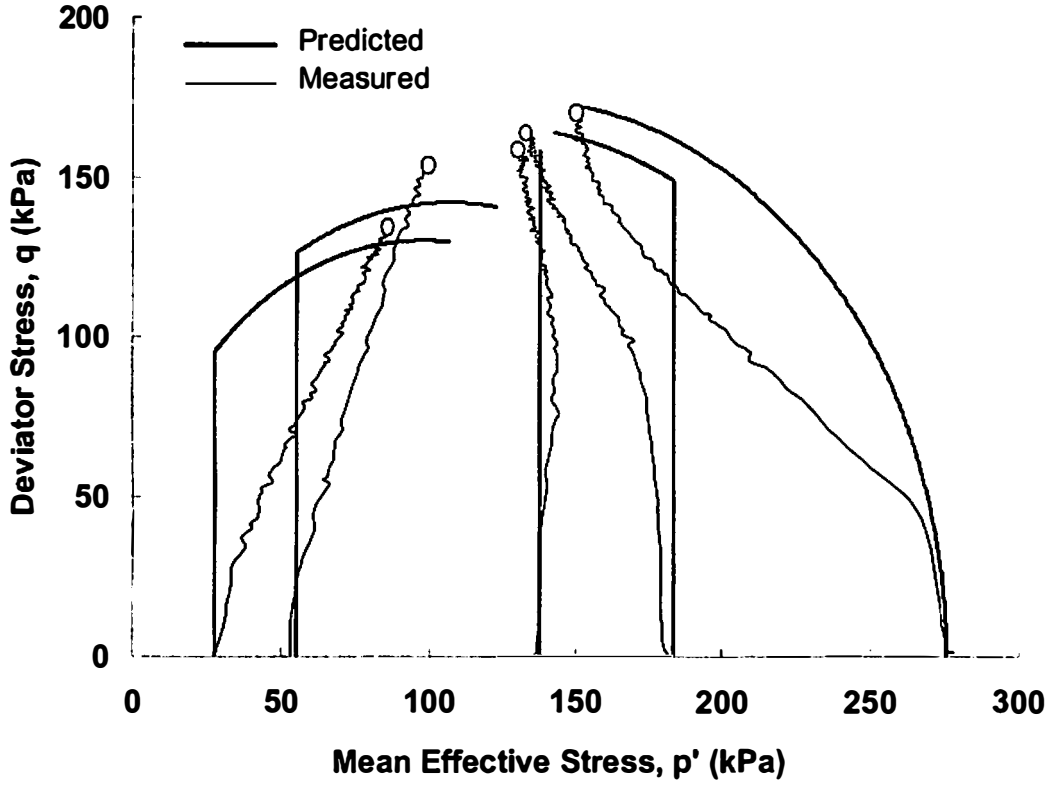

Figure 7.7 Stress Paths in q-p' Plane: MCC Predictions and Experimental Data from True Triaxial Undrained Compression Tests (b=0) on Kaolin Clay

- In general, MCC model shows much higher excess pore pressure evolution during shearing. However, for lightly overconsolidated clay (OCR=1.5 and 2), it gives a good prediction of excess pore pressure at failure. For highly overconsolidated clay, the model predicts much lower pore pressure response as the stress state reaches failure condition.
- MCC model predicts elastic-perfectly plastic behavior for the test performed at OCR=2; however, the experimental data shows initiation of plastic deformation at much lower shear stress level.

Critical State Concept and Failure Criteria

Critical state concept is based on an assumption of unique critical state for a particular type of soil, and this is not supposed to change with the stress state. The yield surface in MCC model is a function of critical state parameter M and pre-consolidation pressure p_o'. A constant M-value gives a circular yield surface in deviatoric plane, and because of the associative flow rule, the plastic potential surface has the same shape as yield surface. Based on experimental observations in the studies performed later by many researchers, Kirby and Wroth (1977) defined M-parameter to be dependent on the intermediate principal stress, and reported that the M-value reaches its maximum for triaxial compression (b=0) and minimum for extension (b=1). In this case, the yield surface remains circular in deviatoric plane but its size changes with the b-value. In that discussion they proposed to determine the M-value based on a constant value of friction

angle, which implicitly assumes the Mohr-Coulomb criteria. However, it is well known that the friction angle is not constant for all the b-values.

In the MCC model formulation, if the M-parameter is assumed as a continuous function of b-value (which is a function of stress state), and it is not constant; then it should provide a non-circular yield surface in deviatoric plane. However, the plastic potential will remain circular in deviatoric plane, and the model would essentially assume a non-associative flow rule. Instead of depending on friction angle, the variation of M-value may be related to the effect of third invariant of stress as shown in equation 3.9 of chapter 3, which should provide a yield surface similar to the one suggested by Lade (1990). In that case, the model would be indirectly adopting the third-invariant-based yield criteria with circular plastic potential surface in deviatoric plane.

Single Hardening Model

Lade (1977) suggested a comprehensive model with a two-component yield surface to describe the general constitutive behavior of frictional materials and referred to double hardening model. Since then this model has been consistently upgraded at various stages. Kim and Lade (1988), and Lade and Kim (1988a,b) published the latest version of this model with single continuous function for yield surface which is referred to as the single hardening (SH) constitutive model. Lade (1990) published the application of this model to NC clay. NC clay was assumed to have no strength under zero effective stress state, which reduced one parameter in the failure criteria i.e. the parameter **a**. Segments of this model involve, Elastic Behavior (parameters **M**, λ and ν), Failure Criterion (η_1 and **m**), Plastic Potential (ψ_2 and μ.), Yield Criteria (**h** and α) and Hardening Criterion (**C** and

p). The major, intermediate and minor principal effective stress values are defined here by σ_1, σ_2 and σ_3 respectively and corresponding strain values with ε_1, ε_2 and ε_3. The stress invariants used in definition of this model are provided in appendix-1 (equations A1.1-A1.6). The formulation of SH model is given in Appendix-3.

Determination of Single Hardening Model Parameters for Kaolin Clay

For clays, SH model requires eleven parameters to be determined from at least one isotropic consolidation and three standard triaxial tests. A cylindrical and a cubical specimen of kaolinite clay were isotropically consolidated with incremental loading in a triaxial cell and true triaxial apparatus respectively. Three consolidated undrained traditional triaxial tests were performed on cylindrical NC kaolinite clay specimens with initial confining pressure of 195 kPa, 274 kPa and 326 kPa.

The single hardening model uses Hook's law to calculate the elastic strains. The Young's modulus is derived as a function of the stress invariants based on the elastic model developed by Lade and Nelson (1987) and Lade (1990) as shown in eq. A5. The Poisson's ratio $\nu = 0.28$ is used as was determined for the MCC model predictions. Assuming that unloading stage during isotropic consolidation was elastic, Young's Modulus (E) was determined for each unloading step, using equation 7.19.

$$E = (1-2\nu)\frac{\Delta I_1}{\Delta \varepsilon_v^e} \tag{7.19}$$

The Young's modulus determined from isotropic consolidation does not include the influence of J_2', because J_2' remains zero during isotropic consolidation. Therefore, the E value was also determined from the initial part of stress-strain curves (assuming

elastic deformation within $\Delta\varepsilon_1 = 0.05\ \%$, based on visual observation of linearity in the stress-strain curve) obtained from three triaxial compression tests, using equation 7.20.

$$E = \frac{\left(\Delta\sigma_1 - 2\nu.\Delta\sigma_3\right)}{\Delta\varepsilon_1} \tag{7.20}$$

Values of E/p_a are plotted against $\left(I_1/p_a\right)^2 + R.J'_2/p_a^2$ in Fig. 7.8, proving the parameter $M = 26$ and $\lambda = 0.60$. Here, I_1 and J'_2 were computed as their average values for the corresponding increments.

Failure locations in the three traditional triaxial tests were defined at peak deviatoric stress. The values of two non-dimensional terms p_a/I_1 and $\left(I_1^3/I_3 - 27\right)$ at failure are plotted in Fig 7.9, which is supposed to give a linear relationship in log-log space. However, from the test data they come out to be so scattered that it is difficult to have confidence in a single regression line. Therefore, in this plot the failure points from undrained as well as drained true triaxial tests (for various b-values) on cubical specimens and hollow cylinder axial torsional tests are also included. The best judgment for a linear relationship in this log-log plot provides the failure surface parameters, $\eta_1 = 50$, and $m = 0.86$.

Lade's model is based on a non-associative flow rule. Therefore, in this model the plastic potential function (g_p, equation A3.3 in Appendix-3) is different from the yield criterion (f_p, equation A3.5). For triaxial compression test, the evolution of plastic strains with the chosen plastic potential surface turns out to provide the relationship 7.21, which can be used to determine the parameters μ and ψ_2.

$$\xi_y = \xi_x/\mu - \psi_2 \tag{7.21}$$

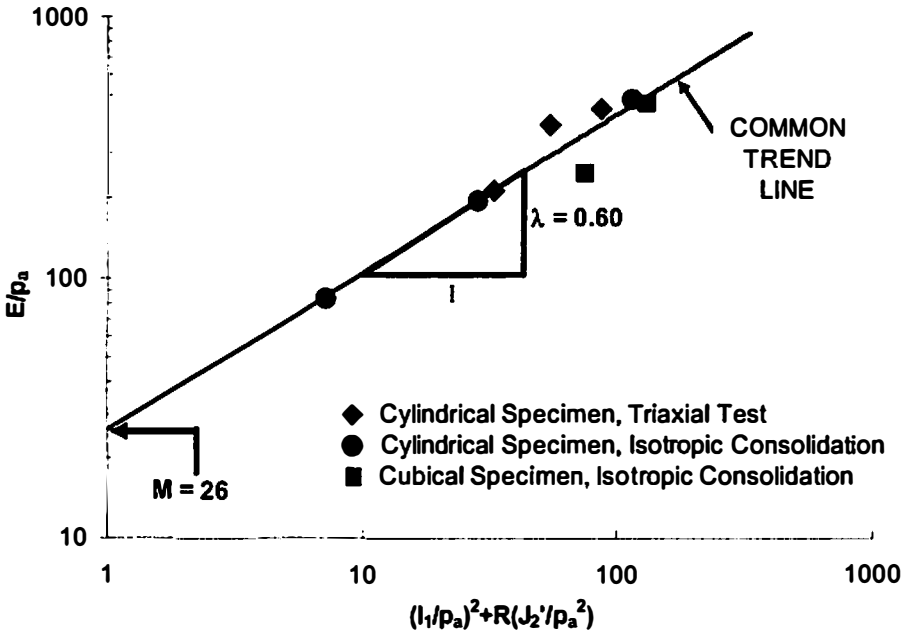

Figure 7.8 Determination of Elastic Parameters for SH Model

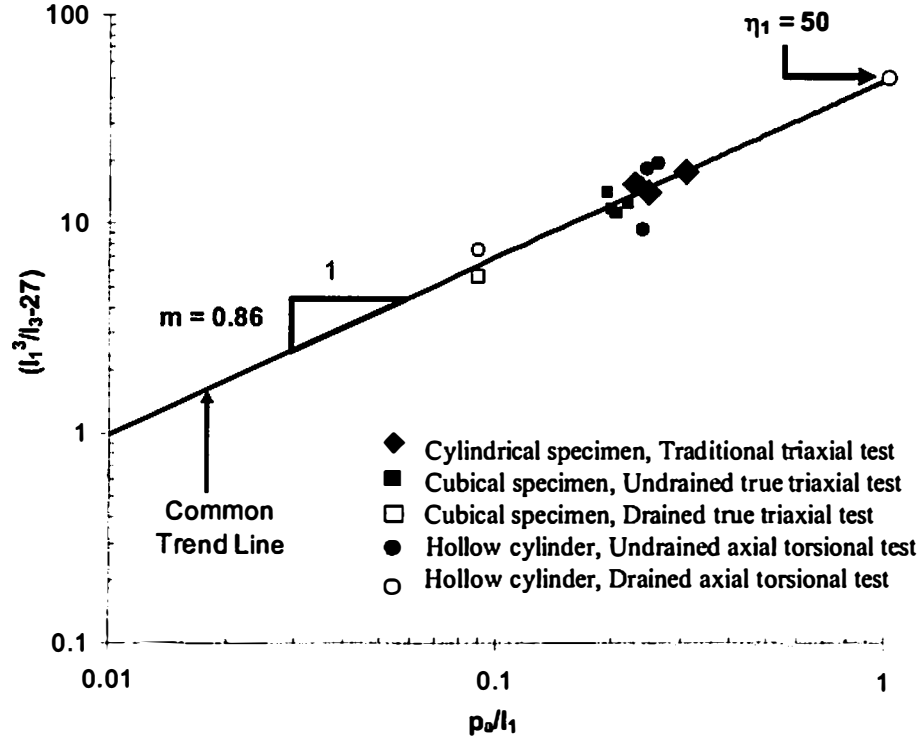

Figure 7.9 Determination of Parameters for Failure Criterion for SH Model

$$\xi_x = \frac{1}{1+\nu_p}\left[\frac{I_1^3}{I_2^2}\left(\sigma_1+\sigma_3+2\nu_p\sigma_3\right)+\psi_1\frac{I_1^4}{I_3^2}\left(\sigma_1\sigma_3+\nu_p\sigma_3^2\right)\right]-3\psi_1\frac{I_1^3}{I_3}+2\frac{I_1^2}{I_2} \qquad (7.22)$$

$$\xi_y = \psi_1\frac{I_1^3}{I_3}-\frac{I_1^2}{I_2} \qquad (7.23)$$

Incremental elastic strains ($\delta\varepsilon_1^e$ and $\delta\varepsilon_3^e$) for the three triaxial tests are computed using Hook's law after getting E from equation A3.1. Plastic strain components are then computed at various stress states following the conditions $\delta\varepsilon_i^p = \delta\varepsilon_i - \delta\varepsilon_i^e$, and $\delta\varepsilon_1 + 2\delta\varepsilon_3 = 0$, to finally determine the incremental plastic strain ratio, $\nu_p = \delta\varepsilon_3^p / \delta\varepsilon_1^p$. Kim and Lade (1988) found that the parameter ψ_1 could be determined by using an empirical relationship between ψ_1 and parameter m, as shown in equation 7.24. The value of ψ_1 for kaolin clay is determined to be $\psi_1 = 0.00188$.

$$\psi_1 = 0.00155m^{-1.27} \qquad (7.24)$$

Using these ν_p values, incremental values of ξ_x and ξ_y are then computed using equation 7.22 and 7.23. ξ_x-ξ_y plot in Fig. 7.10 provides the parameter $\mu = 2.38$ and $\psi_2 = -3.04$. ξ_x is very sensitive to ν_p and computed plastic strain components at small strains (close to hydrostatic stress state) show considerable variation in ν_p values. Therefore, the ξ_x-ξ_y relationship becomes non-linear for initial part of each test. However, the model assumes this relationship to be linear and therefore the parameters are determined by excluding this non-linear part of ξ_x-ξ_y relationship.

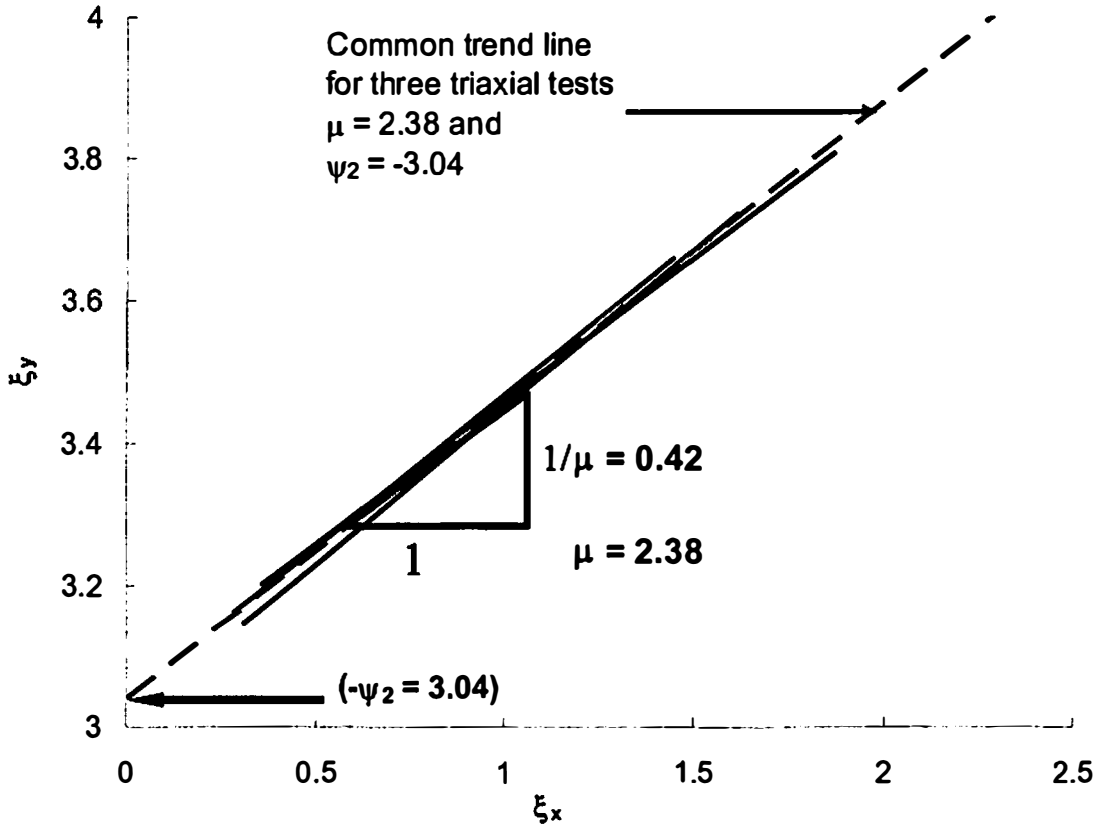

Figure 7.10 Determination of Plastic Potential Function Parameters from Three Traditional Triaxial Tests

The plastic work done during isotropic consolidation is used to determine the hardening parameters, C and p (equation A3.9 in Appendix-3). Assuming $\varepsilon_1 = \varepsilon_v/3$ for isotropic material, plastic strain ε_1^p value at each loading increment in isotropic consolidation test is calculated using equation 7.25.

$$\varepsilon_1^p = \varepsilon_1 - \frac{(1-2\nu)}{E}\frac{I_1}{3} \tag{7.25}$$

Plastic work, W_p/p_a at each step is computed from the relationship $dW_p/p_a = (I_1/p_a).d\varepsilon_1^p$, which is the area under the curve I_1/p_a vs. ε_1^p, as shown in Fig. 7.11(a). Log-log plot between W_p/p_a and I_1/p_a for isotropic consolidation of cylindrical and cubical specimen in Fig. 7.11(b), provides the factor $C = 0.0024$ and exponent $p = 1.74$.

Lade and Kim (1988a) derived their yield surfaces from constant plastic work (W_p) contours (equation A3.4-A3.7 in Appendix-3). Stress level, S varies from $S = 0$ (hence, $q = 0$ from equation A3.6) at hydrostatic stress state to $S = 1$ (and $q = 1$) at failure stress state. Total plastic work being constant along a yield surface, two stress points, **A** on the hydrostatic axis and **B** on the failure surface show $f_p(\sigma_A) = f_p(\sigma_B)$,; therefore, parameter h can be obtained as shown in equation 7.26.

$$h = \ln\frac{\left(\psi_1\frac{I_{1B}^3}{I_{3B}} - \frac{I_{1B}^2}{I_{2B}}\right).e}{27\psi_1 + 3} \Bigg/ \ln\left(\frac{I_{1A}}{I_{1B}}\right) \tag{7.26}$$

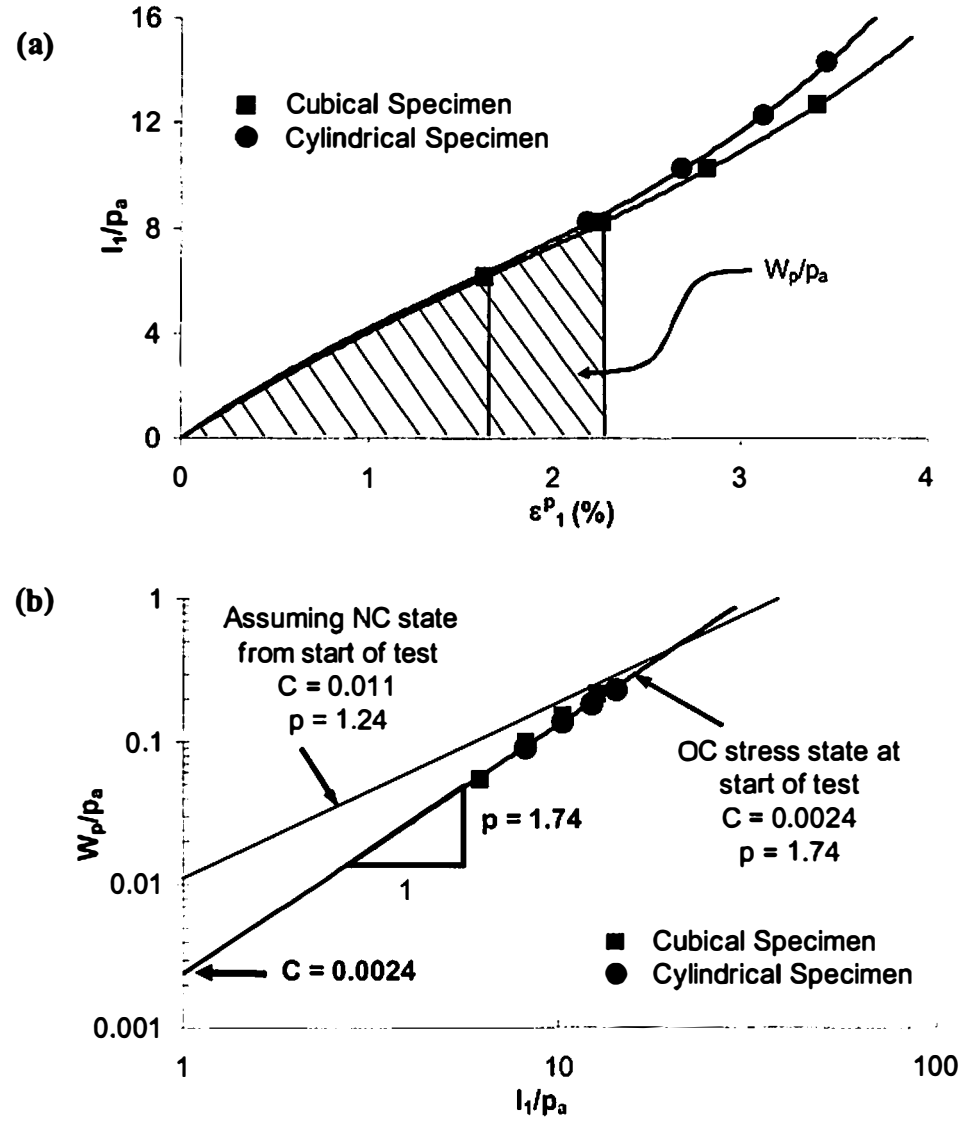

Figure 7.11 Determination of Hardening Parameters from Isotropic Consolidation Test, (a) Plastic Work Computation, (b) Hardening Parameters

For three traditional triaxial tests plastic work is computed at hydrostatic stress state before shearing using equation 7.27, and the plastic work increments ($\Delta W_p = \sigma_1.\Delta\varepsilon_1^p + 2\sigma_3.\Delta\varepsilon_3^p$) are added to this for the stress state to reach failure.

$$W_p = C.p_a\left(\frac{I_1}{p_a}\right)^p \tag{7.27}$$

Using this total plastic work done at failure equation 7.27 gives the hydrostatic stress state for the same yield surface (values summarized in Table 7.2). Parameter h is computed for each test using equation 7.26, and the average parameter value is $h = 0.858$. Stress level, S is plotted against the exponent, q in Fig. 7.12 for the three triaxial tests, in which S is determined by equation A3.7 and q is obtained by rearranging the yield function. A common trend line is found in Fig. 7.12, which satisfies the condition given in equation A3.6 for $\alpha = 0.8$.

$$q = \ln\frac{\left(W_p/D.p_a\right)^{1/\rho}}{\left(\psi_1\frac{I_1^3}{I_3} - \frac{I_1^2}{I_2}\right)\left(\frac{I_1}{p_a}\right)^h} \tag{7.28}$$

Table: 7.2 Calculation of Yield Parameter h

W_p/p_a	Hydrostatic Compression (A)	Triaxial Compression (B)			h
	(I_{1A}/p_a)	(I_{1B}/p_a)	(I_{2B}/p_a)	(I_{3B}/p_a)	
0.256	12.6	3.228	-2.824	0.748	0.889
0.336	15.7	4.045	-4.602	1.605	0.864
0.411	18.5	4.369	-5.297	1.960	0.822

average h = 0.858

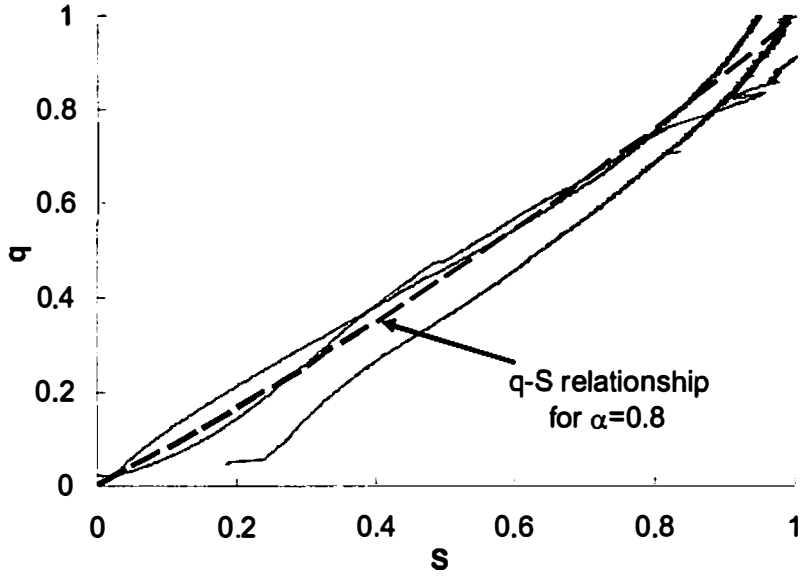

Figure 7.12 Determination of Yield Function Parameter α from Three Traditional Triaxial Tests

Computing Hardening Parameter from Plastic Work

At the start of consolidation, the clay specimen is always over-consolidated (OC), whether the specimen is a reconstituted or undisturbed in-situ specimen. During consolidation, this specimen undergoes very small plastic deformation until it reaches the NC stress state (at pre-consolidation stress). For the same clay with lower pre-consolidation stress p_o', the specimen would show much higher plastic deformation and therefore much higher plastic work done to reach the same stress state. To use the hardening parameter determination method described by Lade (1990), the total plastic work should be calculated from the plastic deformation generated under NC condition throughout and starting from zero stress state. Total plastic work in this condition would be much higher than what can be determined using any of the above-mentioned

consolidation tests. This type of test requires the initial specimen with p'_o=0, which may not even be possible to obtain. Considering these issues, an incremental plastic work approach is proposed to determine hardening parameters. Differential of equation 7.27 and the relationship $dW_p = I_1.d\varepsilon_1^p$ for isotropic consolidation provides equation 7.31 after certain rearrangement.

By differentiating equation 7.27,

$$dW_p = C.p.\left(\frac{I_1}{p_a}\right)^{p-1}.dI_1 \tag{7.29}$$

With, $dW_p = I_1.d\varepsilon_1^p$ and equation 7.28,

$$d\varepsilon_1^p = \frac{C.p}{p_a}\left(\frac{I_1}{p_a}\right)^{p-2} dI_1 \tag{7.30}$$

$$\frac{d(I_1/p_a)}{d\varepsilon_1^p} = \frac{1}{C.p}\left(\frac{I_1}{p_a}\right)^{(2-p)} \tag{7.31}$$

The values of $\Delta(I_1/p_a)/\Delta\varepsilon_1^p$ for various incremental steps beyond the pre-consolidation stress state in isotropic consolidation test can be plotted against the mean value of corresponding I_1/p_a increments. The slope of the best-fit linear relationship in log-log scale should give the exponent $(2-p)$ and the offset should provide the multiplying factor $(C.p)^{-1}$. This exercise is performed for the isotropic consolidation test data in Fig. 7.13, which provides the parameter $C = 0.011$ and $p = 1.24$ for kaolin clay.

The relationship of W_p/p_a with I_1/p_a in Fig. 7.11(b) for new parameters, which assumes consolidation of NC specimen from start of test, shows that the total plastic

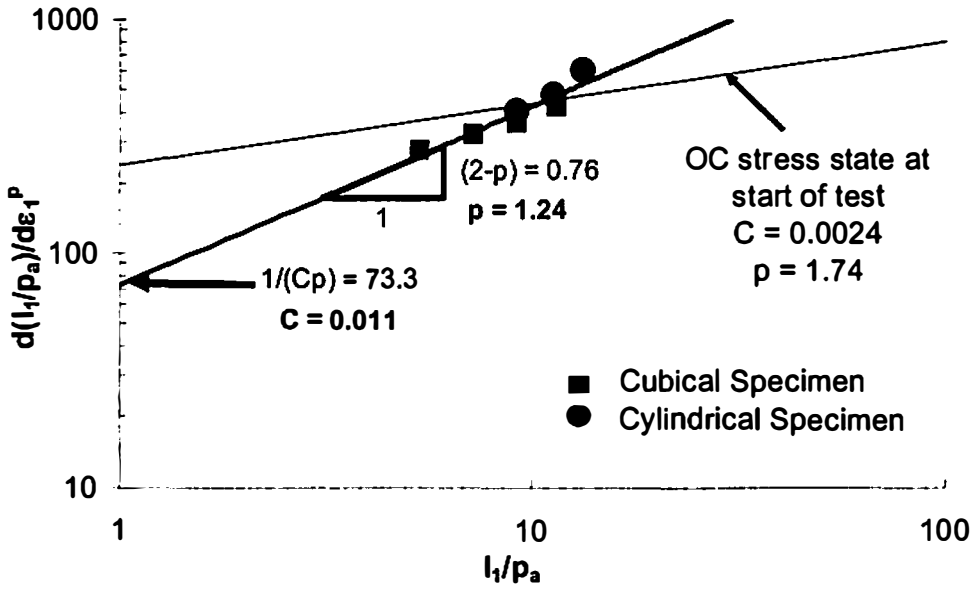

Figure 7.13 Determination of Hardening Parameters From Isotropic Consolidation Test using Incremental Plastic Work Method

work generated to reach a small stress value is much larger than that directly computed from the I_1/p_a vs. ε_1^p relationship for consolidation tests with an OC specimen at the start of test. The plastic work computed at the start of test is zero from the first method; whereas, there should be some plastic work done on the specimen to reach the state at start of test. This plastic work at the start of test is associated with the pre-consolidation stress of specimen. For lower pre-consolidation stress, the associated total plastic work at start of loading should also be lower. Parameters obtained from new approach were used to determine other dependent parameters and to predict the undrained shear behavior of Kaolin, which is presented in subsequent section.

Single Hardening Model Predictions for Kaolin Clay

A computer program was developed to get the single hardening (SH) model predictions for undrained tests. Basic format of the program was similar to the one used

for MCC model predictions; however, it was customized to fit the formulation of SH model. Considering the issues related to localization during softening under undrained condition, explained in chapter 4, the clay behavior is predicted for hardening only. The single hardening model parameters for kaolin clay are listed in Table 7.3.

Figure 7.14 shows a comparison between the SH model predictions and corresponding measured values from a series of constant b-value true triaxial undrained tests performed on NC kaolin clay (p_o'=275kPa). This figure includes six data sets that were presented in chapter 2. The first five tests were performed at different b-values (b=0, 0.25, 0.5, 0.75, and 1.0), in which the major principal direction was along the axis of specimen's cross-anisotropy (δ=0°); and the sixth test was performed as triaxial extension test (b=1), in which the minor principal direction was along the axis of cross-

Table : 7.3 Single Hardening Model Parameters for Kaolin Clay

Single Hardening Model Parameters		Value
Elastic Behavior	ν	0.28
	M	26
	λ	0.6
Failure Criterion	η_1	50
	m	0.86
Plastic Potential Surface	ψ_1	0.00188
	ψ_2	-3.04
	μ	2.38
Hardening Rule	C	0.011
	p	1.24
Yield Criterion	h	0.858
	α	0.8

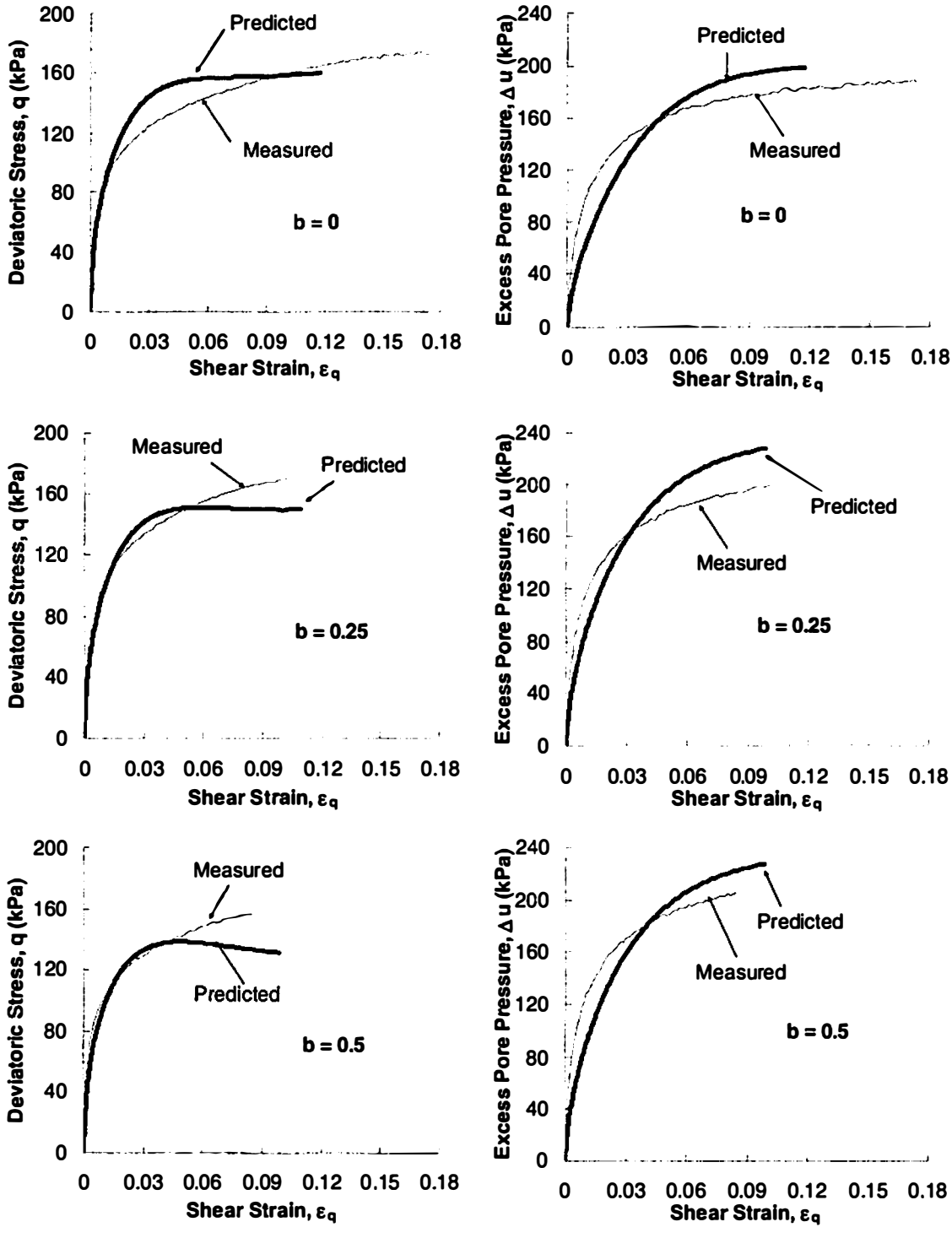

Figure 7.14 Single Hardening Model Predictions and Experimental Data from True Triaxial Undrained Tests on NC Kaolin Clay

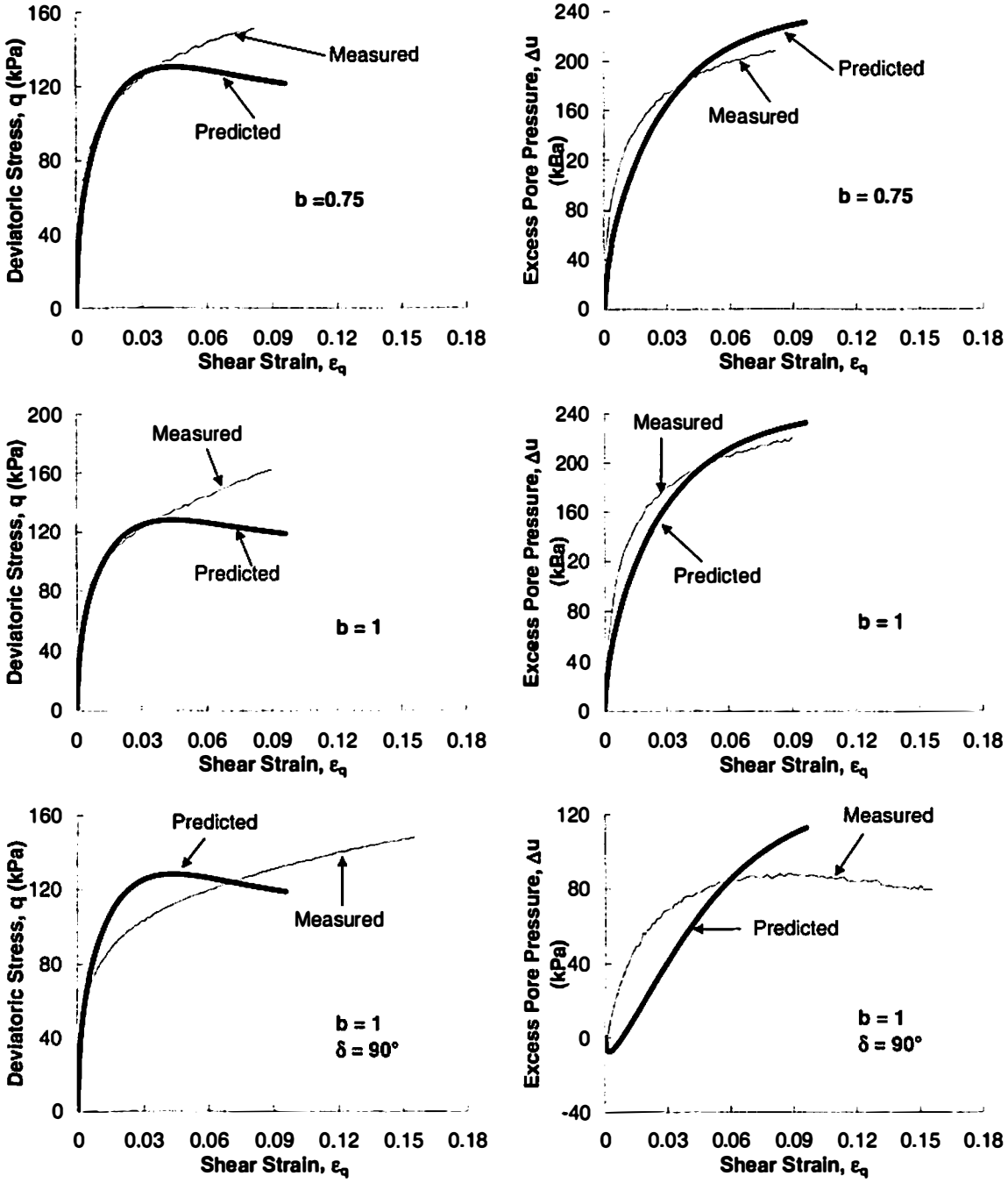

Figure 7.14 Continued

anisotropy (δ=90°). In comparison with the experimental observations, the SH model predictions exhibit following behavior of Kaolin clay.

- SH model gives a reasonable prediction of stress-strain relationship for most b-values; however, for triaxial compression (b=0) and extension (b=1, δ=90°), it predicts much higher shear stress values at strain levels ranging from $\varepsilon_q \approx 1\%$ to $\varepsilon_q \approx 8\%$.
- In each case, the predicted stress-strain relationship shows a peak shear stress level, after that the shear stress decreases as the stress state approaches its failure condition. The peak becomes more prominent for higher b-values. However, the experimental data shows brittle failure response of the clay (especially for b > 0.25), and the shear stress values consistently increase until the stress state reaches its failure condition.
- SH model gives a reasonable prediction of shear strain values at failure; however, for triaxial compression, and extension, it shows failure at much lower strain values.
- In all six cases, the predicted shear strength is lower than the experimentally measured values, and the difference in strength values increases with increase in b-value.
- In all cases, predictions exhibit higher excess pore pressure response at failure. For the extension test, the pore pressure response is not predicted well by this model.
- SH model does not account for the change in orientation of principal stress. It predicts the same stress-strain behavior for the two b=1 cases (δ=0° and δ=90°); however, the experimental data shows significant influence of change in δ-value.

The single hardening model for clays was described to be applicable only for normally consolidated and lightly overconsolidated (OCR < 2.5) clays. Using SH model, the shear strength of heavily overconsolidated clay is usually under-predicted, and most of the stress-strain relationship is predicted to be purely elastic. In Fig. 7.15 and 7.16, the SH model predictions are compared with the corresponding experimental data obtained from a series of true triaxial undrained compression tests (b=0) performed on lightly OC kaolin clay at OCR=1.5, 2. Shear stress-strain relationship and excess pore pressure behavior are shown in Fig. 7.15, and the stress paths are presented in Fig. 7.16. In comparison with the experimental observations, the SH model predictions exhibit following behavior of Kaolin clay.

- The limit of linear elasticity is too high to be acceptable for the highly non-linear stress-strain relationship obtained from experimental data. After the elastic zone, the model predicts much softer response of clay, and finally at failure, the stress state approximated the experimentally observed stress-strain relationship.
- For lightly OC clay, the predicted strength and strain values at failure are reasonable.
- SH model predicts much higher excess pore pressure response of lightly OC clay.
- Predicted effective stress-paths for undrained condition are significantly different at each OCR value.

Conclusions

Soil is a particulate medium with a complex inelastic behavior. Accurate theoretical solutions of boundary value problems in soil mechanics and soil structure interaction problems, even in simple geometries, are extremely difficult or, in many

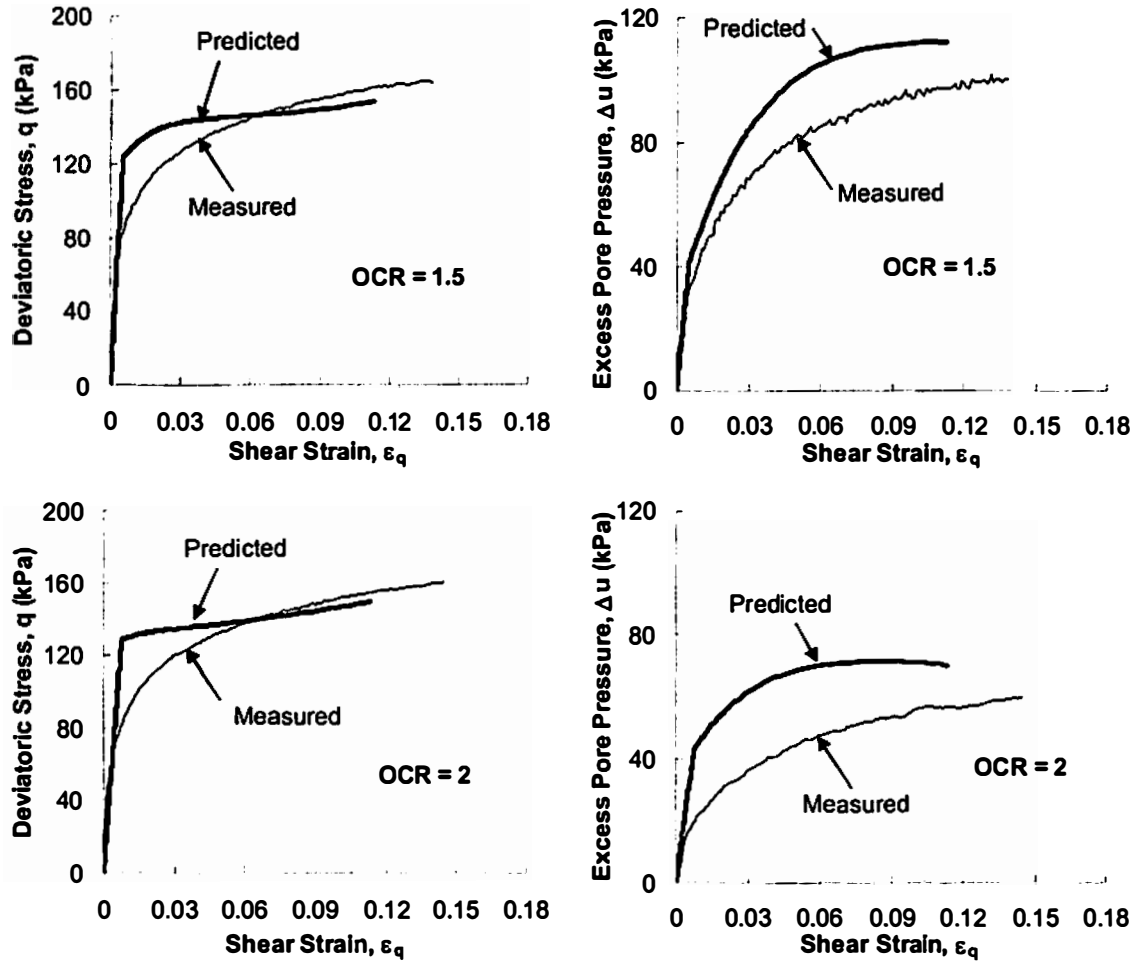

Figure 7.15 Single Hardening Model Predictions and Experimental Data from True Triaxial Undrained Compression Tests (b=0) on OC Kaolin Clay (OCR=1.5 and 2.0)

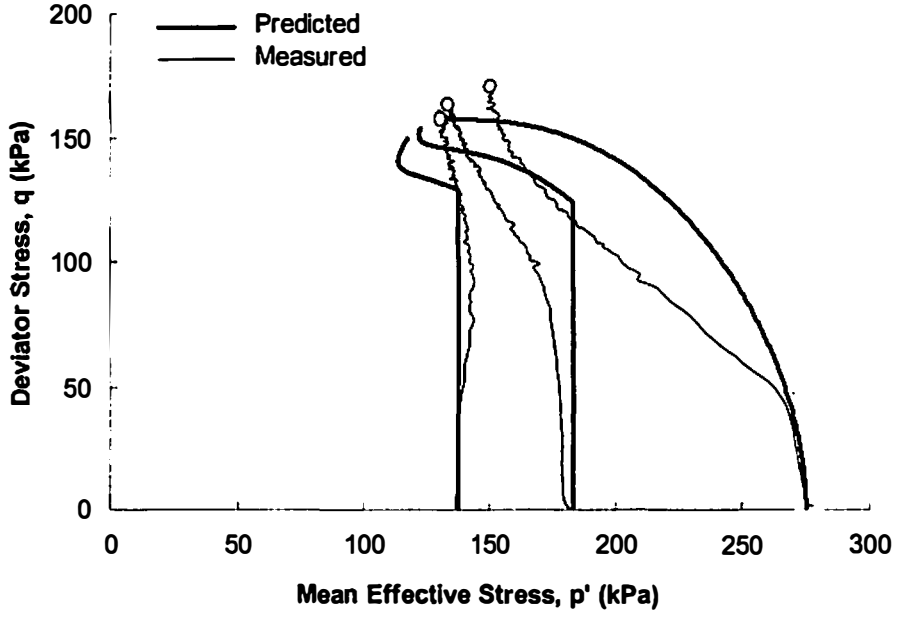

Figure 7.16 Stress Paths in q-p' Plane: Single Hardening Model Predictions and Experimental Data from True Triaxial Undrained Compression Tests (b=0) on Kaolin Clay

cases, impossible to obtain. Appropriate constitutive models of soil behavior may offer a realistic alternative.

A brief review of the elasto-plasticity theory was presented in this chapter. Based on the elasto-plasticity theory, a number of constitutive models have been developed in the past that attempt to describe various aspects of geomaterials. Key features of some of the important constitutive models for frictional materials were reviewed in this chapter. Two of the leading constitutive theories, the Modified Cam Clay (MCC) model and the Single Hardening model, were discussed in detail.

True triaxial undrained shear behavior was predicted by using the MCC model parameters appropriate for Kaolin clay, and the results were compared with the

experimental data. It was shown that the basic assumptions taken during the development of MCC model provide a fair estimate of normalized strength behavior; however, these assumptions oversimplify the model, which leads to the inaccurate predictions of soil's stress-strain relationship and pore pressure behavior.

The single hardening model was formulated in an effort to predict the generalized soil behavior in three-dimensional stress space. This required a complex procedure for the determination of its parameters. A detailed description of this procedure was presented in this chapter while determining the parameters for kaolin clay. Using these parameters, the undrained shear behavior of kaolin clay was predicted, and compared with the experimental observations. In comparison with the MCC model, the single hardening model was found to have a better potential to predict the normally consolidated clay behavior. However, the strength behavior of clay was consistently under predicted for all the anisotropic loading cases. Heavily overconsolidated clay behavior was not considered during the development of single hardening model, and this study showed that this model was unable to predict the experimental behavior of lightly overconsolidated clay behavior. In previous chapters, it was determined that the relative magnitudes of principal stresses and their orientation with respect to the axis of cross anisotropy exhibit their independent influence on the mechanical behavior of clay; however, in single hardening model, the influence of anisotropy was considered only due to the change in relative magnitude of principle stresses.

Chapter 8. A New Unified Elasto-Plastic Three-Dimensional Constitutive Model for Cohesive Soil

Introduction

The principal purpose in attempting to model the constitutive behavior of soils is to use the resulting model as a tool for solving engineering problems. It is desirable in most engineering applications to have a model with reasonable simplicity, which is described using minimum number of parameters, requires least number of experiments to determine its parameters, and can be applied using simple procedures. It is tempting to develop a single model that would describe all the aspects of soil behavior, and, by adjusting certain parameters, would be applicable to all soil types. But in fact, such a model would not fit the criteria of simplicity and would be so complex as to render it virtually useless. A sensible approach is to have a set of models each designed to fulfill a different purpose, and each containing the relevant features for a particular type of soil behavior. This can also be achieved by having several variations of, or a set of independent components in a single model. The critical state concept has been repeatedly used to create variations of modified cam clay model (MCC model, Roscoe and Burland, 1968) in an effort to explain various facets of the observed soil behavior. However, a single model with several independent components, which could provide a convenient framework in understanding the concept and determination of parameters, is needed.

Several experimental studies have shown that a wide range of soils have highly non-linear stiffness at low strains; and in most cases soil specimen fail before reaching the critical state, especially overconsolidated clays. The onset of localized deformations

within the specimens could be a possible reason for premature failure. The stress induced anisotropy has also been observed to have a significant influence on the soil's shear behavior. For various soils, the dilative behavior under shear loading varies significantly, which can also be influenced by the configuration of loading if the soil is anisotropic. Using the well defined and widely accepted concept of elasto-plasticity theory, a constitutive model for isotropically consolidated clays is proposed that entertains some of the above mentioned issues. In the proposed model, an attempt has been made to have a balance between the simplicity of formulation and accuracy of results. It is assumed that the loading is monotonic and that large stress reversals including sudden directional changes in the stress paths are not involved. Temperature and time effects are assumed to be absent.

The basic concept of the proposed model is based on some of the assumptions about clay behavior that were considered in the Cam clay elasto-plasticity (Roscoe and Burland, 1968). The volumetric behavior (elastic or plastic) of clay under shear loading has been defined using the properties of clay that could be determined from its consolidation behavior. The Cam clay plasticity uses volumetric hardening for growth of its yield surface under loading condition, and this is used in the current model as a part of the hardening rule. However, unlike the cam clay plasticity, a non-associative flow rule (different yield and plastic potential functions) is used to describe the clay behavior as it has been widely acknowledged to be most appropriate for geomaterials (Lade, 1990).

The proposed model has two components. In first component, the behavior of normally consolidated (NC) to highly overconsolidated (OC) clay is considered in triaxial compression (b=0) plane. The issues related to brittle failure, dilative capacity, and

nonlinearity of stress-strain relationship are addressed in this component. The second component is an extension to the first one, which describes the soil behavior in three-dimensional stress space.

Framework of the Proposed Model in Triaxial Compression Plane

The stress space in the following formulation has been defined using mean effective stress p', and deviatoric stress q (equation A1.7 and A1.8 in Appendix-1). The corresponding volumetric and shear strains are defined using $d\varepsilon_p$ and $d\varepsilon_q$.

Cam clay elasticity is used to determine recoverable deformations. The elastic volumetric and shear deformation is defined to be uncoupled from each other so as they independently accompany the changes in mean effective stress and shear stress respectively. The relationship between elastic strain increments and the corresponding stress increments is defined in equation A2.1 to A2.3 of appendix-2. These equations require two elastic parameters for a particular clay, the slope of unload-reload curve during isotropic consolidation, κ, and the Poisson's ratio, ν. A general form of incremental stress-strain relationship, during elastic behavior, is shown in equation 8.1.

$$d\varepsilon_{ij}^{e} = \frac{\kappa}{3(1-2\nu)vp'}\left[(1+\nu)d\sigma_{ij} - \nu\delta_{ij}d\sigma_{kk}\right] \tag{8.1}$$

In most elasto-plasticity theories on clays, it is assumed that the initial stress state of a normally consolidated clay lies on yield surface, i.e. the behavior is assumed to be elastic-plastic (the yield surface grows in size) when they are subjected to further loading. The overconsolidated stress state remains inside the yield surface, and its behavior is assumed to be purely elastic. Loading overconsolidated clay takes the stress state towards

initial yield surface. After reaching the yield surface, further loading generates elasto-plastic deformation as the stress state becomes normally consolidated. It has been widely recognized that overconsolidated clays show non-linear stress-strain behavior even at small strains, which is difficult to predict using linear elasticity if the yield surface is assumed as used in cam-clay series of models. As shown in chapter 5, a similar nonlinear stress-strain relationship was observed for Kaolin clay in this study when a series of true triaxial undrained tests were performed in this study at various OCR values. Based on the observed stress-strain curves and effective stress paths shown in Fig. 5.3 and 5.4, a possible shape and size of initial yield surface was suggested. The yield surface in q-p' space was described to have a teardrop shape with its end point at p'=0, which was similar to the one suggested by Lade (1990) based on plastic work contour calculations. A similar shape is assumed for the yield function, f, used in current model as shown in equation 8.2.

$$f = \left(\frac{q}{p'}\right)^2 - L^2 \ln\left(\frac{p'_o}{p'}\right) \tag{8.2}$$

Here, p'_o is the pre-consolidation pressure that represents the consolidation history of clay, and L is another state variable. Both p'_o and L together define the hardening behavior of clay. Figure 8.1 shows the growth of yield surface with changing hardening variables p'_o and L. In Fig. 8.1a, the yield surface is shown for three values of p'_o= 100kPa, 200kPa, and 300kPa, at a constant value of L=1. The surfaces shown are self similar and their sizes have a linear relationship with p'_o. It shows that the yield surface is in fact normalized by p'_o. In Fig. 8.1b, the yield surface is shown for three values of

(a)

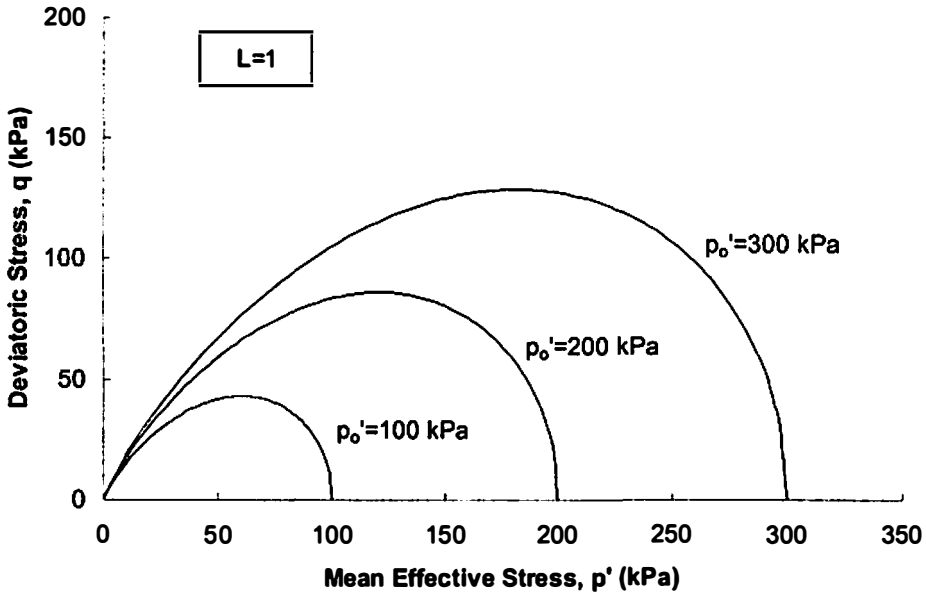

(b)

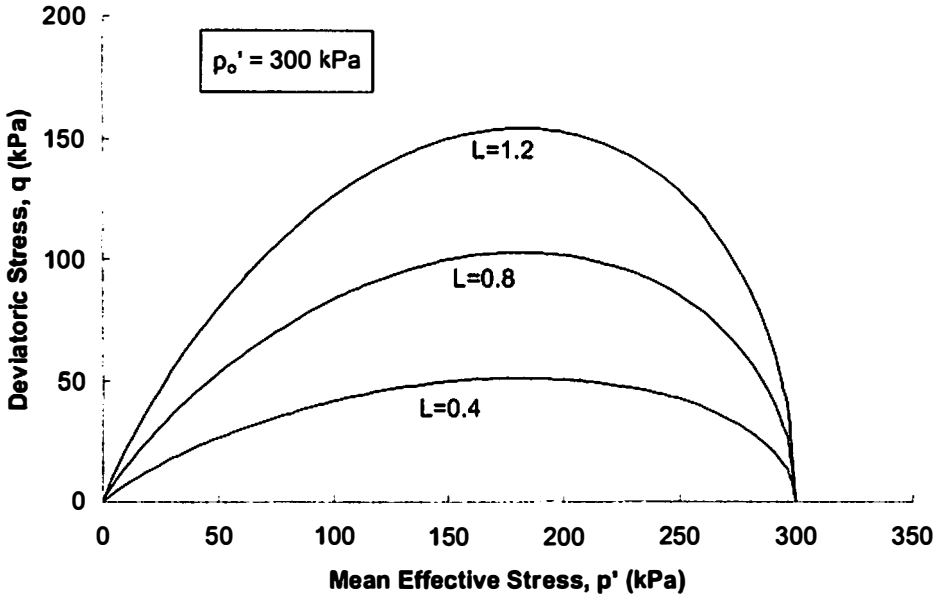

Figure 8.1 Shape of Yield Surface in q-p' Stress Space, (a) Growth of Yield Surface with Change in Consolidation History p_o', and (b) Growth of Yield Surface with Change in State Variable L.

L = 0.4, 0.8, and 1.2, at a constant value of p_o'=300kPa. It can be observed that the yield surface grows only in the direction of shear stress with an increase in the state variable L.

Mayne (1979), and Mayne and Swanson (1981) summarized the undrained strength behavior of different clays reported throughout the geotechnical literature. They showed that for most clays, the normalized strengths (S_u/σ_{vo}') are a function of OCR, which was originally identified by Ladd and Foott (1974). Based on these finding, a failure surface was developed in chapter 5 (equations 5.3 to 5.11) as a function of clay's void ratio. The failure surface in current model is assumed to be the same as what was derived in chapter 5, and it is shown in equation 8.3.

$$q = C_f p' \left(\frac{p_o'}{p'} \right)^{\Lambda_o} \tag{8.3}$$

Two parameters C_f and Λ_o are used to define the failure surface, and are assumed to be soil constants. The failure surface is essentially a function of clay's pre-consolidation pressure p_o' that grows in size with increasing p_o' value. Figure 8.2 shows shape and size of a typical failure surface in comparison with that of a typical initial yield surface.

It was observed during the experimental study that the kaolin clay specimens experienced sudden failure due to localized deformations within the specimens. A detailed description of the observed brittle behavior of clay was presented in chapter 5. To model this behavior in a mathematical framework, the surface defining the ultimate growth of the yield surface has to be separated from the failure surface. This surface is named as a reference surface. It should always be defined out side the failure surface; however, for ductile behavior it would be the same as failure surface. For simplicity of

formulation, the reference surface in triaxial compression plane is assumed to have a similar shape as the failure surface. An additional soil parameter, C_y, is introduced to define the size of reference surface different from corresponding failure surface, as shown in equation 8.3.

$$q_y = C_y p' \left(\frac{p'_o}{p'} \right)^{\Lambda_o} \tag{8.4}$$

In case of ductile response $C_y = C_f$, which reduces one parameter in the model. A typical reference surface in relation with the corresponding failure surface is shown in Fig. 8.2. The growth of yield surface, by changing the state variable L, is controlled by the reference surface; however, the stress state can not exceed the defined failure surface.

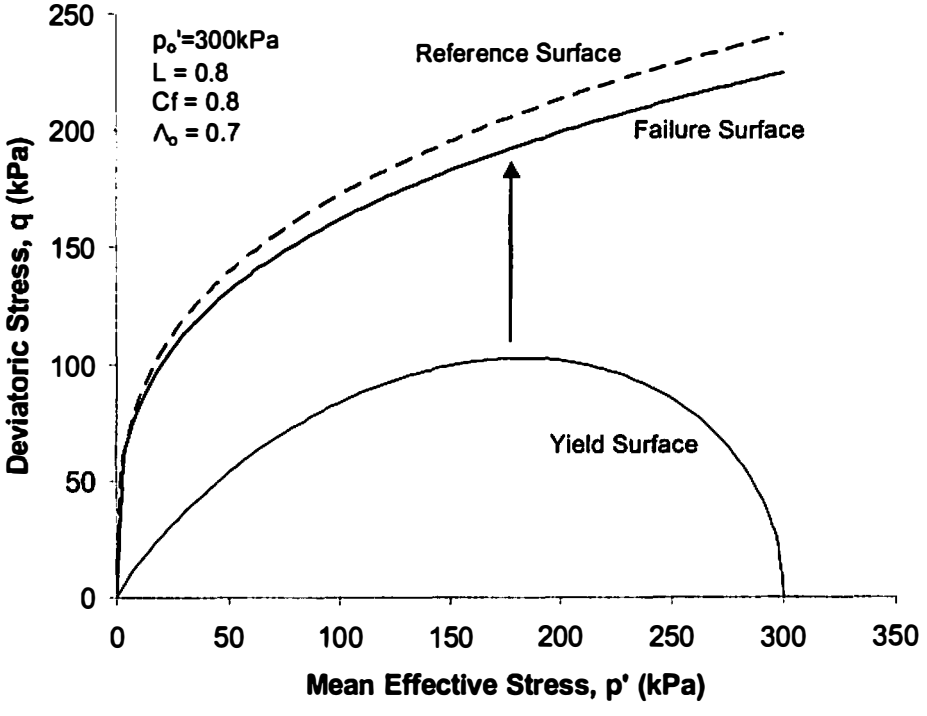

Figure 8.2 Typical Shapes of Yield Surface, Failure Surface, and Reference Surface in q-p' Stress Space

Plastic hardening (growth) of the yield surface was defined using two state variables, p_o' and L. Similar to the Cam clay plasticity, the pre-consolidation pressure p_o' is defined as a function of plastic volumetric strain, and is independent of shear strains. On the contrary, the state variable L is defined as a function of only the plastic shear strains. In mathematical form, the hardening rule is assumed as shown in equation 8.5, and 8.6.

$$\frac{\partial p_o'}{\partial \varepsilon_p^p} = \frac{\mathrm{v} p_o'}{(\lambda - \kappa)} \qquad \frac{\partial p_o'}{\partial \varepsilon_q^p} = 0 \tag{8.5}$$

$$\frac{\partial L}{\partial \varepsilon_p^p} = 0 \qquad \frac{\partial L}{\partial \varepsilon_q^p} = n_L (1 - \xi) \tag{8.6}$$

Here, v and λ are same as they were defined in MCC model description (Fig. 7.4), and n_L is a soil constant. ξ is a stress state mapping function (Dafalias and Herrman 1982, Whittle and Kavvadas 1994) that defines the distance of the current stress state, in relation to the reference surface, from the hydrostatic stress p'-axis at a constant p' value. As given in equation 8.7, ξ is essentially defined as the ratio of current shear stress q to the value of shear stress calculated from reference function q_y (equation 8.4), at constant p'.

$$\xi = \frac{q}{q_y} \tag{8.7}$$

Figure 8.3 shows the graphical representation of the relationship between q and q_y. The ξ function ranges from 0, at p'-axis, to 1, at reference surface. Therefore, the state variable L will have strongest relationship with plastic shear strains at p'-axis; however,

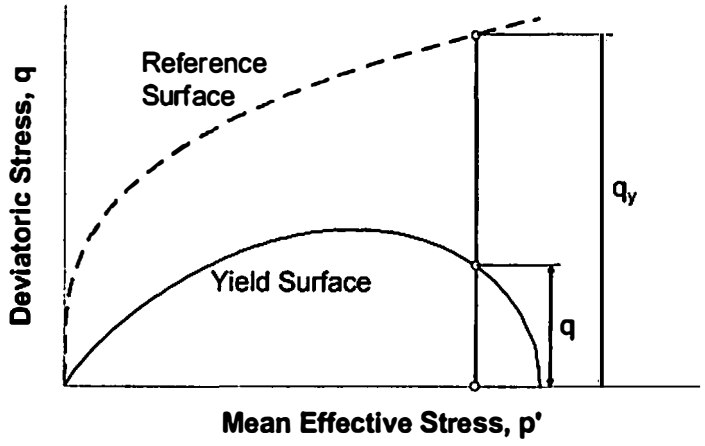

Figure 8.3 Components of Stress State Mapping Function ξ

close to p'-axis, developed shear strains are relatively small. The relationship goes weaker as the stress state moves towards reference surface; eventually, L becomes constant at the reference surface.

The plastic potential function is used to define the direction of strain increments at any stress state of material, which is usually achieved by taking derivatives of the plastic potential function with respect to the defined axes of stress space. In q-p' space, derivatives of the assumed plastic potential function in current model are shown in equation 8.8 and 8.9.

$$\frac{\partial g}{\partial p'} = 2\left(\frac{p'}{p'_o}\right)^{\gamma} - 1 \tag{8.8}$$

$$\frac{\partial g}{\partial q} = n_g\left(\frac{\xi}{1-\xi}\right) \tag{8.9}$$

Parameters γ and n_g are assumed to be soil constants. The mapping function ξ was defined in equation 8.7. Figure 8.4 shows the variation of the plastic potential derivatives

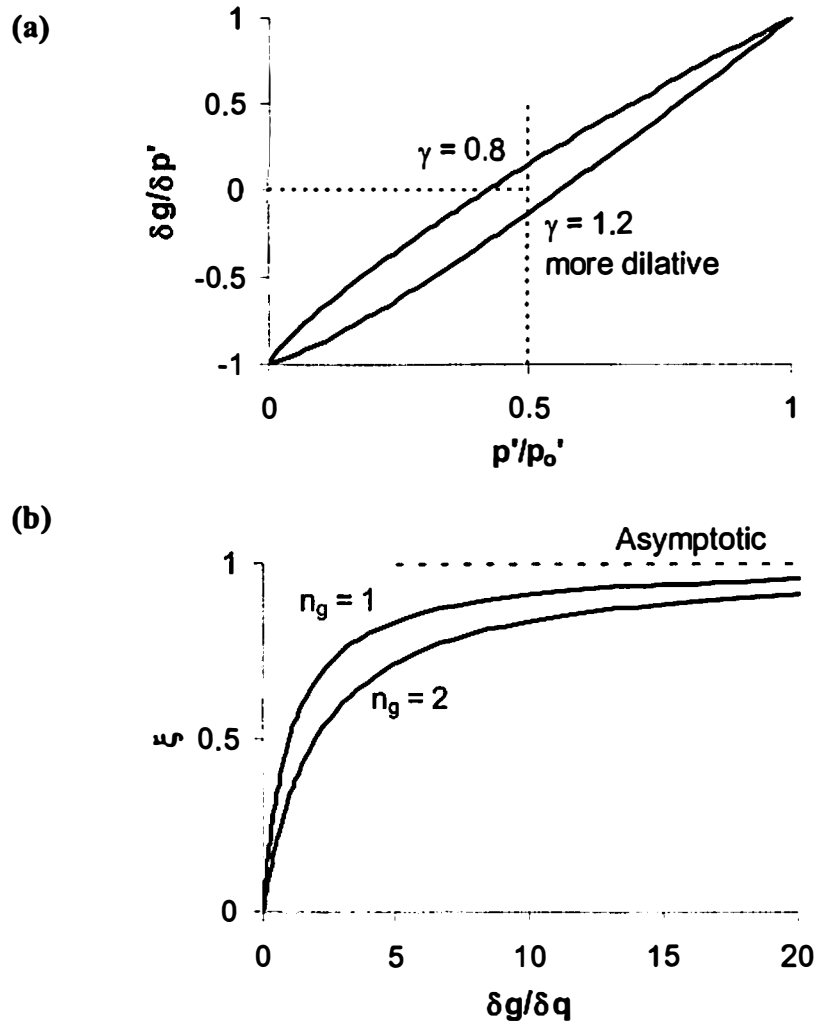

Figure 8.4 Derivatives of Plastic Potential with respect to (a) Mean Effective Stress p', and (b) Deviatoric Stress q.

in stress space. Introducing γ into plastic potential function provides the flexibility of accounting for different volumetric response of different clays, which has been commonly observed in various studies. However, the MCC model assumes γ to be constant, $\gamma=1$. The value of parameter γ is higher if the clay is more dilative clay. Parameter n_g accounts for the variation in evolution of volumetric response as the stress state moves towards the reference surface during incremental shear loading. The shear-strain increment vector remains zero when the stress state moves along hydrostatic axis; it grows to large magnitudes as the stress state goes close to reference surface; eventually, its hyperbolic variation becomes asymptotic to the reference surface. Therefore, if the material is assumed to be ductile (reference surface lies on corresponding failure surface), a limit of shear strain has to be specified as a failure condition.

During elasto plastic deformation, the yield surface grows in size, by following the hardening rule, and the stress state always remains on the current yield surface. This condition can be satisfied using the following consistency condition.

$$\dot{f}=\frac{\partial f}{\partial p'}dp'+\frac{\partial f}{\partial q}dq+\frac{\partial f}{\partial p'_o}dp'_o+\frac{\partial f}{\partial M}dL=0 \tag{8.10}$$

In equation 8.10, the incremental hardening variables can be obtained using equations 8.5 and 8.6, as shown in equation 8.11 and 8.12.

$$dp'_o=\frac{\partial p'_o}{\partial \varepsilon_p^p}d\varepsilon_p^p+\frac{\partial p'_o}{\partial \varepsilon_q^p}d\varepsilon_q^p=\frac{vp'_o}{(\lambda-\kappa)}d\varepsilon_p^p \tag{8.11}$$

$$dL=\frac{\partial L}{\partial \varepsilon_p^p}d\varepsilon_p^p+\frac{\partial L}{\partial \varepsilon_q^p}d\varepsilon_q^p=n_L(1-\xi)d\varepsilon_q^p \tag{8.12}$$

Therefore, equation 8.10 can be rewritten as

$$\left[\frac{\partial f}{\partial p'_o}\frac{vp'_o}{(\lambda-\kappa)}\right]d\varepsilon_p^p+\left[\frac{\partial f}{\partial M}n_L(1-\xi)\right]d\varepsilon_q^p=-\left(\frac{\partial f}{\partial p'}dp'+\frac{\partial f}{\partial q}dq\right) \tag{8.13}$$

The flow rule can be defined as shown in equation 8.14 and 8.15.

$$d\varepsilon_p^p=d\lambda\frac{\partial g}{\partial p'} \tag{8.14}$$

$$d\varepsilon_q^p=d\lambda\frac{\partial g}{\partial q} \tag{8.15}$$

Using equation 8.13 to 8.15, the loading function $d\lambda$ can be obtained as

$$d\lambda=\frac{-1}{n_L(1-\xi)\frac{\partial f}{\partial M}\frac{\partial g}{\partial q}+\frac{vp'_o}{(\lambda-\kappa)}\frac{\partial f}{\partial p'_o}\frac{\partial g}{\partial p'}}\left(\frac{\partial f}{\partial p'}dp'+\frac{\partial f}{\partial q}dq\right) \tag{8.16}$$

As defined in equation 7.6 (chapter 7), the material hardening H can be written as

$$H=-\left[n_L(1-\xi)\frac{\partial f}{\partial L}\frac{\partial g}{\partial q}+\frac{vp'_o}{(\lambda-\kappa)}\frac{\partial f}{\partial p'_o}\frac{\partial g}{\partial p'}\right] \tag{8.17}$$

The derivatives of plastic potential were defined in equation 8.8 and 8.9. The derivatives of yield function with respect to L and p'_o are as shown in equations 8.18 to 8.19.

$$\frac{\partial f}{\partial L}=-2Lp^2\ln\frac{p'_o}{p'} \tag{8.18}$$

$$\frac{\partial f}{\partial p'_o}=-L^2\frac{p'^2}{p'_o} \tag{8.19}$$

Therefore, the hardening function H can be modified to as shown in equation 8.22.

$$H=2n_Ln_g\left[L\xi p'^2\ln\frac{p'_o}{p'}\right]+\frac{vL^2p'^2}{(\lambda-\kappa)}\left[2\left(\frac{p'}{p'_o}\right)^\gamma-1\right] \tag{8.20}$$

A general form of incremental stress-strain relationship, during elasto-plastic behavior, can be written as shown in equation 8.23.

$$d\varepsilon_{ij} = d\varepsilon_{ij}^{e} + d\varepsilon_{ij}^{p} = \frac{\kappa\left[(1+\nu)d\sigma_{ij} - \nu\delta_{ij}d\sigma_{kk}\right]}{3(1-2\nu)\nu p'} + \frac{1}{H}\left\langle \frac{\partial f}{\partial \sigma_{mn}} d\sigma_{mn} \right\rangle \frac{\partial g}{\partial \sigma_{ij}} \qquad (8.21)$$

Determination of Parameters for Kaolin Clay

All the defined parameters in the proposed model can be determined from an isotropic consolidation test, and a triaxial compression test on normally consolidated clay. In the experimental part of this study, data from a series of true triaxial undrained compression tests and constant rate of strain K_o consolidation tests on Kaolin clay was presented in chapter 5. This data is used to determine the model parameters for Kaolin clay. Therefore, chapter 5 is referred to quite frequently in this section.

The basic concept behind the development of the failure surface and its parameters was discussed in chapter 5. Using failure data from the undrained tests performed at various OCR values, parameter Λ_o for Kaolin clay was determined to be Λ_o= 0.9. From CRS test data, an average value of λ was determined to be λ=0.16 assuming that the slope of virgin consolidation line during isotropic consolidation is approximately same as that during K_o consolidation (Wood 1990). Based on Mayne and Swanson's (1981) findings, it was discussed that the swelling index C_S can be determined using the known values of Λ_o and compression index C_C (equation 5.2). Parameters λ and κ provide another form of C_C and C_S using natural log of mean effective stress; therefore the relationship between Λ_o, λ, and κ can be written as

$$\Lambda_o = 1 - \kappa/\lambda \qquad (8.22)$$

Using equation 8.22, the value of κ for kaolin clay defined as κ=0.016. Equation 8.22 can also be used to determination of Λ_o, if data from another triaxial test on overconsolidated clay is not available. In such a case, κ is determined from consolidation test data using e-ln p' relationship observed during unloading. Poisson's ratio for kaolin clay is assumed to be ν = 0.28 as was used in chapter 7 for MCC and single hardening model predictions.

Henceforth, the data obtained from true triaxial compression tests on normally consolidated (p'_o= 275kPa) kaolin clay, shown in Fig. 5.3 to Fig. 5.5 of chapter 5, is referred to as NC data. Failure surface parameter C_f is determined using equation 8.23, which was derived in chapter 5 (equation 5.8) for triaxial compression test on NC clay.

$$q_{fNC} = C_f p'_o \tag{8.23}$$

In equation 8.23, p'_o is the initial pre-consolidation pressure and q_{fNC} is the shear strength in terms of deviatoric stress. From NC data in Fig. 5.3, C_f is determined to be C_f= 0.63. As shown in Fig. 5.3, the stress strain relationship from NC data can be used to determine the shear stress level at the reference surface, which is used to determine C_y= 0.66 by extending equation 8.23 for the reference surface. Use of the method described in chapter 5 for determination of shear stress level at reference surface gives just an approximate value of C_y. However, it will be demonstrated that the soil's behavior can still be predicted within reasonable accuracy.

Hardening rule in equation 8.6 can be rewritten in incremental for as shown in equation 8.24.

$$\frac{\Delta L}{n_L} = (1-\xi)\Delta\varepsilon_q^p \tag{8.24}$$

For NC data, Fig. 8.5 shows a relationship between L and cumulative sum $\Delta L/n_L$, in which L is calculated using yield function (equation 8.2) and $\Delta L/n_L$ is calculated using hardening rule (equation 8.24). During this calculation, incremental p_o' and ξ were calculated using equations 8.5, 8.4 and 8.7. Components of Plastic strains were calculated using equations 8.25 and 8.26.

Under undrained conditions: $\Delta\varepsilon_p^p = -\Delta\varepsilon_p^e$ (8.25)

$$\Delta\varepsilon_q^p = \Delta\varepsilon_q - \Delta\varepsilon_q^e \tag{8.26}$$

Elastic strain components $\Delta\varepsilon_p^e$ and $\Delta\varepsilon_q^e$ were calculated using equation 8.1. The linear relationship shown in Fig. 8.5 provides initial value of L (L_o=0.75), and hardening parameter n_L (= 22). The L_o, together with initial p_o', defines the size of initial yield surface.

At the reference surface, the relative magnitude of the plastic volumetric strain increment vector goes to zero; therefore, $\partial g/\partial p'$=0 (equation 8.8) at reference surface. Applying this condition on NC data, plastic potential parameter γ is determined to be γ=0.92. Flow rule (equation 8.14 and 8.15) defines a relationship between shear and volumetric components of plastic strains as shown in equation 8.27.

$$\frac{d\varepsilon_q^p}{d\varepsilon_p^p} = \frac{\partial g}{\partial q} \Big/ \frac{\partial g}{\partial p'} \tag{8.27}$$

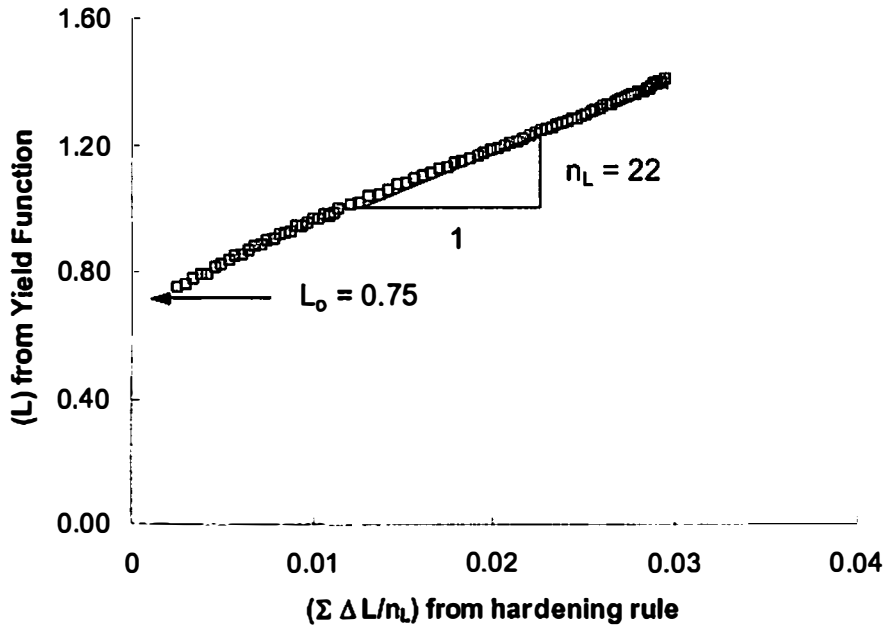

Figure 8.5 Determination of Hardening Parameter n_L, and Initial L Value (L_o)

Using equations 8.8 and 8.9, the above defined relationship can be manipulated to show equation 8.28.

$$\sum\left[R_g \Delta\varepsilon_q^p\right] = n_g \sum \Delta\varepsilon_p^p \tag{8.28}$$

where, R_g is defined as

$$R_g = \frac{(1-\xi)\left\{2\left(p'/p_o'\right)^{\gamma} - 1\right\}}{\xi} \tag{8.29}$$

Figure 8.6 shows that the cumulative sums of $R_g \Delta\varepsilon_q^p$ and $\Delta\varepsilon_p^p$ increments have a linear relationship, which gives plastic potential parameter n_g=3.5.

A summary of all the model parameters determined for kaolin clay is provided in Table 8.1. It is to be noted that L_o and p_o' are state variables. L_o remains constant when

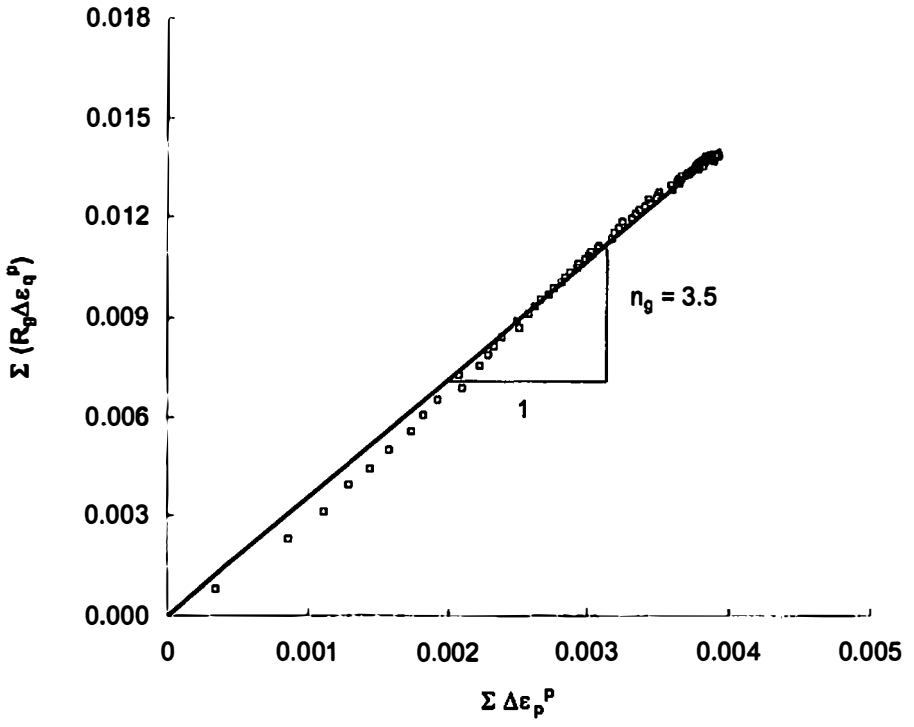

Figure 8.6 Determination of Plastic Potential Parameter n_g

Table : 8.1 Model Parameters for Kaolin Clay

Proposed Model Parameters		**Value**
Elastic Behavior	κ	0.016
	ν	0.28
Failure Surface	C_f	0.63
	Λ_o	0.9
Reference Surface	C_y	0.66
Hardening Parameter	λ	0.16
	n_L	22
Plastic potential	γ	0.92
	n_g	3.5

- $\kappa = 0.016$, is determined from Λ_o and λ using equation 8.22.
- L_o and p'_o have to be determined from state of soil.

the stress state moves along the hydrostatic axis; it changes on application of shear loading if the deformation is elasto-plastic, and follows the hardening rule given in equation 8.6. p_o' follows the hardening rule given in equation 8.5, and it can change with any elasto-plastic loading. In order to get better predictions for natural soils, it is advisable to program calibration tests on the specimens with pre-consolidation history close to the natural state.

Model Prediction for Kaolin Clay

A computer program is developed to get the model predictions for undrained shear tests. In this program, elastic and plastic strain increments (using equations 8.20 and 8.21) are computed for a given effective stress increment. An effective stress increment vector of small magnitude is rotated along a constant b-value plane to satisfy the undrained condition within specified limits; i.e. the cumulative total volumetric strain (sum of total elastic and plastic strain values) never exceeds the range of $\pm 0.0001\%$. Excess pore pressure generated is computed as the difference between mean total stress and mean effective stress at given stress state. The program predicts undrained shear behavior of a single element (of clay material), which has its initial stress state at hydrostatic stress axis, and it requires three state variables e (void ratio), L_o and p_o' to be specified corresponding to that stress state.

- Undrained shear behavior of Kaolin clay has been predicted using the parameters listed in Table 8.1, and by defining the initial values of state variables as $L_o = 0.75$, and $p_o' = 275$kPa. In Fig. 8.7 and 8.8, the model predictions are compared with the corresponding experimental data obtained from a series of true triaxial undrained

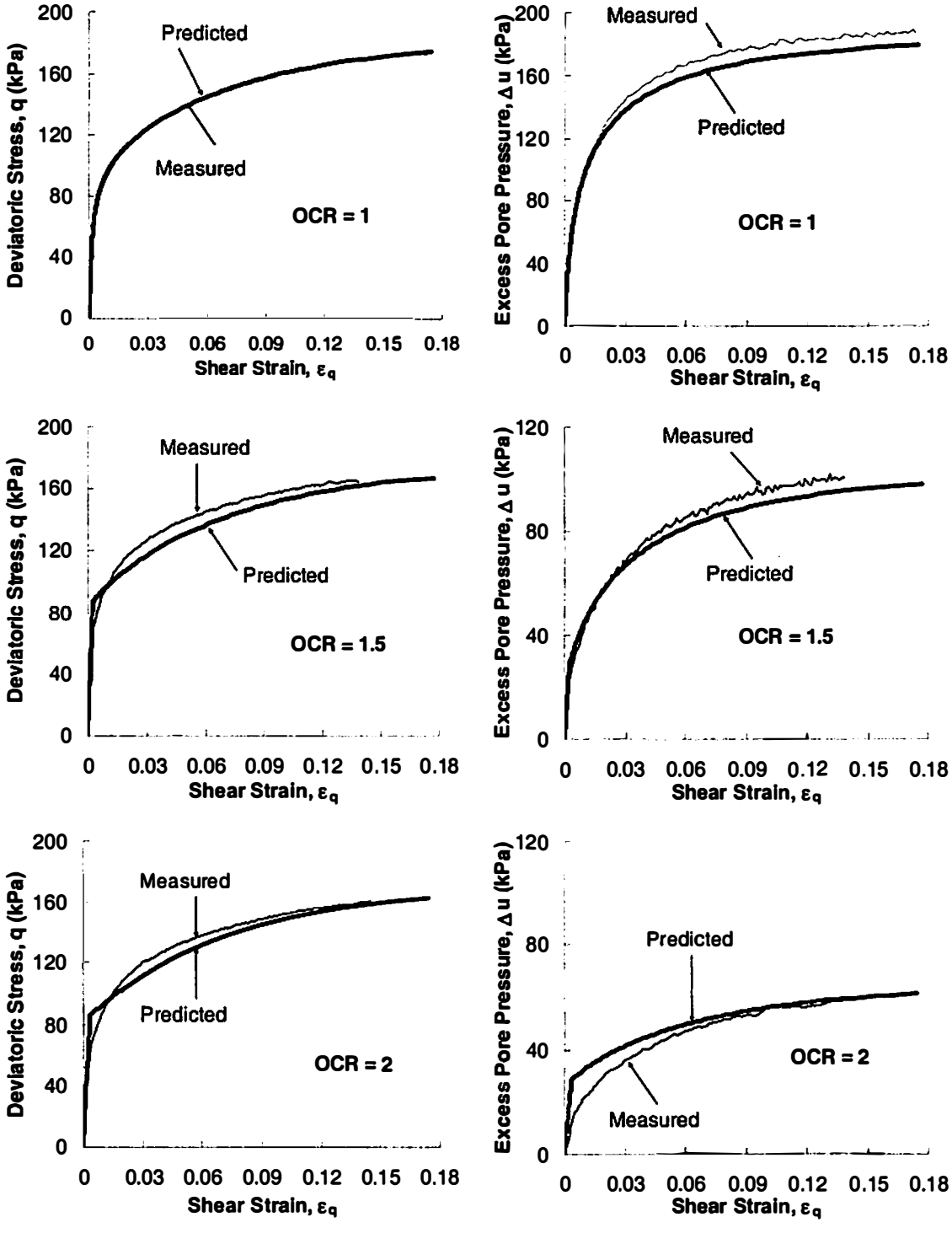

Figure 8.7 Proposed Model Predictions and Experimental Data from True Triaxial Undrained Compression Tests (b=0) on OC Kaolin Clay

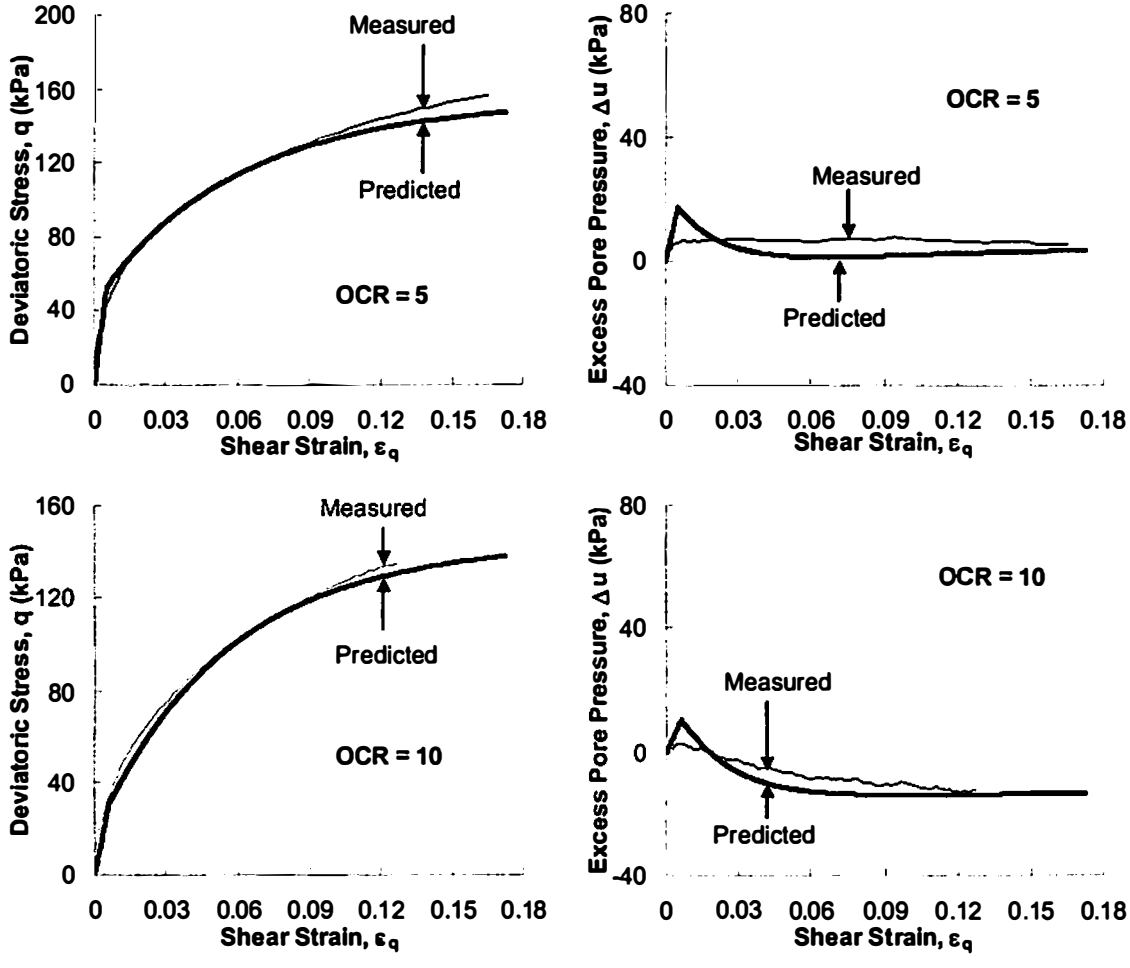

Figure 8.7 Continued

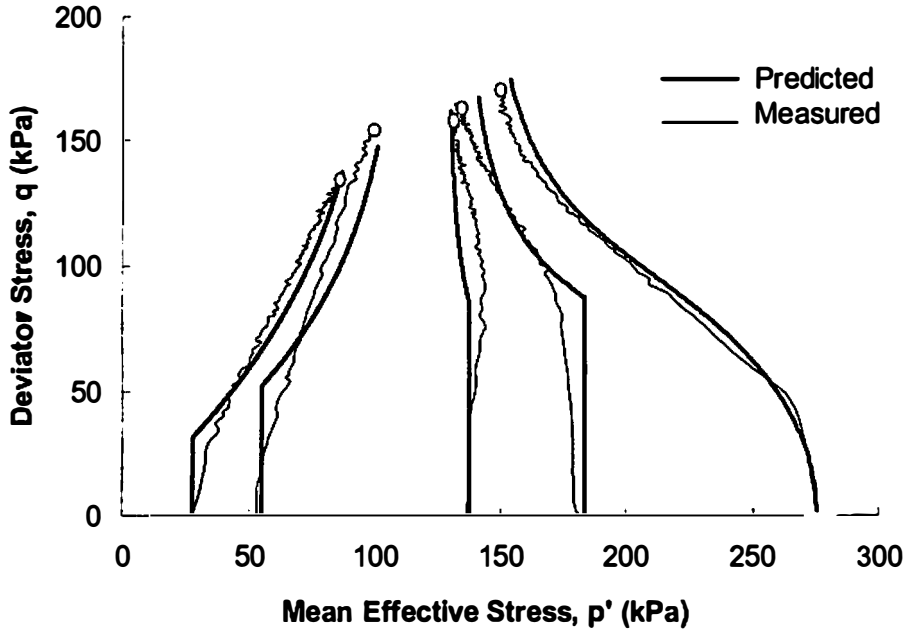

Figure 8.8 Stress Paths in q-p' Plane: Proposed Model Predictions and Experimental Data from True Triaxial Undrained Compression Tests (b=0) on Kaolin Clay

compression tests (b=0) performed at various OCR values (OCR = 1, 1.5, 2, 5, 10). A detailed analysis of the experimental data was presented in chapter 5 (Fig. 5.3 to Fig. 5.5). Shear stress-strain relationship and excess pore pressure behavior are shown in Fig. 8.7, and the stress paths are presented in Fig. 8.8. Following observations can be made based on the comparison between experimental data and model predictions.

- At each OCR value, predicted stress-strain relationship, shear strengths, and pore pressure response show a close agreement with their experimentally observed values.
- Predicted strain values corresponding to failure conditions are identical for all OCR, which has been commonly observed for most clays.
- Like most other elasto-plasticity model, the proposed model shows a kink in stress-strain relationship (for OCR > 1) when the stress state hits the initial yield surface.

The effective stress paths show a sudden change in their slope at the same stress level, as can be observed in Fig. 8.8. Sometimes, transitional plasticity concepts (smooth evolution of plasticity) are used to eliminate this response; however, this can complicate the formulation significantly. Considering a balance between simplicity of formulation and accuracy of results, it is found unnecessary to further modify the proposed model.

- Similar to experimental observations, the predicted effective stress path for OCR=2 shows compressive nature of clay in elasto-plastic region (due to parameter $\gamma < 1$).

Extension of the Proposed Model in Deviatoric Plane

In the proposed elasto-plasticity model for hydrostatically consolidated clays, it is assumed that the elastic behavior of soil is isotropic. Plastic shear stiffness (yielding) of the material is controlled by its reference surface, which is independent of material's failure surface. Since, the proposed model assumes non-associative flow rule; the yield surface and its evolution during elasto-plastic deformation are independent of the failure surface; therefore, the failure surface can be modified freely in the deviatoric plane to improve the general response for stress anisotropy. However, it is preferred in elasto-plasticity theory that the failure surface is continuous and convex in stress space. The reference surface merely defines the size of the yield surface and plastic potential surface (in shear direction); however, the functions used for the yield surface and plastic potential surface have their independent shape properties in stress space. Yield and plastic potential functions are continuous and convex in working stress space; the yield function has a discontinuity only at zero stress state.

Influence of Intermediate Principal Stress

In chapter 3, it was shown that the anisotropy of applied stresses could be defined using two variables; intermediate principal stress ratio, b-value, and angle of major principal direction from axis of cross-anisotropy, δ-angle. Based on the experimental data presented in chapter 3 to chapter 6, it can be concluded that the failure condition is simply a function of applied anisotropic stress state, and it can be assumed to be independent of the direction of applied loading. Based on this observation, a failure surface was formulated in chapter 5 (equation 5.13 and 5.14), which assumes a similar shape in deviatoric plane as was proposed by Lade (1990). Using equation 5.13 and 5.14, the stable state of material (stress state before failure condition) in three-dimensional stress space can be defined using equation 8.30.

$$\frac{I_3}{p'^3} > \left\langle \frac{2}{27}\left(\frac{q_f}{p'}\right)^3 - \frac{1}{3}\left(\frac{q_f}{p'}\right)^2 + 1 \right\rangle \tag{8.30}$$

where $\langle\ \rangle$ are Macaulay brackets. They constrain the failure surface to exist only in positive quadrant of 3D stress space, by which it is considered that the frictional material will fail if one of the acting principal stresses goes to zero. This condition is based on a widely accepted assumption of no cohesion in frictional materials as was considered in Lade's (1990) model. Figure 8.9 shows the constrained failure surface in triaxial compression plane.

It was shown in chapter 5 that the yield behavior (in terms of shear stiffness) of clay was not significantly influenced by the change in relative magnitude of principal stresses when the tests were performed at constant orientation of principal stresses

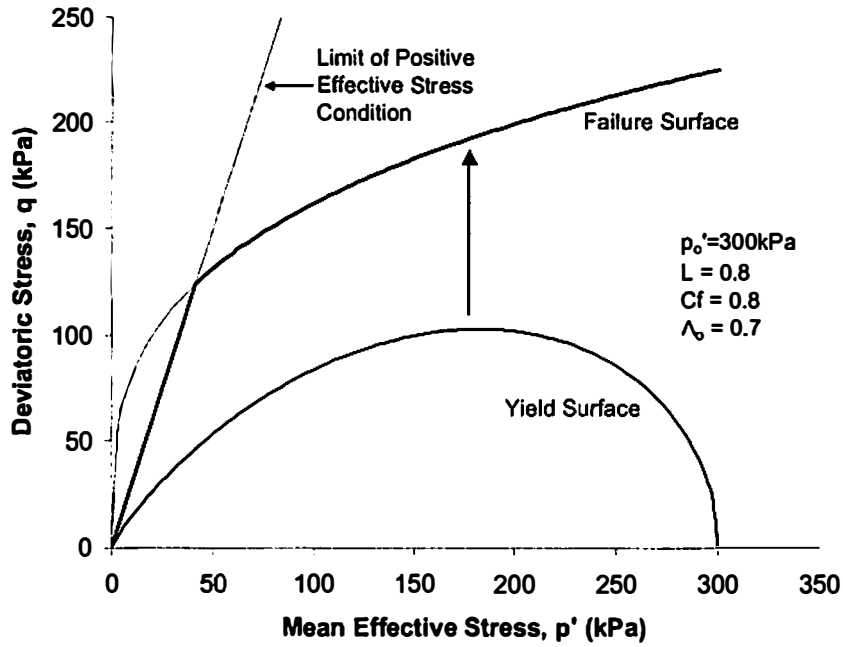

Figure 8.9 Constraining Failure surface to Positive Effective Stress Quadrant of Three-Dimensional Stress Space, (Triaxial Compression Plane)

(δ-angle). Heavily overconsolidated clay shows a small variation from above mentioned condition; however, considering a balance between simplicity of formulation and accuracy of results, it was found unnecessary to consider such type of behavior. As shown in previous chapters, the plastic strain increment vectors at failure condition suggest a circular shape of the plastic potential in deviatoric plane. Considering the simplicity involved in assumption of circular plastic potential surface (no change from what was defined for triaxial compression plane), it would be reasonable to assume that the shape of plastic potential in deviatoric plane is constant throughout shearing. Based on these observations, the reference surface and plastic potential are assumed to be symmetric about hydrostatic stress axis. Equation 8.3 for the reference surface and equations 8.8 and 8.9 for the plastic potential will be used for model predictions.

Model Predictions for Constant b-value True Triaxial Tests ($\delta = 0°$)

A comparison between the model predictions (for b=0.25, 0.5, 0.75 and 1.0) and the corresponding experimental data is shown in Fig. 8.10 for OCR=1, Fig. 8.11 for OCR=5, and Fig. 8.12 for OCR=10. Predicted stress-strain relationship, and pore pressure response for OCR=1 and OCR=5 shows a good agreement with the measured values, which confirms that the assumption of constant reference surface for different b-values is valid. The shear strength of clay at different b-values is also predicted reasonably in most cases. As discussed in chapter 5, the experimental data for OCR=10 shows a strong influence of inherent anisotropy, because of which the model over predicts the stress-strain relationship for b > 0. However, the pore pressure values are predicted with reasonable accuracy.

Influence of Principal Stress Rotation

It has been observed that the yield behavior (elasto-plastic stiffness) of soil changes significantly with the change in orientation of principal stresses, which is usually defined by the angle of major principal direction from axis of soil's cross-anisotropy, δ-angle. Under undrained condition, volumetric response of soil is measured through evolution of pore pressure, which is also influenced by the rotation of principal stresses. In the proposed model, yield behavior is essentially controlled by its reference surface, which is defined by using two parameters C_y and Λ_o. The volumetric response of soil is controlled by the hardening parameter γ. The size of reference surface (C_y) may change with the rotation of principal stress; however, its variation along p' axis (Λ_o) can be assumed constant. Since, the state variable L has a strong relationship with reference

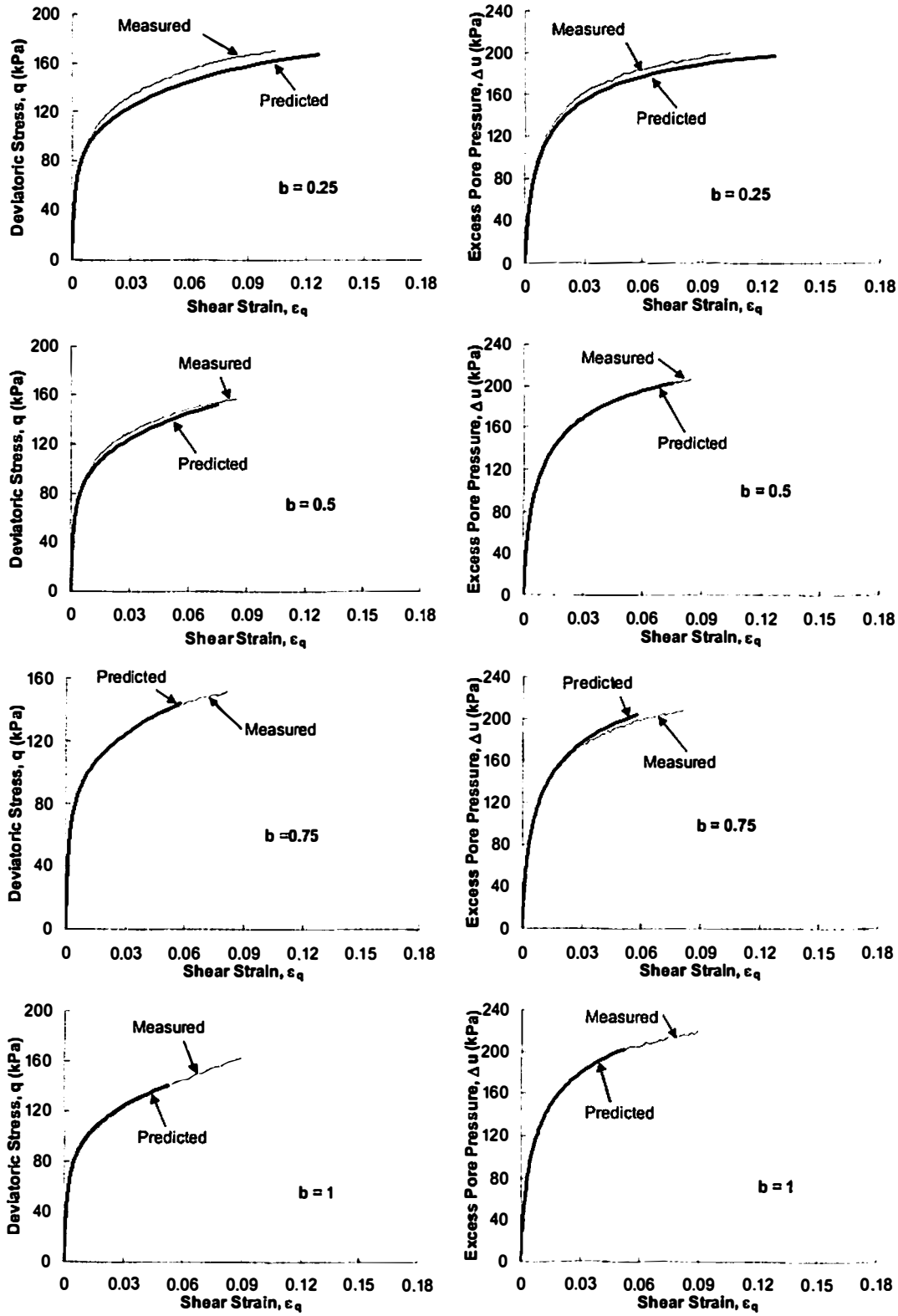

Figure 8.10 Proposed Model Predictions and Experimental Data from True Triaxial Undrained Tests on NC Kaolin Clay

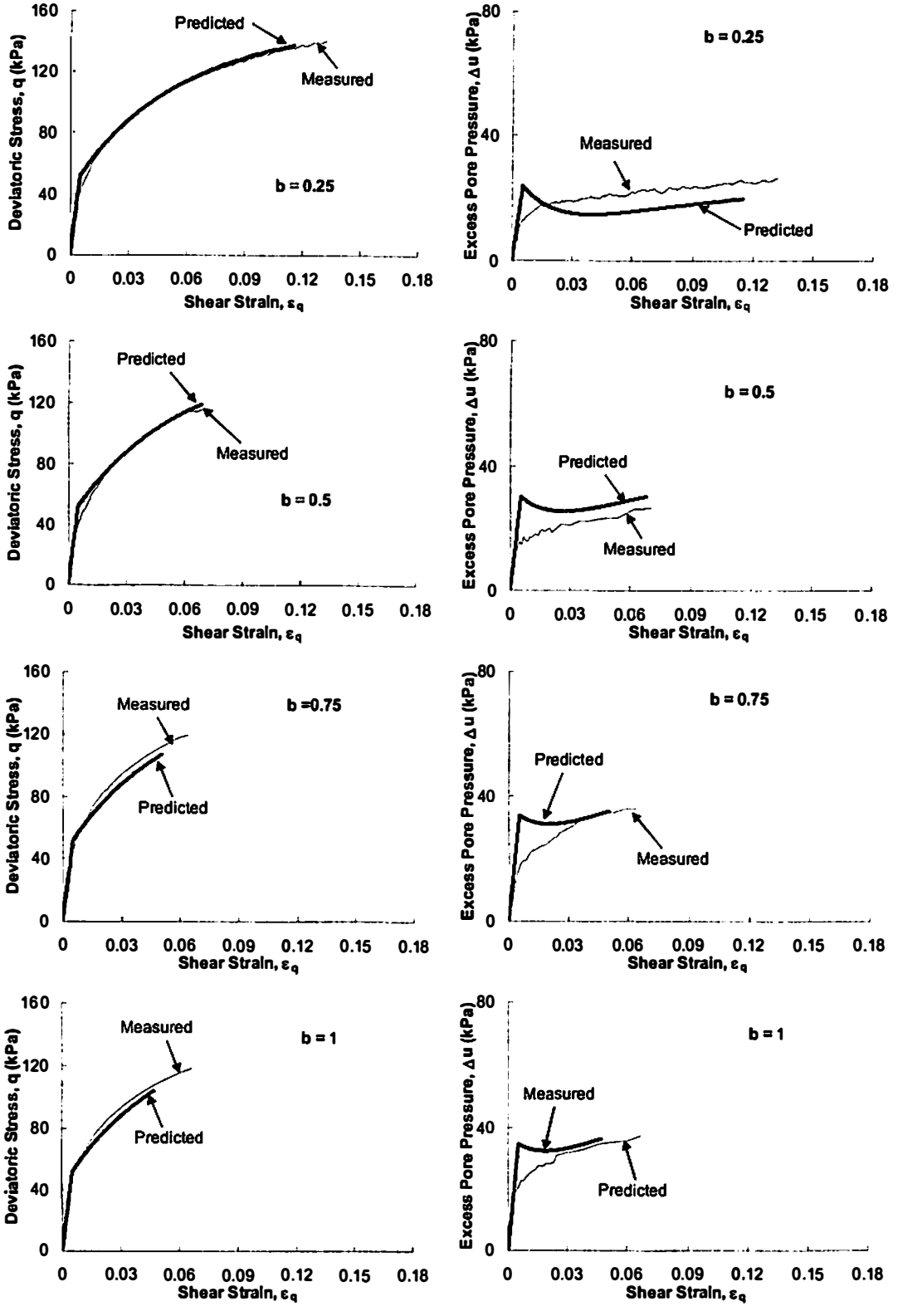

Figure 8.11 Proposed Model Predictions and Experimental Data from True Triaxial Undrained Tests on OC Kaolin Clay (OCR = 5)

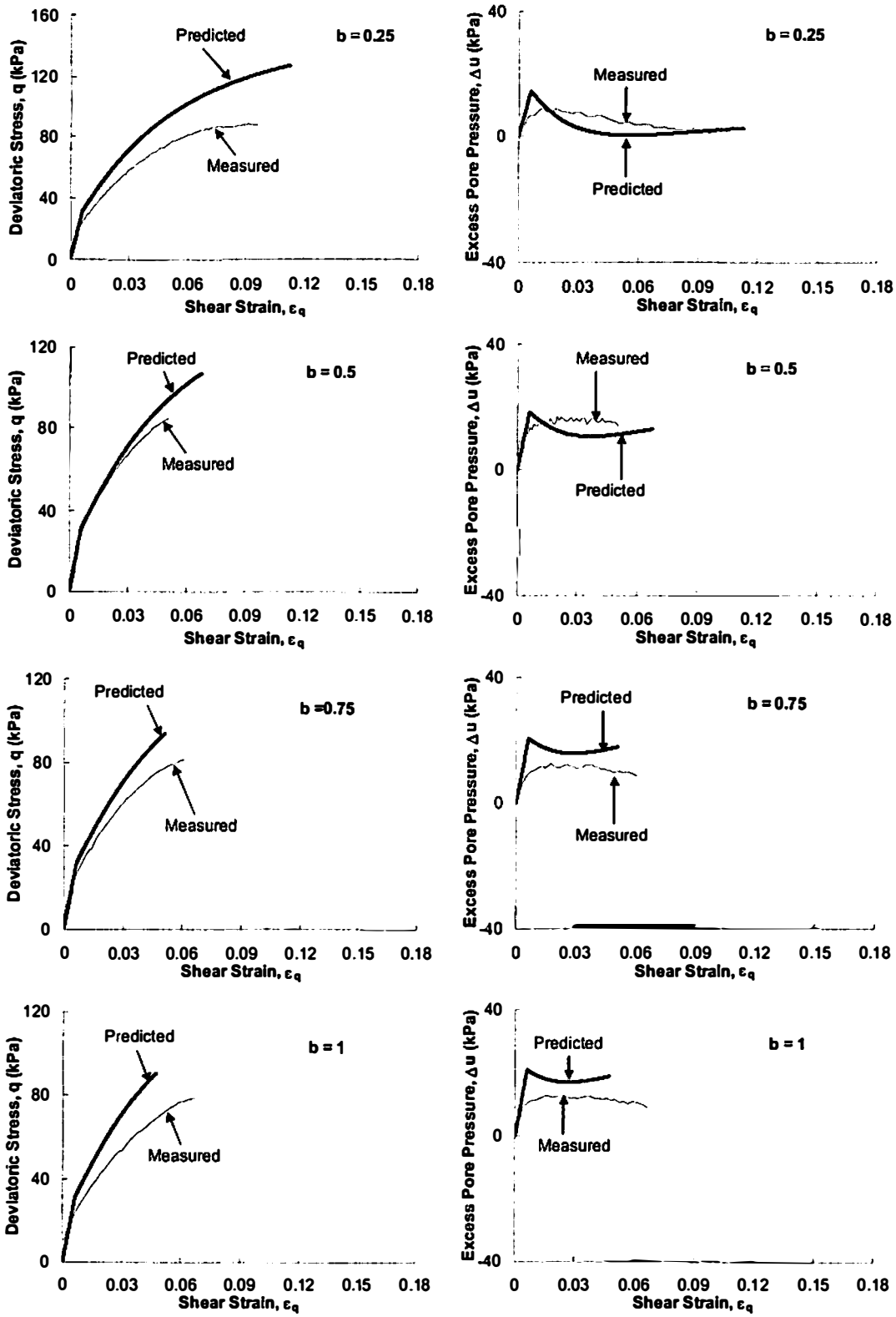

Figure 8.12 Proposed Model Predictions and Experimental Data from True Triaxial Undrained Tests on OC Kaolin Clay (OCR = 10)

surface, and the size of reference surface is controlled by parameter C_y, the initial value of L can be defined in relation with C_y as shown in equation 8.31.

$$L_o = l_o C_y \tag{8.31}$$

where l_o is an anisotropic state variable. As discussed in previous section, the failure surface has a strong relationship with three-dimensional stress state; however, it is assumed to be independent of δ-angle. In order to predict the influence of principal stress rotation using proposed model, it is essential to determine a continuous relationship between the angle of rotation and the two affected parameters, C_y and γ. However, the true triaxial testing on cubical specimens can only be used for two extreme cases of principal stress rotation, δ=0° and δ=90°.

Model Predictions for extension tests (δ = 90°)

Using the parameters listed in Table 1, the anisotropic state variable l_o (equation 8.31) is determined to be l_o=1.136. Using NC data shown in Fig. 3.4 (chapter 3), the values of two parameters C_y and γ for extension tests are determined to be C_y= 0.52, and γ=0.75. Undrained shear behavior of true triaxial extension test on NC clay has been predicted by using the above parameters, and its comparison with the corresponding experimental data (Fig. 3.4 in chapter 3) is shown in Fig. 8.13. Predicted stress-strain relationship, and pore pressure response shows a good agreement with the measured values. The shear strength and the strain value at failure condition are also predicted reasonably using the proposed model. These observations show the strength of the proposed model to predict the anisotropic behavior of clays. The proposed model can be

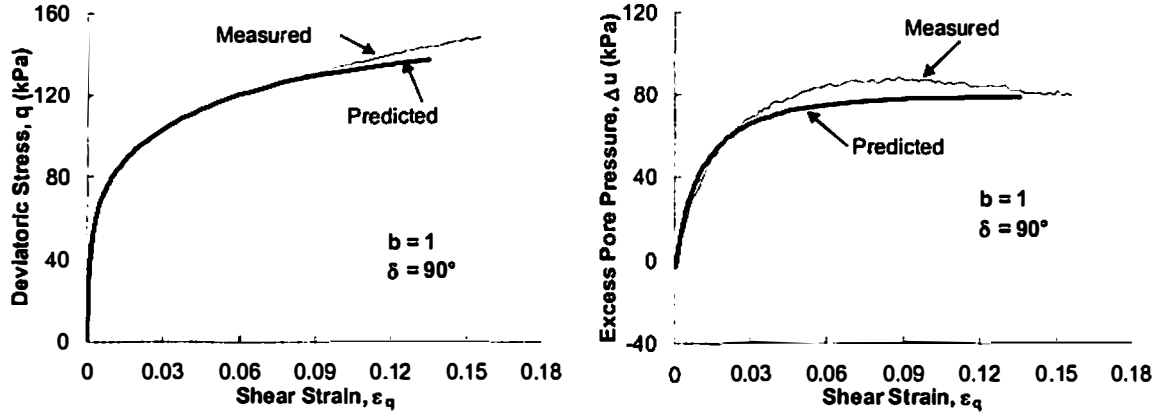

Figure 8.13 Proposed Model Predictions and Experimental Data from True Triaxial Undrained Tests on NC Kaolin clay (b=1, δ=90°)

easily modified to predict the behavior for intermediate angles of principal stress rotation; however, it will require a normalized relationship between the angle of rotation (δ-angle) and the two model parameters, C_y and γ.

Conclusions

The Elasto-plasticity theory provides a reasonable mathematical description of the stress strain behavior when appropriate governing functions or surfaces are employed. It has been shown in various studies that different materials can be described only by using different governing functions. Therefore, a usual approach in the development of a constitutive model for a particular material involves three necessary steps consecutively; to perform an experimental study, relate the observed normalized behavior to the concepts of basic mechanics, and develop the model's formulation after taking certain assumptions for simplicity.

A new constitutive model was proposed in this research that can predict the behavior of normally consolidated to overconsolidated clays. Basic formulation of the model was expressed in the stress space using two stress invariants; mean effective stress p', and deviatoric stress q. The proposed rate independent model for hydrostatically consolidated clays was formulated to follow a non-associative flow rule. The shape of yield surface was defined on the basis of an acceptable range of elastic deformation that was determined from the experimental observations. The failure condition was derived from the widely recognized normalized undrained shear strength behavior of various overconsolidated clays. Elasticity was assumed to be isotropic. The plastic behavior was defined to be controlled by a reference surface, which was different from the failure surface. An additional parameter was introduced in the model to consider that the volumetric response of various clays under shear loading could be significantly different; and even for the same clay, if it is anisotropic, various configurations of applied shear loading could produce significantly different volumetric response.

The basic concept of proposed model was formulated in the triaxial compression plane. It was then extended to the deviatoric plane on the basis of experimentally observed normalized behavior of kaolin clay. The model parameters were either directly measured in standard types of laboratory tests, or were obtained from well-defined parametric studies. Through the use of these parameters, the model was validated by comparing the predicted and measured stress strain relationship and pore pressure behavior.

Chapter 9. Conclusions and Recommendations

This chapter summarizes the accomplishments from this study along with conclusions and recommendations for the future research.

Summary and Conclusions

The current research included experimental and theoretical evaluation of the three-dimensional mechanical behavior of cohesive soils. The main objective of this study was to investigate the following; the effect of inherent and stress induced anisotropy on the three-dimensional mechanical response of clay, the influence of clay's microfabric on its consolidation and shear behavior, and the role of loading history in the observed shear stiffness and strength of an anisotropic clay. In order to achieve this goal, a series of strain controlled true triaxial undrained tests were performed on remolded cubical specimens of Kaolin clay. A comprehensive analysis of the experimental data obtained was presented, and the observed normalized behavior was used to formulate a theoretical framework. In order to compare the results obtained from various anisotropic loading conditions, the stress and strain terms were calculated in three-dimensional invariant form.

The three-dimensional undrained shear tests were performed using a flexible boundary electro-pneumatic true triaxial system with independent control of the three principal stresses. External loading on the specimen was applied using flexible membranes in order to minimize the interference of loading boundaries. A Proportional–Integral–Differential (PID) based real-time feedback control system was employed to achieve the desired test conditions. The PID algorithm was able to show a precise and

repeatable control over the test conditions if the PID coefficients were chosen carefully with appropriate consideration to the effect of specimen stiffness. The PID coefficients suitable for testing were found to be a function of shear stress level and the overconsolidation ratio (OCR) because the specimen stiffness was observed to be varying significantly with the increase in shear stress level or the OCR value. A procedure was developed to obtain reproducible specimens of Kaolin clay with controlled microfabric. The uniform and homogeneous specimens with two distinct microfabrics, flocculated and dispersed, were obtained by consolidating the Kaolin clay slurry under K_o condition (at 207 kPa axial stress), as a result they had a certain degree of cross-anisotropy. The preferred orientation of particles forming the dispersed microfabric added to this anisotropy in the dispersed specimens, which was termed as fabric induced anisotropy.

Identification of strain localization onset is an important aspect in defining the point of shear failure precisely, because, beyond this point, the test data without exact information about specimen deformation is not reliable. A method for the determination of the onset of localization was proposed in this study based on true triaxial test data. During all the undrained shear tests performed in this study, specimens were observed to have localized deformation close to the peak deviatoric stress location, which was therefore considered as the failure location.

The stress-strain behavior observed from the three types of laboratory tests: combined axial-torsional tests on hollow cylinder, lubricated end triaxial tests on full cylinder, and true triaxial tests on cubical specimens, was significantly different. The specimen shapes and the influence of different boundary conditions played a significant

role in this observation. It was determined that various aspects of the soil behavior should be analyzed using the data obtained from a single testing method.

The experimental data obtained from the constant b-value tests performed on flocculated specimens indicated that the relative magnitude of principle stresses (b-value) had no significant influence on the generalized shear stress-strain ($q - \varepsilon_q$) relationship. However, the increased influence of inherent anisotropy at higher OCR values showed a small variation in the stress strain relationship with the change in b-value. The fabric-induced anisotropy in dispersed specimens showed a significant influence on the stress strain relationship even for the normally consolidated case. The specimen strength and the strain at failure were observed to be decreasing with an increase in b-value. For all the test conditions and varying microfabric, the strength data (stress at failure) could be normalized in deviatoric plane using a failure surface based on third invariant of stress tensor. The plastic strain increment vectors in deviatoric plane, close to failure, could be described using a circular plastic potential surface. The shear strength of clay was observed to be independent of the principal stress rotation (δ-angle); whereas, the shear stress-strain relationship showed notable change with a change in δ-angle.

In comparison with the flocculated specimens, the dispersed specimens showed higher plastic but lower elastic deformation during hydrostatic consolidation. The fabric-induced anisotropy showed its major influence on how the specimens deformed (anisotropically) during hydrostatic consolidation, and it affected the evolution of pore pressure significantly when the dispersed specimens were subjected to different stress paths. The dispersed specimens exhibited much stiffer response in the stress-strain

relationship, achieved higher strength, failed at lower strain values, and showed much lower pore pressure evolution in comparison with flocculated specimens.

A brief review of the two well-recognized constitutive theories developed for isotropically consolidated soils, the Modified cam clay (MCC) model and the Single hardening model, was presented. Both the models did not predict well the mechanical behavior of kaolin clay observed in the current study. A new constitutive framework was developed in this study to predict the observed true triaxial mechanical response of cohesive soils. A teardrop shape for the initial yield surface in triaxial compression plane (b=0) was proposed on the basis of a reasonable range of elastic deformation estimated from the experimental data. Using the concept of normalized undrained strength behavior of overconsolidated clays proposed by Ladd and Foott (1974), a dynamic failure surface was derived as a function of stress state and the pre-consolidation history. The failure surface was then extended in the deviatoric plane by introducing the third invariant of stress tensor in its formulation. To capture the brittle response of clay that was observed due to localized deformations, a reference surface was proposed to control the plastic deformation during shearing, which was different from the failure surface. For simplicity, the influence of b-value on the reference surface was neglected in the deviatoric plane. The new model was able to predict the true triaxial response of Kaolin clay with reasonable accuracy.

Recommendations for Future Research

- In this research, all the testing was performed using remolded specimens of identical clay in an effort to study the influence of anisotropy, loading history and the change

in microfabric on its mechanical response. However, it is necessary to perform similar studies on other cohesive soils to confirm the findings of this research for natural soils.

- The isotropic pre-consolidation pressure before shearing was constant for all the true triaxial tests performed on normally consolidated to overconsolidated clay specimens. Most often, the soil behavior is linearly normalized for various pre-consolidation stress levels; however, it is experimentally proven that the assumption of linearity may not valid for big increments in pre-consolidation stress. Another issue is the type of loading applied during consolidation. In this study, the specimens were isotropically consolidated before shearing; however, the soil behavior may be significantly different if the specimens were consolidated anisotropically (under K_o condition or at a constant shear stress ratio). The consolidation process may significantly change the anisotropy of soil.
- In this study, the specimens were sheared under undrained condition; however, both undrained and drained conditions may exist in various field problems. The influence of anisotropy under three-dimensional loading may be significantly affected by the drainage conditions. It would be interesting to perform a series of tests under drained conditions and correlate the results with the observations from undrained testing.
- The true triaxial device used for testing is capable of measuring pore pressure outside as well as inside the specimen. To check the saturation level, the specimen was isotropically loaded by an increment of 5kPa under undrained condition, and the pore pressure values were recorded with time. The external and internal pore pressure measurements showed difference in the time taken to reach equilibrium, which could

be expected for fine-grained soils due to its low permeability. Study of its cause and effect may offer a better understanding of the undrained shear behavior dependency on strain rate, specimen shape and size, and drainage path. It would be interesting to see similar arrangements for internal pore pressure measurements in other testing methods as the pore pressure equilibrium and its dissipation rate can significantly effect the observed consolidation and shear behavior of clays.

- Using a true triaxial device, the principal stresses applied on the specimen can rotate by 90° only. In order to study the influence of principal stress rotation, a cubical specimen can be formed by trimming off a larger specimen in such a way that its faces have an angle with the direction of deposition.
- The specimen shapes and boundary conditions used in a testing method may significantly influence the observed mechanical response of soil. In most cases, the specimen is assumed to be a single element for analysis of data, which may not be enough to interpret the soil behavior accurately. Simulation of these tests, using various numerical methods (e.g. finite element or finite difference method) with correct understanding of the test boundary conditions, may provide a better insight.
- Although, the non-uniformity of deformation associated with the use of flexible boundary condition was small enough and therefore neglected in this study, it should be further investigated to improve the test conditions.
- In order to study the non-uniformity and localized deformations within the specimens during true triaxial testing, a method should be developed so that the deformation profile can be scanned accurately in three-dimensional space.

- In the current study, the shape of failure surface in deviatoric plane was reasonably described using the third invariant of stress tensor, which was independent of the principal stress rotation with the axis of cross anisotropy. The specimens were observed to have developed localized deformations or shear bands (in most cases) at failure location. McKyes and Yong (1971) reported that the clay particles in the proximity of observed shear bands at failure aligned themselves along the failure plane. If we can assume this to be true for other cohesive materials as well, then based on the observations from current study, the failure condition at the macro level may be derived using a correlation between the interparticle forces at micro level and the void ratio of the soil at macro level. However, at present, the mechanical behavior of clay at micro level, i.e. the mechanics of clay particles and the interparticle interactions is largely unknown. For this matter, a comprehensive study could be performed using the latest facilities available at present that are being used for crystalline theory and nanotechnology. This study would also be able to answer the questions related to the onset and propagation of localized deformations in soils.
- The results obtained for heavily overconsolidated Kaolin clay showed that the influence of anisotropy in the stress-strain relationship could change significantly with the confining pressure acting on the specimen. The anisotropy of soil was found to be largely associated with the recoverable deformations. Based on this observation, the proposed model can be modified to incorporate anisotropic elasticity of clay; however, this will introduce more parameters and require more tests to determine them.

- The reference surface proposed in the model can be defined as a function of both b-value and δ-angle, which will capture the whole array of possibilities in the applied anisotropic loading. However, a more comprehensive data set is needed to establish a relationship for the normalized stress-strain response of clays in deviatoric plane. The δ-angle is commonly used to represent principal stress rotation, which is defined as the angle of σ_1-direction with the axis of cross-anisotropy. For the b=1 case, the σ_1 ($=\sigma_2$) acts along two orthogonal directions, which creates confusion in defining a single δ-angle. A new way should be established to define the rotation of principal stress, which will better represent experimental conditions and observations.
- The proposed model in the current study was mostly based on the mechanical response of flocculated microfabric specimens. The influence of fabric induced anisotropy and the effect of fabric in volumetric response of clay was not included in the proposed model. The model could be modified to predict the response of dispersed microfabric specimens; however, it will make more sense if the fabric of clay is introduced in the form of a model parameter, which will require a continuous relationship between the microfabric and the mechanical properties of clay. However, it is difficult to obtain specimen with known intermediate microfabric, because a method of quantifying intermediate microfabrics (maybe as a degree of dispersion) itself has not been established yet.

List of References

List of References

Arthur, J. R. F. (1988). "Cubical devices: versatility and constraints." *Advanced Triaxial Testing of Soil and Rock, ASTM STP 977*, Robart T. Donaghe, Ronald C. Chaney, Marshall L. Silver, Eds., American Society for Testing and Materials, Philadelphia, pp. 743-765

Barden, L. and Sides, G. (1971). "Sample disturbance in investigation of clay structure." *Geotechnique*, Vol. 21, No. 3, pp. 211-222.

Berre, T. (1982). "Triaxial testing at the Norwegian geotechnical institute." *Geotechnical Testing Journal*, Vol. 5, No. 1, pp. 3-17.

Bishop, A. W. and Henkel, D. J. (1960). "The shear strength of saturated remolded clays." *Proceedings of ASCE Research Conference on Shear Strength of Cohesive Soils*, Boulder, Colorado, pp. 533-554.

Broms, B. B. and Casbarian, A. O. (1965). "Effects of rotation of principal stress axes and of the intermediate principal stress on the shear strength." *Proceedings of the sixth international conference on soil mechanics and foundation engineering*, Montreal, Vol. 1, pp. 179-183.

Burland, J. B. (1990). "On the compressibility and shear strength of natural clays." *Geotechnique*, Vol. 40, No. 3, pp. 329-378.

Callisto, L. and Calabresi, G. (1998). "Mechanical Behaviour of a Natural Soft Clay." *Geotechnique,* Vol. 48, No. 4, pp. 495-513.

Carty, W. M. (1999). "The Colloidal Nature of Kaolinite." *American Ceramic Society Bulletin*, 77 (8), 72-76.

Casagrande, A. (1932). "The structure of clay and its importance in foundation engineering." *Contributions of Soil Mechanics*, 1925-1940, Boston Society of Civil Engineers, pp 72-112.

Dafalias, Y. F. (1986). "Bounding Surface Plasticity. I: Mathematical Foundation and Hypoplasticity." *Journal of Engineering Mechanics*, Vol. 112, No. 9, pp. 966-987.

Dafalias, Y. F. and Herrmann, L. R. (1986). "Bounding Surface Plasticity. II: Application to Isotropic cohesive Soils." *Journal of Engineering Mechanics*, Vol. 112, No. 12, pp. 1263-1291.

Dafalias, Y. F. (1987). "An anisotropic critical state clay plasticity model." *In Constitutive laws for engineering materials* (eds C. S. Desai, E. Krempl, P. D. Kiousis and T. Kundu), vol. 1, pp. 513–521. Amsterdam: Elsevier.

Desai, C. S. and Faruque, M. O. (1984). "Constitutive Model for (Geological) Materials." *J. Eng. Mech. ASCE*, vol. 110, no. 9, pp. 1391-1408.

Dimaggio, F. L., and Sandler, I. S. (1971). "Mathematical model for granular soil." *Journal of Engineering Mechanics Division*, ASCE, Vol. 97, No. EM3, pp. 935-950.

Drucker, D. C., Gibson, R. E., and Henkel, D. J. (1957). "Soil mechanics and work hardening theories of plasticity." *Transactions of ASME*, Vol. 122, pp. 338-346.

Duncan, J. M. and Chang C. Y. (1970). "Non Linear Analysis of Stress and Strain in Soils." *ASCE Journal of Soil Mechanics and Foundations Division*, Vol. 96, No. SM5, pp. 1629-1653.

Duncan, J. M. and Seed, H. B. (1966). "Anisotropy and Stress Reorientation in Clay." *ASCE Journal of Soil Mechanics and Foundations Division*, Vol. 92, No. SM5, pp. 21-50.

Egan, J. A. (1977). "A Critical State Model for the Cyclic Loading Pore Pressure Response of Soils." *PhD Thesis*, Cornell University, Ithaca, New York, USA.

FLAC (1999). "Fast Lagrangian Analysis of Continua: User Guide." *Itasca Consulting Group*, Minneapolis, MN, Version 3.4.

Frantziskonis, G., Desai, C. S. and Somasundaram, S. (1986). "Constitutive Model for Nonassociative Behavior." *J. Eng. Mech. ASCE*, vol. 112, no. 9, pp. 923-946.

Germaine, J. T. (1982). "Development of the directional shear cell for measuring cross-anisotropic clay properties," *ScD thesis*, Massachusetts Inst. of Tech., Cambridge, Mass.

Graham, J., Noonan, M. L., and Lew, K. V. (1983). "Yield States and Stress-Strain Relationships in a Natural Plastic Clay." *Canadian Geotechnical Journal,* Vol. 20, pp. 502-516.

Graham, J., Pinkney, R. B., Lew, K. V., and Trainor, P. G. S. (1982). "On Curve Fitting and Laboratory Data," *Canadian Geotechnical Journal,* Vol. 19, pp. 201-205.

Habib, M. P. (1953). "Influence of the Variation of the Intermediate Principal Stress on the Shearing Strength of Soil." *Proceedings of third international conference on soil mechanics and foundation engineering,* Vol. 1, pp. 131.

Hambly, E. C. (1972). "Plane Strain Behavior of Remoulded Normally Consolidated Kaolin." *Geotechnique,* Vol. 22, pp. 301-317.

Han, C. and Vardoulakis, I. (1991). "Plain Strain Compression Experiments on Water-saturated Fine-grained Sand." *Geotechnique,* Vol. 41, pp. 29-44.

Haythornthwaite, R. M. (1960). "Stress and Strain in Soils." *Plasticity*, New York, Pergamon press, Inc., pp. 1958.

Hazen, I., and Penumadu, D. (1999). "Resonant column testing of clay specimens with controlled microfabric." *Report No. 99-02, Dept. of Civil & Env. Engg.,* Clarkson University, Potsdam, NY.

Henkel, D. J. (1959). "The Relationship Between the Strength, Pore-water Pressure, and Volume-change Characteristics of Saturated clay." *Geotechnique,* Vol. 9, pp. 119-135.

Henkel, D. J. (1960). "The Shear Strength of Saturated Remoulded Clay." *Proceedings of the ASCE Research conference on Shear Strength of Cohesive Soils,* Boulder, Colo., pp. 533-554.

Hill, R. (1962). "Acceleration Waves in Solids." *J. Mech. and Physics of Solids,* Vol. 10, pp. 1-16.

Houston, W. N. and Mitchell, J. K. (1968). "Property interrelationships in sensitive clays." *Journal of Soil Mechanics and foundation division, ASCE,* Vol. 95, No. SM4, pp. 1037-1062.

Hvorslev, M. J. (1937). "Über die Festigkeitseigenschaften Gestörter Bindiger Böden." ("On the Physical Properties of Remoulded Cohesive Soils"). *Ingeniorvidenskabelige Skrifter.* A. No. 45. 159 pp.

Hvorslev, M. J. (1960). "Physical Components of the Shear Strength of Saturated Clays." *ASCE Research Conf. on Shear Strength of Cohesive Soils,* University of Colorado, Boulder, Colorado, June 1960, pp. 69-273.

Jamiolkowski, M., Ladd, C.C., Germaine, J.T., and Lancellotta, R. (1985). "New developments in field and laboratory testing of soils." *Proceedings of the 11th International Conference on Soil Mechanics and Foundation Engineering,* Vol. 1, pp. 57-153.

Kim, Moonkyum (1988). "A Study of Constitutive Models for Frictional Materials." *PhD. Thesis*, University of California, Los Angeles.

Kim, M. K. and Lade, P.V. (1988). "Single Hardening Constitutive Model for Frictional Materials I: Plastic Potential Function." *Computers and Geotechnics,* Vol. 5, pp. 307-324.

Kirby, R. C., and Wroth, C. P. (1977). "Application of Critical State Soil Mechanics to the Prediction of Axial Capacity for Driven Piles in Clay." *9th Offshore Technology Conference,* OTC paper No. 2942,

Kirkgard, M. M. (1988). "An experimental study of the three-dimensional behavior of normally consolidated anisotropic clay." *PhD thesis*, University of California, Los Angeles.

Kirkgard, M. M. and Lade, Poul V. (1993). "Anisotropic Three-Dimensional Behavior of a normally consolidated clay." *Canadian Geotechnical journal,* 30, pp. 848-858.

Kjellman, W. (1936). " Report on an apparatus for consummate investigation of the mechanical properties." *Proceedings of the First International Conference on Soil Mechanics and Foundation Engineering, Cambridge, Mass.*, Vol. 2, pp. 16-20.

Ko, H.Y., and Scott, R.F. (1967). "A New Soil Testing Apparatus." *Geotechnique*, Vol. 17, No. 1, pp. 40-57.

Krizek, R. J., Edil, T. B., and Ozaydin, I. K. (1975). "Preparation and identification of samples with controlled fabric." *Engineering Geology*, Vol. 9, No. 1, pp. 13-38.

Kulhawy, F. H., Mayne, P. W. (1990). "Section 4- strength." *Manual on Estimating soil Properties for Foundation Design,* Electric Power Research Institute, El-6800, Project: 1493-6,

Ladd, C. C., and Foott, R. (1974). "New design procedure for stability of soft clays," *ASCE Journal of the Geotechnical Engineering Division*, Vol. 100, No. GT7, pp. 763-786.

Lade, P. V. (1977). "Elasto-Plastic Stress-Strain Theory for Cohesionless Soil With Curved Yield Surface." *Int. J. Solids Structures,* Vol. 13, pp. 1019-1035.

Lade, P. V. (1977). "Stress-Strain Theory for Normally Consolidated Clay." *3rd Int. Conf. Numerical Methods Geomechanics*, Aachen, pp. 1325-1337.

Lade, P.V. (1978). "Cubical Triaxial Apparatus for Soil Testing." *Geotechnical Testing Journal*, Vol. 1, No. 2, pp. 93 - 101.

Lade, P. V. (1990). "Single Hardening Model with Application to NC Clay." *Journal of Geotechnical Engineering,* Vol. 116, No. 3, pp. 394-415.

Lade, P. V., Duncan, James M. (1973). "Cubical Triaxial tests on Cohesionless Soil." *Journal of the Soil Mechanics and Foundations Division*, Vol. 99, No. SM10, pp. 793-812.

Lade, P.V. and Kim, M. K. (1988). "Single Hardening Constitutive Model for Frictional Materials II: Yield Criterion and Plastic Work Contours." *Computers and Geotechnics,* Vol. 6, pp. 13-29.

Lade, P.V. and Kim, M. K. (1988). "Single Hardening Constitutive Model for Frictional Materials III: Comparision With Experimental Data." *Computers and Geotechnics,* Vol. 6, pp. 31-47.

Lade, P. V. and Musante, H. M. (1978). "Three-Dimensional Behavior of Remolded Clay." *ASCE Journal of Geotechnical Engineering Division,* Vol. 104, No. GT2, pp . 193-209.

Lade, P. V., Nelson, R. B., and Ito, Y. M. (1987). "Nonassociated Flow and Stability of Granular Materials." *ASCE Journal of Engineering Mechanics*, Vol. 113, No. 9, pp. 1302-1318.

Lade, P. V., Nelson, R. B., and Ito, Y. M. (1988). "Instability of Granular Materials with Nonassociated Flow." *ASCE Journal of Engineering Mechanics*, Vol. 114, No. 12, pp. 2173-2191.

Lambe, T. W. (1958). The structure of compacted clays. Proc. *American Society of Civil Engineers*, Vol. 84, No. SM2, pp. 1-34.

Lin, H. and Penumadu, D. (2002). "Interpretation of combined axial-torsional test for 3-D constitutive behavior of geo-materials." *Proceedings of the 15th ASCE Engineering Mechanics Conference*, Columbia University, NY, USA.

Mandeville, D. and Penumadu, D. (2000). "Testing procedures for obtaining fixed inclination of major principal stress for 3-D testing of cohesive soil." *Proceedings, 14th Engineering Mechanics Conference (EM 2000),* Texas, Austin, USA.

Mandeville, D. and Penumadu, D. (2003). "True Triaxial Testing System for Clay with Proportional-Integral-Differential Control." *ASTM Geotechnical Testing Journal*, 27, No. 2, GTJ11756, pp. 1-12.

Martin, R. T. (1965). "Quantitative fabric of consolidated Kaolinite." *Massachusetts Institute of Technology, Research Report R65-47*, Soils Publication No.179.

Mayne, P. W. (1979). "Discussion of "Normalized Deformation parameters for Kaolin" By H. G. Poulos." *Geotechnical Testing Journal.* Vol. 1, No. 2, pp. 102-106.

Mayne, P. W. and Holtz, R.D. (1985). "Effect of Principal Stress Rotation on Clay Strength." *Proceedings of the eleventh international conference on soil mechanics and foundation engineering, San Francisco,* Vol. 2, pp. 579-582.

Mayne, P. W. and Swanson, P. G. (1981). "The Critical-State Pore Pressure Parameter from Consolidated-Undrained Shear Test." *Laboratory Shear Strength of Soil, ASTM STP 740, ASTM*, pp. 410-430.

McConnachie, I. (1974). "Fabric Changes in Consolidated Kaolin." *Geotechnique*, Vol. 24, No. 2, pp. 207-222.

McKyes, E. and Yong, R. N. (1971). "Three Techniques for Fabric Viewingas Applied to Shear distortion of Clay." *Clays and Clay Minerals*, Vol. 19, pp. 289-293.

Mesri, G. and Godlewski, P. M. (1977). "Time- and stress-compressibility interrelationship." *Journal of Geotechnical Engineering Division, ASCE*, Vol. 103, No. No. GT5, pp. 417-430.

Mitchell, R. J. (1970). "On the Yielding and Mechanical Strength of Leda Clay." *Canadian Geotechnical Journal*, Vol. 7, pp. 297-312.

Mitchell, J. K. (1964). "Shearing Resistance of Soil as a Rate Process." *Journal of Soil Mechanics and foundation Division, ASCE*, Vol. 90, No. SM1, pp. 29-61.

Mitchel, J. K. (1993). "Fundamentals of soil Behavior." *Second Edition, John Wiley and Sons Inc.*

Mitchell, J. K. and McConnell, J. R. (1965). "Some Characteristics of the elastic and plastic deformation of clay on initial loading." *Proceedings of the sixth international conference on Soil Mechanics and Foundation Engineering*, Vol. 1, pp. 313-317.

Morgenstern, N. R. and Tchalenko, J. S. (1967). "Microstructural observations on shear zones and slips in natural clays." *Proceedings of the Geotechnical Conference, Oslo*, Vol. 1, pp. 147-153.

Mroz, Z. (1963). "Non-associated flow laws in plasticity." *Journal de Mecanique.* Vol. 2, no. 1, pp 21-42.

Nakai, T. and Matsuoka, H. (1983). "Shear behavior of sand and clay under three-dimensional stress conditions." *Soils and Foundations*, Vol. 23, No. 2, pp. 26-42.

Nakai, T. and Matsuoka, H. (1986). "A Generalized Elastoplastic Constitutive Model for Clay in Three Dimensional Stresses." *Soils and Foundations*, Vol. 26, No. 3, pp. 81-98.

Olson, R. E. and Mesri, G. (1970). "Mechanisms Controlling the Compressibility of Clay." *Journal of Soil Mechanics and Foundation division, ASCE*, Vol. 96, No. SM6, pp. 1863-1878.

Palmer, A. C. and Rice, J. R. (1973). "The Growth of Slip Surfaces in the Progressive Failure of Over-consolidated Clay." *Proc. of the Royal Society of London series a-Mathematical Physical and Eng. Sciences*, A332, pp. 527-548.

Parry, R. H. G. (1960). "Triaxial Compression and Extension Tests on Remoulded Saturated Clay." *Geotechnique,* Vol. 10, 1960, pp. 166-180.

Parry, R. H. G. and Nadarajah, V. (1973). "Observations on Laboratory Prepared, Lightly Overconsolidated Specimens of Kaolin," *Geotechnique,* Vol. 24, No. 3, pp. 345-358.

Pearce, J. A. (1971). "A New Triaxial Apparatus." *Proceedings, Roscoe Memorial Symposium*, G. T. Foulis, Henley on Thames, pp. 330-339.

Penumadu, D. (1996). "Evaluating Clay Microfabric Using scanning Electron Microscopy and Digital Information Processing." *Transportation Research record 1526*, pp. 112-120.

Penumadu, D., Skandarajah, A. and Chameau, J. L. (1998). "Strain-rate Effects in Pressuremeter Testing Using a Cuboidal Shear Device: Experiments and Modeling," *Canadian Geotechnical Journal,* Vol. 35, pp. 27-42.

Perry, R. H., 1973, Chemical Engineers Handbook, 5th edition.

Prashant A. and Penumadu D. (2004). "Effect of intermediate principal stress on overconsolidated kaolin clay." *ASCE, Journal of Geotechnical and Geoenvironmental Engineering*, Vol. 130, No. 3, pp. 284-292.

Prashant A. and Penumadu D. (2003). "A Laboratory Study of Normally Consolidated Kaolin Clay." In Review, *Canadian Geotechnical Journal.*

Prevost, J. H. (1978a). "Anisotropic Undrained Stress-Strain Behavior of Clays." *Journal of Geotechnical Engineering Division.* Vol. 104. No. GT8. pp. 1075-1090.

Prevost, J. H. (1978b). "Plasticity Theory for Soil Stress-Strain Behavior." *Journal of Geotechnical Engineering Division.* Vol. 104. No. EM5. pp. 1177-1194.

Prevost, J. H. (1981). "Nonlinear Anisotropic Stress-Strain-Strength Behavior of Soils." *Laboratory Shear Strength of Soil. ASTM STP 740.* Eds. R. N. Yong and F. C. Townsend. pp. 431-455.

Quigley, R. M. and Thompson, C. D. (1966). 'The fabric of anisotropically consolidated sensitive marine clay." *Canadian Geotechnical Journal.* Vol. 3, No. 2, pp. 61-73.

Reddy, K.R., Saxena, S.K., and Budiman, J.S. (1992). "Development of a True Triaxial Testing Apparatus." *Geotechnical Testing Journal*, Vol. 1, No. 2, pp. 89-105.

Rendulic, L. (1936). "Relation Between Void Ratio and Effective Principal Stresses for a Remoulded Silty Clay." *Proceedings of First international conference on soil mechanics and foundation engineering,* Vol. 3, pp. 48-51.

Rice, J. R. (1975). "On the Stability of Dilatant Hardening for Saturated Rock Mass." *J. of Geophysical Research*, Vol. 80, No. 11, pp. 1531-1536.

Roscoe, K. H. and Burland, J. B. (1968). "On the generalized stress– strain behaviour of 'wet clay'." *Engineering plasticity* (eds J. Heyman and F. A. Leckie), pp. 535–609. Cambridge: Cambridge University Press.

Roscoe, K. H., Schofield, A. N. and Thurairajah, A. (1963). "Yielding of clays in state wetter than critical." *Geotechnique,* Vol. 8, pp. 22-53.

Roscoe, K. H., Schofield, A. N. and Wroth, C. P. (1958). "On Yielding of Soils." *Geotechnique,* Vol. 13, No. 2, pp. 211-240.

Rowe, P.W., and Barden, L. (1964). "Importance of free ends in triaxial testing." Journal of Soil Mechanics and Foundation Division, Vol. 90, No. SM1, pp. 1-27.

Saada, A.S. (1988). "Hollow cylinder torsional devices: their advantages and limitations." *Advanced Triaxial Testing of Soil and Rock, ASTM STP 977*, pp. 766-795.

Saada, A.S. and Bianchini, G.F. (1975). "The strength of one-dimensionally consolidated clays." *Journal of the Geotechnical Engineering Division-ASCE*, Vol. 101, No. 11, pp. 1151-1164

Schofield, A. N. and Wroth, C. P. (1968). "Critical State Soil Mechanics." *Maidenhead, McGraw-Hill.*

Seah, T. H. (1990). "Anisotropy of normally consolidated Boston blue clay." *ScD thesis*, Massachusetts Inst. of Tech., Cambridge, Mass.

Seed, H. B. and Chan, C. K. (1959). "Structure and Strength Characteristics of Compacted Clays." *Journal of Soil Mechanics and Foundation Division, ASCE*, Vol. 85, No. SM5, pp. 87-128.

Seed, H. B., Mitchell, J. K., and Chan, C. K. (1962). "Swell and swell pressure characteristics of compacted clays." *Highway Research Board Bulletin*, 313, pp. 12-39.

Sheeran, D. E. and Krizek, R. J. (1971). "Preparation of Homogeneous Soil Samples by Slurry Consolidation." *Journal of Materials*, Vol. 6, No.2, pp. 356-373.

Shibata, T. and Karube, D. (1965). "Influence of the Variation of the Intermediate Principal Stress on the Mechanical Properties of Normally Consolidated Clays." *Proceedings of the sixth international conference on soil mechanics and foundation engineering, Montreal,* 2/48, pp. 359-363.

Sivakugan, N., Chameau, J. L., Holtz, R. D. and Altshaeffl, A. G. (1988). "Servo-Controlled Cuboidal Shear Device." *Geotechnical Testing Journal*, Vol. 11, No. 2, pp. 119-124.

Skempton, A.W. (1954). "The pore pressure coefficients A and B." *Geotechnique*, Vol. 4, pp. 143-147.

Soga, K. (1994). "Mechanical behavior and constitutive modeling of natural structured soils." *PhD. Thesis*, Dept. of Civil & Env. Engg., University of California, Berkeley, CA.

Sture, S., and Desai, C. S. (1979). "Fluid Cushion Truly Triaxial or Multiaxial Testing Device." *Geotech. testing J.*, Vol. 2, No. 1, pp. 20-33.

Tavenas, F., Rosiers, Des, J. P., Leroueil, S., Rochelle, La, P., and Roy, M. (1979). "The Use of Strain Energy as a Yield and Creep Criterion for Overconsolidated Clays." *Geotechnique,* Vol. 29, No. 3, pp. 285-303.

Terzaghi, K. (1925). "Erdbaumechanik auf Bodenphysikalischer Grundlage." *Deuticke, Vienna*, pp. 399.

P. A. Thiessen (1942). "Wechselseitige Adsorption von Kolloiden," *Ztachr. Elektrochem*, Vol. 48, No. 12, pp. 675-681.

Vaid, Y. P. and Campanella, R. G. (1974). "Triaxial and Plane Strain Behavior of Natural Clay." *Journal of the Soil Mechanics and Foundations Division*, Vol. 100, No. GT3, pp. 207-224.

Vardoulakis, I. (1982). "Stability and Bifurcation of Soil Samples." In: *Constitutive Relations for Soils*, (Editors G. Gudehus et al.), Balkema, Rotterdam, pp. 477-483.

Vardoulakis, I. (1985). "Stability and Bifurcation of Undrained, Plane Rectilinear Deformations on Water-saturated Granular Soils." *Int. J. for Numerical and Analytical Methods in Geomechanics*, Vol. 9, pp. 339-414.

Vardoulakis, I. and Sulem, J. (1995). "Bifurcation Analysis in Geomechanics." *Chapman and Hall Publication*, London.

Vardoulakis, I. (1996). "Deformation of Water-saturated sand: I Uniform Undrained Deformation and Shear Banding. II The effect of Pore-water Flow and Shear Banding." *Geotechnique*, Vol. 46, No. 3, pp. 441-472.

Wang, Q. and Lade, P. V. (2001). "Shear Banding in True Triaxial Tests and Its Effect on Failure in Sand." *Journal of Engineering Mechanics*, Vol. 127, No. 8, pp. 754-761.

Whittle, A. J. and Kavvadas, M. J. (1994). "Formulation of MIT-E3 Constitutive Model for Overconsolidated Clays." *Journal of Geotechnical Engineering*. Vol. 120, No. 1, pp. 173-198.

Whittle, A. J., DeGroot, D. J., Ladd, C. C. and Seah, T. H. (1994). "Model prediction of anisotropic behavior of Boston blue clay." *Journal of Geotechnical Engineering, ASCE*, 120(1), 199-224.

Wissa, A. E. Z., Christian, J. T., Davis, E. H., and Heiberg, S. (1971). "Consolidation at constant rate of strain." *Journal of the Soil Mechanics and Foundations Division*, Vol. 97, No. SM10, pp. 1393-1413.

Wood, D. M. (1990). "Soil behaviour and critical state soil mechanics." *Cambridge: Cambridge University Press.*

Wu, T. H., Loh, A. K., and Malvern, L. E. (1963). "Study of Failure Envelop of Soils." *Journal of the Soil Mechanics and Foundations Division*, Vol. 89, No. SM1, pp. 145-181.

Yong, R. N. and McKyes, E. (1967). "Yielding of Clay in Complex Stress Field." *Proceedings of third panamerican conference on soil mechanics and foundation engineering, Caracas, Venezuela,* Vol. 1, pp. 131-143.

Yong, R. N. and McKyes, E. (1971). "Yield and Failure of Clay Under Triaxial Stresses." *Journal of the Soil Mechanics and Foundations Division*, Vol. 97, No. SM1, pp. 159-176.

Appendices

Appendix 1. Stress Invariants

Invariants of Stress Tensor:

Invariants of stress tensors are shown in terms of principal stress values, σ_1, σ_2, and σ_3, and their general form in three-dimensional stress space are shown using index notation.

First invariant:
$$I_1 = \sigma_{kk} = \sigma_1 + \sigma_2 + \sigma_3 \tag{A1.1}$$

Second invariant:
$$I_2 = \frac{1}{2}\left(\sigma_{ij}\sigma_{ji} - \sigma_{kl}\sigma_{lk}\right) = -\left(\sigma_1\sigma_2 + \sigma_2\sigma_3 + \sigma_3\sigma_1\right) \tag{A1.2}$$

Third invariant:
$$I_3 = \det\left(\sigma_{ij}\right) = \sigma_1\sigma_2\sigma_3 \tag{A1.3}$$

Deviatoric Stress Invariants:

Second Invariant
$$J_2' = \frac{1}{2}s_{ij}s_{ji} = \frac{1}{3}I_1^2 + I_2 \tag{A1.4}$$

$$J_2' = \frac{1}{6}\left[\left(\sigma_1 - \sigma_2\right)^2 + \left(\sigma_2 - \sigma_3\right)^2 + \left(\sigma_3 - \sigma_1\right)^2\right]$$

Third Invariant
$$J_3' = \frac{1}{2}s_{ij}s_{jk}s_{kl} = \frac{2}{27}I_1^3 + \frac{1}{3}I_1I_2 + I_3 \tag{A1.5}$$

Deviatoric stress
$$s_{ij} = \sigma_{ij} - \frac{1}{3}\delta_{ij}\sigma_{kk} \tag{A1.6}$$

Another form of stress and strain invariants used throughout in this study:

Mean Effective Stress
$$p' = I_1/3 = \left(\sigma_1' + \sigma_2' + \sigma_3'\right)/3 \tag{A1.7}$$

Deviatoric Stress
$$q = \sqrt{3J_2} = \sqrt{\frac{\left(\sigma_1' - \sigma_2'\right)^2 + \left(\sigma_2' - \sigma_3'\right)^2 + \left(\sigma_3' - \sigma_1'\right)^2}{2}} \tag{A1.8}$$

Shear Strain
$$\varepsilon_q = \frac{1}{3}\sqrt{2\left\{\left(\varepsilon_1 - \varepsilon_2\right)^2 + \left(\varepsilon_2 - \varepsilon_3\right)^2 + \left(\varepsilon_3 - \varepsilon_1\right)^2\right\}} \tag{A1.9}$$

Derivatives of Stress Tensor Invariants:

$$\frac{\partial I_1}{\partial \sigma_{ij}} = \delta_{ij} \tag{A1.10}$$

$$\frac{\partial I_2}{\partial \sigma_{ij}} = \sigma_{ij} - \delta_{ij}\sigma_{kk} \tag{A1.11}$$

$$\frac{\partial I_3}{\partial \sigma_{ij}} = \frac{1}{2} e_{imn} e_{jqr} \sigma_{mq} \sigma_{nr} \tag{A1.12}$$

where, δ_{ij} and e_{imn} are defined as

$$\begin{cases} \delta_{ij} = 1 & \text{if, } i = j \\ \delta_{ij} = 0 & \text{if, } i \neq j \end{cases} \tag{A1.13}$$

$$\begin{cases} e_{ijk} = 1 & \text{if, } ijk = 123, 231, 312 \\ e_{ijk} = -1 & \text{if, } ijk = 321, 132, 213 \\ e_{ijk} = 0 & \text{if, } i = j,\ i = j,\ j = k, \text{ or } i = j = k \end{cases} \tag{A1.14}$$

Appendix 2. Modified Cam-Clay Model: Formulation in Principal Stress Space

Elastic Deformation:

Elastic Bulk modulus, $$K' = vp'/\kappa \quad \text{(A2.1)}$$

where, v is specific volume, $v = 1 + e$, and e is void ratio.

Yong's Modulus E can be defined using elastic bulk modulus as

$$E = 3(1-2\nu)vp'/\kappa \quad \text{(A2.2)}$$

Using Hook's Law, the incremental elastic strains can be defined as

$$d\varepsilon_i^e = \frac{1}{E}\left[(1+\nu)\delta_{ij} - \nu e_j\right]d\sigma_j \quad \text{(A2.3)}$$

where, e_j = 1 for j = 1, 2, and 3.

Plastic Deformation:

Yield Surface and Plastic Potential Surface:

$$f(\sigma_i, p_o) = g(\sigma_i, p_o) = q^2 - M^2\left[p'(p_o' - p')\right] \quad \text{(A2.4)}$$

Differentiate equation A2.4,

$$\frac{\partial f}{\partial \sigma_i} = 3(\sigma_i - p') - \frac{M^2}{3}(p_o' - 2p') \quad \text{(A2.5)}$$

Hardening Rule:

$$\frac{\partial p_o'}{\partial \varepsilon^p} = \frac{\nu p_o'}{(\lambda - \kappa)} \quad \text{(A2.6)}$$

From equation 7.8, and assuming $\zeta_f = \zeta_g = p_o'$,

$$H = -\frac{\partial f}{\partial p_o'}\left(\frac{\partial p_o'}{\partial \varepsilon^p}\sum_{i=1}^{3}\frac{\partial g}{\partial \sigma_i}\right)$$

$$H = \left(-M^2 p'\right)\left(\frac{\mathrm{v}p_o'}{(\lambda-\kappa)}\left(-M^2\left(p_o'-2p'\right)\right)\right) \qquad \text{(A2.7)}$$

Therefore, plastic strain increments (using equation 7.9),

$$d\varepsilon_i^p = \frac{-(\lambda-\kappa)}{M^4 \mathrm{v}p_o' p'\left(p_o'-2p'\right)}\left\langle\frac{\delta f}{\delta \sigma_j}\delta\sigma_j\right\rangle\frac{\delta f}{\delta \sigma_i} \qquad \text{(A2.8)}$$

Therefore, total elasto-plastic strain equation can be written as

$$d\varepsilon_i = d\varepsilon_i^e + d\varepsilon_i^p = \left[\frac{\kappa(1+\nu)\delta_{ij} - \nu e_j}{3(1-2\nu)\mathrm{v}p'} - \frac{(\lambda-\kappa)}{M^4 \mathrm{v}p_o' p'\left(p_o'-2p'\right)}\left(\frac{\delta f}{\delta \sigma_i}\frac{\delta f}{\delta \sigma_j}\right)\right]\delta\sigma_j \qquad \text{(A2.9)}$$

Critical State is reached when the following condition exists.

$$\frac{q}{p'} = M, \text{ and } \mathrm{v} = \Gamma - \lambda \ln\left(\frac{p_o'}{2}\right)$$

where,

$$\Gamma = \mathrm{v}_\lambda - (\lambda-\kappa)Ln(2)$$

Appendix 3. Single Hardening Model Formulation

Single hardening model is defined using stress invariants I_1, I_2, I_3, and J'_2. These stress invariants are described in equation A1.1 to A1.4 of Appendix-1.

Elastic Behavior:

$$E = Mp_a\left[\left(\frac{I_1}{p_a}\right)^2 + R\frac{J'_2}{p_a^2}\right]^{\lambda} \tag{A3.1}$$

where, p_a is the atmospheric pressure.

$$R = 6\frac{1+\nu}{1-2\nu}$$

Elastic stains are computed as

$$d\varepsilon_{ij}^{e} = \frac{(1+\nu)}{E}d\sigma_{ij} - \frac{\nu}{E}\delta_{ij}d\sigma_{kk} \tag{A3.2}$$

Plastic Behavior:

Failure criterion:

$$f_n = \left(\frac{I_1^3}{I_3} - 27\right)\left(\frac{I_1}{p_a}\right)^m = \eta_1 \tag{A3.3}$$

Plastic potential function:

$$g_p = \left[\psi_1\frac{I_1^3}{I_3} - \frac{I_1^2}{I_2} + \psi_2\right]\left[\frac{I_1}{p_a}\right]^{\mu} \tag{A3.3}$$

where, $\psi_1 = 0.00155m^{-1.27}$

Yield Criterion:

$$f = f_p(\sigma) - f'_p(W_p) = 0 \tag{A3.4}$$

where, $f_p'(W_p)$ is hardening rule, and $f_p(\sigma)$ is yield Function,

$$f_p(\sigma)=\left[\psi_1\frac{I_1^3}{I_3}-\frac{I_1^2}{I_2}\right]\left[\frac{I_1}{p_a}\right]^h e^q \tag{A3.5}$$

$$q=\frac{\alpha S}{1-(1-\alpha)S} \tag{A3.6}$$

$$S=\frac{f_n}{\eta_1}=\frac{1}{\eta_1}\left(\frac{I_1^3}{I_3}-27\right)\left(\frac{I_1}{p_a}\right)^m \tag{A3.7}$$

Hardening Rule:

$$f_p'(W_p)=\left(\frac{1}{D}\right)^{1/\rho}\left(\frac{W_p}{p_a}\right)^{1/\rho} \tag{A3.8}$$

$$D=\frac{C}{(27\psi_1+3)^\rho} \tag{A3.9}$$

$$\rho=\frac{p}{h} \tag{A3.10}$$

Plastic Deformation is determined using the Flow Rule:

$$d\varepsilon_{ij}^p=d\lambda\frac{\partial g_p}{\partial\sigma_{ij}} \tag{A3.11}$$

$$d\lambda=\frac{dW_p}{\mu.g_p} \tag{A3.12}$$

where, incremental plastic work dW_p is computed as

$$dW_p=D.p_a.\rho.f_p^{\rho-1}.df_p \tag{A3.13}$$

Therefore, total elasto-plastic strain equation can be written as

$$d\varepsilon_{ij} = d\varepsilon_{ij}^{e} + d\varepsilon_{ij}^{p}$$
$$= \left(\frac{(1+\nu)}{E} d\sigma_{ij} - \frac{\nu}{E} \delta_{ij} d\sigma_{kk} \right) + \frac{D.p_a.\rho.f_p^{\rho}.df_p}{\mu.g_p.f_p} \left\langle \frac{\delta f_p}{\delta \sigma_{kl}} d\sigma_{kl} \right\rangle \frac{\delta g_p}{\delta \sigma_{ij}} \quad \text{(A3.14)}$$

Derivatives of yield and Plastic Potential Functions with respect to Stress Components:

Yield Function:

$$\frac{\partial f_p}{\partial \sigma_{ij}} = \frac{\partial f_p}{\partial I_1} \frac{\partial I_1}{\partial \sigma_{ij}} + \frac{\partial f_p}{\partial I_3} \frac{\partial I_3}{\partial \sigma_{ij}} \quad \text{(A3.15)}$$

Plastic Potential Function:

$$\frac{\partial g_p}{\partial \sigma_{ij}} = \frac{\partial g_p}{\partial I_1} \frac{\partial I_1}{\partial \sigma_{ij}} + \frac{\partial g_p}{\partial I_2} \frac{\partial I_2}{\partial \sigma_{ij}} + \frac{\partial g_p}{\partial I_3} \frac{\partial I_3}{\partial \sigma_{ij}} \quad \text{(A3.16)}$$

In these equations, the derivatives of yield and plastic potential functions with respect to stress invariants can be defined as shown in equations A3.17 to A3.21. The derivatives of stress invariants with respect to stress components can be used from equation A1.10 to A1.12 of Appendix-1.

$$\frac{\partial f_p}{\partial I_1} = \frac{\left(\frac{I_1}{p_a} \right)^m \left(3I_1^3 + mI_1^3 - 27I_3 \right)}{I_1 I_3} \quad \text{(A3.17)}$$

$$\frac{\partial f_p}{\partial I_3} = -\frac{I_1^3 \left(\frac{I_1}{p_a} \right)^m}{I_3^2} \quad \text{(A3.18)}$$

$$\frac{\partial g_p}{\partial I_1} = \frac{\left(\frac{I_1}{p_a} \right)^{\mu} \left[(3\psi_1 + \mu) I_1^3 I_2 - (2+\mu) I_1^2 I_3 + \mu \psi_1 I_2 I_3 \right]}{I_1 I_2 I_3} \quad \text{(A3.19)}$$

$$\frac{\partial g_p}{\partial I_2} = \frac{I_1^2 \left(\frac{I_1}{p_a} \right)^{\mu}}{I_2^2} \tag{A3.20}$$

$$\frac{\partial g_p}{\partial I_3} = \frac{-\psi_1 I_1^3 \left(\frac{I_1}{p_a} \right)^{\mu}}{I_3^2} \tag{A3.21}$$

Appendix 4. Relationship between Third Invariant of Stress Tensor and Shear Stress Ratio

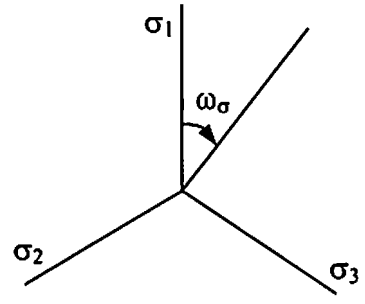

Figure A4.1 Lode Angle in Deviatoric Plane

As shown in Fig. A4.1, the angle of stress vector from σ_1 axis in deviatoric plane is often represented by the angle ω_σ. It is known as the Lode angle. Using the stress invariants in deviatoric plane, Nayak and Zienkiewicz (1972) defined a relationship for ω_σ as shown in equation A4.1.

$$\omega_\sigma = \frac{1}{3}\cos^{-1}\left\{\frac{3\sqrt{3}}{2}\frac{J_3'}{(J_2')^{3/2}}\right\} \tag{A4.1}$$

where, $0 \le \omega_\sigma \le \pi/3$, and ω_σ has a constant relationship with intermediate principal stress as shown in equation A4.2.

$$\tan(\omega_\sigma) = \frac{b\sqrt{3}}{2-b} \tag{A4.2}$$

The deviatoric stress invariants are related to the invariants of stress tensor (shown in Appendix-1).

$$J_3' = \frac{2}{27} I_1^3 + \frac{1}{3} I_1 I_2 + I_3 \tag{A4.3}$$

$$J_2' = \frac{1}{3} I_1^2 + I_2 \tag{A4.4}$$

In Appendix-1, the mean effective stress p' and deviatoric stress q were defined in terms of the stress invariants:

$$J_2' = \frac{q^2}{3} \tag{A4.5}$$

$$I_1 = 3p' \tag{A4.6}$$

From equations A4.3 to A4.6,

$$I_2 = J_2' - \frac{1}{3} I_1^2 = \frac{q^2}{3} - 3p'^2 \tag{A4.7}$$

$$J_3' = p' \frac{q^2}{3} - p'^3 + I_3 \tag{A4.8}$$

Using the relationships defined above, equation A4.1 can be defined as

$$\cos(3\omega_\sigma) = \frac{27}{2} \frac{p' \frac{q^2}{3} - p'^3 + I_3}{q^3} \tag{A4.9}$$

Using the definition of shear stress ratio, $\eta = q / p'$, equation A4.9 can be rearranged to equation A4.10.

$$\frac{I_3}{p'^3} = \frac{2\eta^3}{27} \cos(3\omega_\sigma) - \frac{\eta^2}{3} + 1 \tag{A4.10}$$

Variation of η for I_3/p'^3 to be constant

If $\eta = \eta_o$ at $\omega_\sigma = 0$, then equation A4.10 gives,

$$\frac{I_3}{p'^3} = \frac{2}{27}\eta_0{}^3 - \frac{\eta_0{}^2}{3} + 1 \qquad \text{(A4.11)}$$

For I_3/p'^3 to be constant, equation A4.11 gives the variation of η as

$$2\eta^3\cos(3\omega_\sigma) - 9\eta^2 = 2\eta_0{}^3 - 9\eta_0{}^2 = k \qquad \text{(A4.12)}$$

For $\frac{I_3}{p'^3}$ to be positive, $0 \le k \le 27$.

A general solution for the cubic equation defined in equation A4.12 is,

$$\eta = \frac{\sqrt{k/12}}{\cos\left(\frac{1}{3}\cos^{-1}\left(-\cos(3\omega_\sigma)\sqrt{k/27}\right)\right)} \qquad \text{(A4.12)}$$

This relationship also defines the variation of η with b-value under the condition that $\frac{I_3}{p'^3}$ is constant because ω_σ and b-value have a constant relationship as was shown in equation A4.2.

Appendix 5. Procedure for Projecting Principal Stress State onto an Octahedral/Deviatoric Plane

The specimens subjected to various proportional loading conditions do not fail at the same value of mean effective stress or octahedral normal stress; however, the difference is usually small enough to allow for linear interpolation of principal stresses so that their mean value in all cases is a constant. This is under the assumption that the soil has no cohesion and the failure surface is straight for a small increment. Modified principal stress values can be computed using equation A5.1.

$$\left(\sigma_1^*, \sigma_2^*, \sigma_3^*\right) = \left(\sigma_1, \sigma_2, \sigma_3\right) \frac{3.\sigma_{oct}}{\left(\sigma_1 + \sigma_2 + \sigma_3\right)} \tag{A5.1}$$

this gives,

$$\sigma_{oct} = \frac{1}{3}\left(\sigma_1^* + \sigma_2^* + \sigma_3^*\right) \tag{A5.2}$$

From Fig. A5.1 and Fig A5.2, the value of a:

$$a = \sqrt{\frac{3}{2}}\left(\sigma_1^* - \sigma_{oct}\right) \tag{A5.3}$$

Similarly, the value of b and c:

$$b = \sqrt{\frac{3}{2}}\left(\sigma_2^* - \sigma_{oct}\right) \tag{A5.4}$$

$$c = \sqrt{\frac{3}{2}}\left(\sigma_3^* - \sigma_{oct}\right) \tag{A5.5}$$

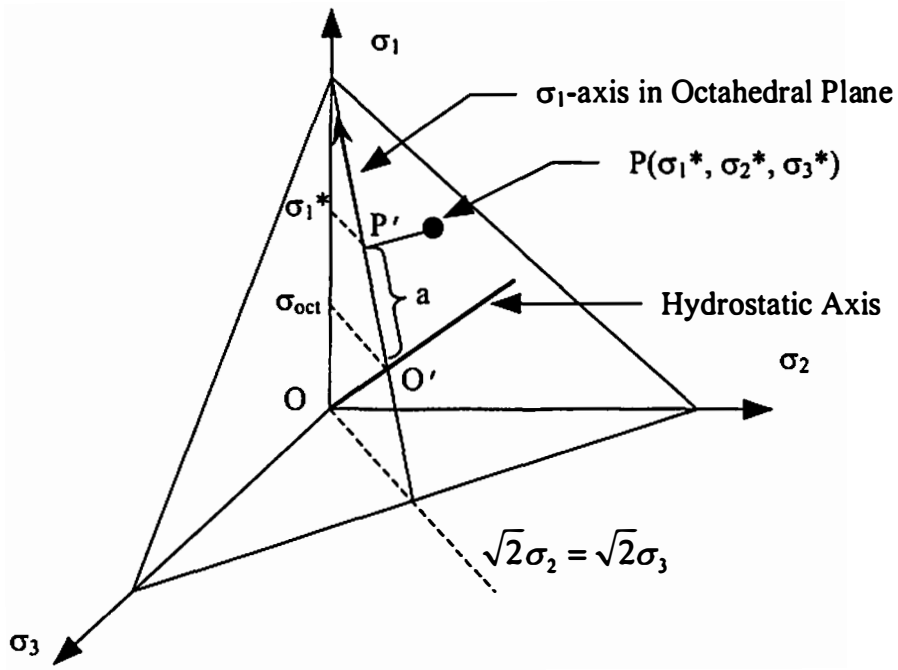

Figure A5.1 Three-dimensional Stress Space: Projection of Point P on σ_1-axis in Octahedral Plane

$$\sin(\theta) = \frac{1}{\sqrt{3}}$$

$$\cos(\theta) = \sqrt{\frac{2}{3}}$$

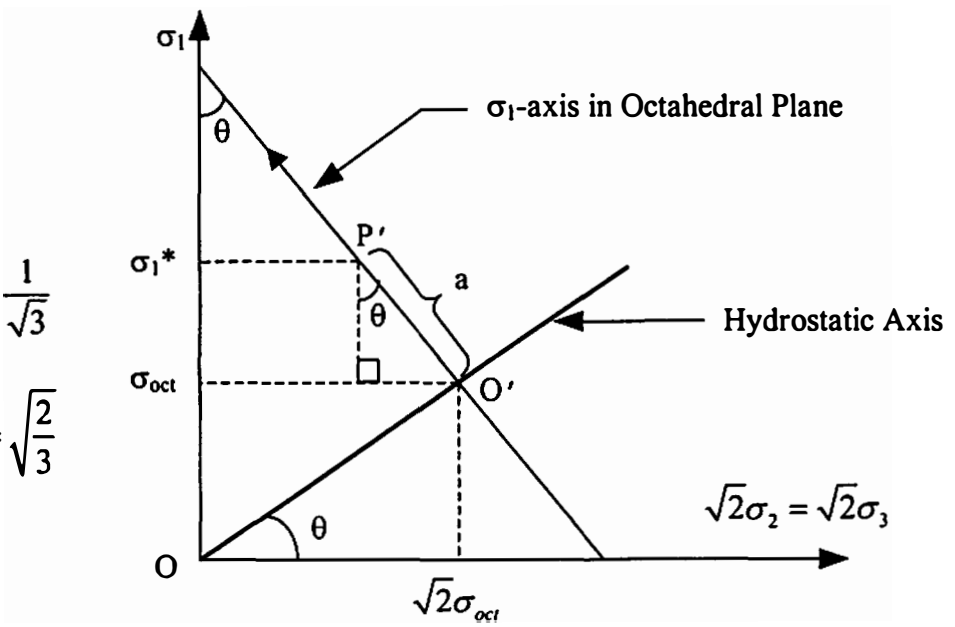

Figure A5.2 Triaxial Plane: Offset of Point P along σ_1-axis from Origin in Octahedral Plane

Figure A5.3 shows the projections a, b, and c for a general stress point in 3-D stress space. Figure A5.4 shows the same projections in the octahedral plane with orthogonal basis along x, and y-axis. From Fig. A5.4, y-coordinate is equal to a:

$$y = \sqrt{\frac{3}{2}}\left(\sigma_1^* - \sigma_{oct}\right) \tag{A5.6}$$

From Fig. A5.4, x-coordinate:

$$x = \frac{\sqrt{3}}{3}(-a - 2c) \tag{A5.7}$$

Substituting equation A5.4 and A5.5 into equation A5.7:

$$x = \frac{\sqrt{3}}{3}\left(\sigma_2^* - \sigma_3^*\right) \tag{A5.8}$$

The direction of principal strain increments can be considered to be in the direction principal stress directions. The magnitude of strain increment is immaterial, only the direction of strain increment vector is of interest, which depends on the relative magnitudes of strain increments. The slope of strain increment in octahedral plane with coordinate basis x and y is:

$$\frac{dy}{dx} = \frac{y}{x} = \sqrt{3}\frac{\left(\Delta\varepsilon_1 - \Delta\varepsilon_m\right)}{\left(\Delta\varepsilon_2 - \Delta\varepsilon_3\right)} \tag{A5.9}$$

$$\Delta\varepsilon_m = \frac{1}{3}\left(\Delta\varepsilon_1 + \Delta\varepsilon_2 + \Delta\varepsilon_3\right) \tag{A5.10}$$

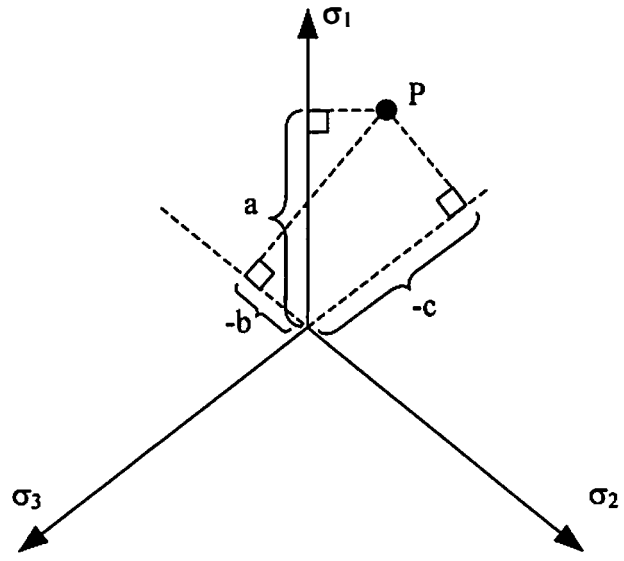

Figure A5.3 Co-ordinates of Stress Point P in Octahedral Plane with Basis along σ_1, σ_2, and σ_3

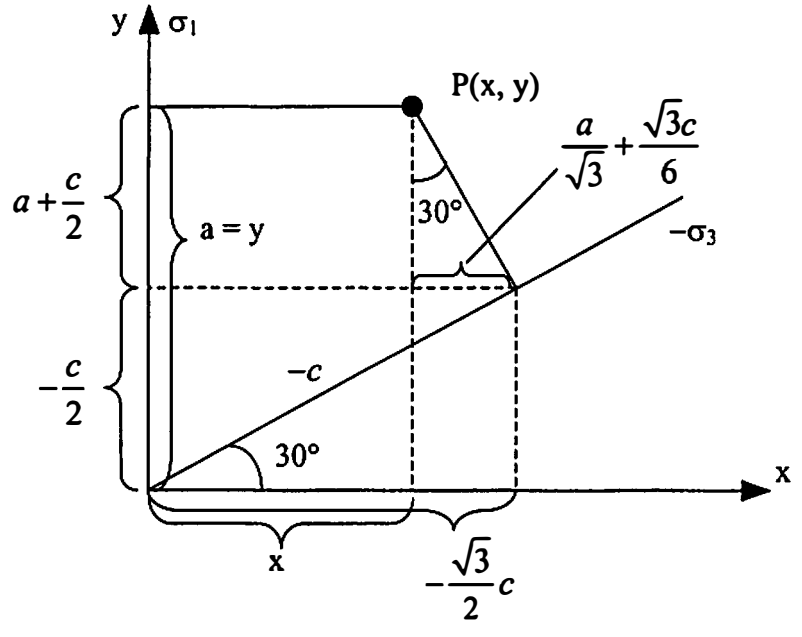

Figure A5.4 Co-ordinates of Stress Point P in Octahedral Plane with Basis along x and y

Vita

Amit Prashant was born in Kanpur, U.P., India, on July 27, 1976. He attended one of the best high schools in state and graduated in 1993. Following high school, Amit attended University of Roorkee, India, (currently known as Indian Institute of Technology, Roorkee) and graduated in 1997 with a bachelor of engineering degree in civil engineering. During his stay in Roorkee, he participated in many student activities and received uninterrupted merit scholarship for his academic performance. Upon completion of college, he began his engineering career working with Consulting Engineering Services (India) Ltd. in New Delhi, India, where he worked on a research project by Indian Road Congress. Realizing his interest in research and development, Amit decided to pursue for higher studies. In July 1999, Amit accepted a Graduate Research Assistantship from Clarkson University at Potsdam, NY, and started to pursue a master's degree in civil engineering under the supervision of Dr. D. Penumadu. Later, his study was approved for direct Ph.D program. In August 2001, Dr. Penumadu joined The University of Tennessee at Knoxville (UTK), and Amit followed him and transferred to UTK. Amit's research during the Ph.D program focused mainly on the study of the mechanical behavior of geomaterials using innovative experimental techniques and advanced constitutive modeling theories. He graduated as a Doctor of Philosophy in Civil Engineering in May 2004.